UNIVERSITY OF LJUBLJANA
FACULTY OF MATHEMATICS AND PHYSICS
DEPARTMENT OF PHYSICS

Lara Ulčakar

NON-EQUILIBRIUM DYNAMICS OF TOPOLOGICAL INSULATORS

Doctoral thesis

ADVISER: doc. dr. Tomaž Rejec
COADVISER: doc. dr. Jernej Mravlje

Ljubljana, 2020

UNIVERZA V LJUBLJANI
FAKULTETA ZA MATEMATIKO IN FIZIKO
ODDELEK ZA FIZIKO

Lara Ulčakar

NERAVNOVESNA DINAMIKA TOPOLOŠKIH IZOLATORJEV

Doktorska disertacija

MENTOR: doc. dr. Tomaž Rejec
SOMENTOR: doc. dr. Jernej Mravlje

Ljubljana, 2020

Acknowledgements

First I would like to thank my supervisors Tomaž Rejec, Jernej Mravlje and Anton Ramšak for their guidance and being at hand whenever I needed help. I greatly appreciate all of the freedom they gave me so I could pursue the topics that I found most intriguing and also for being able to organize the working schedule myself. The topic of my thesis belongs to a field, which was new for all of us and it was really exciting to discover it together. I had a lot of fun during our discussions and due to their open and friendly relationship I really felt as a part of a team. I am also grateful to Anton Ramšak for working with me on projects independent of my thesis and thus giving me a broader research spectrum.

I would also like to thank Domenico Monaco for our successful collaboration and his knowledge of mathematical physics, both of which contributed to my thesis. I would like to acknowledge Rok Žitko for giving initial stimulus for my personally favourite research project. I greatly appreciate my friends Gal Lemut, Michał Pacholski and Brecht Donvil who also work in my field and with whom I had a lot of interesting discussions, research visits and visits of summer schools.

Neravnovesna dinamika topoloških izolatorjev

Izvleček

Topološki izolatorji so pasovni izolatorji z netrivialno topologijo pasovne strukture, ki porodi robna stanja z energijo znotraj energijske reže in z njimi povezan transport brez disipacije. Doktorsko delo je posvečeno neravnovesnemu obnašanju topoloških izolatorjev, ki so bili v času zvezno preklopljeni čez topološki fazni prehod. Obravnavamo Chernov izolator, ki ga opisuje Qi-Wu-Zhangov model, in topološki izolator s simetrijo na obrat časa, ki ga predstavlja Bernevig-Hughes-Zhangov model. Za neravnovesni stanji sistemov pokažemo, da imata podobne transportne lastnosti. Po počasnih preklopih se (spin) Hallova prevodnost približa vrednosti v končnem osnovnem stanju, deviacije od le te pa padajo s časom preklopa kot potenčna funkcija. To obnašanje je v skladu s Kibble-Zurekovim mehanizmom. Obnašanje topoloških invariant zavisi od simetrijskega razreda sistema. Chernovo število se ohranja skozi čas, medtem ko časovni razvoj podre simetrijo na obrat časa in tako je klasifikacija z invarianto $\mathbb{Z}_2$ nesmiselna. Raziskava preklopov iz trivialne v topološko fazo Chernovega izolatorja v obliki traku pokaže, da se robna stanja pojavijo in so po počasnih preklopih zasedena. Ker ostane Chernovo število nespremenjeno, je po preklopu korespondenca rob-notranjost kršena. Kritične in neravnovesne lastnosti Chernovih izolatorjev smo proučevali tudi v realnem prostoru ob prisotnosti šibkega nereda. V osnovnem stanju se v profilu lokalnega Chernovega markerja pojavi kritična dolžinska skala, ki se sklada s skaliranjem dolžinske skale, ocenjene iz širine vrhu Berryjeve ukrivljenosti. Med preklopom čez fazni prehod dolžinska skala raste in se ustali pri vrednosti, ki se povečuje s časom preklopa po napovedih Kibble-Zurekovega mehanizma.

Ključne besede: topološki izolator, kvantni fazni prehod, simetrija na obrat časa, preklop, Kibble-Zurekov mehanizem, Landau-Zenerjev model, Hallov pojav, robno stanje, topološka invarianta, lokalni Chernov marker, kritični eksponent

PACS: 73.20.At, 03.65.Vf, 72.20.-i, 73.43.-f, 71.23.-k, 73.23.-b

Non-equilibrium dynamics of topological insulators

Abstract

Topological insulators are band insulators with a non-trivial band topology that leads to the presence of in-gap edge states at the boundaries and the associated dissipationless transport. The thesis is focused on non-equilibrium behaviour that arises when a topological insulator is slowly quenched, i.e. is smoothly driven across a topological phase transition. We study a Chern insulator, represented by the Qi-Wu-Zhang model, and a time-reversal symmetric topological insulator, described by the Bernevig-Hughes-Zhang model, and find similar non-equilibrium transport. For slow quenches, the (spin) Hall conductivity approaches that of the final ground state. The deviations from this value diminish as a power-law as the quench becomes slow, which is consistent with the Kibble-Zurek prediction. Conversely, the behaviour of topological invariants differs. The Chern number is conserved under a unitary evolution, while the classification of time-reversal symmetric phases breaks down since the time evolution dynamically breaks the time-reversal symmetry. We also investigate a Chern insulator in ribbon geometry and show that after the system is driven from a trivial to a topological phase, the in-gap states emerge and are populated with electrons. As the Chern invariant remains unchanged, the bulk-boundary correspondence is broken. In order to explore the critical properties and the non-equilibrium dynamics in real space, we introduce a weak disorder to a Chern insulator. In the ground state, the local Chern marker exhibits a critical length scale in its inhomogeneous profile that behaves consistently with the one extracted from the width of the peak in the Berry curvature. During the quench, the length scale grows and saturates to a value that increases with the quench time, as predicted by the Kibble-Zurek mechanism.

Keywords: topological insulator, quantum phase transition, time-reversal symmetry, quench, Kibble-Zurek mechanism, Landau-Zener model, Hall effect, edge state, topological invariant, local Chern marker, critical exponent

PACS: 73.20.At, 03.65.Vf, 72.20.-i, 73.43.-f, 71.23.-k, 73.23.-b

Contents

List of symbols and abbreviations

Abbreviation	Description
QWZ	Qi-Wu-Zhang
BHZ	Bernevig-Hughes-Zhang
LCM	local Chern marker
BZ	Brillouin zone

Symbol	Description
$\mathbf{k}$	crystal momentum
$\mathbf{k}_c$	momentum where the energy gap closes
q	small deviation from energy gap closing, $\lvert\mathbf{k} - \mathbf{k}_c\rvert$
N	linear size of a system with periodic boundary conditions
N_i	linear size of a system in ribbon geometry, $i = x, y$
$\hat{\sigma}_i$	Pauli matrices denoting orbital degrees of freedom, $i = x, y, z$
$\hat{s}_i$	Pauli matrices denoting spin degrees of freedom, $i = x, y, z$
$E_n(\mathbf{k})$	eigenenergy corresponding to the n-th energy band and $\mathbf{k}$
$\hat{H}$	Hamiltonian operator
$\Omega_n(\mathbf{k})$	Berry curvature of the n-th energy band
C	Chern number
$c(\mathbf{r})$	local Chern marker
N_{bulk}	$\mathbb{Z}_2$ topological invariant
θ	Wannier center flow
$\hat{\mathcal{T}}$	time-reversal symmetry operator
$\hat{\mathcal{C}}$	particle-hole symmetry operator
$\hat{\Gamma}$	chiral symmetry operator

Symbol	Description
$\mathbf{E}$	electrical field
$\mathbf{A}$	vector potential
τ_E	characteristic time of switching on of electric field
$\hat{\mathbf{J}}$	current operator
$\hat{\mathbf{J}}^{\text{spin}}$	spin current operator
e	electric charge of an electron
σ_{xy}	Hall conductivity
$\sigma_{xy}^{\text{spin}}$	spin Hall conductivity
G_{xy}	Hall conductance
G_0, σ_0	e^2/h
σ_0^{spin}	$e/2\pi$
ξ	typical length scale or the correlation length
τ_r	typical time scale or relaxation time
ν	correlation length critical exponent
z	dynamical critical exponent
t_F	freeze-out time
τ	quench duration
u	control parameter
u_c	critical point
N_{exc}	total density of excitations
$n_{\text{exc}}(\mathbf{k})$	momentum distribution of excitations

Throughout the thesis we set $\hbar = 1$ and the lattice constant to 1.

Chapter 1

Introduction

The topological insulators are band insulators that at the boundaries host gapless conducting states which avoid dissipation. The occurrence of these edge states has a topological origin. Namely, the electronic structure can be given a geometric significance and in the associated 'shape' one can recognize a global, detail-independent, *topological* property that is preserved upon deformations of the electronic structure that preserve the band gap. Due to the change of the topological property on going from the topological inside of the topological insulator to the non-topological surroundings, the gapless edge states appear at the boundary. The quest for identifying different kinds of topological matter along its promise for potential future applications in nano-electronics, spintronics and quantum computation [1, 2, 3, 4, 5, 6] has made topological insulators one of the focal points of condensed matter physics for the last decade. The field has started out in 1980 with the discovery of the integer quantum Hall effect [7] that takes place in a two-dimensional electron gas in the presence of a strong magnetic field. Haldane [8] showed in 1988 that the anomalous quantum Hall effect can appear also in systems in the absence of magnetic field. The real boost however happened when a different insulating phase of matter – the time-reversal symmetric topological insulator – that exhibits the spin Hall effect was theoretically [9, 10, 11] predicted in 2005 and experimentally confirmed [12] in 2007. This was followed by the prediction of three-dimensional topological insulators [13] that exhibit surface states and topological superconductors [14, 15, 16], in which Majorana zero modes appear at the edges of a one-dimensional system. Several examples of topological insulators were confirmed in experimental setups, such as semiconductor quantum wells [12, 17], ultracold atoms [18, 19, 20, 21], graphene-like heterostructures [22, 23, 24, 25], and in solid state materials [26, 27, 28, 29, 30]. This vast interest in topological matter led to novel physical realizations of topological insulators such as photonic topological insulators [31] and other kinds of topological systems such as Weyl semimetals [32], non-Hermitian topological systems [33], and crystalline topological insulators [34] (where the topological properties demand preservation of certain crystalline symmetries).

Topological insulators [35, 36] are interesting also conceptually as they fall out of the scope of the Landau's theory of phase transitions [37]. According to the Landau's theory, a phase transition occurs when a certain symmetry of a system is spontaneously broken. The phase transition to an ordered phase is signalled by the appearance of a non-vanishing value of the local order parameter, a quantity that changes upon symmetry operations and that would hence vanish provided the

symmetry was respected. Or put differently, in quantum systems, the spontaneous symmetry breaking is accompanied with the degeneracy of the ground state. For example, a ferromagnet breaks rotational symmetry despite the fact that the fundamental interactions are isotropic. This is signalled in a non-zero magnetization, which is the local order parameter that is equal to zero in the high-symmetry paramagnetic phase. Topological insulators do not belong to this classification paradigm as they do not break any symmetries, have no degenerate ground states and no local order parameter. However, they do exhibit different phases of matter, which are signalled in macroscopic properties such as the quantum (spin) Hall effect and the presence of gapless boundary modes. These properties are insensitive to smooth changes in material's parameters that do not cross a quantum phase transition. They are usually in one-to-one correspondence with the topological invariant, an integer-valued highly non-local order parameter that characterizes different phases of topological insulators. For example, the topological invariant of systems exhibiting the quantum Hall effect is the Chern number and may take any integer value and it is proportional to the Hall conductivity.

The topological insulators have to be distinguished from the systems with topological order [38], which are also characterized with a topological invariant. However, topological order is usually associated with exotic phases arising from many-body physics, such as the fractional quantum Hall effect [39] and $\mathbb{Z}_2$ spin liquids [40]. These systems exhibit degenerate ground states, anyonic quasiparticles and long-range entanglement, all of which topological insulators lack. While this work focuses on topological insulators that are well described in terms of single particle quantum mechanics, strong electron-electron interactions give rise to interesting phenomena. For example, strong interactions may drive a trivial band insulator, possibly across a first-order phase transition [41, 42, 43], into a topological phase [44, 45, 46, 47].

Topological phases of matter and their characterization with topological invariants is understood through concepts of adiabatic transformations and topological equivalence. An adiabatic transformation is a smooth change of system's parameters that does not close the energy gap and conserves system's symmetries, such as the time-reversal symmetry, the particle-hole symmetry and the chiral symmetry. Two systems are topologically equivalent if they can be transformed one into the other with an adiabatic transformation. While the two systems may differ in microscopic details, they have the same macroscopic transport properties and the same topological invariant. A trivial insulator is a system that has the topological invariant equal to zero and is topologically equivalent to the atomic limit. A system in the atomic limit has a set of exponentially localized Wannier states that respect all the system's symmetries and when the distance between the atoms is taken to infinity, the Wannier states coincide with localized atomic orbitals. The topological invariant of such systems is zero. The topological invariant can be calculated from the geometric properties of the bulk. For translation invariant systems it can be expressed as an integral of a curvature function over the whole Brillouin zone, which implies the global nature of the topological invariant. This is reminiscent of the mathematical topological classification of two-dimensional closed surfaces. Two surfaces are topologically equivalent when they have the same genus. A traditional example is a coffee cup, which is topologically equivalent to a doughnut as both of them have the genus equal to 1. Genus is calculated with the Gauss-Bonnet theorem, which relates it to the surface integral of the curvature of the 2D surface. In

solid state systems the Brillouin zone plays the role of the surface and, in the case of a system that exhibits the quantum Hall effect, the Berry curvature plays the role of the curvature. The Berry curvature is related to the Berry phase, which is a phase that a system acquires after a cyclic adiabatic process.

Topological insulators belong to different symmetry classes [14, 15, 48, 49], for example the quantum Hall effect and the spin Hall effect are described by a distinct topological invariant. Topological properties depend on the dimensionality and the presence or absence of the time-reversal symmetry, the particle-hole symmetry and the chiral symmetry. The system can be either trivial or may exhibit different topological phases that are characterized by a topological invariant, which may belong to integers $\mathbb{Z}$, for example in the quantum Hall effect, or is of the $\mathbb{Z}_2$ type, taking values 0 or 1, as for example in the spin Hall effect.

As already mentioned, D-dimensional topological systems exhibit in-gap states that are localized at a $(D-1)$-dimensional boundary between systems belonging to the same symmetry class and being in different topological phases. This thesis is dedicated to the study of two-dimensional topological systems, which have one-dimensional boundaries - edges. The edge states are one-dimensional as they propagate along the edge of the system. Bulk-boundary correspondence relates the number of edge states to the change of the topological invariant across the boundary. This theorem also implies topological protection of the edge states against dissipation due to disorder present at the edges: even if the edge is disordered, the electrons in edge states do not dissipate as long as the bulk stays intact. In a system, exhibiting the quantum Hall effect, this results in a perfect quantization of the Hall conductance. The electrons in the edge states are called chiral as all of them propagate in one direction. Different behaviour is expected in 2D topological insulators with time-reversal symmetry that exhibit the spin Hall effect. Due to time-reversal symmetry, all of the energy eigenstates come in degenerate pairs called Kramer pairs. Each edge state has a counter propagating edge state. One pair of such edge states is topologically protected against disorder that respects the time-reversal symmetry. The electrons in the edge states are called helical, as the direction of propagation is connected to their spin when the projection of spin is a conserved quantity.

While the ground-state physics of topological insulators is already well established, less is known about their response to time-dependent driving, which is a fundamental question and is currently a subject of an active investigation. Besides theoretical interest, knowing the response to time-dependent driving is of practical importance since some realizations of topological insulators with ultracold atoms require time-dependent driving. A prominent example are Floquet insulators [50, 51, 52], in which the periodic driving of a trivial insulator induces a non-trivial topological phase. The work presented in this thesis belongs to another line of investigation, which focuses on the dynamical critical properties of topological systems. These properties are probed by studying quenches across a topological phase transition. A quench induces a change of the Hamiltonian, such that the starting and the final Hamiltonians have different topological phases. Often, a quench is understood as a sudden change of a Hamiltonian's parameters. In this thesis, we study *slow* quenches where the change of parameters is a continuous function of time. As different topological phases are separated by the energy gap closing, the system ends up in a non-equilibrium state after the quench no matter how slow the quench

was performed. The dynamics is well described by the Landau-Zener model, which provides an exact solution for the wave function in the case of a two-band system. We use this model throughout the thesis to analytically explain the non-equilibrium properties such as the number of excitations and the transport coefficients.

The non-equilibrium nature of the resulting systems is signalled in transport and topological properties, which deviate from the ones of the final Hamiltonian ground state. The post-quench topological properties were shown to highly depend on the symmetry class of the quenched system [53]. In the case of two-dimensional Chern insulators, the Chern number remains well defined and is equal to the one evaluated in the initial state [50, 54, 55, 56]. On the other hand, the winding number [53, 57, 58], describing the phase of one-dimensional systems with the chiral symmetry like the Su-Schrieffer–Heeger model [59], and the $\mathbb{Z}_2$ invariant for the two-dimensional time-reversal symmetric topological insulators [53, 56], are not well defined after a quench since the time-evolution breaks the chiral or the time-reversal symmetry of the state, which is needed for classification with the corresponding invariants.

Contrary to topological properties, the transport properties were shown to approach the values in the final ground state [56, 60, 61, 62] in the limit of an infinitely slow quench. The ground-state value is never fully reached since during the quench the energy gap closes and thus the excitations are always present. For slow quenches, the deviation of the transport coefficients from the ground state value can be connected to the density of excitations that are present in the system.

The density of excitations [56, 63, 64] follows the Kibble-Zurek scaling [65, 66]. The Kibble-Zurek mechanism [65, 66, 67] describes non-equilibrium properties of a system that was driven in a finite time over a symmetry breaking second order phase transition. In equilibrium, the relaxation time and the correlation length diverge as a function of the control parameter approaching the critical point by a power called the critical exponent [68]. Because of the divergence the system evolves non-adiabatically across the critical point. In the case of phase transitions with spontaneous symmetry breaking that entail a degeneracy of the ground state, such a process produces regions corresponding to different choices of the ground state. At meeting points of these regions topological defects can be formed. The size of the regions is set by the equilibrium correlation length at a 'freeze-out' time, an approximate time at which the system stopped evolving adiabatically. The density of topological defects is estimated as the inverse volume of the regions. The Kibble-Zurek scaling was observed experimentally in tunnel Josephson junctions [69, 70], multiferroics [71, 72, 73], ion Coulomb crystals [74, 75], Bose-Einstein condensates [76], and in a Rydberg atom quantum simulator [77].

Returning to topological insulators, the fact that the Kibble-Zurek scaling occurs in these systems is not expected on the first sight. However, topological insulators exhibit the critical behaviour close to the phase transition. For example, in Chern insulators the critical increase of a length scale has been noticed in the Berry curvature [78]. Some hope for establishing the analogy with systems with a local order parameter stems also from the discovery of the local Chern marker (LCM) that was introduced in reference [79] as a local indicator of the topological phase in Chern insulators. Furthermore, in reference [80] Caio et al. showed that in the ground state, the LCM exhibits a length scale that has the same critical behaviour as the length scale extracted from the Berry curvature. We show that the critical length scale is

revealed in the inhomogeneous profile of the LCM in the presence of weak disorder which breaks the translational invariance. The LCM exhibits roughly homogeneous regions, where it deviates below or above the average value that is equal to the Chern number. The size of these regions grows as a power-law as the topological phase transition is approached. Quenches across the topological phase transition directly reveal the Kibble-Zurek physics in real space. During the quench the growth of the inhomogeneities in the LCM follows the freeze-out behaviour and at the end of the quench their size obeys the Kibble-Zurek scaling.

This dissertation is structured as follows. In the introductory chapter 2, the concepts of the band theory, the quantum Hall effect, the topological equivalence, the Chern insulator, the time-reversal symmetric topological insulator, the edge states and symmetry classes are explained and experimental realizations of two-dimensional topological insulators are shortly reviewed. Chapter 3 introduces the Landau-Zener model and the solution of the time-dependent Schrödinger equation for an avoided two-level crossing, followed by the Kibble-Zurek mechanism. The chapter ends with a scaling theory of topological phase transitions. The following part of the thesis presents the main results on the non-equilibrium dynamics of topological insulators. Chapter 4 is dedicated to phase transitions and dynamical response in translation invariant systems, namely the Qi-Wu-Zhang (QWZ) model for the Chern insulator and the Bernevig-Hughes-Zhang (BHZ) model for the time-reversal symmetric topological insulators. Chapter 5 deals with the edge physics of a Chern insulator in ribbon geometry after a quench across a topological phase transition and its response to a weak electric field. In chapter 6, a weak disorder is introduced to the QWZ model and the ground state and post-quench properties are studied in real space.

Chapter 2

Topological band insulators

The topological insulators can be described in terms of the single particle band theory, which is thoroughly depicted in this chapter. We begin in section 2.1 with the definition of a band insulator and in section 2.2 we present the integer quantum Hall effect. In section 2.3 we introduce a model for a Chern insulator and for a time-reversal symmetric topological insulator in two dimensions and in section 2.4 we explain the edge physics of the corresponding systems. While the Chern insulator is topologically equivalent to systems exhibiting the integer quantum Hall effect, the time-reversal symmetric topological insulator has different topological properties due to the presence of the time-reversal symmetry. Besides the time-reversal symmetry, a presence of the particle-hole symmetry and/or the chiral symmetry also changes the topological properties. In section 2.5 we present the full categorization of topological matter according to those symmetries. At last, we present in section 2.6 experimental realizations of two-dimensional topological insulators.

2.1 Band insulator

A solid state system may be described as consisting of the *bulk* and the *boundaries*. The bulk is the translation invariant interior of the system which is usually considered in the thermodynamic limit. In the absence of electron-electron interactions, its electronic properties are described by the band theory. The band theory is based on the Bloch's theorem, which states that due to the translational symmetry the eigenstates of the Hamiltonian $\hat{H}$ may be chosen as plane waves $|\Psi_n(\mathbf{k})\rangle = |\mathbf{k}\rangle \otimes |\psi_n(\mathbf{k})\rangle$ with definite momentum $\mathbf{k}$ that belongs to the first Brillouin zone. The Hamiltonian is of block-diagonal form in the plane wave basis $\hat{H} = \sum_{\mathbf{k}} |\mathbf{k}\rangle\langle\mathbf{k}| \otimes \hat{H}(\mathbf{k})$, $\hat{H}(\mathbf{k})$ being the Bloch Hamiltonian with eigenstates $|\psi_n(\mathbf{k})\rangle$ and eigenenergies $E_n(\mathbf{k})$. Eigenenergies constitute the energy bands, that are indexed by n. The many-body ground state of such a system is a Slater determinant of single-body eigenstates $|\Psi_n(\mathbf{k})\rangle$ with an energy up to the Fermi level. An insulator is a system with the Fermi energy inside a band energy gap, which separates filled valence bands from empty conduction bands.

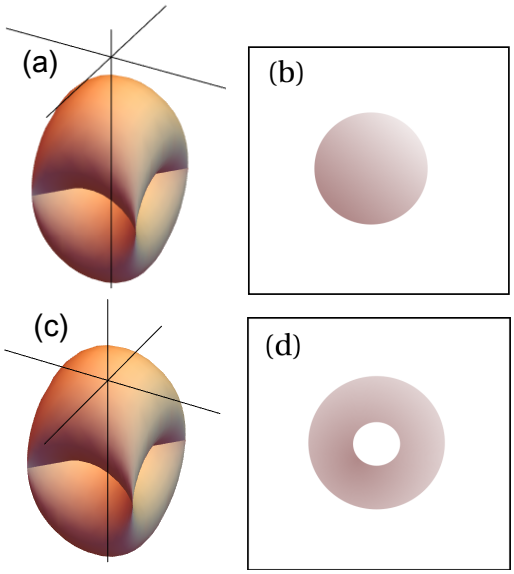

Figure 2.1: Schematic representation of (a), (b) topologically trivial systems and (c), (d) topologically non-trivial systems. Surface $\mathbf{d}(\mathbf{k})$ (2.6) for the QWZ model (4.1) as $\mathbf{k}$ sweeps through the whole Brillouin zone in (a) a trivial phase and (c) a topological phase, where the origin is included inside the closed surface. (b) shows a sphere and (d) a torus.

2.2 Integer quantum Hall effect

Topological insulators are systems that are topologically distinct from the atomic limit (or vacuum). Historically one of the first examples of an insulating state that is not topologically equivalent to the vacuum is the integer quantum Hall state [7]. The state appears when the two-dimensional electron gas is subjected to a strong perpendicular magnetic field B. The energy spectrum of electrons consists of quantized Landau levels with energies $\varepsilon_n = \hbar\omega_c(n + 1/2)$, where $\omega_c = |e|B/m$ is the cyclotron frequency, m being the electron mass and e its charge. In the semiclassical picture, the electrons travel in circular orbits with frequency ω_c. When N_F Landau levels are filled and the rest are empty, the system is an insulator due to the presence of the energy gap $\hbar\omega_c$. However, when electric field is applied in the plane of electron gas (y-direction), the Hall current arises perpendicularly to the electric field (x-direction) and the proportionality constant, the Hall conductivity, is quantized,

$$\sigma_{xy} = N_F \frac{e^2}{h}. \tag{2.1}$$

The presence of the magnetic field breaks the invariance of the lattice for translations for primitive vectors of the Bravais lattice. However, it is possible to define a magnetic unit cell with the area h/eB that includes one flux quantum, such that the system is translation invariant for translations for primitive vectors of such a magnetic unit cell. Therefore, the Bloch's theorem applies and the states are labelled by a crystal momentum $\mathbf{k}$ and form a band structure $E_n(\mathbf{k}) = \varepsilon_n$.

The difference between a trivial insulator and a quantum Hall state was explained by Thouless in 1982 [81] to lie in different topologies of the systems' Bloch Hamil-

tonians $\hat{H}(\mathbf{k})$. Adiabatically connected Hamiltonians belong to the same equivalence class, which are characterized by an integer valued *topological invariant* C, the Chern number, in the context of integer quantum Hall effect also known as TKNN (Thouless-Kohmoto-Nightingale-den Nijs) invariant. The theory of topological classes stems from the mathematical theory of fiber bundles [82]. Physically, the Chern number is connected to the Berry phase of the Bloch states $|\psi_n(\mathbf{k})\rangle$: when an electron, initially in the state $|\psi_n(\mathbf{k})\rangle$, is adiabatically transferred in momentum space around a closed loop, it acquires a Berry phase that is up to multiple of 2π equal to the line integral of *the Berry connection*

$$\mathbf{A}_n(\mathbf{k}) = -i\langle\psi_n(\mathbf{k})|\nabla_{\mathbf{k}}|\psi_n(\mathbf{k})\rangle. \tag{2.2}$$

This can be also expressed as an integral of *the Berry curvature*

$$\Omega_n(\mathbf{k}) = i\partial_{k_x}\langle\psi_n(\mathbf{k})|\partial_{k_y}|\psi_n(\mathbf{k})\rangle - i\partial_{k_y}\langle\psi_n(\mathbf{k})|\partial_{k_x}|\psi_n(\mathbf{k})\rangle \tag{2.3}$$

over momenta enclosed by the loop the electron has travelled. The Berry curvature may also be expressed in a gauge invariant form with the projector onto the n-th band $\hat{P}_n(\mathbf{k}) = |\psi_n(\mathbf{k})\rangle\langle\psi_n(\mathbf{k})|$ as

$$\Omega_n(\mathbf{k}) = i\mathrm{Tr}\{\hat{P}_n(\mathbf{k})[\partial_{k_x}\hat{P}_n(\mathbf{k}), \partial_{k_y}\hat{P}_n(\mathbf{k})]\}. \tag{2.4}$$

Integral of the Berry curvature over the whole Brillouin zone yields the Chern number C_n of the n-th energy band. Summing such contributions over all of the occupied bands gives the Chern number

$$C = -\frac{1}{2\pi}\sum_n \int \mathrm{d}\mathbf{k}\,\Omega_n(\mathbf{k}). \tag{2.5}$$

Authors of reference [81] calculated σ_{xy} (2.1) using the Kubo formula and showed that the number of occupied Landau levels N_F and the Chern number C are equal. When dealing with two-band systems, the Bloch Hamiltonian can be written in the following form,

$$\hat{H}(\mathbf{k}) = \mathbf{d}(\mathbf{k})\cdot\hat{\boldsymbol{\sigma}}, \tag{2.6}$$

where $\hat{\boldsymbol{\sigma}} = (\hat{\sigma}_x, \hat{\sigma}_y, \hat{\sigma}_z)$ are Pauli operators and $\mathbf{d}(\mathbf{k}) = (d_x(\mathbf{k}), d_y(\mathbf{k}), d_z(\mathbf{k}))$. In this case, the Chern number can be interpreted as the number of times the surface $\mathbf{d}(\mathbf{k})$ winds about the origin when $\mathbf{k}$ sweeps through the whole Brillouin zone. The surface $\mathbf{d}(\mathbf{k})$ of a trivial and a topological phase of the QWZ model are shown in figure 2.1(a) and figure 2.1(c). The characterization of the topological phase of an insulator with the Chern number carries similarities with the mathematical classification of two-dimensional surfaces. Two-dimensional surfaces can be topologically classified according to genus. Genus may be computed by using the Gauss-Bonnet theorem [82], which relates it to the integral of the Gaussian curvature over the closed surface. The Chern number is an integral of the Berry curvature over the Brillouin zone, thus it can be in this analogy connected to the genus (see figure 2.1).

2.3 Models for topological insulators

2.3.1 Haldane model - Chern insulator

A topological insulator is a band insulator that is topologically non-trivial. The first non-trivial system in the absence of external magnetic field was proposed by Haldane

in 1988 [8] and was based on spin-less graphene. Graphene is a two dimensional honeycomb lattice based on carbon atoms. As the honeycomb lattice consists of sublattices A and B, its energy dispersion consists of two energy bands. In the case of graphene they touch at two points $\mathbf{K}$ and $\mathbf{K}' = -\mathbf{K}$. In the vicinity of a gap-closing point, the energy dispersion is linear, forming a *Dirac cone*, and the Bloch Hamiltonian is equal to a two-dimensional massless Dirac Hamiltonian with $\mathbf{d}(\mathbf{k}) = (\hbar v_F q_x, \hbar v_F q_y, 0)$, where v_F is the Fermi velocity and $\mathbf{q} = (q_x, q_y, q_z) = \mathbf{k} - \mathbf{K}$ is small. The graphene model possesses the inversion symmetry and the time-reversal

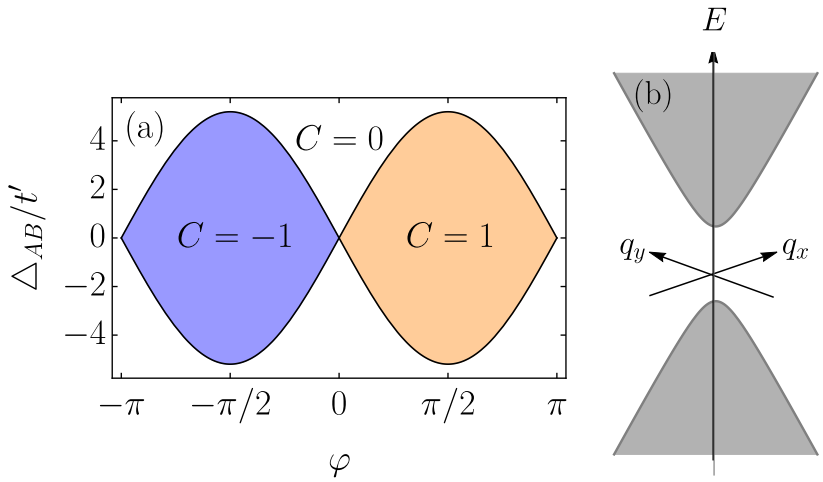

Figure 2.2: (a) Phase diagram of the Haldane model, consisting of a trivial phase (white) and two topologically non-trivial distinct phases with Chern numbers $C = 1$ (orange) and $C = -1$ (blue). (b) The energy dispersion close to momentum $\mathbf{K}$ where the energy gap closes.

symmetry (see section 2.3.2). Breaking either of the symmetries opens the band gap and the system is for momenta $\mathbf{k} = \mathbf{q} + \mathbf{K}$ close to the minimum of the energy gap at $\mathbf{K}$ described by the massive Dirac Hamiltonian with

$$\mathbf{d}(\mathbf{k}) = (\hbar v_F q_x, \hbar v_F q_y, m). \tag{2.7}$$

m is called a *mass term* and it is equal to the half of the energy gap. The inversion symmetry is broken by introducing a crystal field that introduces a difference $\triangle_{AB}$ between the on-site energies of the sublattices. This opens the band gap $m = \triangle_{AB}$ and a system becomes a trivial insulator. The energy dispersion about momentum $\mathbf{K}$ is shown in figure 2.2(b). Haldane proposed that opening the band gap by breaking the time-reversal symmetry will induce a new state of matter - *a topological Chern insulator*. The time-reversal symmetry was broken by introducing complex second nearest neighbour hoppings $t'e^{i\varphi}$, which produce a staggered pattern of magnetic flux in a unit cell, such that the total flux through the unit cell is zero. The phase diagram, shown in figure 2.2(a), consists of a trivial phase and two distinct topological phases. The topological phases are characterized by the Chern number C, which in the case of this model takes the values -1, 1 (topological) and 0 (trivial). In the topological phase, the system exhibits the anomalous quantum Hall effect with Hall conductivity $\sigma_{xy} = Ce^2/h$.

2.3.2 Kane-Mele model - time-reversal symmetric topological insulator

In 2005 Kane and Mele showed [9, 10] that topologically non-trivial states may also arise in systems with time-reversal symmetry. The specific model they studied was spin-full graphene in the presence of the spin-orbit interaction $\hat{\mathbf{s}} \cdot \hat{\mathbf{p}}$ and the Rashba interaction [9] $(\hat{\mathbf{s}} \times \hat{\mathbf{p}}) \cdot \mathbf{e}_z$, where $\hat{\mathbf{s}} = (\hat{s}_x, \hat{s}_y, \hat{s}_z)$ is the vector of the Pauli operators acting on the spin degree of freedom and $\hat{\mathbf{p}}$ is the momentum operator. The spin-orbit interaction introduces complex second nearest-neighbour hopping amplitudes and opens the energy gap of Dirac cones. Due to the time-reversal symmetry, the Hall current is zero in this system. However, the *spin Hall effect* takes place, meaning that applying an electric field in y-direction will induce a spin current J_x^{spin} in x-direction,

$$J_x^{\text{spin}} = \sigma_{xy}^{\text{spin}} E_y. \tag{2.8}$$

The proportionality constant $\sigma_{xy}^{\text{spin}}$ is called the spin Hall conductivity. In the absence of the Rashba interaction, the spin sectors are decoupled and the model is simply two copies of the Haldane model with opposite signs of the Hall conductivity. Thus, the spin Hall conductivity is quantized in the units of $e/2\pi$. Systems with time-reversal symmetry, exhibiting the spin Hall effect, were established as a novel topological phase [10], called the *time-reversal symmetric topological insulator*. In order to understand this state of matter, let us first explain the constraints that the time-reversal symmetry imposes on the system.

The time-reversal symmetry is represented by an antiunitary operator $\hat{\mathcal{T}} = i\hat{s}_y K$, K being the complex conjugation. A defining property of an antiunitary operator is its action on the scalar product $\langle \hat{\mathcal{T}}\psi | \hat{\mathcal{T}}\varphi \rangle = \langle \psi | \varphi \rangle^*$, where $|\psi\rangle$ and $|\varphi\rangle$ are two arbitrary states. Taking $|\varphi\rangle = \hat{\mathcal{T}}|\psi\rangle$ and evaluating the scalar product

$$\langle \hat{\mathcal{T}}\psi | \psi \rangle^* = \langle \hat{\mathcal{T}}^2\psi | \hat{\mathcal{T}}\psi \rangle = -\langle \psi | \hat{\mathcal{T}}\psi \rangle = -\langle \hat{\mathcal{T}}\psi | \psi \rangle^*, \tag{2.9}$$

yields that the states are orthogonal. States $|\psi\rangle$ and $\hat{\mathcal{T}}|\psi\rangle$ are called the Kramers partners. Note that this property follows from $\hat{\mathcal{T}}^2 = -1$. A system is time-reversal symmetric when its Bloch Hamiltonian satisfies the following condition:

$$\hat{\mathcal{T}} \hat{H}(\mathbf{k}) \hat{\mathcal{T}}^{-1} = \hat{H}(-\mathbf{k}). \tag{2.10}$$

The time-reversal symmetry with the property $\hat{\mathcal{T}}^2 = -1$ entails the system with *Kramers degeneracy*: every eigenstate $|\psi_n(\mathbf{k})\rangle$ of $\hat{H}(\mathbf{k})$ with energy $E_n(\mathbf{k})$ has a degenerate time-reversed partner $\hat{\mathcal{T}}|\psi_n(\mathbf{k})\rangle$. This follows from the time-independent Schrödinger equation for the eigenstate $|\psi_n(\mathbf{k})\rangle$

$$\hat{H}(\mathbf{k})|\psi_n(\mathbf{k})\rangle = E_n(\mathbf{k})|\psi_n(\mathbf{k})\rangle. \tag{2.11}$$

Rewriting the Hamiltonian as in equation (2.10) one obtains

$$\hat{\mathcal{T}}^{-1} \hat{H}(-\mathbf{k}) \hat{\mathcal{T}} |\psi_n(\mathbf{k})\rangle = E_n(\mathbf{k})|\psi_n(\mathbf{k})\rangle, \tag{2.12}$$

and acting from the left with $\hat{\mathcal{T}}$ one ends up with

$$\hat{H}(-\mathbf{k}) \hat{\mathcal{T}} |\psi_n(\mathbf{k})\rangle = E_n(\mathbf{k}) \hat{\mathcal{T}} |\psi_n(\mathbf{k})\rangle. \tag{2.13}$$

The state $\hat{\mathcal{T}}|\psi_n(\mathbf{k})\rangle$ is the eigenstate of $\hat{H}(-\mathbf{k})$ with the energy $E_n(\mathbf{k})$, which also implies that the spectrum is symmetric $E_n(\mathbf{k}) = E_n(-\mathbf{k})$. Every eigenvalue is (at

least) twice degenerate at the special points called the *time-reversal invariant momenta* $\mathbf{k}_{\mathrm{TRIM}}$. These momenta map unto themselves under inversion, one of which is at the center of the Brillouin zone and others at the edges.

Hamiltonians with the time-reversal symmetry belong to a different symmetry class than the Chern insulator and their phase is characterized by the $\mathbb{Z}_2$ topological invariant N_{bulk}. It distinguishes between the topological insulator ($N_{\mathrm{bulk}} = 1$) and the trivial band insulator ($N_{\mathrm{bulk}} = 0$). The Hamiltonians with different N_{bulk} cannot be adiabatically deformed into one another without breaking the time-reversal symmetry and closing the band gap. There are several equivalent definitions of the $\mathbb{Z}_2$ invariant, the first one proposed by Kane and Mele in reference [10] being:

$$N_{\mathrm{bulk}} = \frac{1}{2\pi i} \oint_{\partial \frac{1}{2}\mathrm{BZ}} d \log[\mathrm{Pf}(m)] \bmod 2, \tag{2.14}$$

where the integral is taken along the edge of the half Brillouin zone. $\mathrm{Pf}(m)$ is the Pfaffian of a matrix m, which consists of the matrix elements of the time-reversal operator $\hat{\mathcal{T}}$,

$$m_{m,n}(\mathbf{k}) = \langle \psi_m(\mathbf{k}) | \hat{\mathcal{T}} | \psi_n(\mathbf{k}) \rangle. \tag{2.15}$$

Here, $|\psi_n(\mathbf{k})\rangle$ is an occupied eigenstate. For systems with inversion symmetry, the invariant simplifies to the expression given by signs of the Pfaffian at time-reversal symmetric momenta

$$(-1)^{N_{\mathrm{bulk}}} = \prod_i \mathrm{sgn}(\mathrm{Pf}[m(\mathbf{k}_{\mathrm{TRIM},i})]). \tag{2.16}$$

If a two-dimensional system conserves the spin projection $\hat{s}_z$, then the system may be decomposed into two independent Chern insulators with Chern numbers $C_\uparrow$ and $C_\downarrow$. The time-reversal symmetry requires the total Chern number to be zero $C = C_\uparrow + C_\downarrow = 0$, however the difference gives the $\mathbb{Z}_2$ invariant as [35]

$$N_{\mathrm{bulk}} = \left[\frac{1}{2}(C_\uparrow - C_\downarrow) \right] \bmod 2. \tag{2.17}$$

2.4 Edge states and the bulk-boundary correspondence

2.4.1 Chern insulator

The fundamental property of the topological systems is the existence of in-gap conducting states that appear at the boundary between regions with different values of the topological invariant. The existence of such states was originally predicted at the boundary between the system exhibiting the integer quantum Hall effect and the vacuum [83]. In the semiclassical picture, schematically shown in figure 2.4, the electrons in the bulk move about circular orbits, while at the edge they undergo a skipping motion in one direction. Such states that propagate only in one direction are called *chiral*. As there are no counter propagating edge states, electrons in the edge states cannot scatter and are thus robust against any kind of disorder. This accounts for a perfect quantization of the Hall conductance.

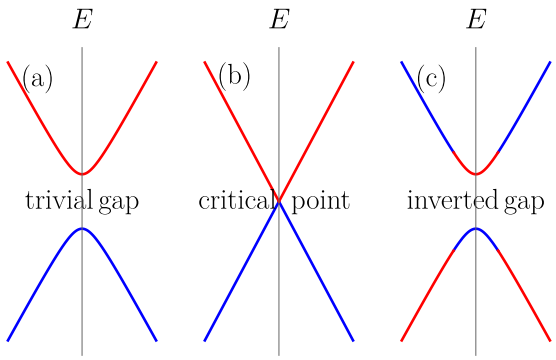

Figure 2.3: Schematic representation of (a) a trivial band structure, (b) a band structure at a critical point and (c) an inverted band structure. Red colour represent the orbital $|A\rangle$ and the blue colour the orbital $|B\rangle$.

The existence of the in-gap states is related to *the band inversion* [84], where the orbital character of the bands is inverted close to the gap closing. This concept is depicted in figure 2.3, where the red colour corresponds to the orbital $|A\rangle$ and the blue colour to the orbital $|B\rangle$. In the trivial phase, the orbital $|A\rangle$ corresponds to the conduction band and the orbital $|B\rangle$ to the valence band. On crossing the critical point into the topological phase, the bands change orbital character at the gap closing point, resulting in an inverted band structure. At the interface between a trivial insulator and a topological insulator the states appear at the interface with energy inside the gap and thus interpolate between the trivial and the topological band structure and thus preserve the orbital character.

To discuss this more rigorously, consider an interface along x-direction of a trivial insulator with a mass parameter $m > 0$ and a topological insulator with an inverted band structure $-m$. Across the boundary, the mass term changes sign and is thus space dependent $m \to m(y)$. Solving the massive Dirac equation (2.6) with $\mathbf{d}(\mathbf{k}) = (\hbar v_F q_x, \hbar v_F q_y, m(y))$ by exchanging $\mathbf{q} \to -i\nabla$ gives an exact solution for the edge state

$$\psi_{q_x}(x, y) \propto e^{iq_x x} e^{-\int_0^y dy' m(y')/v_F} \begin{pmatrix} 1 \\ 1 \end{pmatrix} \tag{2.18}$$

with the energy $E(q_x) = \hbar v_F q_x$, ranging from the valence band to the conduction band. The dispersion of the in-gap states has a positive group velocity $dE/dq_x = \hbar v_F$, meaning that the states are right moving chiral edge modes.

Adiabatic changes of the Hamiltonian on either side of the interface may change the energy dispersion of the in-gap states, for example it may develop a kink such that it crosses the E_F twice with positive and once with negative group velocity. The difference of right-moving N_R and left-moving states N_L is robust to such changes and equal to the change of the topological invariant across the boundary $\triangle n$,

$$N_R - N_L = \triangle n. \tag{2.19}$$

This relation is called *the bulk-boundary correspondence*. As discussed below, the presence of disorder may induce scattering between counter-propagating states, therefore $\triangle n$ states are topologically protected.

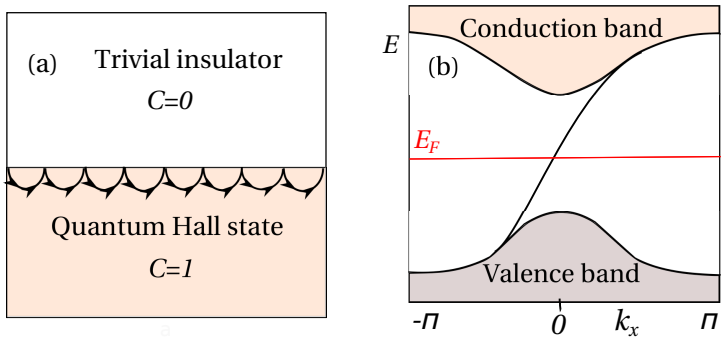

Figure 2.4: (a) Schematic representation of the edge states as skipping cyclotron orbits at the interface between the quantum Hall state and a normal insulator. (b) The energy dispersion of a semi infinite strip described by the Haldane model in the topological phase.

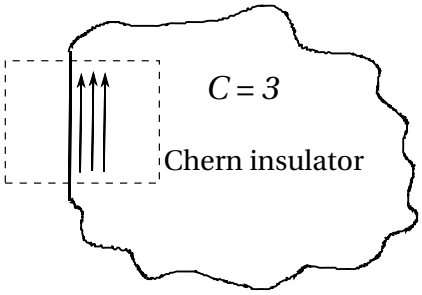

Figure 2.5: Schematic representation of a Chern insulator with Chern number $C = 3$ and a disordered edge. The region inside the dashed rectangle represents the clean part of the edge where the disorder was adiabatically turned off.

The edge states were until now introduced at a clean boundary along $y = 0$, such that the momentum k_x was a good quantum number. In this sense, the edge is a clean one-dimensional conductor. The question is, what happens if the boundary is disordered? One-dimensional conductors are known to become Anderson localized [85] for any value of disorder, which turns them into insulators. The fact that edge disorder cannot localize the edge states of a topological insulator is explained by the following argument. Disorder on the edge has an insignificant effect on the bulk. Let us then take a small part of the edge, indicated with a dashed square in figure 2.5, which is still large enough that it can be considered as 'bulk'. We then adiabatically deform the Hamiltonian of that region such that the disorder is turned off. Since this region is clean, it contains the edge states (2.18). Consider now a particle occupying the edge mode at the Fermi energy E_F. At the interface with a disordered part of the edge, the particle cannot scatter back into the clean region as there are no edge modes in the spectrum that travel in the opposite direction. It also cannot stop at the boundary since then the particles would accumulate. The particle also cannot travel inside the bulk since its energy is deep inside the band gap. Thus, the particle has to travel all around the disordered part of the system in order to return to the clean region. Low energy conducting modes are thus also present at disordered edges.

2.4.2 Time-reversal symmetric topological insulator

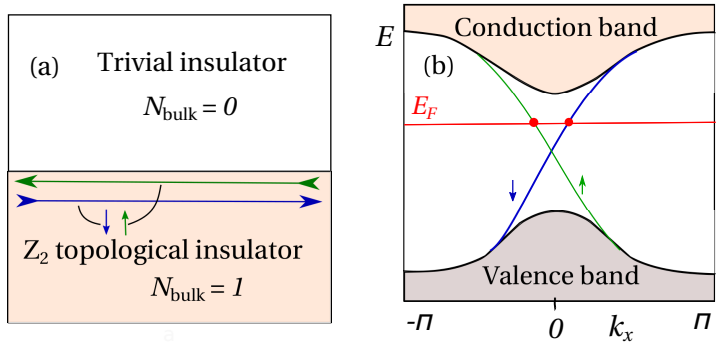

Figure 2.6: (a) Boundary between a time-reversal symmetric topological insulator and a trivial insulator hosts a pair of counter propagating edge states with opposite spin polarization. (b) Energy dispersion of a time-reversal symmetric topological insulator with an edge, blue and green lines denoting the edge states.

The bulk-boundary correspondence also holds for time-reversal symmetric topological insulators. Figure 2.6(a) shows a schematic representation of the boundary and figure 2.6(b) the corresponding energy dispersion as a function of momentum k_x along the edge. At a boundary between a vacuum and a topological insulator a Kramers pair of counter propagating modes appears inside the gap. These in-gap modes are again localized at the edge and they have opposite polarizations of spin. Such states are called *helical* due to the correlation between the momentum and the spin. Even though the modes are counter propagating, they do not scatter with their Kramers partner due to the time-reversal symmetry [9]. However, when there are $N_K > 1$ Kramers partner edge modes, the counter propagating modes belonging to different Kramers partners may scatter. Therefore, only systems with an odd N_K have a single topologically protected Kramers pair, while systems with an even number N_K have none. The number of protected pairs of edge modes is equal to $\triangle N_{\text{bulk}} \bmod 2$, where $\triangle N_{\text{bulk}}$ is the change of the $\mathbb{Z}_2$ invariant across the boundary.

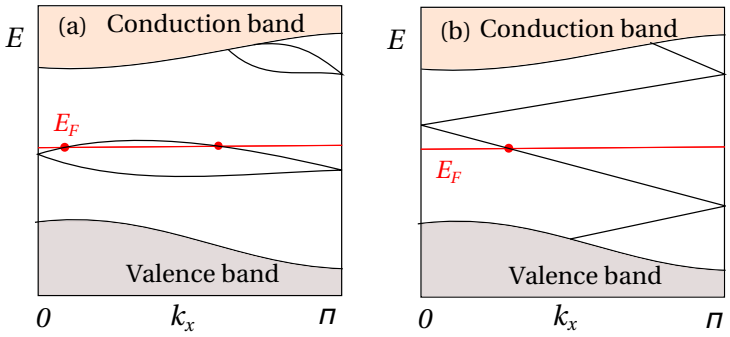

Figure 2.7: Schematic representation of the edge states in a system with time-reversal symmetry in (a) a trivial phase with an even number of edge states crossing the Fermi energy E_F and in (b) a topological phase with an odd number of edge states. Only half of the Brillouin zone is shown because the diagram is symmetric about time-reversal symmetric momenta 0 and π due to the time-reversal symmetry.

Let us further explain why the parity of the number of in-gap state partners is connected to the topological phase of the system. Figure 2.7 shows the energy dispersion of two different time-reversal symmetric systems as a function of momentum k_x. The dispersion is shown for momenta belonging to a half of the Brillouin zone $0 < k_x < \pi$ as the other half $-\pi < k_x < 0$ is the mirror image due to the time-reversal symmetry. The in-gap states are doubly degenerate at time-reversal symmetric momenta $k_x = 0$ and $k_x = \pi$, while they are in general split for a general k_x. There are two different scenarios of how the in-gap states interpolate between degeneracy points: the in-gap states may connect pairwise as in figure 2.7(a), intersecting the Fermi energy an even number of times. By adiabatically transforming the Hamiltonian, it is possible to push such pairs of states inside the conduction or the valence band and thus clean the gap of states. The second scenario is such that an odd number of in-gap states crosses the Fermi level. As the time-reversal invariant momenta have to be degenerate, there is no such adiabatic transformation of the Hamiltonian that could push the states out of the gap.

2.5 Classification of topological matter according to symmetries

Despite the fact that the Haldane model and the Kane-Mele model are very similar systems, both hosting non-interacting electrons on a honeycomb lattice with short range tunnelling amplitudes, they are described by distinct topological invariants. The distinction is the presence of the time-reversal symmetry in the Kane-Mele model, which destroys the non-trivial Chern phases, however it may induce a $\mathbb{Z}_2$ topological phase. As shown in references [14, 15, 48, 49], based on the theory of equivalence classes of random matrices by Altland and Zirnbauer [86], the type of the topological invariant may be specified according to the symmetries and the dimensionality of the lattice. The symmetry class is determined by the presence or absence of time-reversal symmetry with operator $\hat{\mathcal{T}}$, the particle-hole symmetry with operator $\hat{\mathcal{C}}$ and the chiral symmetry with operator $\hat{\Gamma}$, and the values of the their squared operators ± 1. The classification is shown in table 2.1, where entries $\mathbb{Z}$, $\mathbb{Z}_2$ and 0 denote the type of the topological invariant. The table is periodic for dimensionality D with period 8.

The particle-hole symmetry is antiunitary and its operator $\hat{\mathcal{C}} = \hat{U}K$ is a product of a unitary operator $\hat{U}$ and complex conjugation K. The system possesses the particle-hole symmetry when its Bloch Hamiltonian satisfies the following relation

$$\hat{\mathcal{C}}\hat{H}(\mathbf{k})\hat{\mathcal{C}}^{-1} = -\hat{H}(-\mathbf{k}), \tag{2.20}$$

It follows that every eigenstate with energy E has a partner with the energy $-E$.

The chiral symmetry $\hat{\Gamma}$ is unitary and imposes the following restriction on the Bloch Hamiltonian

$$\hat{\Gamma}\hat{H}(\mathbf{k})\hat{\Gamma}^{-1} = -\hat{H}(\mathbf{k}). \tag{2.21}$$

It gives a rise of the symmetric spectrum about $E = 0$ and in the eigenbasis of the operator $\hat{\Gamma}$ the Hamiltonian is of block-off-diagonal form. When the particle-hole symmetry and the time-reversal symmetry are present, the chiral symmetry is equal to their product $\hat{\Gamma} = \hat{\mathcal{T}}\hat{\mathcal{C}}$.

Symmetry				D							
AZ	$\hat{\mathcal{T}}$	$\hat{\mathcal{C}}$	$\hat{\Gamma}$	1	2	3	4	5	6	7	8
A	0	0	0	0	$\mathbb{Z}$	0	$\mathbb{Z}$	0	$\mathbb{Z}$	0	$\mathbb{Z}$
AIII	0	0	1	$\mathbb{Z}$	0	$\mathbb{Z}$	0	$\mathbb{Z}$	0	$\mathbb{Z}$	0
AI	1	0	0	0	0	0	$\mathbb{Z}$	0	$\mathbb{Z}_2$	$\mathbb{Z}_2$	$\mathbb{Z}$
BDI	1	1	1	$\mathbb{Z}$	0	0	0	$\mathbb{Z}$	0	$\mathbb{Z}_2$	$\mathbb{Z}_2$
D	0	1	0	$\mathbb{Z}_2$	$\mathbb{Z}$	0	0	0	$\mathbb{Z}$	0	$\mathbb{Z}_2$
DIII	-1	1	1	$\mathbb{Z}_2$	$\mathbb{Z}_2$	$\mathbb{Z}$	0	0	0	$\mathbb{Z}$	0
AII	-1	0	0	0	$\mathbb{Z}_2$	$\mathbb{Z}_2$	$\mathbb{Z}$	0	0	0	$\mathbb{Z}$
CII	-1	-1	1	$\mathbb{Z}$	0	$\mathbb{Z}_2$	$\mathbb{Z}_2$	$\mathbb{Z}$	0	0	0
C	0	-1	0	0	$\mathbb{Z}$	0	$\mathbb{Z}_2$	$\mathbb{Z}_2$	$\mathbb{Z}$	0	0
CI	1	-1	1	0	0	$\mathbb{Z}$	0	$\mathbb{Z}_2$	$\mathbb{Z}_2$	$\mathbb{Z}$	0

Table 2.1: Classification of topological matter according to Altland and Zirnbauer (AZ) into 10 symmetry classes [86]. $\hat{\mathcal{T}}$ denotes the time-reversal symmetry, $\hat{\mathcal{C}}$ the particle-hole symmetry and $\hat{\Gamma}$ the chiral symmetry, and the values below signal the presence (± 1) and the absence (0) of the symmetries. ± 1 is the squared value of the symmetry operator, for example $\hat{\mathcal{T}}^2 = \pm 1$. The topological classification is denoted by the corresponding topological invariants ($\mathbb{Z}$, $\mathbb{Z}_2$ and 0) and depends on the spatial dimension of the system D and on the symmetries. The table is periodic with $D \to D + 8$.

Recently, a lot of attention has been given to topological crystalline insulators [34], whose topological nature arises from the crystal symmetries: point-group symmetries such as inversion, mirror and rotation; and also space-group symmetries, such as glide planes and screw axes. However, these topological phases are considered as weaker since their topological features are susceptible to disorder, which breaks the crystal symmetries. Also, not all the phases can host topological surface states since the edge by itself may break the crystal symmetry that entails the system with topology.

2.6 Experimental realizations of topological insulators

In 2005 Kane and Mele showed that a topological phase may arise in graphene [9]. The presence of the spin-orbit interaction induces a topological phase. However, the bulk energy gap is of the order of μeV, which is too small to probe the topological insulator properties at temperatures accessible in experiments. Since then, several experimental realizations of topological insulators with a large enough energy gap have been successfully confirmed, the first one being in 2007 in HgTe quantum wells [12]. As our research is focused on two-dimensional topological insulators, we present in this section systems which realize them, namely quantum wells, cold atoms and van der Waals heterostructures [87] of graphene and other materials.

Besides topological insulators in two dimensions, there are many different realizations of time-reversal invariant topological insulators in three dimensions [6, 88], such as $Bi_{1-x}Sb_x$ [13, 26], Bi_2Te_3 [28, 29], Sb_2Te_3 [28, 30], Bi_2Se_3 [27]. These systems exhibit a massless Dirac dispersion with spin–momentum locking at the boundaries. The chemical doping of 3D topological insulators with transition metal elements such as Cr or V induces a spontaneous magnetization, which breaks the time-reversal symmetry and opens a mass gap at the Dirac point of the surface states. The anomalous quantum Hall effect [89] may arise at the surfaces when the Fermi energy lies inside the energy gap of the surface state. Chiral edge states emerge at the edges and account for the quantization of the Hall conductance, which was experimentally confirmed in various experiments [90, 91].

Edge excitations with fractional charges in one dimensional topological matter have been found early on in organic polymer trans-polyacetylene [59] and recently they were also realized in cold atoms [92, 93].

2.6.1 Quantum wells

The first experiment that confirmed a two-dimensional topological material was performed on a CdTe/HgTe/CdTe quantum well [11, 12]. This system consists of a few-nanometers thick layer of HgTe sandwiched by $Hg_xCd_{1-x}Te$ alloy (the experiment used alloy composition $x = 0.3$). Gate voltage V_g controls the Fermi level. It is a two-dimensional system as the electrons are trapped in a HgTe layer, for example $x - y$ plane in figure 2.8. Confinement along direction z results in a quantization of the energy and as electrons are free to move along the HgTe layer ($x - y$ direction), the resulting energy dispersion consists of two-dimensional subbands. By changing the thickness of the HgTe layer one may control the energy gap between the low-

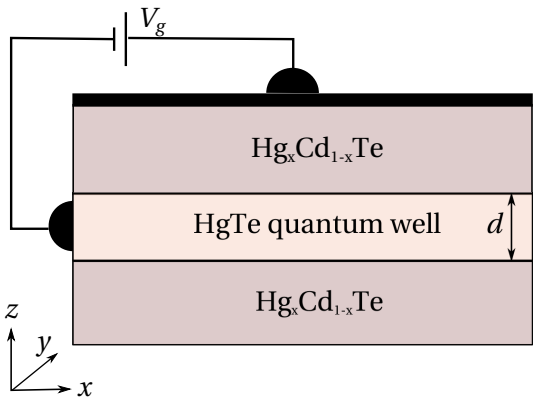

Figure 2.8: Schematic representation of a CdTe/HgTe/CdTe quantum well where a layer of HgTe of thickness d is sandwiched by two $Hg_xCd_{1-x}Te$ layers. The metallic electrode set the voltage V_g that adjusts the Fermi energy of electrons confined to HgTe layers.

est conduction band and the highest valence band. The bands touch at a critical thickness 6.45nm and for a thickness higher than the critical value, the energy gap reopens and the band structure inverts for momenta close to the gap closing. In this regime, the system is in the topological phase. The energy gap is up to 10meV, which is large enough to study the ground state properties at temperatures accessible in experiments. In order to obtain a simple effective description of the system at low energies, only two spinful subbands, the uppermost valence and lowermost conduction subbands, about their extremal points in the Brillouin zone are retained. The effective 4×4 Hamiltonian that describes this system is the BHZ model. Changing the HgTe layer thickness corresponds to changing the staggered orbital binding energy of the BHZ model (parameter u as in section 4.2.1 and critical thickness corresponds to $u = -2$).

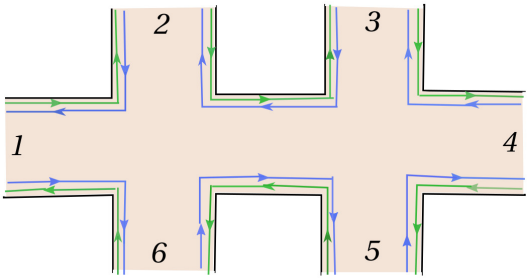

Figure 2.9: Schematic representation of a Hall bar, with six terminals connected to metallic contacts. Blue and green lines represent the counter propagating edge states.

The topological phase was confirmed by measuring quantized conductance of a Hall bar in the absence of magnetic field. A Hall bar is depicted in figure 2.9. In order to prove the edge transport, four-terminal resistance $R_{14,23} = V_{23}/I_{14}$ was measured, V_{23} being the voltage between contacts 2 and 3 and I_{14} the current flowing between contacts 1 and 4. A simple calculation using the Landauer-Büttiker formalism yields that the resistance is expected to be $R_{14,23} = 1/(2G_{23})$ with $G_{23} = e^2/h$. This was

observed for a wide range of gate voltages V_g as shown in figure 2.10. When the gate voltage puts the Fermi levels in one of the neighbouring bands, the material becomes conducting, which is signalled in diminished resistance. This results in a plateau form of the conductance. The experiment was conducted for different widths of the Hall bar and the results for narrower samples (red, green) show that the resistance is independent of the Hall bar width. This proves that the electric current flows along the edges.

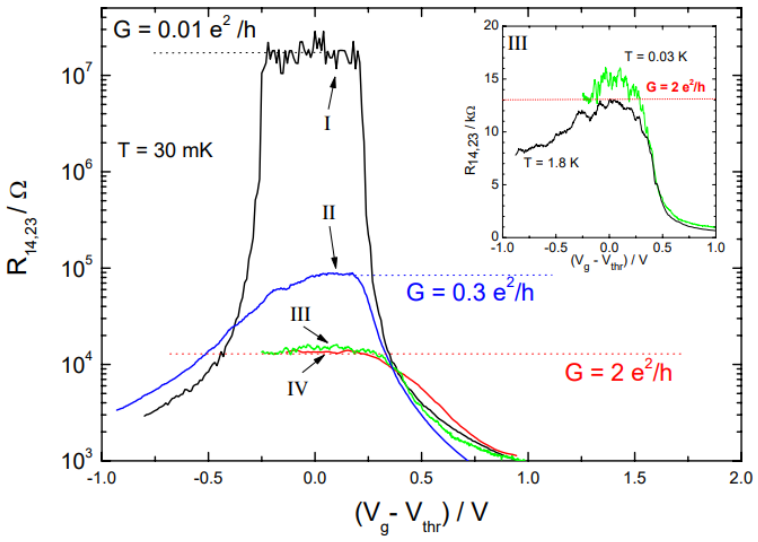

Figure 2.10: Four terminal resistance $R_{14,23}$ for various thickness of a HgTe layer at temperature $T = 30$ mK, (I) $d = 5.5$ nm (trivial) and (II-IV) $d = 7.3$ nm (topological). The size of the bar varies, in (I,II) it is $20.0 \times 13.3\,\mu\text{m}^2$, in (III) $1.0 \times 1.0\,\mu\text{m}^2$ and (IV) $1.0 \times 0.5\,\mu\text{m}^2$. The inset shows measurements at $T = 30$mK and 1.8 mK of device size III. The figure is taken from reference [12]

Another theoretically proposed and experimentally confirmed two-dimensional topological insulator is a AlSb/InAs/GaSb/AlSb quantum well [17, 94] with an energy gap up to 4 meV.

2.6.2 Graphene-like heterostructures

In more recent experiments, time-reversal symmetric topological insulators in two dimensions have also been realized in graphene-like heterostructures. There, a layer of graphene is placed in proximity to a compound consisting of heavy elements with high spin-orbital coupling. When all materials included in the heterostructure are two-dimensional, the structure is called a van-der-Waals heterostructure [87]. An example of a van-der-Waals heterostructure is shown in figure 2.11. The spin-orbital coupling present in natural graphene is enhanced due to proximity effect [95], which produces a large energy gap. This allows for the spin Hall effect at high temperatures.

The first successful example was in graphene grown by chemical vapour deposition on a copper foil [22]. Graphene is decorated with metallic copper adatoms, which enhance the spin-orbital coupling and thus the energy gap up to 20 meV through the proximity effect. Soon after the successful fabrication of a graphene

based topological insulator, another experiment [24] studied the graphene/MoS_2 van der Waals heterostructure, where the spin-orbital coupling is again enhanced by a proximity of MoS_2 and allows for detection of the spin Hall effect at room temperature. A relevant candidate for our studies is the van der Waals heterostruc-

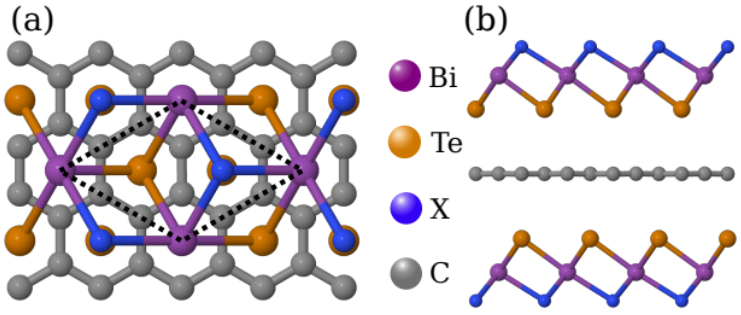

Figure 2.11: (a) Top and (b) side view of the structure of graphene sandwiched by ternary bismuth tellurohalide layers. The figure is taken from reference [25].

ture formed of graphene and ternary bismuth tellurohalide (BiTeX) layers [25]. A schematic representation of the graphene/BiTeX heterostructure is shown in figure 2.11. Bismuth is a heavy element with a high spin-orbital coupling, which accounts for the band gap up to 40 meV. It was theoretically shown that mechanical strain inherently present in a fabricated sample could induce topological phase transition. Changing the mechanical strain in time across a topological phase transition would allow for experimental study of the dynamical response of topological insulators outside of cold atoms.

An alternative to graphene is bismuthene, a single layer of bismuth atoms ordered in a honeycomb lattice. It has been predicted to be topologically non-trivial for free-standing layers [96, 97, 98], however it is unfortunately not a stable system. It is stable when grown on top of a wide-gap substrate SiC(0001) [23]. With angle-resolved photoelectron spectroscopy (ARPES) it was shown that such a heterostructure has a huge energy gap of ≈ 0.8 eV, such that topological properties could be observed at high temperatures. The theoretical prediction and the experimental measurement of the energy dispersion are shown in figure 2.12(a). The edge states appeared at two boundaries between a bismuthene and a substrate step, which was inserted in the middle of bismuthene. Their presence was confirmed by measuring differential conductance $\mathrm{d}I/\mathrm{d}V$, which reflects the local density of states. The measurements shown in figure 2.12(b) and (c) show an exponential decay of the in-gap states from the edge on either side of the substrate step.

2.6.3 Ultracold atoms

Ultracold fermionic atoms in optical lattices are an important experimental realization of topological insulators. In experiments with ultracold atoms the parameters of the simulated model are precisely controlled [99]. Tuning the parameters of the optical lattice enables studying the dynamical response of topological insulators, for instance, the behaviour of the system that is driven across a topological phase transition. This is also the only technique, which has realized some of the most important models for a Chern insulator, such as the Haldane model [8, 20], the

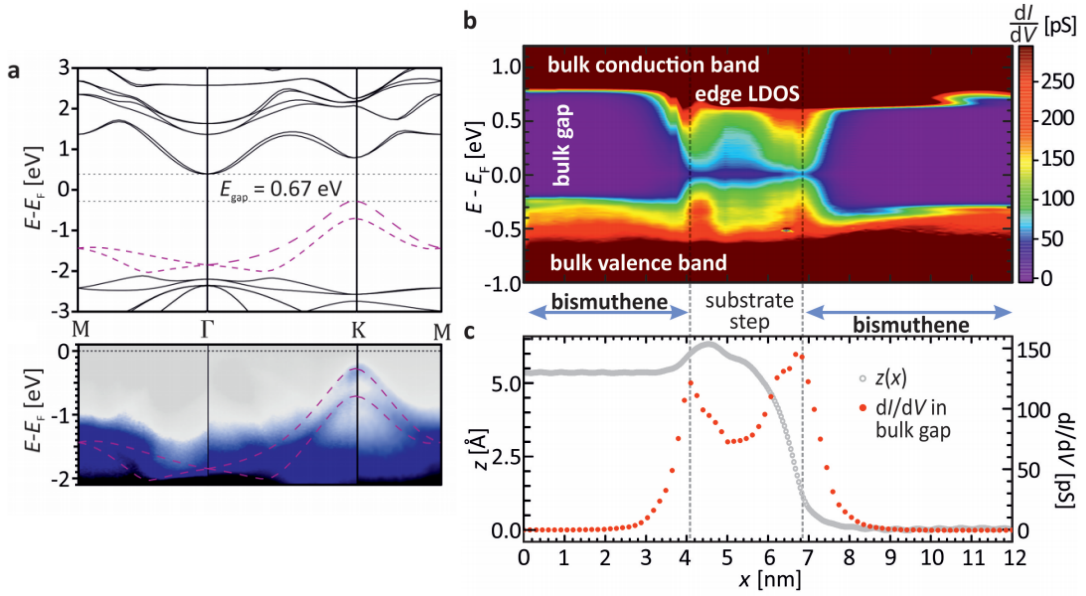

Figure 2.12: (a) Theoretical density functional theory prediction of the band structure and APRES measurements through the Brillouin zone. (b) $\mathrm{d}I/\mathrm{d}V$ at different positions across the bismuthene and step substrate. (c) Topographic $z(x)$ of the substrate step and $\mathrm{d}I/\mathrm{d}V$ integrated over the gap. The figure is taken from reference [23].

Hofstadter model [18, 100, 101] and the Qi-Wu-Zhang model [19, 21, 102]. Below, an experimental realization of the Haldane model is described [20], however most of the steps apply to a general quantum simulation with ultracold atoms.

The first step of experiment is to trap fermionic atoms in a magneto-optical trap and pre-cool them with laser cooling [103], which relies on atom scattering of photons. Further cooling is reached with evaporative cooling, where the trapping potential is decreased, which allows for atoms with higher energy to escape [104]. The cooled (about 10^4 of ^{40}K) fermionic atoms are later loaded to a periodically modulated optical (honeycomb) lattice [105], which is formed by the interference of counter-propagating laser beams. The cooled atoms are trapped in the minima of a periodic potential and the resulting arrangement resembles the crystal lattice. In order to break the inversion symmetry, an energy off-set $\triangle_{AB}$ is put between sublattice A and B.

Chern insulators have broken time-reversal symmetry due to the presence of internal magnetic fluxes, which allows for a quantized Hall effect in the absence of an external magnetic field. In ultracold atoms, the atoms are charge neutral and therefore not subjected to the Lorentz force, which breaks the time-reversal symmetry. The desired effect is achieved by periodically translating the lattice in x and y directions with a phase difference φ [106]. The effective Hamiltonian $\hat{H}_{\mathrm{eff}}$ describes a desired model for a Chern insulator and it is defined as

$$\hat{U}(T) = \exp\left(-i\hat{H}_{\mathrm{eff}}T\right), \tag{2.22}$$

where $\hat{U}(T)$ is the time-evolution operator over a period of driving T.

The topological phase diagram was obtained by measuring the Berry curvature.

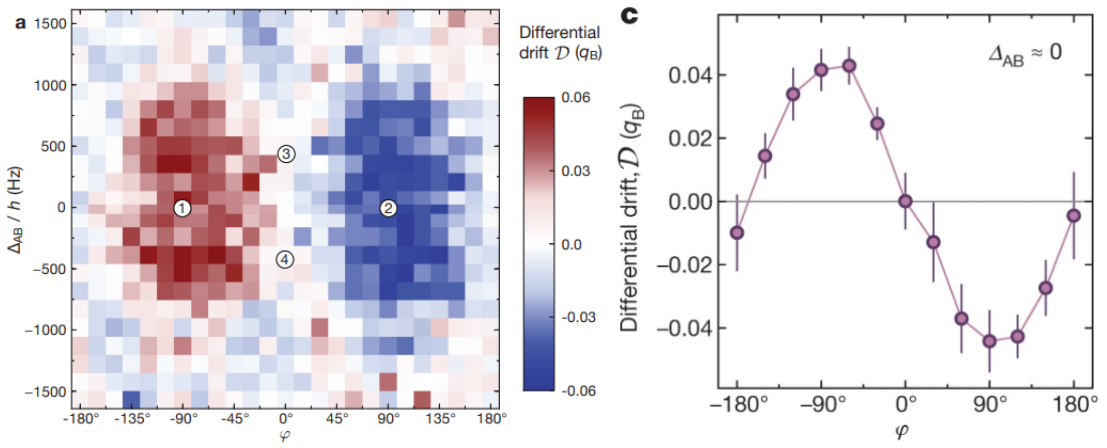

Figure 2.13: (a) Differential drift in x direction obtained from Bloch oscillations in the opposite k_y direction, with the starting $k_x = q_B = 2\pi/\lambda$. For comparison see the phase diagram in Figure 2.2. (c) Differential drift along $\triangle_{AB} = 0$. The figure is taken from reference [20].

The Berry curvature is point-antisymmetric in the trivial phase when only the inversion symmetry is broken. In the topological phase, when only the time-reversal symmetry is broken, it is point-symmetric. Semi-classical approximation yields that the Berry curvature is the proportionality constant between the drift of a particle in k-space and the induced velocity in an orthogonal direction

$$\begin{aligned} \dot{x} &= \frac{1}{\hbar}\partial_{k_x} E(k_x, k_y) - \dot{k_y}\Omega(k_x, k_y), \\ \dot{y} &= \frac{1}{\hbar}\partial_{k_y} E(k_x, k_y) + \dot{k_x}\Omega(k_x, k_y). \end{aligned} \tag{2.23}$$

In order to probe the topology, a wave packet was moved along the k_y-direction such that its trajectory in momentum space samples regions where the Berry curvature is non-zero and thus acquires velocity in x-direction. By applying an on-site energy gradient along y-direction, the wave packet underwent one Bloch oscillations along k_y. Measuring the drift in momentum space in k_x gives the integral of the Berry curvature along k_y. In order to obtain better results and as the velocity caused by the Berry curvature inverts when inverting the force, the differential drift [107] is measured, which is equal to subtracting the result for an opposite force gradient. The measurements 2.13 are in agreement with the topological phase diagram shown in figure 2.13.

Chapter 3

Dynamics of a quantum phase transition

A quantum phase transition is a fundamental change of the ground state of a Hamiltonian that happens upon a change of a certain parameter of the Hamiltonian [108]. The parameter inducing the phase transition is called *the control parameter* and the value at which the change happens is called *the critical point*. Second order phase transitions are characterized by an energy scale which vanishes at the critical point in the thermodynamic limit of infinite system size. Therefore, changing the control parameter in time will always produce excitations since the quantum state of the system cannot adiabatically follow the instantaneous ground state near the critical point. The resulting non-equilibrium system exhibits rich dynamics upon crossing the critical point. Recent development in experiments with ultracold atoms provides unprecedented opportunities to study quantum phase transitions as there, the parameters of the system may be precisely changed in time in a desired way [109, 110, 111, 112, 113, 114, 115]. Besides the purely academic interest, studies of systems that were driven across a phase transition are becoming essential for practical applications such as adiabatic preparation of the ground state for quantum simulations and adiabatic quantum computation [116, 117].

Many time-dependent passages across a critical point, for example a quantum Ising model [67, 118] and topological phase transitions [56, 63, 64, 119], may be modelled with a Landau-Zener model. It describes a two-level anti-crossing, where the energy gap between two quantum states changes linearly with time. The exact analytical solution of the time-dependent Schrödinger equation is known and with it the probability for a non-adiabatic transition. The later serves as a general estimate for the non-adiabaticity of a process. The Landau-Zener model and its solution are presented in section 3.1.

The dynamics of many systems undergoing a quantum phase transition with an isolated critical point between two gapped phases is well described by *the Kibble-Zurek mechanism* [66, 67, 120, 121]. The essence of this mechanism is its simplified paradigm for the time-evolution across a critical point, called the adiabatic-impulse approximation. It separates the dynamics into an adiabatic regime, that is when the control parameter is far away from the critical point, and an impulse or instantaneous quench across a region close to the critical point, where the relaxation time diverges. It predicts an emergence of topological defects, the size and the density of which scale with transition time as a power-law, where the power exponent is determined by the

equilibrium critical exponents for the corresponding critical point. The Kibble-Zurek mechanism is in length explained in section 3.2.

The topological phase transitions are characterized by a divergence of the typical length scale and typical time scale, too. In order to describe topological phase transitions and connect the non-equilibrium dynamics in topological insulators to the Kibble-Zurek mechanism, we present in section 3.3 the calculation of the typical length scale. Following references [78, 122, 123, 124] we show that it can be extracted from the curvature function, the integral of which over the Brillouin zone gives the topological invariant.

3.1 Landau-Zener dynamics

The Landau-Zener formula [125, 126] gives an exact solution to the time-dependent Schrödinger equation of a two-level system with avoided crossing, where the energy separation of two quantum states is a linear function of time. It gives an exact formula for the probability of a non-adiabatic transition. Many integrable models that are driven in time across a quantum phase transition may be mapped to a set of independent Landau-Zener avoided crossings, as for example a quantum Ising model [67, 118] and topological phase transitions [56, 63, 64, 119]. The Landau-Zener model is defined by a two-level time-dependent Hamiltonian

$$\hat{H} = \begin{pmatrix} \varepsilon(t) & \triangle \\ \triangle^* & -\varepsilon(t) \end{pmatrix}, \tag{3.1}$$

with a constant coupling $\triangle$ and

$$\varepsilon(t) = \frac{\alpha}{2} t, \tag{3.2}$$

which depends linearly on time. The Hamiltonian is written in the basis of *diabatic states* $|0\rangle$ and $|1\rangle$, which have the corresponding energies $\varepsilon(t)$ and $-\varepsilon(t)$. While the diabatic states are time-independent, the instantaneous eigenstates on the Hamiltonian, *the adiabatic states*, depend on the time-dependent value of parameter ε as

$$\begin{aligned} |\uparrow(\varepsilon)\rangle &= \cos\frac{\vartheta}{2}|0\rangle + e^{i\varphi}\sin\frac{\vartheta}{2}|1\rangle, \\ |\downarrow(\varepsilon)\rangle &= -\sin\frac{\vartheta}{2}|0\rangle + e^{i\varphi}\cos\frac{\vartheta}{2}|1\rangle, \end{aligned} \tag{3.3}$$

where $\cos\vartheta = \varepsilon/\sqrt{|\triangle|^2+\varepsilon^2}$, $\sin\vartheta = |\triangle|/\sqrt{|\triangle|^2+\varepsilon^2}$ and $e^{i\varphi} = \triangle^*/|\triangle|$. The eigenenergies are $E_\uparrow(\varepsilon) = E_\mathrm{g}(\varepsilon)/2$ and $E_\downarrow(\varepsilon) = -E_\mathrm{g}(\varepsilon)/2$ and the energy gap

$$E_\mathrm{g}(\varepsilon) = 2\sqrt{|\triangle|^2+\varepsilon^2} \tag{3.4}$$

is minimal in the center of avoided crossing at $\varepsilon = 0$. The adiabatic (solid) and diabatic energies (dashed) are schematically shown in figure 3.1. Notice that for $\varepsilon \to -\infty$, the adiabatic state $|\uparrow(-\infty)\rangle$ is equal to the diabatic state $|1\rangle$ and $|\downarrow(-\infty)\rangle$ to $|0\rangle$. For $\varepsilon \to \infty$ the adiabatic states change polarity, $|\uparrow(\infty)\rangle = |0\rangle$ and $|\downarrow(\infty)\rangle = |1\rangle$. At $\varepsilon = 0$, the adiabatic states are in superposition of diabatic states with equal probability.

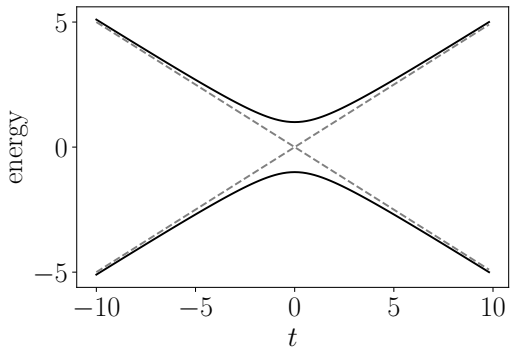

Figure 3.1: Avoided crossing in the Landau-Zener model for $\alpha = 1$ and $\triangle = 1$. Solid lines represent the eigenvalues of $\hat{H}(t)$, the energies of the adiabatic states, and dashed lines the energies of the diabatic states.

The Landau-Zener problem is the following: the particle starts at $t \to -\infty$ in the low-energy state $|0\rangle$. What is the probability for a diabatic transition of the particle to the state $|0\rangle$ at $t \to \infty$? Landau [125], Majorana [127], Zenner [126] and Stückelberg [128] independently found the solution in 1932, while Zener also presented the exact solution to the time dependent Schrödinger equation

$$-i\frac{\mathrm{d}}{\mathrm{d}t}|\psi(t)\rangle = \hat{H}(t)|\psi(t)\rangle. \tag{3.5}$$

Let the wave function be expressed as

$$|\psi(t)\rangle = c_0(t)e^{i\int \varepsilon(t)\mathrm{d}t}|0\rangle + c_1(t)e^{-i\int \varepsilon(t)\mathrm{d}t}|1\rangle, \tag{3.6}$$

with the initial conditions $|c_0(-\infty)| = 1$ and $c_1(-\infty) = 0$. The exact solution for any time t is given by

$$\begin{aligned} c_0(t) &= e^{-i\alpha t^2/4}e^{-\pi\gamma/4}e^{-i\pi/4}\frac{\triangle}{|\triangle|}\times \\ &\quad \left(D'_{-n-1}(iz) + \frac{z}{2}D_{-n-1}(iz)\right), \\ c_1(t) &= e^{i\alpha t^2/4}\sqrt{\gamma}e^{-\pi\gamma/4}D_{-n-1}(iz), \end{aligned} \tag{3.7}$$

where $z = \sqrt{i\alpha}t$, $\gamma = |\triangle|^2/|\alpha|$, $n = -i|\triangle|^2/\alpha$ and D_n is the Weber function [129]. The probability for the transition to the higher-energy state $|0\rangle$ at $t \to \infty$ is equal to

$$P = |c_0(\infty)|^2 = e^{-2\pi|\triangle|^2/\alpha}. \tag{3.8}$$

This result serves as a criterion for an adiabatic transition. For a slow enough variation of the energy difference, $\alpha \ll 2\pi|\triangle|^2$, equation (3.8) tells us that no such transition will take place, as the system will always be in the instantaneous eigenstate of the Hamiltonian at that moment of time.

The excitation probability P can be obtained in a closed form expression also for the case where the driving stops at $t = 0$. The eigenstates of the Hamiltonian at $t = 0$ are $|\uparrow\rangle = \frac{1}{\sqrt{2}}(\frac{\triangle}{|\triangle|}|0\rangle + |1\rangle)$ and $|\downarrow\rangle = \frac{1}{\sqrt{2}}(-\frac{\triangle}{|\triangle|}|0\rangle + |1\rangle)$ and the probability of

finding an electron in the state with the higher energy $|\uparrow\rangle$ is

$$\begin{aligned} P &= \frac{1}{2}\left|c_1(0)+\frac{\triangle^*}{|\triangle|}c_0(0)\right|^2 = \\ &= \frac{\pi}{4}e^{-\frac{\pi|\triangle|^2}{2\alpha}}\left|\frac{-1+i}{\Gamma\left(\frac{1}{2}+i\frac{|\triangle|^2}{2\alpha}\right)}+\frac{|\triangle|}{\sqrt{\alpha}\Gamma\left(1+i\frac{|\triangle|^2}{2\alpha}\right)}\right|^2 \approx \frac{1}{64}\frac{\alpha^2}{|\triangle|^4}, \end{aligned} \tag{3.9}$$

where $\Gamma(x)$ is the gamma function and the last approximate form holds when $\alpha/|\triangle|^2 \ll 1$. This result was obtained in [120, 130, 131] and shown to hold also for the case where the driving starts at $t = 0$ and ends in $t \to \infty$.

Another closed form result is the probability for transition with initial $t \to -\infty$ to $t \to \infty$ under an asymmetric driving function:

$$\varepsilon(t) = \begin{cases} \frac{\alpha}{2}t,\, t \le 0 \\ \delta\frac{\alpha}{2}t, t > 0 \end{cases}, \tag{3.10}$$

where factor $\delta \neq 1$. The probability for transition [120, 130, 131] is

$$\begin{aligned} P &= 1-\frac{1}{2}\sinh\left(\frac{\pi|\triangle|^2}{\alpha\delta}\right)e^{-\frac{\pi|\triangle|^2}{2}(\frac{1}{\alpha}+\frac{1}{\alpha\delta})}\left|\frac{\Gamma(\frac{1}{2}+\frac{i|\triangle|^2}{2\alpha\delta})}{\Gamma(\frac{1}{2}+\frac{i|\triangle|^2}{2\alpha})}+\sqrt{\delta}\frac{\Gamma(1+\frac{i|\triangle|^2}{2\alpha\delta})}{\Gamma(1+\frac{i|\triangle|^2}{2\alpha})}\right|^2 \\ &\approx \frac{1}{64}(1-\delta)^2\frac{\alpha^2}{|\triangle|^4}. \end{aligned} \tag{3.11}$$

In the adiabatic limit of $\alpha \ll 1$ and for $\triangle \neq 0$ the excitation probability P is exponentially small in the standard (symmetric) Landau-Zener model, but in the non-symmetric case and when the driving is performed only until $t = 0$, there is much slower power-law decay $P \propto \alpha^2$. This is due to the fact that in the asymmetric driving cases an instantaneous rate of the transition $d\varepsilon/dt$ is a discontinuous function of time, which leads to additional excitations.

3.2 Kibble-Zurek mechanism

The Kibble-Zurek mechanism was first developed by Kibble [65] as a cosmological theory describing the formation of the early universe and was later applied to condensed matter systems by Zurek [66, 67]. It describes non-equilibrium properties of a system that was driven in a finite time τ over a symmetry breaking second order phase transition. It predicts emergence of topological defects and connects their density and size to the equilibrium critical exponents.

Second order phase transitions are characterized by the divergence of the relaxation time τ_r and the correlation length ξ. They diverge as a function of the control parameter u on approaching the critical point u_c by a power determined by the dynamical critical exponent z and the correlation length critical exponent ν [68],

$$\begin{aligned} \tau_r(u) &\propto |u-u_c|^{-z\nu}, \\ \xi(u) &\propto |u-u_c|^{-\nu}. \end{aligned} \tag{3.12}$$

The correlation length manifests itself in the ground state as the typical length scale.

The dynamics of the system is described by a simplified scheme called *the adiabatic-impulse approximation*. It considers a system that exhibits a high-symmetry phase for $u < u_c$ and a low-symmetry phase for $u > u_c$, where u is the control parameter and u_c the critical point. Let the system be driven by a linear quench of u

$$u(t) = t/\tau + u_c \tag{3.13}$$

from a high-symmetry to the low-symmetry phase. In the beginning of the quench for $t \to -\infty$, when the relaxation time is much smaller than the time needed to reach the critical point, the system evolves adiabatically. This is also the case for times long after crossing the critical point. However, in the vicinity of the critical point, the relaxation time diverges and the dynamics is approximately frozen. The dynamics is therefore separated in three regimes: adiabatic, frozen and again adiabatic. An approximate time at which the system freezes is called *the freeze-out time* $-t_F$. It is estimated as the time at which the time needed to reach the critical point is equal to the relaxation time, $t_F = \tau_r(-t_F)$, yielding the relation

$$t_F \sim \tau^{z\nu/(1+z\nu)}. \tag{3.14}$$

The schematic representation of this scheme is shown in figure 3.2(a). In the case of phase transitions with spontaneous symmetry breaking that entail a degeneracy of the ground state, such a process produces regions corresponding to different choices of the ground state. The size of the regions is set by the equilibrium correlation length

$$\xi(-t_F) \sim \tau^{\nu/(1+z\nu)} \tag{3.15}$$

at a freeze-out time. Different choices of the ground state are explained by causality: when the system freezes, the information about the choice of the ground state in some local region travels with the speed of sound estimated as the ratio of the correlation length and the relaxation time $c = \xi/\tau_r$. At meeting points of these regions topological defects can be formed. The density of topological defects is predicted to be

$$n \sim \frac{\xi(-t_F)^d}{\xi(-t_F)^D} \sim \tau^{-(D-d)\nu/(1+z\nu)}, \tag{3.16}$$

where D is the dimension of the system and d the dimensionality of the topological defect.

The Kibble-Zurek scaling was observed experimentally in tunnel Josephson junctions [69, 70], multiferroics [71, 72, 73], ion Coulomb crystals [74, 75], Bose-Einstein condensates [76, 132, 133], and in a Rydberg atom quantum simulator [77]. For example in multiferroics, shown in figure 3.3, the cooling from a disordered phase at a high temperature results in domains of a size that depends on the cooling rate. Vortex-like defects appear at the meeting point of several domains and their density exhibits the Kibble-Zurek scaling. Another prime example is vortex formation in Bose-Einstein condensates. Cooling a thermal cloud at a finite rate across a critical point for Bose-Einstein condensation produces coherent regions of the condensate where the phase of the condensate wavefunction is chosen independently and is approximately constant (see figure 3.4). When different regions merge at a point, an overall phase may accumulate along a closed loop surrounding the point. This creates a vortex with an accumulated phase that is a multiple of 2π. Their density is given by the Kibble-Zurek scaling for one-dimensional defects. Figure 3.4 shows

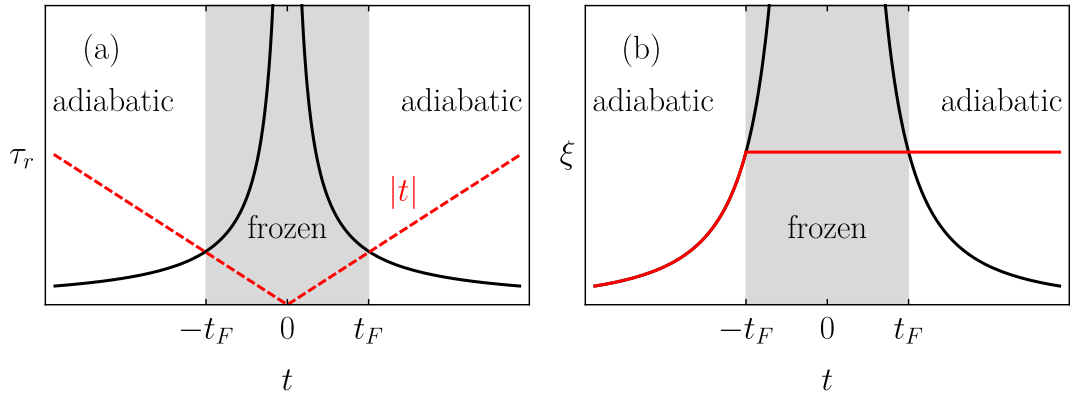

Figure 3.2: Schematic representation of the freeze-out captured by the adiabatic-impulse approximation. The freeze-out zone $(-t_F, t_F)$ is marked with a shaded region. (a) The relaxation time and (b) the correlation length in the ground state (black) and in the non-equilibrium state during the quench.

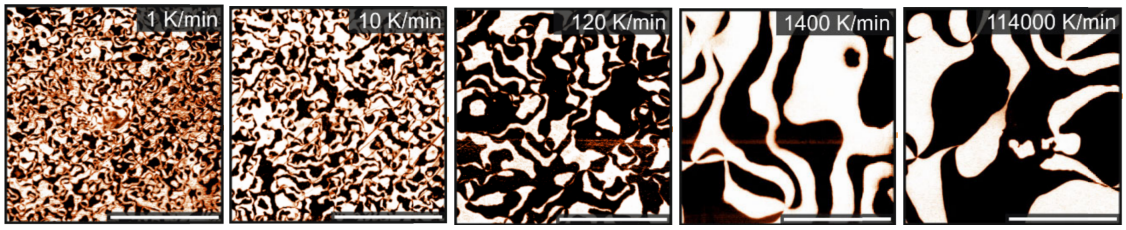

Figure 3.3: Spatial maps of the multiferroic $DyMnO_3$ after cooling with different cooling rates from the disordered to the ordered phase [73]. Ferroelectric domains are larger for smaller cooling rates, resulting in lower density of vortex-like defects that appear at the meeting points of different ferroelectric domains. The scale bar in all images is 5 μm.

expansion images of Bose-Einstein condensate and vortices manifest as dark regions with a low density of particles.

3.3 Length scale in topological insulators

In order to calculate the dynamical and the correlation length critical exponents, one has to look into the ground state properties of a system close to the critical point. The critical exponent $z\nu$ is extracted from the characteristic time scale, which is in topological insulators given by the inverse of the band gap.

The calculation of the typical length scale is ambiguous at the first glance since topological insulators have no local Landau order parameter and the topological invariant jumps discretely at the critical point. One could study a system with edges and extract the length scale from the decay length of the edge states. However, as we mostly deal with bulk systems, we follow works by Chen et al. [78, 122, 123, 124] for the calculation of the length scale for inversion-symmetric systems. They propose two methods for calculation of the length scale, both of which are explained in the following subsections.

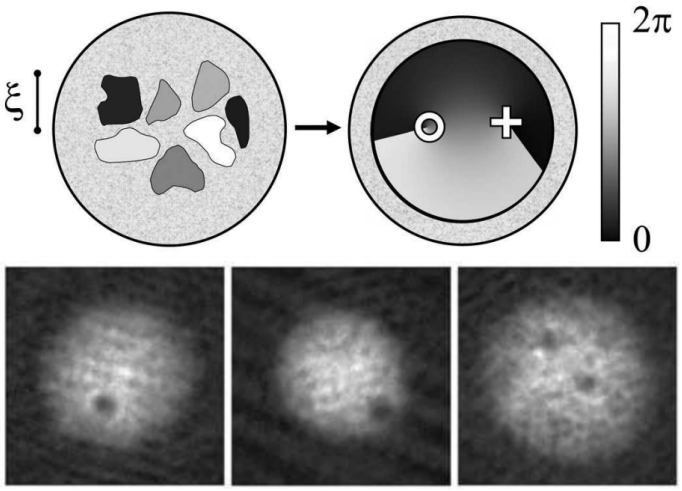

Figure 3.4: (Top) Scheme of a vortex formation. (Left) Cooling the thermal gas (mottled gray shade) across a critical temperature for Bose-Einstein condensation results in regions of approximate size ξ with different choices of the phase of a wave-function. (Right) After the initial regions merge and the phase profile becomes continuous, vortices with a quantized phase appear. The phase is depicted by the shade of gray ranging from 0 to 2π and a cross (circle) represents a positive (negative) vortex. (Bottom) Experimental measurement of vortex formation. 200-μm-square expansion images of a Bose-Einstein condensate created in a harmonic trap with a single (left, center) and two vortices (right). Images are taken from reference [132].

3.3.1 Calculation from the curvature function

Let $F(\mathbf{k}, u)$ be the curvature function at momentum $\mathbf{k}$ and control parameter u, from which the topological invariant C in D dimensions is calculated as

$$C = \int \mathrm{d}^D \mathbf{k} F(\mathbf{k}, u). \tag{3.17}$$

While the topological invariant stays unchanged upon adiabatically changing the parameter u, the profile of the curvature function changes. In majority of systems approaching the critical point $u \to u_c$ the curvature function develops a divergence at the high-symmetry point $\mathbf{k}_0$ where the energy gap closes. The diverging peak changes sign upon crossing the critical point, resulting in a jump of the topological invariant. The peak of the curvature function can be well fitted by the Ornstein-Zernike form

$$F(\mathbf{k}_0 + \delta\mathbf{k}, u) = \frac{F(\mathbf{k}_0, u)}{1 \pm \xi^2 |\delta\mathbf{k}|^2}. \tag{3.18}$$

ξ explicitly characterizes the scale invariance at the critical point and represents the typical length scale of the system. The critical behaviour is summarized as:

$$\begin{aligned} &\lim_{u \to u_c^+} F(\mathbf{k}_0, u) = -\lim_{u \to u_c^-} F(\mathbf{k}_0, u) = \pm\infty, \\ &\lim_{u \to u_c} \xi = \infty. \end{aligned} \tag{3.19}$$

The divergence of the above quantities is a power law characterized by the critical exponents

$$|F(\mathbf{k}_0, u)| \propto |u - u_c|^{-\gamma}, \quad \xi \propto |u - u_c|^{-\nu}, \tag{3.20}$$

with $\gamma = D\nu$ as a consequence of topological invariant conservation upon closing on to the critical point.

3.3.2 Curvature renormalization group approach

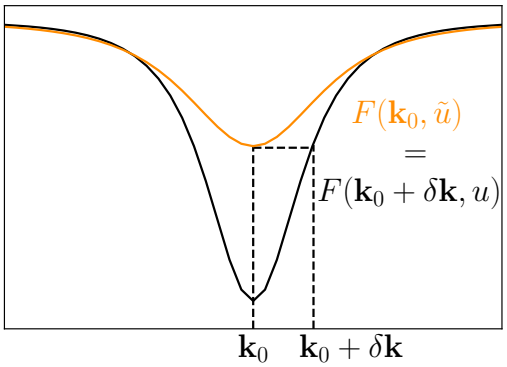

Figure 3.5: The deviation-reduction mechanism: For a given $\mathbf{k}_0 + \delta\mathbf{k}$ and u, one has to find $\tilde{u}$ such that $F(\mathbf{k}_0, \tilde{u}) = F(\mathbf{k}_0 + \delta\mathbf{k}, u)$.

The critical behaviour can also be extracted from the curvature renormalization group (RG) approach. The topological phase transitions are identified by an iterative method that searches for a trajectory called the RG flow in the parameter space of u, along which the maximum of the curvature function is reduced. By iteratively seeking $\tilde{u}$, such that

$$F(\mathbf{k}_0, \tilde{u}) = F(\mathbf{k}_0 + \delta\mathbf{k}, u), \tag{3.21}$$

where $\delta\mathbf{k}$ is a small deviation satisfying $F(\mathbf{k}_0+\delta\mathbf{k}, u) = F(\mathbf{k}_0-\delta\mathbf{k}, u)$, this procedure gradually reduces the value of the curvature function at $\mathbf{k}_0$ as demonstrated in figure 3.5. This is known as the deviation-reduction mechanism. Under the iterative

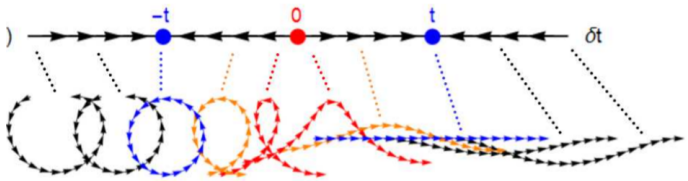

Figure 3.6: RG flow of the control parameter δt in the Su–Schrieffer–Heeger model [59], figure is taken from [78]. The curvature function is the Berry connection $\partial_k \varphi(k)$. $\varphi(k)$ is depicted (coloured arrows) as a vector field in the complex space for each configuration.

application of equation (3.21), the parameters u follow the RG flow: they travel away from the critical point at u_c towards a fixed point u_f. When the flow stops at u_f, the curvature function is invariant under procedure in equation (3.21) and has the form $F(\mathbf{k}_0, u_f) = F(\mathbf{k}_0 + \delta\mathbf{k}, u_f)$. By expanding equation (3.21) in both $\mathrm{d}u = \tilde{u} - u$, displacement along the j coordinate $= \delta\mathbf{k} = (0, \ldots, \delta k_j, \ldots, 0)$ and $\delta k_j^2 \equiv \mathrm{d}l$, one

obtains the RG equation

$$\frac{\mathrm{d}u}{\mathrm{d}l} = \frac{1}{2}\frac{\partial_{k_j}^2 F(\mathbf{k},u)|_{\mathbf{k}=\mathbf{k}_0}}{\partial_u F(\mathbf{k}_0,u)}. \tag{3.22}$$

Combining the scaling equation with the Lorentzian shape of the curvature function at $\mathbf{k}_0$, one arrives to the explicit formula for the correlation length

$$\xi(u) = \left|\frac{\mathrm{d}u}{\mathrm{d}l}\frac{\partial_u F(\mathbf{k}_0,u)}{F(\mathbf{k}_0,u)}\right|^{\frac{1}{2}}. \tag{3.23}$$

Chapter 4

Quenches in translation invariant systems

Topological insulators have promising ground state properties. However, many proposals on how to realize topological insulators include time-dependent driving, which produces systems out of equilibrium. A prominent example are Floquet insulators [50, 51, 52], in which the periodic driving of a trivial insulator induces a non-trivial topological phase. Other experimental proposals suggest that a topological phase may be induced by making a quench from a trivial to a topological phase [134, 135]. Therefore, an important line of investigation is the one focusing on dynamical critical properties by studying quenches across topological phase transitions. Studies on this topic have been made for topological superconductors [136, 137, 138], $p + ip$ superfluids [55, 139] and topological insulators [52, 53, 54, 56, 57, 60, 61, 62, 119, 140, 141, 142, 143, 144, 145].

Response to quenches could be studied in various experimental setups. Time-dependent Hamiltonians can be realized in ultracold atoms [18, 146, 147, 148, 149]. Dynamics of time-reversal symmetric systems could be studied experimentally with HgTe/CdTe and InAs/GaSb/AlSb Type-II semiconductor quantum wells where the quench could perhaps be performed by varying the inversion breaking electric potential in the z-direction, which can be tuned by a top gate in experiments [150, 151, 152]. Other studies suggest that a topological phase transition can be achieved by mechanical stress, for example in graphene and ternary bismuth tellurohalide layers [25].

Many examples and important features of topological insulators are captured by the band theory. Therefore, the question of how do translation invariant systems respond to quenches is fundamental. This chapter, following our published work [56, 153], reports a study of the non-equilibrium response to such quenches of a two-dimensional Chern insulator, represented by the QWZ model (section 4.1), and a two-dimensional time-reversal symmetric topological insulator (section 4.2), represented by the BHZ model. The models belong to different symmetry classes and we use this to discuss which dynamical properties are generic and which depend on the symmetry class of the system.

Topological properties of post-quench states are shown to depend strongly on the symmetry class. These are probed by inspecting a topological invariant that is by definition conserved by any adiabatic evolution. We show that the topological invariant of Chern insulators, the Chern number, is conserved for an arbitrary time

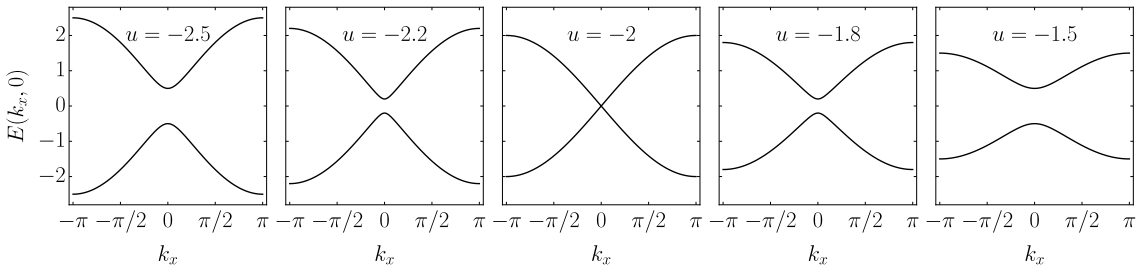

Figure 4.1: Energy dispersion of the QWZ model along $k_y = 0$ for different values of u that range across the critical point at $u_c = -2$.

evolution even if during the evolution the band gap closes [50, 55, 56]. On the other hand, a post-quench time-reversal symmetric topological insulator has an ill-defined $\mathbb{Z}_2$ invariant, since in general time-evolution breaks the time-reversal symmetry of a state. We also explore quenches that break the time-reversal symmetry of the Hamiltonian and keep the band gap open at all times. Such quenches adiabatically change the $\mathbb{Z}_2$ invariant, however they cannot be realized for Chern insulators.

The two studied cases behave similarly as far as the excitations and the post-quench transport are concerned. The reason for that is that the corresponding phase transitions are accompanied by the divergence of the time scale and the length scale and that the quench dynamics can be modelled by the Landau-Zener dynamics. Examining the ground state critical properties, we determine the equilibrium critical exponents by which the typical time scale and the typical length scale diverge. We show that the excitations, transport properties, and the post-quench length scale are well described by the Kibble-Zurek mechanism. We show that the quench dynamics is well captured by the adiabatic-impulse approximation.

4.1 Chern insulators

4.1.1 Qi-Wu-Zhang model

We study a Chern insulator described by the QWZ model [102], which resides on a two-dimensional square lattice. It was experimentally realized in ultracold atoms [19, 21]. It is also known as the 'half BHZ model' as it is the spin-up block of the BHZ model (see section 4.2.1) for the quantum spin Hall effect. In translation invariant systems, the Hamiltonian is of a block-diagonal form in the plane wave basis $\hat{H} = \sum_{\mathbf{k}} |\mathbf{k}\rangle\langle\mathbf{k}| \otimes \hat{H}(\mathbf{k})$, where $\mathbf{k} = (k_x, k_y)$ is vector from the first Brillouin zone (BZ), $\mathrm{BZ} = \{(k_x, k_y), k_x, k_y \in [-\pi, \pi)\}$. The momentum-space Hamiltonian $\hat{H}(\mathbf{k})$ is

$$\hat{H}(\mathbf{k}) = (u + \cos k_x + \cos k_y)\hat{\sigma}_z + \sin k_x \hat{\sigma}_x + \sin k_y \hat{\sigma}_y, \tag{4.1}$$

where the Pauli matrices $\hat{\sigma}_i$ represent the internal degrees of freedom due to a presence of two orbitals $|A\rangle$ and $|B\rangle$ per unit cell. The lattice spacing is set to 1 and $\hbar = 1$. The Hamiltonian contains staggered orbital binding energy u, which controls the energy gap between the valence and the conduction band and the topological phase.

The energy spectrum of the QWZ model, shown in figure 4.1, consists of two

energy bands,

$$E(\mathbf{k}) = \pm\sqrt{\sin^2 k_x + \sin^2 k_y + (u + \cos k_x + \cos k_y)^2}. \tag{4.2}$$

Negative energies form the valence band and correspond to the eigenstates $|\psi_v(\mathbf{k})\rangle$, while the positive energies form the conduction band and belong to the eigenstates $|\psi_c(\mathbf{k})\rangle$. The energy spectrum has an energy gap, which closes at the critical values $u_c \in \{-2, 0, 2\}$ at different critical momenta $\mathbf{k}_c$ called the Dirac points, namely:

- for $u_c = -2$, at $\mathbf{k}_c = 0$,
- for $u_c = 0$, at $\mathbf{k}_c = (0, \pi)$ and $\mathbf{k}_c = (\pi, 0)$,
- for $u_c = 2$, at $\mathbf{k}_c = (\pi, \pi)$.

Expanding the dispersion relation to the first order in the deviation of the momentum from $\mathbf{k}_c$ we obtain band dispersions $\pm\sqrt{q^2 + \delta u^2}$, where $q = |\mathbf{k} - \mathbf{k}_c| \ll \pi$ and $\delta u = u - u_c$. At a critical value of u the two bands form a Dirac cone, characterized by the linear dispersion near the Dirac point.

The QWZ model possesses the inversion symmetry,

$$\hat{H}(-\mathbf{k}) = \hat{\sigma}_z \hat{H}(\mathbf{k}) \hat{\sigma}_z, \tag{4.3}$$

and the particle-hole symmetry,

$$\hat{H}(-\mathbf{k}) = -\hat{\sigma}_x \hat{H}(\mathbf{k})^* \hat{\sigma}_x, \tag{4.4}$$

which puts it in the class D of topological phases of matter, which are characterized by the topological invariant, the Chern number $C \in \mathbb{Z}$. The Chern number (2.5) is the surface integral of the Berry curvature $\Omega(\mathbf{k})$ (2.3). In the case of the QWZ model, there is only one occupied band, therefore there is no sum over occupied bands as in equation (2.5) and we omit the redundant band index n. The Chern number depends on the parameter u as

$$C = \begin{cases} 1, & 0 < u < 2, \\ -1, & -2 < u < 0, \\ 0, & |u| > 2. \end{cases} \tag{4.5}$$

The gap closing at u_c separates different topological phases with distinct Chern numbers.

4.1.2 Numerical implementation

Numerical results are obtained from simulations on a finite system. In order to maintain translation invariance, periodic boundary conditions are imposed. In a system with an even number N of unit cells in x and y directions, the Brillouin zone consists of momenta $\mathbf{k}_{n,m} = (-\pi + \triangle_k n, -\pi + \triangle_k m)$, with $n, m \in 0, \ldots N-1$, which are elements of a $N \times N$ grid with discretization step $\triangle_k = \frac{2\pi}{N}$. A plaquette with index (n, m) is an elementary square of this grid, its lower left corner being the momentum $\mathbf{k}_{n,m}$. The occupied states $|\psi_{n,m}\rangle = |\psi_v(\mathbf{k}_{n,m})\rangle$ belong to their corresponding grid points.

When calculating the Berry curvature and the Chern number in systems of finite size, it is useful to follow a method [154], which evades the partial derivatives and gives a correct value of the Chern number already for small system sizes. The Chern number is calculated as a net Berry flux. The Berry flux through the (n, m)-th plaquette is defined as the modulus 2π of the sum of relative phases of the states residing on the corners on the loop about the plaquette,

$$F_{n,m} = -\arg(\langle\psi_{n,m}|\psi_{n+1,m}\rangle\langle\psi_{n+1,m}|\psi_{n+1,m+1}\rangle \langle\psi_{n+1,m+1}|\psi_{n,m+1}\rangle\langle\psi_{n,m+1}|\psi_{n,m}\rangle). \tag{4.6}$$

The Chern number is then equal to the sum of Berry fluxes $F_{n,m}$ through all the plaquetes in the Brillouin zone,

$$C = -\frac{1}{2\pi}\sum_{n,m} F_{n,m}. \tag{4.7}$$

It the thermodynamic limit with $N \to \infty$, the Berry curvature at $\mathbf{k}_{n,m}$ can be expressed with the Berry flux as

$$\Omega(\mathbf{k}) = \lim_{\triangle_k \to 0} \frac{F_{n,m}}{\triangle_k^2}. \tag{4.8}$$

4.1.3 Critical properties

The typical time scale and the typical length scale start to diverge as a power law for values of u approaching the critical point. The energy gap is for small momenta near the critical point equal to

$$\triangle E(\mathbf{k}) = 2\sqrt{|\mathbf{k} - \mathbf{k}_c|^2 + (u - u_c)^2}. \tag{4.9}$$

The typical time scale is set by the inverse of the band gap, which at u_c closes at $\mathbf{k}_c$. On approaching the critical point, the band gap closes linearly and τ_r has the form

$$\tau_r(u) = (\triangle E(\mathbf{k}_c))^{-1} = \frac{2}{|u - u_c|}, \tag{4.10}$$

yielding the critical exponent $z\nu = 1$.

The behaviour of the typical length scale near the critical point may be read out of the Berry curvature. The exact expression for the Berry curvature is

$$\Omega(\mathbf{k}) = \frac{\cos k_x + \cos k_y + u\cos k_x \cos k_y}{2((u + \cos k_x + \cos k_y)^2 + \sin k_x^2 + \sin k_y^2)^{3/2}}. \tag{4.11}$$

Close to the critical point at $u_c = -2$ and $\mathbf{k}_c = (0, 0)$ it can be expanded for small momenta $k = |\mathbf{k}| \ll 1$ as

$$\Omega(\mathbf{k}) = \frac{u + 2}{|u + 2|}\frac{1}{2(u + 2)^2 - k^2(5 + 4u)}. \tag{4.12}$$

The Berry curvature is symmetric about $\mathbf{k}_c$, where it exhibits a peak of Lorentzian form, shown in figures 4.2(a) and (b). On approaching the critical point, the peak grows and its width shrinks. As shown in figure 4.2(c), rescaling the Berry curvature with $|u - u_c|^{-1}$ collapses the curves for different values of u to a universal curve

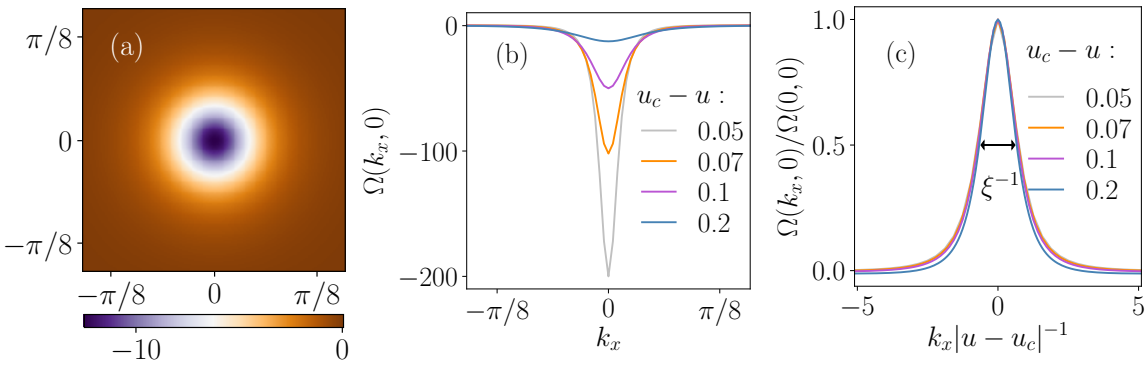

Figure 4.2: Berry curvature (a) at $u = -2.2$ and (b) for various u at $k_y = 0$. (c) Normalized Berry curvature for various u at $k_y = 0$ as a function of $k_x|u - u_c|^{-1}$.

which indicates that the typical length scale diverges as $\xi \propto |u - u_c|^{-1}$. The analytical expression for the correlation length can be extracted from equation (4.12) by reshaping it into a Lorentzian form,

$$\xi(u) = \sqrt{\frac{3}{2}\frac{1}{(u+2)^2} - \frac{2}{u+2}}. \tag{4.13}$$

Close to the critical point, the correlation length diverges with a power $\nu = 1$, while for u away from the critical point it deviates from this power due to the second term in the square root. The same result is also obtained by the expression (3.23) given by the curvature RG approach.

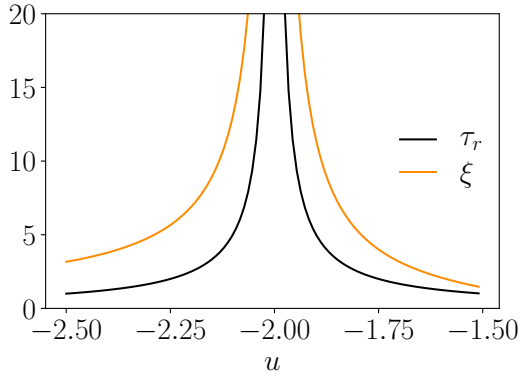

Figure 4.3: Typical time scale τ_r and typical length scale ξ of the QWZ model in the vicinity of the phase transition at $u_c = -2$.

4.1.4 Dynamics of the phase transition

The quenches are performed by smoothly varying the parameter u as

$$u(t) = u_0 + (u_1 - u_0)\sin^2\left(\frac{\pi}{2}\frac{t}{\tau}\right) \tag{4.14}$$

for $t \in [0, \tau]$ from deep in the trivial regime at $u_0 = -2.5$ to deep in the topological regime at $u_1 = -1.5$. Initially, the system is in the ground state, i.e., with the valence band filled and the conduction band empty. The time evolved states

$$|\varphi(t, \mathbf{k})\rangle = \overrightarrow{\mathcal{T}} e^{-i \int_0^t dt' \hat{H}(t')} |\psi_v(0, \mathbf{k})\rangle = c_v(t, \mathbf{k}) |\psi_v(t, \mathbf{k})\rangle + c_c(t, \mathbf{k}) |\psi_c(t, \mathbf{k})\rangle, \quad (4.15)$$

which evolved from the initial valence band $|\psi_v(0, \mathbf{k})\rangle$, are during the quench a superposition of the valence band state $|\psi_v(t, \mathbf{k})\rangle$ and the conduction band state $|\psi_c(t, \mathbf{k})\rangle$ of the instantaneous Hamiltonian $\hat{H}(t)$. The time evolution is analytically solvable for slow quenches, for which the dynamics of the whole system decomposes into a set of independent Landau-Zener models. This is shown in reference [108] to be true for any translation-invariant non-interacting fermion model. For slow quenches, the dynamics becomes non-adiabatic about $\tau/2$, where $u(t)$ is close to u_c and has a linear dependence:

$$u\left(\frac{\tau}{2} + \delta t\right) \approx -2 + \frac{(u_1 - u_0)\pi}{2\tau} \delta t. \quad (4.16)$$

Due to a slow quench, only the states with momenta close to the gap closing at $\mathbf{k}_c = (0, 0)$ will evolve non-adiabatically. Their time evolution is dictated by the Hamiltonian in equation (4.1), which can be for small momenta $|\mathbf{k}| \ll 1$ approximated by

$$\hat{H}(t, \mathbf{k}) \approx \begin{pmatrix} \frac{(u_1 - u_0)\pi}{2\tau} \delta t & k_x - i k_y \\ k_x + i k_y & -\frac{(u_1 - u_0)\pi}{2\tau} \delta t \end{pmatrix}. \quad (4.17)$$

This corresponds to the Landau-Zener model with $\triangle = k_x - i k_y$ and the transition velocity $\alpha = \frac{(u_1 - u_0)\pi}{\tau}$. The time-evolved states $|\varphi(t, \mathbf{k})\rangle$ are therefore given by the exact expression given by equation (3.7). The probability for a non-adiabatic passage to the conduction band is given by the equation (3.8). Electrons that are far away from the gap closing will evolve adiabatically and stay for all times in the valence band.

4.1.5 Density of excitations

During the quench, the energy gap closes at the critical point $u_c = -2$ for $\mathbf{k}_c = (0, 0)$, which makes the time evolution non-adiabatic. Due to the non-adiabatic dynamics, excitations are produced in the conduction band with the probability

$$n_{\text{exc}}(t, \mathbf{k}) = |\langle \psi_c(t, \mathbf{k}) | \varphi(t, \mathbf{k}) \rangle|^2 = |c_c(t, \mathbf{k})|^2. \quad (4.18)$$

This probability is called *the momentum distribution of excitations*. The total density of excitations in the system is the integral or, for finite systems with which one works when conducting numerics, the sum of the momentum distribution of excitations over the whole Brillouin zone,

$$N_{\text{exc}}(t) = \frac{1}{N^2} \sum_{\mathbf{k} \in \text{BZ}} n_{\text{exc}}(t, \mathbf{k}). \quad (4.19)$$

The momentum distribution of excitations after the quench with $\tau = 2$ is shown in figure 4.4(a). The excitations are generated in the vicinity of $\mathbf{k}_c$, where the density

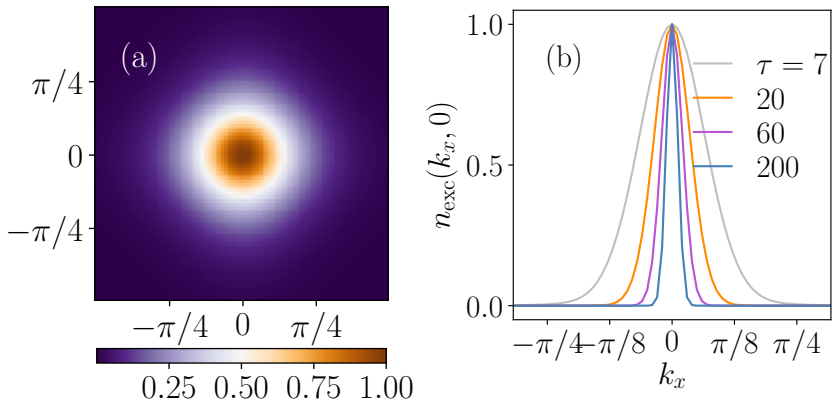

Figure 4.4: Momentum distribution of excitations (a) in the Brillouin zone for $\tau = 2$ and (b) along the $k_y = 0$ line for several quench times.

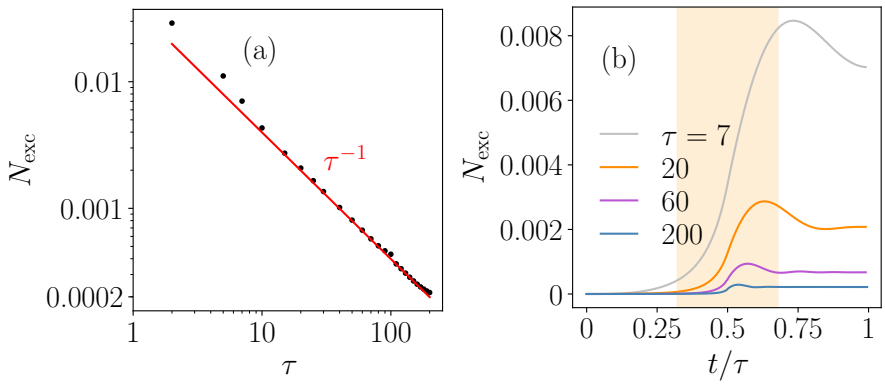

Figure 4.5: (a) Total number of excitations after the quench as a function of quench time τ, presented in the log-log scale. The red line denotes the analytical result which scales as τ^{-1}. Total number of excitations during quenches for several quench times. The orange region denotes the freeze-out regime for the $\tau = 20$ quench.

is maximal. Figure 4.4(b) shows the momentum distribution of excitations along $k_x = 0$ after quenches with different quench times. For all quench times, the number of excitations is equal to 1 at $\mathbf{k}_c$. The width of the distribution of excitations is larger for faster quenches. The momentum distribution of excitations is captured by the Landau-Zener formula (3.8) for the probability for transition,

$$n_{\mathrm{exc}}(\mathbf{k}) = e^{-|\mathbf{k}-\mathbf{k}_c|^2 2\tau/|u_0-u_1|}. \tag{4.20}$$

Therefore, rescaling the excitation densities with the prefactor $\tau^{1/2}$ along the k_y collapses them on a universal curve. Maximal momentum at which the excitations are present k_0 can be estimated from the excitations density as $k_0^2 2\tau/|u_0 - u_1| = 1$, yielding the result $k_0 = \sqrt{|u_0 - u_1|/2\tau}$.

Integrating the momentum distribution of excitations (4.20) over the Brillouin zone yields the total number of excitations [56, 63, 64, 119]

$$N_{\mathrm{exc}} = \frac{|u_1 - u_0|}{8\pi\tau}. \tag{4.21}$$

The total number of excitations as a function of τ is shown in figure 4.5(a), black points denoting the numerical results and the red line the analytical result (4.21). As u is a linear function of time near the gap closing at $t = \tau/2$, we can compare these results to the predictions of the Kibble-Zurek scaling for linear quenches. The Kibble-Zurek mechanism predicts that the total number of excitations is given by the formula for the density of zero-dimensional defects (3.16). Inserting the dimension $D = 2$ and the critical exponents $\nu = 1$ and $z\nu = 1$, as calculated in section 4.1.3, the Kibble-Zurek formula gives the same scaling $N_{\text{exc}} \propto \tau^{-1}$ as the exact Landau-Zener calculation (4.21).

Figure 4.5(b) shows the total number of excitations during quenches with different quench times. The orange region, starting at $\tau/2 - t_F$ and ending at $\tau/2 + t_F$, represents the freeze-out regime for the quench with $\tau = 20$. The excitation generation starts on the entry to the freeze-out regime at $\tau/2 - t_F$ and has an approximately constant rate throughout the freeze-out regime. The number of excitations saturates at a constant value approximately at $\tau/2 + t_F$. For faster quenches the region of excitation generation is larger. These observations are in compliance with the adiabatic-impulse approximation, the backbone of the Kibble-Zurek mechanism. It predicts for the QWZ model that the time when the evolution becomes non-adiabatic scales as $t_F \propto \sqrt{\tau}$, see equation(3.14).

4.1.6 Non-equilibrium correlation length

In this section we show that the length scale, predicted by the Kibble-Zurek mechanism, also emerges after a quench in topological insulators. The dynamical critical properties of the length scale may be observed from the time evolution of the Berry curvature. The Berry curvature of a non-equilibrium system is calculated by replacing the pre-quench eigenstates $|\psi_v(\mathbf{k})\rangle$ in equation (2.3) with the corresponding time-evolved states. The Berry curvature at the end of quenches with different quench times is shown in figure 4.6(a). During the quench, the Berry curvature develops a peak at $\mathbf{k}_c = (0, 0)$, which is consistent with the fact that the Berry curvature of the ground state grows on approaching the critical point, where it eventually diverges. The peak growth stops approximately at the freeze-out time $\tau/2 - t_F$, where t_F is given by equation (3.14). This scale was already noticed earlier as the time, at which the excitation generation starts. Afterwards, for $t > \tau/2 - t_F$, the Berry curvature stops following the ground state one.

The correlation length ξ is estimated as the inverse width at half maximum of the Berry curvature. Figure 4.6(b) shows the evolution of ξ of non-equilibrium states corresponding to different quench times (coloured lines). This is compared to the critical behaviour of ξ of the corresponding instantaneous ground states (black line). Before entering the freeze-out zone (the shaded region for $\tau = 20$), the system evolves adiabatically and its ξ is equal to the ground-state one. In the freeze-out zone, the system stops evolving adiabatically and its ξ starts to deviate from the ground-state one: it increases linearly with a speed independent of the quench time. Only after the system exits the freeze-out zone, ξ oscillates about an approximately constant value. We find the velocity to be equal to 0.6, independent of the quench time. It is thus of the order of the Fermi velocity (which is unity for our choice of unit for hopping). The fact that the velocity does not vary in the freeze-out regime follows from the scaling analysis. Close to the critical point the only relevant length

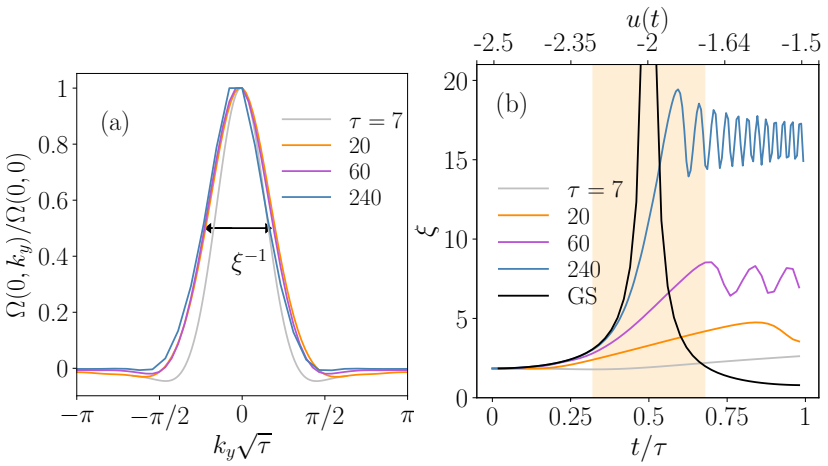

Figure 4.6: (a) Berry curvature along the $k_x = 0$ line at the end of a quench for various τ, plotted as a function of $k_y\sqrt{\tau}$. (b) ξ during quenches with various τ (colored) and ξ of instantaneous ground states (black). The shaded region is the freeze-out zone for the $\tau = 20$ quench.

scale is ξ and the time scale τ_r. Their ratio $\xi/\tau_r \propto |u - u_c|^{z\nu-\nu}$ determines the velocity of the spreading of the information through the system. As $z\nu - \nu = 0$, the velocity of correlation length growth does not depend on u and thus on τ. The linear increase of ξ in the freeze-out regime does not affect the scaling with τ at the end of the quench, it changes only the constant prefactor. Similar results were observed in quenches performed in a Rydberg atom quantum simulator [77]. This behaviour goes beyond the adiabatic-impulse approximation, which identifies the saturation of the length scale with the entry to the freeze-out zone [67].

The post-quench form of the Berry curvature for different quench times is shown in figure 4.6(a). It exhibits a peak at $\mathbf{k} = 0$ of the width proportional to $\tau^{-1/2}$, giving rise to a length scale proportional to $\tau^{1/2}$. Taking into account that $z\nu = 1$ [56], this result follows the Kibble-Zurek scaling. The Kibble-Zurek mechanism relates the characteristic length with the density of point defects $n \propto \xi^{-2}(t_F)$, making our results in agreement with earlier work [56, 63, 64, 119], which showed that excitation density scales as τ^{-1}.

4.1.7 Conservation of the Chern number

By definition, topological invariants do not change during adiabatic transformations of the Hamiltonian that respect the important symmetries. However, more general non-adiabatic transformations during which the band gap can close, were found to preserve the Chern number (at least for two band systems) by D'Allesio and Rigol in reference [50], too. Below we generalize the proof of the conservation of the Chern number to the case of multiple band systems.

Let the system be in a state with the Chern number C and the Berry curvature $\Omega_n(\mathbf{k})$ with N_F occupied states $|\psi_n(\mathbf{k})\rangle$. We limit our discussion to translational symmetric transformations described by a unitary operator $U(\mathbf{k})$, so each state is transformed as

$$|\psi_n(\mathbf{k})\rangle \to |\psi'_n(\mathbf{k})\rangle = U(\mathbf{k})|\psi_n(\mathbf{k})\rangle. \tag{4.22}$$

The Berry curvature after the transformation is

$$\begin{aligned}\Omega'_n(\mathbf{k}) = i\partial_{k_x}\langle U(\mathbf{k})\psi_n(\mathbf{k})|\partial_{k_y}|U(\mathbf{k})\psi_n(\mathbf{k})\rangle \\ -i\partial_{k_y}\langle U(\mathbf{k})\psi_n(\mathbf{k})|\partial_{k_x}|U(\mathbf{k})\psi_n(\mathbf{k})\rangle = \\ = \Omega_n(\mathbf{k}) + i\partial_{k_x}\langle\psi_n(\mathbf{k})|U(\mathbf{k})^\dagger[\partial_{k_y}U(\mathbf{k})]|\psi_n(\mathbf{k})\rangle \\ -i\partial_{k_y}\langle\psi_n(\mathbf{k})|U(\mathbf{k})^\dagger[\partial_{k_x}U(\mathbf{k})]|\psi_n(\mathbf{k})\rangle,\end{aligned} \tag{4.23}$$

where we used $\partial_{k_i}|U(\mathbf{k})\psi_n(\mathbf{k})\rangle = [\partial_{k_i}U(\mathbf{k})]|\psi_n(\mathbf{k})\rangle + U(\mathbf{k})\partial_{k_i}|\psi_n(\mathbf{k})\rangle$. Note that expressions $\langle\psi_n(\mathbf{k})|\hat{O}(\mathbf{k})|\psi_n(\mathbf{k})\rangle = \mathrm{Tr}[\rho_n(\mathbf{k})\hat{O}(\mathbf{k})]$ are smooth in $\mathbf{k}$ when $\hat{O}(\mathbf{k})$ and the density matrix $\rho_n(\mathbf{k}) = |\psi_n(\mathbf{k})\rangle\langle\psi_n(\mathbf{k})|$ are smooth in $\mathbf{k}$. When $U(\mathbf{k})$ is smooth in $\mathbf{k}$, which is true for time evolutions with Hamiltonians that are smooth in $\mathbf{k}$, the second and the third term in $\Omega_n(\mathbf{k})$ are continuous functions of $\mathbf{k}$ and the Chern number can be written as

$$\begin{aligned}C' = C - \frac{1}{2\pi}\sum_{n=1}^{N_F}\int \mathrm{d}k_y \int \mathrm{d}k_x\, i\partial_{k_x}\langle\psi_n(\mathbf{k})|U(\mathbf{k})^\dagger[\partial_{k_y}U(\mathbf{k})]|\psi_n(\mathbf{k})\rangle - \\ \frac{1}{2\pi}\sum_{n=1}^{N_F}\int \mathrm{d}k_x \int \mathrm{d}k_y\,(-i)\partial_{k_y}\langle\psi_n(\mathbf{k})|U(\mathbf{k})^\dagger[\partial_{k_x}U(\mathbf{k})]|\psi_n(\mathbf{k})\rangle.\end{aligned} \tag{4.24}$$

Using the periodicity of $U(\mathbf{k})$ and $|\psi_n(\mathbf{k})\rangle$ over the Brillouin zone, the first integral over k_x and the second integral over k_y are zero (or, put differently, each component of the vector field $\langle\psi_n(\mathbf{k})|U(\mathbf{k})^\dagger[\partial_{k_i}U(\mathbf{k})]|\psi_n(\mathbf{k})\rangle$ is smooth in $\mathbf{k}$, hence the Stokes theorem can be applied). Hence, we obtain $C' = C$, i.e. the Chern number is conserved under a unitary transformation.

To show that our proof reduces to the one for two-band systems done by D'Allesio and Rigol in reference [50], we calculate the time derivative of the Chern number (4.24). $U(\mathbf{k})$ now represents the time evolution operator and by taking into account that $\partial_t U^\dagger(\mathbf{k})[\partial_{k_i}U(\mathbf{k})] = -iU^\dagger(\mathbf{k})[\partial_{k_i}\hat{H}(\mathbf{k})]U(\mathbf{k})$, we get

$$\begin{aligned}\partial_t C' = -\frac{1}{2\pi}\sum_{n=1}^{N_F}\int \mathrm{d}\mathbf{k}\,\Big(\partial_{k_x}\langle\psi'_n(\mathbf{k})|[\partial_{k_y}\hat{H}(\mathbf{k})]|\psi'_n(\mathbf{k})\rangle \\ -\partial_{k_y}\langle\psi'_n(\mathbf{k})|[\partial_{k_x}\hat{H}(\mathbf{k})]|\psi'_n(\mathbf{k})\rangle\Big).\end{aligned} \tag{4.25}$$

For a two-band Hamiltonian $\hat{H}(\mathbf{k}) = -\frac{1}{2}\mathbf{B}(\mathbf{k})\cdot\hat{\boldsymbol{\sigma}}$ and the state expressed with the density matrix $\hat{\rho}(\mathbf{k}) = \frac{1}{2}(\hat{\sigma}_0 + \mathbf{S}(\mathbf{k})\cdot\hat{\boldsymbol{\sigma}})$, we obtain the result from reference [50]

$$\partial_t C' = \frac{1}{4\pi}\int \mathrm{d}\mathbf{k}\left[\partial_{k_x}(\mathbf{S}(\mathbf{k})\cdot\partial_{k_y}\mathbf{B}(\mathbf{k})) - \partial_{k_y}(\mathbf{S}(\mathbf{k})\cdot\partial_{k_x}\mathbf{B}(\mathbf{k}))\right], \tag{4.26}$$

which vanishes after the application of the Stokes theorem due to the smoothness of $\mathbf{S}(\mathbf{k})\cdot\partial_{k_i}\mathbf{B}(\mathbf{k})$ at all times.

4.1.8 Evaluation of the Hall conductivity

Chern insulators feature in the topological phase the anomalous quantum Hall effect. The presence of a small electrical field in x-direction $\mathbf{E} = E_x\mathbf{e}_x$ will induce a charge

current in the perpendicular y-direction. The proportionality constant σ_{yx} between the J_y and the electrical field is called *the Hall conductivity*,

$$J_y = \sigma_{yx} E_x, \tag{4.27}$$

which is quantized in the units of $\sigma_0 = \frac{e^2}{h}$ and proportional to the Chern number,

$$\sigma_{xy} = \frac{e^2}{h} C. \tag{4.28}$$

Note that conductivity is antisymmetric $\sigma_{xy} = -\sigma_{yx}$. The current operator is equal to

$$\hat{\mathbf{J}} = e\, i[\hat{H}, \hat{\mathbf{r}}], \tag{4.29}$$

where $\hat{\mathbf{r}}$ is the position operator. In the Bloch basis it translates to the following form

$$\hat{\mathbf{J}} = \sum_{\mathbf{k}} |\mathbf{k}\rangle\langle\mathbf{k}| \otimes e \nabla_{\mathbf{k}} \hat{H}(\mathbf{k}). \tag{4.30}$$

The current is equal to the expectation value of $\hat{\mathbf{J}}$. Therefore, the Hall conductivity can be evaluated as

$$\sigma_{yx} = \frac{1}{E_x} \sum_{n=1}^{N_F} \int \frac{\mathrm{d}\mathbf{k}}{(2\pi)^2} \langle \psi_n(\mathbf{k}) | e \partial_{k_y} \hat{H}(\mathbf{k}) | \psi_n(\mathbf{k}) \rangle, \tag{4.31}$$

where the sum over n runs over all occupied bands $|\psi_n(\mathbf{k})\rangle$. The current in the

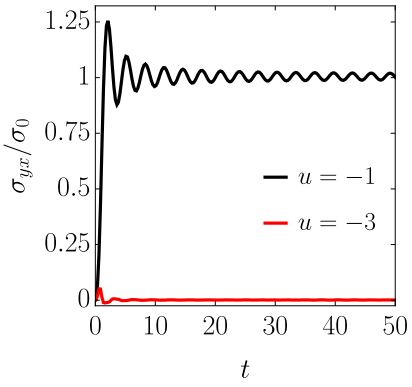

Figure 4.7: Hall conductivity of a state that evolved adiabatically in time from the ground state at $u = -3$ (red) and $u = -1$ (black) due to the time-dependent vector potential.

ground state is zero. By adiabatically turning on a weak time-dependent electric field we induce a current in the linear response. States $|\psi_n(\mathbf{k})\rangle$ in equation (4.31) are therefore time-evolved states. In this work we induce the electric field of the form

$$E_x(t) = E_0 \left(1 - e^{-t/\tau_E}\right) \tag{4.32}$$

with $\tau_E = 10$ and $E_0 = 0.0001$. In order to preserve the translation invariance, one may introduce a homogeneous electric field via a spatially-homogeneous time dependent vector potential $A_x(t) = -\int E_x(t)\mathrm{d}t$ [155]. The vector potential is introduced

to the Hamiltonian as a shift of momentum:

$$\hat{H}(\mathbf{k}) \to \hat{H}(\mathbf{k} - e\mathbf{A}(t)). \tag{4.33}$$

The Hall conductivity as a function of time is shown in figure 4.7. One can see a sharp distinction between the result in the topological phase where, following a steep rise, the Hall conductivity oscillates around a quantized value and the trivial regime, where it oscillates around zero instead. The frequency of these oscillations is equal to the band gap. The amplitude of the oscillations diminishes with time and it also becomes smaller if the electric field is turned on more adiabatically (i.e., with longer τ_E).

4.1.9 Non-equilibrium Hall conductivity

Hall conductivities, evaluated as the electric field is turned on after the quench from $u_0 = -3$ to $u_1 = -1$, are for several quench durations shown in figure 4.8 (a). As for systems in the ground state, the Hall conductivity first experiences transient behaviour and then oscillates around a non-zero value $\bar{\sigma}_{yx}$, with the frequency equal to the band gap of the final Hamiltonian. As seen in the plot 4.8(a) and as discussed in more detail below, the oscillations become small for slow enough quenches and $\bar{\sigma}_{yx}$ approaches the value characteristic of the final Hamiltonian [56, 62].

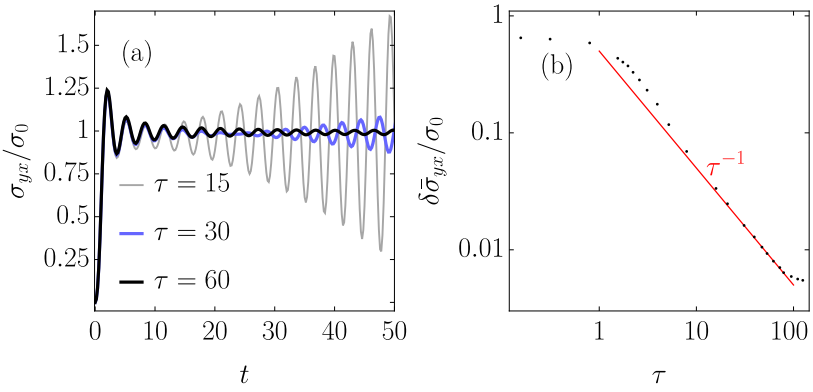

Figure 4.8: (a) Hall conductivity of the non-equilibrium states, resulting from the quench with $\tau = 15$ (grey, thin), $\tau = 30$ (blue) and $\tau = 60$ (black). (b) Time-averaged Hall conductivity after the quench converges for $\tau \to \infty$ to the ground-state value of the post-quench Hamiltonian. The red curve corresponds to the analytical estimate in equation (4.35). The quenches started at $u_0 = -3$ and ended at $u_1 = -1$.

The dependence of $\bar{\sigma}_{yx}$ on the quench duration τ is presented in figure 4.8 (b). The deviations from the ground-state values vanish for slow quenches as τ^{-1}. In order to understand the observed behaviour, we evaluated the Hall conductivity using the time-dependent perturbation theory [56, 60] (see section 4.1.10). We obtained the following analytical formula for the time-averaged Hall conductivity at large times:

$$\bar{\sigma}_{yx} = \frac{e^2}{(2\pi)^2} \sum_{n\in\{v,c\}} \int \mathrm{d}\mathbf{k}\, n_n(\mathbf{k})\Omega_n(\mathbf{k}), \tag{4.34}$$

where $n_n(\mathbf{k})$ is the occupation of the n-th energy band at $\mathbf{k}$. The Hall conductivity is expressed as an integral of the Berry curvature (2.3) of the n-th energy band of

the static Hamiltonian after the quench without electric field, weighted by the band occupancy. The Berry curvature of the conduction band $\Omega_c(\mathbf{k})$ has the opposite sign to that of the valence band $\Omega_v(\mathbf{k})$. Therefore, the excitations above the ground state diminish the time-averaged Hall conductivity, which explains the dependence seen in figure 4.8 (b). For slow quenches excitations occur in a small region in k-space and thus contribute little to the integral in equation (4.34). Therefore, the time-averaged conductivity converges for long τ to the ground-state one. The expression for the Hall conductivity can be further simplified to

$$\bar{\sigma}_{xy} \approx \frac{e^2}{2\pi}\left(1 - \frac{|u_1 - u_0|}{4\tau}\right), \tag{4.35}$$

where the Landau-Zener formula for the energy band occupancy (4.21) was used and the Berry curvature was approximated by its value at $\mathbf{k}_c = (0, 0)$ (similar was done in reference [61]). For slow enough quenches deviation of $\bar{\sigma}_{xy}$ from the ground state value is proportional to the total number of excitations and hence obeys the Kibble-Zurek scaling.

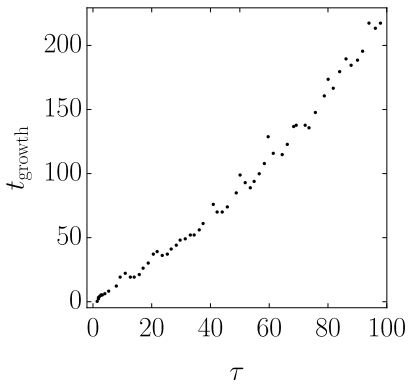

Figure 4.9: (c) Time at which the amplitude of oscillations in the Hall response after the quench increases for 10% above the minimal amplitude. The quench started at $u_0 = -3$ and ended at $u_1 = -1$.

Finally, let us consider oscillations around the time-averaged value. For short times oscillations diminish and for later times they start to grow quadratically (see section 4.1.10). The time t_{growth} after which the amplitude of oscillations starts to grow increases with the duration of the quench τ. In order to give a somewhat more quantitative estimate of the behaviour, t_{growth} is defined as the time after which the amplitude of the oscillations increases by 10% above the minimal amplitude found for a given τ, figure 4.9. Note that t_{growth} is roughly linear in τ, which means that for slow quenches there is a long time window where these oscillations are not important. In Section 4.1.10 it is shown that the growth of the oscillations occurs due to the non-zero off-diagonal elements of the density matrix in the basis of the eigenstates of the final Hamiltonian. Actually, often in evaluations of the Hall conductivity [142, 156, 157] only the diagonal parts of the density matrix are retained, which is supported by the argument that a measurement of the Hall conductivity unavoidably introduces decoherence and collapses the quenched state to a state represented by a diagonal Gibbs ensemble.

4.1.10 Perturbative evaluation of the Hall conductivity

The Hall conductivity is exactly calculated as the expectation value of the current operator (4.31), which is evaluated for a Hamiltonian with explicitly included electric field. For small electric fields, one can evaluate the Hall conductivity also perturbatively. Let the electrons after the quench occupy the states

$$|\varphi_\alpha(\mathbf{k})\rangle = \sum_{n=1}^{M} c_{\alpha,n}(\mathbf{k}) e^{-iE_n(\mathbf{k})t} |\psi_n(\mathbf{k})\rangle, \tag{4.36}$$

where momentum $\mathbf{k}$ runs over the whole BZ and $\alpha = 1, \dots N_F$ over all occupied energy bands. n runs over all M energy bands, and $|\psi_n(\mathbf{k})\rangle$ is the eigenstate with corresponding eigenenergy $E_n(\mathbf{k})$ of the post-quench Hamiltonian $\hat{H}(\mathbf{k})$ without electric field. The response due to the electric field can be evaluated using the time-dependent perturbation theory. The electric field is added to the system via a time-dependent vector potential $\mathbf{A}(t) = A_x(t)\mathbf{e}_x$ as in equation (4.33). For small $A_x(t)$, this can be approximated with an expansion up to the linear order,

$$\hat{H}(\mathbf{k} - e\mathbf{A}(t)) \approx \hat{H}(\mathbf{k}) - e\mathbf{A}(t) \cdot \nabla_{\mathbf{k}} \hat{H}(\mathbf{k}) = H(\mathbf{k}) - eA_x(t)\partial_{k_x} \hat{H}(\mathbf{k}). \tag{4.37}$$

The presence of a time-dependent perturbation causes the occupied states to evolve in time, therefore the amplitudes become time-dependent: $c_{\alpha,n}(\mathbf{k}) \to c_{\alpha,n}(t, \mathbf{k})$. In the first order perturbation theory, which is concise for small and adiabatic perturbations, the states evolve as $c_{\alpha,n}(t, \mathbf{k}) \approx c_{\alpha,n}(\mathbf{k}) + \delta c_{\alpha,n}(t, \mathbf{k})$ where

$$\delta c_{\alpha,n}(t, \mathbf{k}) = -i \sum_{n'=1}^{M} \int_0^t dt' M_{n,n'}(t', \mathbf{k}) e^{i\triangle_{n,n'}(\mathbf{k})t'} c_{\alpha,n'}(\mathbf{k}). \tag{4.38}$$

Here, $M_{n,n'}(t', \mathbf{k}) = \langle \psi_n(\mathbf{k})| - eA_x(t')\partial_{k_x}\hat{H}(\mathbf{k})|\psi_{n'}(\mathbf{k})\rangle$ is the matrix element of the perturbation and $\triangle_{n,n'}(\mathbf{k}) = E_n(\mathbf{k}) - E_{n'}(\mathbf{k})$. Inserting the time-evolved states in the equation (4.31) and obtaining only the first order terms in A_x gives

$$\begin{aligned} \sigma_{yx}(t) = \frac{2}{E_x} \mathrm{Re} \sum_{\alpha=1}^{N_F} \sum_{n,m=1}^{M} \int_{\mathrm{BZ}} \frac{\mathrm{d}\mathbf{k}}{(2\pi)^2} \times \\ c^*_{\alpha,n}(\mathbf{k}) \delta c_{\alpha,m}(t, \mathbf{k}) e^{i\triangle_{n,m}t} \langle \psi_n(\mathbf{k})| e\partial_{k_y} \hat{H}(\mathbf{k}) |\psi_m(\mathbf{k})\rangle. \end{aligned} \tag{4.39}$$

The explicit time-dependent expression for the Hall conductivity is

$$\begin{aligned} \sigma_{yx}(t) = \frac{2e^2}{(2\pi)^2} \mathrm{Re} \sum_{\alpha}^{N_F} \sum_{n,n'm=1}^{M} \int \mathrm{d}\mathbf{k}\, c^*_{\alpha,n}(\mathbf{k}) c_{\alpha,n'}(\mathbf{k}) \times \\ f_{nn'm}(t, \mathbf{k}) \langle \psi_n(\mathbf{k}) \partial_{k_y} \hat{H} |\psi_m(\mathbf{k})\rangle \langle \psi_m(\mathbf{k})| \partial_{k_x} \hat{H} |\psi_{n'}(\mathbf{k})\rangle, \end{aligned} \tag{4.40}$$

$$f_{nn'm}(t, \mathbf{k}) = -i\, e^{i\triangle_{nm}(\mathbf{k})t} \int_0^t e^{i\triangle_{mn'}(\mathbf{k})t'} A_x(t')\, \mathrm{d}t' / E_x(t). \tag{4.41}$$

In equation (4.40) the Hall conductivity is expressed with time-independent coefficients of the post-quench state $c_{\alpha,n}(\mathbf{k})$, likewise time-independent matrix elements

of $\partial_{k_y}\hat{H}$ and $\partial_{k_x}\hat{H}$ and a time-dependent function $f_{nn'm}(t, \mathbf{k})$ which is expressed in terms of energies of the states $E_n(\mathbf{k})$ and the dependence of the electric field on time. This expression holds for a general system with multiple energy bands. In the case of the QWZ model, the number of energy bands is $M = 2$ and only one state per $\mathbf{k}$ is occupied, so the index α will be in further discussion omitted. It turns out that for parameters used in this work, equation (4.40) gives results that are essentially the same as that of the full evaluation. A comparison between the results of equation (4.40) (blue line) and of the full evaluation (black, dotted line) is shown in figure 4.10 (a).

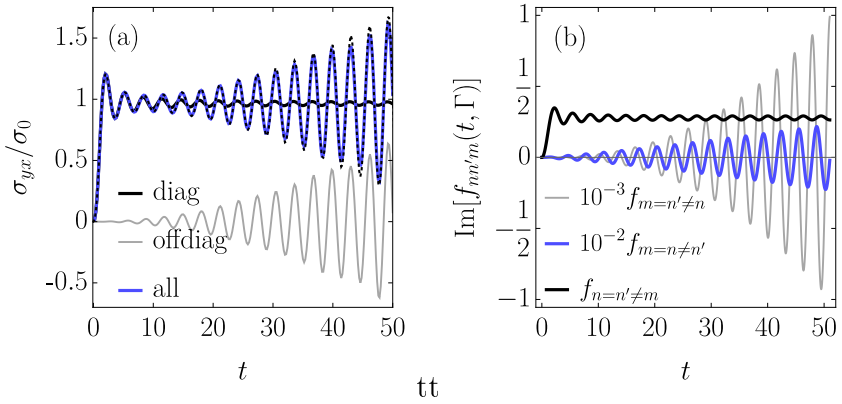

tt

Figure 4.10: (a) Diagonal (black), off-diagonal (grey), all terms (blue) in $\sigma_{yx}(t)$ according to equation (4.40) and $\sigma_{yx}(t)$ resulting from the full evaluation of equation (4.31) (black, dotted) for the system after the quench for $\tau = 15$, $u_0 = -3$ and and $u_1 = -1$. (b) Imaginary part of the time-dependent element $f_{nn'm}(t, (0, 0))$, for the system at parameters $u = -1$, is shown for different index combinations. In both figures the electric field is turned on as in equation (4.32).

The expression (4.40) is convenient for the interpretation of the results. The contributions to the Hall conductivity that include diagonal elements of the density matrix in the basis of Hamiltonian eigenstates $|c_n(\mathbf{k})|^2$ (hereafter referred to as 'diagonal terms'), and contributions including off-diagonal elements of the density matrix $c_n^*(\mathbf{k})c_{n'}(\mathbf{k})$ (referred to as 'off-diagonal terms') behave differently, see figure 4.10 (a). One can see that the diagonal terms give rise to the finite average value of σ_{yx}. The frequency of the decaying small oscillations around this average value is given by the magnitude of the gap. The off-diagonal terms, on the other hand, exhibit oscillations around 0 with the magnitude that for long times increases in time quadratically. The observed time-dependence can be considered analytically by evaluating the time-dependent function $f_{nn'm}(t, \mathbf{k})$.

The diagonal terms contain $\langle\psi_n(\mathbf{k})|\partial_{k_y}\hat{H}|\psi_m(\mathbf{k})\rangle\langle\psi_m(\mathbf{k})|\partial_{k_x}\hat{H}|\psi_n(\mathbf{k})\rangle$, which is non-vanishing only for index combinations $n \neq m$, where it is imaginary. Therefore, only the imaginary part of the function $f_{nnm}(t, \mathbf{k})$ contributes to the integral. The explicit evaluation for long times ($t \gg \tau_E$) yields

$$\mathrm{Im}[f_{nnm}(t, \mathbf{k})] = \frac{1}{\triangle_{nm}^2(\mathbf{k})} - \frac{\cos[\triangle_{nm}(\mathbf{k})t] + \triangle_{nm}(\mathbf{k})\tau_E \sin[\triangle_{nm}(\mathbf{k})t]}{\triangle_{nm}(\mathbf{k})^2[1 + \triangle_{nm}^2(\mathbf{k})\tau_E^2]}. \tag{4.42}$$

For long times, the function at every $\mathbf{k}$ oscillates around a finite mean value $1/\triangle_{nm}(\mathbf{k})^2$. The amplitude of oscillations vanishes with $\tau_E \to \infty$.

We now turn to the off-diagonal terms. The leading off-diagonal terms are given by index combinations $m = n' \neq n$ and the corresponding time-dependent function for long times grows quadratically with t, $f_{nmm}(t, \mathbf{k}) = i\, e^{-i\triangle_{nm}(\mathbf{k})t}[(t-\tau_E)^2 + \tau_E^2]/2$. Other off-diagonal index combinations give rise to oscillations that grow linearly with time and are hence important only initially. Figure 4.10 (b) shows the imaginary part of the function $f_{nn'm}(t, \mathbf{k})$ for different index combinations.

Finally, we note that in the limit of an infinitely slow quench, excitations are present with probability 1 only at $\mathbf{k}$ where the band gap closes. For such a system, the off-diagonal elements of the density matrix $c_n^*(\mathbf{k})c_{n'}(\mathbf{k})$ are equal to zero for every $\mathbf{k}$, meaning that the growth of oscillations never occurs.

4.2 Time-reversal symmetric topological insulators

4.2.1 Bernevig-Hughes-Zhang model

The BHZ model describes a two-dimensional time-reversal symmetric $s = 1/2$ system on a square crystalline lattice with two orbitals per unit cell. Its bulk momentum-space Hamiltonian is given by

$$\begin{aligned}\hat{H}(\mathbf{k}) = \hat{s}_0 \otimes [(u + \cos k_x + \cos k_y)\hat{\sigma}_z + \sin k_y \hat{\sigma}_y] \\ + \hat{s}_z \otimes \sin k_x \hat{\sigma}_x + c\, \hat{s}_x \otimes \hat{\sigma}_y,\end{aligned} \tag{4.43}$$

where $\hat{s}_0$ is the identity operator in spin space and $\hat{s}_i$ and $\hat{\sigma}_i$ are Pauli operators acting on the spin and local orbital degrees of freedom, respectively. $c \in \mathbb{R}$ is the amplitude of the coupling operator of the spin sectors and u is the staggered orbital binding energy. The Hamiltonian is expressed in the units of inter-cell hopping amplitude which is equal in both x and y directions. The lattice constant is set to 1. When $c = 0$, the original BHZ model [11] is recovered, in which the perpendicular projection of the spin s_z is conserved. It is equal to two independent copies of the QWZ model and it describes the low-energy physics of the HgTe/CdTe quantum wells. In systems with band inversion asymmetry and structural inversion asymmetry, such as InAs/GaSb/AlSb Type-II semiconductor quantum wells [94], terms that couple states with opposite spin projections and preserve the time-reversal symmetry arise. Such terms are modelled with the simplified $c \neq 0$ term.

The energy spectrum consists of four energy bands with energy dispersions $E_n(\mathbf{k})$ and the corresponding eigenstates $|\psi_n(\mathbf{k})\rangle$. In the half-filled systems considered in this work, the ground state has completely occupied lower two energy bands (denoted with band index $n = 1, 2$) and empty upper two energy bands ($n = 3, 4$). Therefore, the ground state is presented by the set of states

$$\{|\psi_n(\mathbf{k})\rangle,\, \mathbf{k} \in \mathrm{BZ},\, 1 \leq n \leq N_F = 2\}. \tag{4.44}$$

The Hamiltonian has the inversion symmetry

$$\hat{H}(-\mathbf{k}) = \hat{s}_z \otimes \hat{\sigma}_z \hat{H}(\mathbf{k})\, \hat{s}_z \otimes \hat{\sigma}_z, \tag{4.45}$$

and the time-reversal symmetry with the time-reversal operator $\hat{\mathcal{T}} = i\hat{s}_y K$ as the BHZ Hamiltonian fulfils the requirement (2.10). As the time-reversal operator is of the $\hat{\mathcal{T}}^2 = -1$ type, this entails the system with Kramers degeneracy (see section 2.3.2). The model belongs to the AII symmetry class, which is characterized by

the $\mathbb{Z}_2$ topological invariant. A system with edges in the topological phase exhibits a pair of edge states that is topologically protected against dissipation. The presence of the edge state pair is given by the $\mathbb{Z}_2$ invariant.

4.2.2 Topological properties

In numerical evaluation it is convenient to use a gauge invariant definition of the $\mathbb{Z}_2$ invariant N_{bulk}: it is equal to the parity of the number of times the *Wannier centre flow* $\theta_n(k_y)$, in range $k_y \in (0, \pi)$, crosses an arbitrarily chosen fixed value $\tilde{\theta} \in [-\pi, \pi)$ [158],

$$N_n(\tilde{\theta}) = \text{number of solutions } k_y \in (0,\pi) \text{ of } \theta_n(k_y) = \tilde{\theta}, \tag{4.46}$$

$$N_{\text{bulk}} = \left(\sum_{n=1}^{N_F} N_n(\tilde{\theta}) \right) \bmod 2. \tag{4.47}$$

The Wannier centre flow $\theta_n(k_y)$ is equal to the phase of the n-th eigenvalue of the Wilson loop, a multi-band generalization of the Berry phase. The Wilson loop is defined as

$$W(k_y) = M^{(12)} M^{(23)} \dots M^{(N-1,N)} M^{(N,1)}, \tag{4.48}$$

$$M^{(kl)}_{nm} = \langle \psi_n(k\delta_k - \pi, k_y) | \psi_m(l\delta_k - \pi, k_y) \rangle, \tag{4.49}$$

where $\delta_k = 2\pi/N$ is the discretization step in the momentum space of a lattice with periodic boundary conditions and $N \times N$ sites. Matrices $W(k_y)$ and $M^{(kl)}$ are of dimension $N_F \times N_F$. Wannier centre flow can be associated with the position expectation value relative to the nearest lattice site [154]. The $\mathbb{Z}_2$ invariant is well defined only for systems in which the Wannier centre flow is symmetric about and doubly degenerate at $k_y = 0, \pi$. These two characteristics of the Wannier centres are imposed by the time-reversal symmetry. For pedagogical discussion see reference [154]. A graphical description of this method is shown in figure 4.11(b).

The phase diagram of the BHZ model, shown in figure 4.11 (a), describes the topological phase of the ground state of the Hamiltonian (4.43) at parameters $P = (u, c)$. It consists of three insulating regions: the trivial regime with $N_{\text{bulk}} = 0$ (white) and two topological regimes with $N_{\text{bulk}} = 1$ (grey). Insulating regimes are separated from each other by a broad Dirac semimetal regime (blue region) in which the system has a closed band gap with linear dispersion. The boundaries between different regimes are given in the next section. Upon changing the sign of c, the $\mathbb{Z}_2$ invariant remains unchanged, which is a consequence of the following symmetry of the Hamiltonian: $\hat{s}_z \hat{H}_{-c}(\mathbf{k}) \hat{s}_z = \hat{H}_c(\mathbf{k})$.

4.2.3 Properties of the energy bands

Inspecting the presence of the band gap for various values of parameters u and c shows that the system consists of three insulating regimes that are separated from each other by a broad Dirac semimetal regime in which the system has a closed band gap with linear dispersion. The upper boundary between the semimetal and the trivial insulator regimes is $c(u) = \sqrt{2 - u^2/2}$, while the lower boundaries between the topological insulator and semimetal regimes are $c(u) = \sqrt{1 - (u-1)^2}$ and $c(u) = \sqrt{1 - (u+1)^2}$. In the semimetal regime the band gap closes at different points in the Brillouin zone, in particular for $P_{01} = (-2, 0)$ at $\mathbf{k}_c = (0, 0)$, for

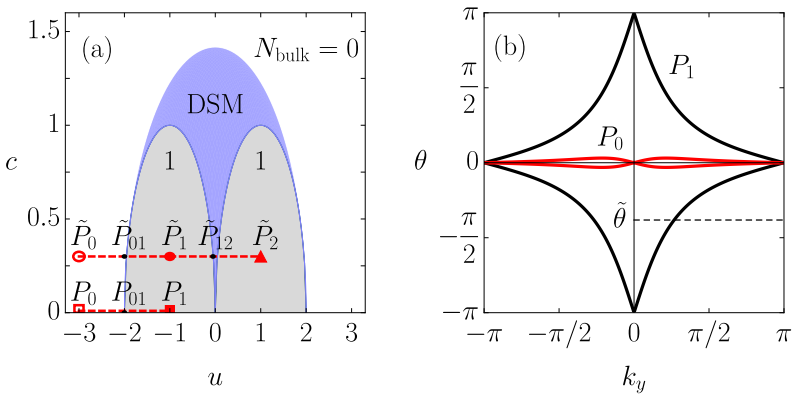

Figure 4.11: (a) Phase diagram of the BHZ model in $P = (u, c)$ parameter space. The grey coloured area marks topological insulator parameter regimes where $N_{\text{bulk}} = 1$, white area the trivial insulator regime with $N_{\text{bulk}} = 0$ and the blue area the Dirac semimetal regime. Points $P_0 = (-3, 0)$, $\tilde{P}_0 = (-3, 0.3)$, $P_1 = (-1, 0)$, $\tilde{P}_1 = (-1, 0.3)$ and $\tilde{P}_2 = (1, 0.3)$ mark initial and final points between which parameters of the Hamiltonian are quenched (red, dashed). Several band gap closing points are marked as P_{01}, $\tilde{P}_{01}$ and $\tilde{P}_{12}$. (b) Wannier centre flows for the ground state of the Hamiltonian at P_0 (red) and P_1 (black). The dashed black line presents a chosen $\tilde{\theta}$ used for the determination of the $\mathbb{Z}_2$ invariant.

$P = (0, 0)$ at $\mathbf{k}_c = (0, \pi)$ and $(\pi, 0)$, for $P = (2, 0)$ at $\mathbf{k}_c = (\pi, \pi)$ and for $P = (\pm 1, 1)$ at $\mathbf{k}_c = (\pm\pi/2, 0)$ and $(0, \pm\pi/2)$. Graphs of the energy dispersion are shown at the band gap closing points P_{01}, $\tilde{P}_{01}$ and $\tilde{P}_{12}$ in figure 4.12.

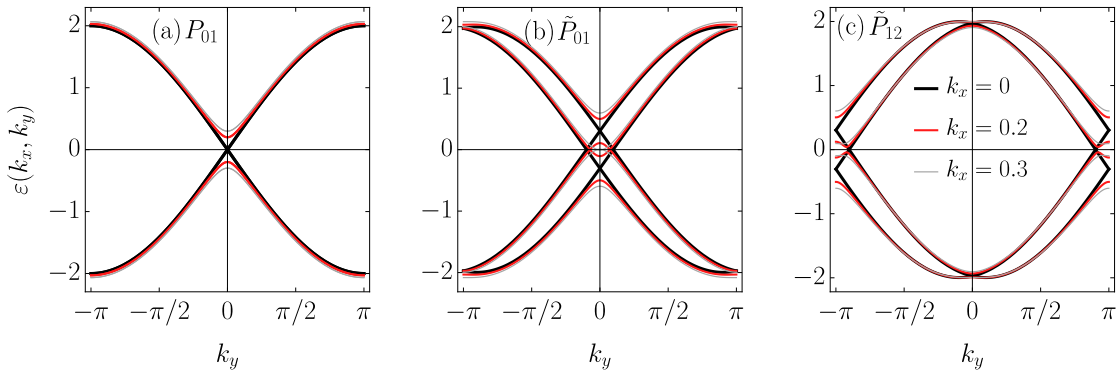

Figure 4.12: Band dispersions at (a) P_{01}, (b) $\tilde{P}_{01}$ and (c) $\tilde{P}_{12}$ for $k_x = 0$ (black), $k_x = 0.2$ (blue) and $k_x = 0.3$ (red).

For $0 < c \ll 1$ simple analytical expressions are found for the energy dispersion near the gap closing. Let u_c and $\mathbf{k}_c$ be the values of u and $\mathbf{k}$, respectively, where the band gap closes at $c = 0$. They coincide with the ones of the QWZ model presented in section 4.1.1. For system with $0 < c \ll 1$ ($c = 0.3$ is small enough), the band gap closes at momenta close to $\mathbf{k}_c$. Expanding the Hamiltonian (4.43) to the first order in the deviation of the momentum from $\mathbf{k}_c$ we obtain band dispersions

$$\begin{aligned} &\pm\sqrt{(q-c)^2 + (u-u_c)^2}, \\ &\pm\sqrt{(q+c)^2 + (u-u_c)^2}, \end{aligned} \tag{4.50}$$

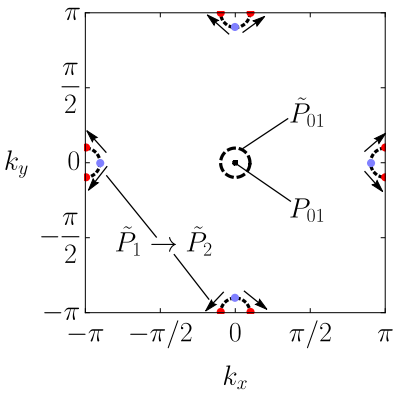

Figure 4.13: Band gap closing in k space. At P_{01}, the gap closes in a single point $\mathbf{k} = (0, 0)$, while at $\tilde{P}_{01}$ on a whole circle with radius c. However, when changing u from $\tilde{P}_1$ to $\tilde{P}_2$ and keeping c constant, the gap closes gradually starting at blue points and moving to red ones, as indicated with arrows, tracing out a circle of radius c.

where $q = |\mathbf{k} - \mathbf{k}_c| \ll \pi$. For $c = 0$ the band gap between two spin degenerate valence bands and two spin degenerate conduction bands closes at $\mathbf{k}_c$ with linear dispersion $\pm q$ while for $0 < c \ll 1$ the band gap between the upper valence band and the lower conduction band closes on a circle with radius c around $\mathbf{k}_c$, again with linear dispersion $\pm |q - c|$. Figure 4.12 shows cross-sections of band dispersions for different k_x at different band gap closing points P. Note that when c is not small enough, the behaviour of the band gap closing changes when crossing over $u_c = 0$. On entering the semimetal regime, the band gap closes only at four points in momentum space (blue points in figure 4.13). However, keeping c constant and changing the parameter u through the whole semimetal regime, the four points split into eight points that with the progressing u move along circles centered at momenta $(\pm\pi, 0)$ and $(0, \pm\pi)$. When they reach the Brillouin zone boundary (red points in figure 4.13), the band gap opens and the insulating topological regime is reached. For example, for the particular value of u corresponding to figure 4.12 (c) the gap is closed only at $k_x = 0$.

4.2.4 Evaluation of the spin Hall conductivity

Time-reversal symmetric topological insulators feature in the topological phase the spin Hall effect [10]. The presence of a small electrical field in x-direction $\mathbf{E} = E_x \mathbf{e}_x$ will induce a spin current in a perpendicular y-direction. The proportionality constant $\sigma_{xy}^{\text{spin}}$ between the spin current J_y^{spin} and the electrical field is called *the spin Hall conductivity*,

$$J_y^{\text{spin}} = \sigma_{yx}^{\text{spin}} E_x. \tag{4.51}$$

In systems with a conserved s_z component of spin, the spin Hall conductivity is quantized in the units of $e/2\pi$ and can be expressed with the Chern numbers of uncoupled spin-up and spin-down subspaces,

$$\sigma_{xy}^{\text{spin}} = \frac{e}{2\pi} \left(\frac{C_\uparrow - C_\downarrow}{2} \right) \mod 2. \tag{4.52}$$

In systems with a non-conserved s_z component of spin, for example due to Rashba interaction, the spin Hall conductivity is in general not quantized.

The spin current is the expectation value of the spin current operator $\hat{\mathbf{J}}^{\text{spin}}$. The definition of the spin current remains an active subject of discussions [155, 159, 160, 161, 162]. The commonly used operator that is defined simply as the product of spin and velocity

$$\hat{\mathbf{J}}^{\text{spin}} = \frac{1}{2}\left\{ i[\hat{H}, \hat{\mathbf{r}}], \frac{1}{2}\hat{s}_z \right\} \tag{4.53}$$

suffers from three flaws when the spin is not a conserved quantity: the spin current is not conserved, it can be non-zero in insulators with localized eigenstates only, so it cannot describe transport [163], and lastly there is no mechanical or thermodynamic force in conjugation with this current, so it does not fit into the near-equilibrium transport theory. Recently, a spin current operator that is defined as a time derivative of the spin displacement $\hat{\mathbf{r}}\hat{s}_z$ and evades these issues, was proposed in reference [159]

$$\hat{\mathbf{J}}^{\text{spin}} = i\left[\hat{H}, \frac{1}{2}\hat{\mathbf{r}}\hat{s}_z\right]. \tag{4.54}$$

Note that the operator is not translation invariant due to

$$\hat{\mathbf{J}}^{\text{spin}} = i\hat{\mathbf{r}}\underbrace{\left[\hat{H}, \frac{1}{2}\hat{s}_z\right]}_{\text{transl.-inv.}} + \underbrace{i\left[\hat{H}, \hat{\mathbf{r}}\right]\frac{1}{2}\hat{s}_z}_{\text{transl.-inv.}}. \tag{4.55}$$

For the evaluation of such an operator in a translation invariant system see reference [162]. As shown in reference [162], the two definitions of the spin current give the same result for systems with a unit cell that has all of internal degrees of freedom positioned on the same spatial position. This is the case for the BHZ model, therefore the translation invariant definition of the spin current (4.53) may be used. Using the relation

$$i[\hat{H}, \hat{\mathbf{r}}] = \sum_{\mathbf{k}} |\mathbf{k}\rangle\langle\mathbf{k}| \otimes \nabla_{\mathbf{k}}\hat{H}(\mathbf{k}) \tag{4.56}$$

and taking into account that for the BHZ model $\hat{s}_z$ and $\nabla_{\mathbf{k}}\hat{H}(\mathbf{k})$ commute, we obtain the expression for the spin current operator in the Bloch basis

$$\hat{\mathbf{J}}^{\text{spin}} = \sum_{\mathbf{k}} |\mathbf{k}\rangle\langle\mathbf{k}| \otimes \frac{1}{2}\hat{s}_z\nabla_{\mathbf{k}}\hat{H}(\mathbf{k}). \tag{4.57}$$

The spin Hall conductivity can be evaluated as

$$\sigma_{yx}^{\text{spin}} = \frac{1}{E_x}\sum_{n=1}^{N_F}\int \frac{\mathrm{d}\mathbf{k}}{(2\pi)^2}\langle\psi_n(\mathbf{k})|\frac{1}{2}\hat{s}_z\partial_{k_y}\hat{H}(\mathbf{k})|\psi_n(\mathbf{k})\rangle, \tag{4.58}$$

where the sum over n runs over all occupied bands.

As in section 4.2.4, the spin current is induced by introducing a homogeneous time-dependent vector potential $A_x(t)$ to the Hamiltonian as (4.33), such that $E_x(t) = -\partial_t A_x(t)$ is equal to (4.32) with $\tau_E = 10$ and $E_0 = 0.0001$.

The spin Hall conductivity as a function of time is shown in figure 4.14(a). It exhibits the same behaviour as the Hall conductivity from section 4.1.8, that is rising steeply as the electric field is turned on and then oscillating with diminishing

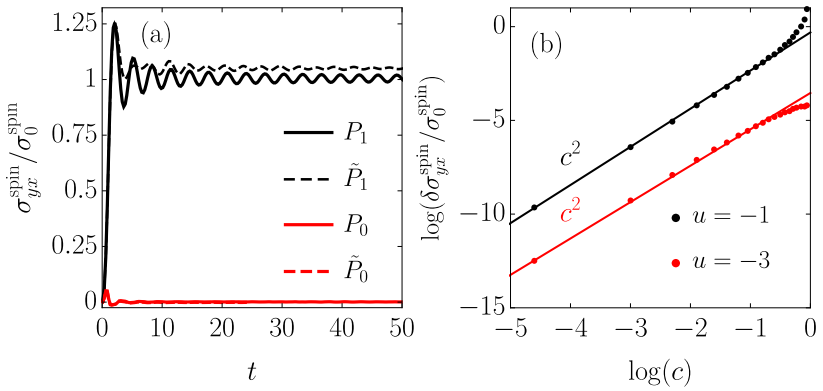

Figure 4.14: (a) Spin Hall conductivities at P_0 (red), $\tilde{P}_0$ (red, dashed), P_1 (black), $\tilde{P}_1$ (black, dashed), where $\sigma_0^{\mathrm{spin}} = e/2\pi$. (b) Scaling of the spin Hall conductivity with c from the value at $c = 0$, for a system in a trivial phase at -3 (red) and in a topological phase at $u = -1$ (black).

oscillations about long-time average value. The long-time average of the spin Hall conductivity in the system with parameters P_1 is quantized and equal to (4.52), whereas for system at P_0 it is equal to 0. For a system at parameters $\tilde{P}_1$ the average value is not quantized, its deviation scales with the magnitude of s_z-symmetry breaking as c^2 [162]. The deviation from zero is observed for parameters $\tilde{P}_0$, where the deviation of the long-time average also scales as c^2. Scaling of the deviation from the quantized value is shown in figure 4.14(b).

4.2.5 Calculation of the critical exponents

The critical exponent $z\nu$ characterizes the divergence of the relaxation time and can be extracted from the inverse of the band gap. Noting that the spectrum near the gap closing is of the form $\pm\sqrt{(q \pm c)^2 + (u - u_c)^2}$, we find that the minimal gap vanishes as $\triangle E = 2|u - u_c|$ and the relaxation time diverges as

$$\tau_r(u) = \frac{2}{|u - u_c|}, \tag{4.59}$$

yielding the critical exponent $z\nu = 1$.

The correlation length critical exponent ν is calculated from the curvature function $F(\mathbf{k}, u) = (\hat{\mathbf{k}}_s \cdot \nabla_{\mathbf{k}})^2 \mathrm{Pf}(m)$, where $\hat{\mathbf{k}}_s$ is the scaling direction and m is the matrix of the time-reversal operator $\hat{\mathcal{T}}$ from equation (2.15). The curvature function derives from the definition (2.16) of the invariant [122]. The length scale is obtained from the curvature function $F(\mathbf{k}, u)$ at time-reversal symmetric momenta $\mathbf{k}_{\mathrm{TRIM}}$ from equation (3.23). Using this approach, the critical exponent ν of the BHZ model are: $\nu = 1$ for $c = 0$ and $\nu = 1/2$ for $c \neq 0$.

4.2.6 Dynamics of the phase transition

The quenches are performed by smoothly varying the parameter u as in equation (4.14) and keeping the parameter c constant. During the quench, the Hamiltonian stays time-reversal symmetric. Three different quenches are considered, a quench

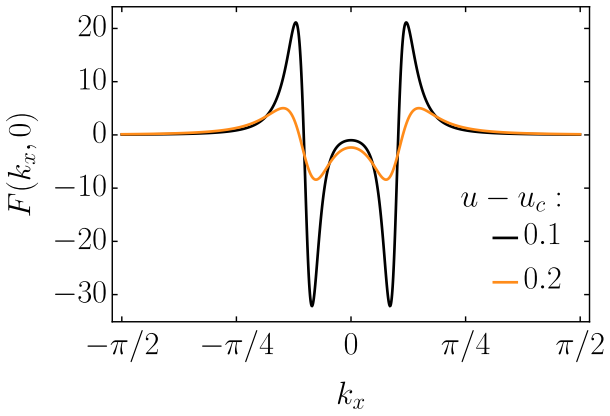

Figure 4.15: Curvature function of the BHZ model for $c = 0.3$ and different values of control parameter u.

$P_0 \to P_1$ starting at $P_0 = (-3, 0)$ and ending at $P_1 = (-1, 0)$, a quench $\tilde{P}_0 \to \tilde{P}_1$ starting at $\tilde{P}_0 = (-3, 0.3)$ and ending in $\tilde{P}_1 = (-1, 0.3)$, and a quench $\tilde{P}_1 \to \tilde{P}_2$ starting in $\tilde{P}_1 = (-1, 0.3)$ and ending in $\tilde{P}_2 = (1, 0.3)$.

Initially, the system is in the ground state (4.44), i.e., with the two valence bands filled and the two conduction ones empty. The time-evolved states

$$|\varphi_\alpha(t, \mathbf{k})\rangle = \overrightarrow{\mathcal{T}} e^{-i \int dt' \hat{H}(t')} |\psi_\alpha(0, \mathbf{k})\rangle = \sum_{n=1}^{4} c_{\alpha,n}(t, \mathbf{k}) |\psi_n(t, \mathbf{k})\rangle, \tag{4.60}$$

which evolved from the initial lower bands $\alpha = 1, 2$, become during the quench superpositions of all bands. The quench $P_0 \to P_1$ is completely analogous to the quenches studied in section 4.1 since the BHZ model with $c = 0$ is equal to two uncoupled time-reversal copies of the QWZ model. During the quench, the energy gap closes between both pairs of valence and conduction bands, such that it is described by two independent Landau-Zener models. In the case of quenches with non-zero c the energy gap closes only between the upper valence band and the lower conduction band. Therefore for slow quenches, the lower valence band evolves adiabatically and no excitations are produced in the upper conduction band. The non-equilibrium dynamics happens purely between the upper valence and lower conduction band for momenta close to the energy gap closing at $|\mathbf{k}| = c$. The dynamics is dictated by an effective 2-band Hamiltonian

$$\hat{H}_{\text{eff}}(t, \mathbf{k}) \approx \begin{pmatrix} \frac{(u_1 - u_0)\pi}{2\tau} \delta t & q - c \\ q - c & -\frac{(u_1 - u_0)\pi}{2\tau} \delta t \end{pmatrix}, \tag{4.61}$$

where it was additionally taken into account that $c \ll 1$, meaning that only momenta close to $\mathbf{k}_c$ undergo non-equilibrium dynamics. We denoted $q = |\mathbf{k} - \mathbf{k}_c| \ll \pi$ and expanded $u(t)$ to the first order about $t = \tau/2$ as in equation (4.16). $\hat{H}_{\text{eff}}(t, \mathbf{k})$ satisfies the Landau-Zener model with $\triangle = q - c$ and the transition velocity $\alpha = \frac{(u_1 - u_0)\pi}{\tau}$. The momentum distribution of excitations in the lower conduction band is therefore given by the Landau-Zener formula for a non-adiabatic transition (3.8)

$$n_{\text{exc}}(\mathbf{k}) = e^{-(q-c)^2 2\tau/|u_0 - u_1|}. \tag{4.62}$$

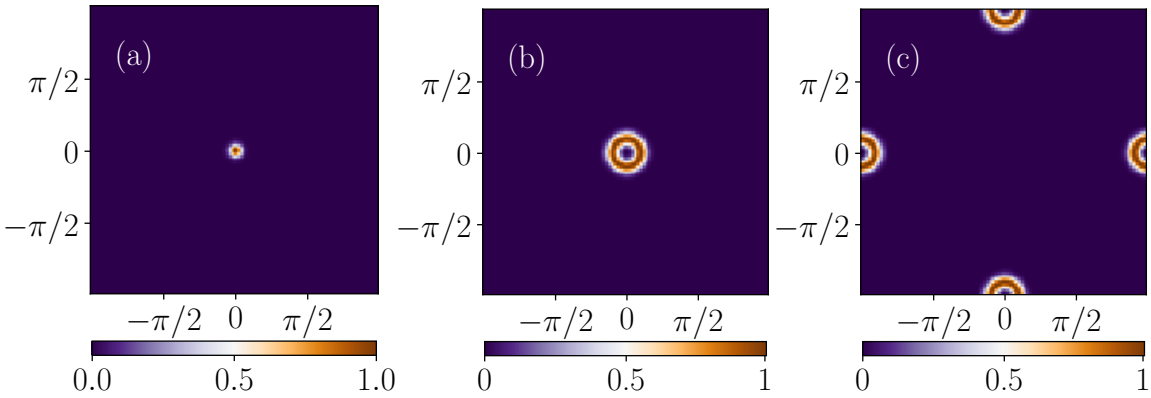

Figure 4.16: Momentum distribution of the excitations after quenches (a) $P_0 \to P_1$, (b) $\tilde{P}_0 \to \tilde{P}_1$, and (c) $\tilde{P}_1 \to \tilde{P}_2$, for $\tau = 60$.

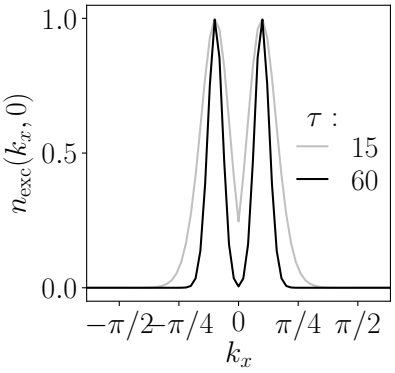

Figure 4.17: Momentum distribution of excitations along $k_y = 0$ axis after the $\tilde{P}_0 \to \tilde{P}_1$ quench with $\tau = 15$ (grey) and $\tau = 60$ (black).

Figure 4.16 shows the momentum distribution of excitations after $P_0 \to P_1$, $\tilde{P}_0 \to \tilde{P}_1$, and $\tilde{P}_1 \to \tilde{P}_2$ quenches with $\tau = 60$. Figure 4.17 shows the momentum distribution of excitations along the $k_x = 0$ line after various quench times. The number of excitations is equal to 1 at momenta where the energy gap closed. For the $P_0 \to P_1$ quench, the number of excitations is equal to one at $\mathbf{k} = (0, 0)$, whereas for $\tilde{P}_0 \to \tilde{P}_1$ and $\tilde{P}_1 \to \tilde{P}_2$ quenches that happens on a whole circle with radius c (see figure 4.13).

Integrating the momentum distribution of excitations over the whole Brillouin zone (4.19) yields the total density of excitations

$$\begin{aligned} N_{\mathrm{exc}} &= \frac{|u_1 - u_0|}{4\pi\tau}, \quad c = 0, \\ N_{\mathrm{exc}} &= c\sqrt{\frac{|u_1 - u_0|}{8\pi\tau}}, \quad 0 < c \ll 1. \end{aligned} \tag{4.63}$$

In systems with zero and non-zero c the density of excitations scales differently with τ. As u is a linear function of time near the gap closing at $t = \tau/2$, we can compare these results to the predictions of the Kibble-Zurek scaling for zero-dimensional defects (3.16). The critical exponents, $\nu = 1$ and $z = 1$ for $c = 0$ and $\nu = 1/2$ and $z = 2$ for $0 < c \ll 1$ as calculated in section 4.2.5, give the same behaviour as found from the Landau-Zener formula.

4.2.7 Non-equilibrium spin Hall conductivity

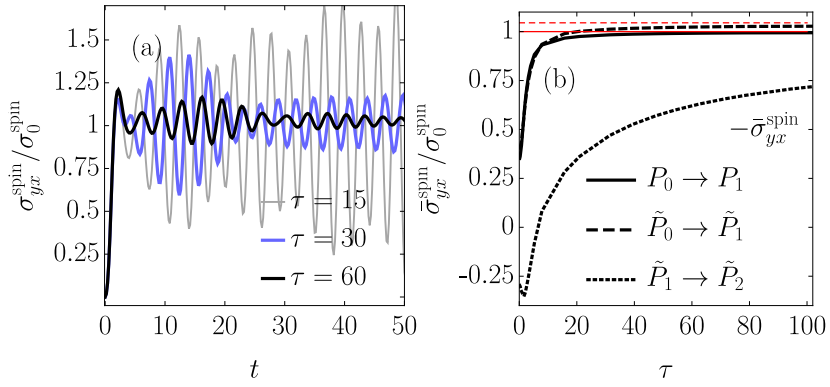

Figure 4.18: (a) Spin Hall conductivity of the non-equilibrium states, resulting from the quench from $\tilde{P}_0$ to $\tilde{P}_1$, with $\tau = 15$ (grey, thin), $\tau = 30$ (blue) and $\tau = 60$ (black). (b) Time-averaged spin Hall conductivity after the $P_0 \to P_1$ quench (black, solid) converges for $\tau \to \infty$ to the ground-state value of $\hat{H}(P_1)$ (red) and for systems after the $\tilde{P}_0 \to \tilde{P}_1$ (black, dashed) to the ground-state value of $\hat{H}(\tilde{P}_1)$ (red, dashed). Time-averaged spin Hall conductivity after the $\tilde{P}_1 \to \tilde{P}_2$ quench (black, dotted) is multiplied by a factor of -1 and converges to the ground-state value of $\hat{H}(\tilde{P}_2)$.

Spin Hall conductivities, evaluated as the electric field is turned on after the quench, are for several quench durations from $\tilde{P}_0$ to $\tilde{P}_1$ shown in figure 4.18 (a). The behaviour is analogous to the one observed in post-quench Hall conductivity discussed in section 4.1.9. After a steep rise following the turning on of the electric field right after the quench, the spin Hall conductivity oscillates around a non-zero value $\bar{\sigma}_{xy}^{\mathrm{spin}}$, with the frequency equal to the band gap of the final Hamiltonian. The oscillations become small for slow enough quenches until the revival time that grows linearly with quench time (see discussion in section 4.1.9). As shown in figure 4.18 (b) the average value $\bar{\sigma}_{xy}^{\mathrm{spin}}$ approaches the value characteristic of the final Hamiltonian.

In order to analyse $\bar{\sigma}_{yx}^{\mathrm{spin}}$ one may use the result of time-dependent perturbation theory, presented in section 4.1.10 where the charge current was measured. Exchanging the charge current operator with the spin current operator yields the formula for the long-time average value of the spin Hall conductivity

$$\bar{\sigma}_{yx}^{\mathrm{spin}} = \frac{e}{(2\pi)^2} \sum_{n=1}^{2N_F} \int \mathrm{d}\mathbf{k}\, n_n(\mathbf{k}) \Omega_n^{\mathrm{spin}}(\mathbf{k}), \tag{4.64}$$

$$\Omega_n^{\mathrm{spin}}(\mathbf{k}) = -2\,\mathrm{Im} \sum_{\substack{m=1 \\ m\neq n}}^{2N_F} \frac{\langle \psi_n(\mathbf{k}) | \frac{1}{2}\hat{s}_z \partial_{k_y} \hat{H}(\mathbf{k}) | \psi_m(\mathbf{k}) \rangle \langle \psi_m(\mathbf{k}) | \partial_{k_x} \hat{H}(\mathbf{k}) | \psi_n(\mathbf{k}) \rangle}{(E_n(\mathbf{k}) - E_m(\mathbf{k}))^2}. \tag{4.65}$$

where $n_n(\mathbf{k})$ is the occupation of the n-th energy band at $\mathbf{k}$ with eigenenergy $E_n(\mathbf{k})$. The spin Hall conductivity is expressed as an integral of the spin Berry curvature $\Omega_n^{\mathrm{spin}}(\mathbf{k})$ [164] weighted by the band occupancy. The spin Berry curvature of the upper valence band is shown for parameters P_1, $\tilde{P}_1$ and $\tilde{P}_2$ in figure 4.19. The spin Berry curvature of conduction bands has the opposite sign to that of the valence bands. Therefore, the excitations above the ground state diminish the time-averaged

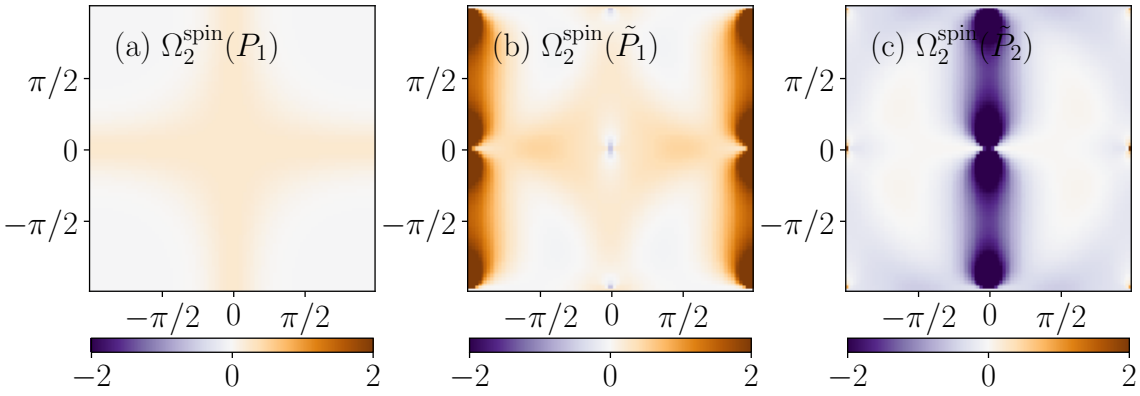

Figure 4.19: Spin Berry curvature of the upper valence band of the BHZ model at parameters (a) P_1, (b) $\tilde{P}_1$, and (c) $\tilde{P}_2$.

spin Hall conductivity, which explains the dependence seen in figure 4.18 (b). As in section 4.1.9, estimates of the spin Hall conductivity can be made by taking into account that for slow quenches excitations, which contribute to deviations of $\sigma_{yx}^{\text{spin}}$ from the ground state value, occur in a small region in momentum space about the gap-closing momenta. By approximating $\Omega_n^{\text{spin}}(\mathbf{k})$ with its average value over gap-closing momenta, $\bar{\sigma}_{yx}^{\text{spin}}$ is then proportional to the total density of excitations, given by equation (4.63). Therefore, the deviation of the spin Hall conductivity from the ground state one scales differently for systems with $c = 0$ and $c \neq 0$ and follows the Kibble-Zurek scaling,

$$\begin{aligned} \delta\sigma_{yx}^{\text{spin}} &\propto \tau^{-1}, \quad c = 0, \\ \delta\sigma_{yx}^{\text{spin}} &\propto \tau^{-1/2}, \quad 0 < c \ll 1. \end{aligned} \tag{4.66}$$

The formula equation (4.65) is also useful for the discussion of different magnitudes of the deviations from ground-state values for different quench protocols as seen in figure 4.18 (b) (straight lines denote ground-state values). Namely, after the $\tilde{P}_1 \to \tilde{P}_2$ quench, the response deviates from the ground-state result much more than the responses after the other two quenches. This is due to two facts. First, the number of produced excitations is larger and, second, the excitations occur at momenta where the spin Berry curvature is large, see figure 4.19(c). More precisely, the number of excited electrons is approximately two times larger for $\tilde{P}_1 \to \tilde{P}_2$ than for the $\tilde{P}_0 \to \tilde{P}_1$ quench. The number is roughly given by the length of the circles in figure 4.13. During the $\tilde{P}_1 \to \tilde{P}_2$ quench, the band gap closing points cover two full circles. Second, the value of the spin Berry curvature where those excitations occur is larger for the former quench protocol. For the $P_0 \to P_1$ and the $\tilde{P}_0 \to \tilde{P}_1$ protocols, the spin Berry curvatures are small in the region with excited electrons, hence the deviations from the ground-state value of the spin Hall conductivity are smallest there.

4.2.8 Wannier center flow and $\mathbb{Z}_2$ invariant after a quench

The quench breaks the time-reversal symmetry of the system even if the system was initially time-reversal symmetric and so was the time-dependent Hamiltonian. This is because the time-reversal symmetry is anti-unitary and does not commute with the time-evolution operator [53]. Below, we show how this is reflected in the shape

of the Wannier centre flows.

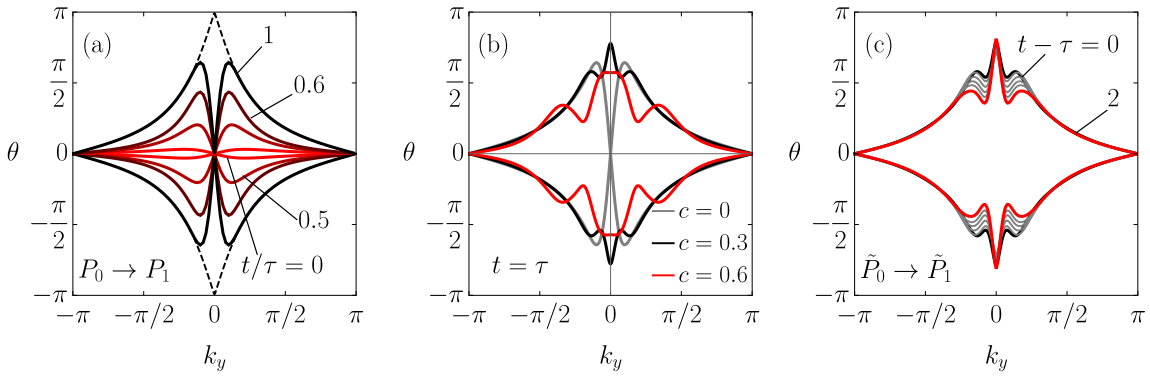

Figure 4.20: (a) Wannier centre flows of the ground state at P_1 (black, dashed) and of non-equilibrium states at various times during the quench from P_0 to P_1 with $\tau = 15$: $t/\tau = 0$ (red), $t/\tau = 0.5$ (dark red), $t/\tau = 0.6$ (darker red), and after the quench at $t/\tau = 1$ (black). (a) Wannier centre flow of systems with $c = 0$ (grey), $c = 0.3$ (black) and $c = 0.6$ (red) at the end of the quench from $u_0 = -3$ to $u_1 = -1$ with quench time $\tau = 15$. (b) Wannier centre flow at $t = \tau$ (black), $t = \tau + 2$ (red) and times in between (grey) after the $\tilde{P}_0 \to \tilde{P}_1$ quench.

Figure 4.20 (a) shows the Wannier centre flows at different times during the quench $P_0 \to P_1$ with $\tau = 15$. The system starts in the trivial phase with the shape of the Wannier centre flow as in figure 4.11 (b) (red line). With progressing time, the Wannier centre flow evolves into the diamond shape characteristic of the ground state at P_1 (black, dashed) for $|k_y|$ larger than a certain k_0, but deviates from that for $|k_y| < k_0$. The shape of the Wannier centre flow can be related to the valence band occupancy. For momenta far from this point, the states are in the ground state, which causes the ground state shape of Wannier centre flow. An approximate momenta k_0 at which the states are excited to conduction band, can be estimated from equation (4.62) as $k_0 \sim \sqrt{|u_1 - u_0|/2\tau}$. The Wannier centre flow stays doubly degenerate at $k_y = 0$ and $k_y = \pi$ for all times which is required for the calculation of the $\mathbb{Z}_2$ invariant according to equation (4.47). Therefore, the $\mathbb{Z}_2$ invariant seems to be conserved under time evolution for $c = 0$. However, the double degeneracy of Wannier centre flow is present due to inversion symmetry of the system, which is contrary to the time-reversal symmetry not broken by time evolution. Inversion symmetry constrains the Wannier centre flow at time-reversal symmetric momenta K_y to 0, π or in the case of multi-band system to pairs with different sign $\theta_1(K_y) = -\theta_2(K_y)$ [165]. As the two occupied bands of the BHZ model correspond to two independent Chern insulators, the Wannier centres can only take values 0 or π at K_y. Since the system evolves smoothly under the Schrödinger equation, the Wannier centre flow $\theta(K_y)$ cannot jump from 0 to π, therefore it stays pinned to the initial value for all times.

Alternatively, for $c = 0$ one could define the $\mathbb{Z}_2$ invariant also from the difference of the Chern numbers (2.17). This quantity is conserved by the quench due to the conservation of the Chern numbers, and neither the inversion symmetry nor the limitation to two occupied bands is necessary in this case.

These considerations do not apply to systems with $c \neq 0$ that do not conserve s_z and hence to the general case with time-reversal symmetry. Figure 4.20 (b) shows

Wannier centre flows of systems for several values of c after the quench from a trivial to a topological regime. Contrary to the case with $c = 0$, Wannier centre flows of the systems with $c \neq 0$ are not degenerate at $k_y = 0$ which renders the $\mathbb{Z}_2$ invariant ill-defined. The fact that the Wannier centre flow for the two bands takes opposite values at $k_y = 0$ is a manifestation of the inversion symmetry that is still present in the state. After the quench, the Wannier centre flow becomes time-dependent. An example of time evolution of Wannier centre flow after the $\tilde{P}_0 \to \tilde{P}_1$ quench is shown in figure 4.20 (c).

4.2.9 Slow quenches with symmetry breaking

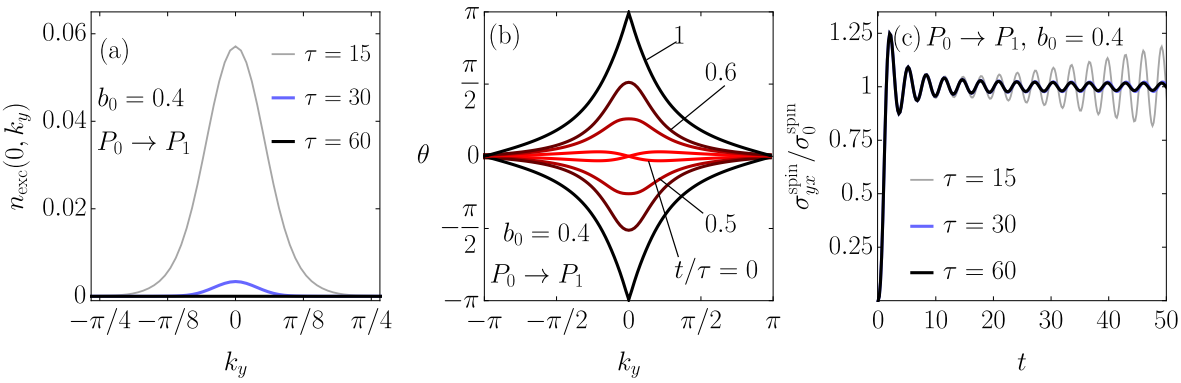

Figure 4.21: Properties of the system quenched from P_0 to P_1 with a time-reversal symmetry breaking term of amplitude $b_0 = 0.4$. (a) Momentum distribution of excitations along $k_x = 0$ after the quench for $\tau = 15$ (grey, thin), $\tau = 30$ (blue) and $\tau = 60$ (black). (b) Wannier centre flows of the non-equilibrium state at different times during the quench with $\tau = 15$, $t/\tau = 0$ (red), $t/\tau = 0.5$ (dark red), $t/\tau = 0.6$ (darker red), and $t/\tau = 1$ (black). (c) Spin Hall conductivity of the systems after quenches with $\tau = 15$ (grey, thin), $\tau = 30$ (blue) and $\tau = 60$ (black). The latter two graphs overlap as the quench with such τ and b_0 is already adiabatic.

When an important symmetry of the Hamiltonian associated to a certain class of topological insulators is broken during a quench, different topological ground states can become adiabatically connected [154], i.e., the band gap can remain open everywhere during the quench. The topological invariant becomes ill-defined in this case. Such processes can be studied by adding a convenient time-reversal symmetry breaking term

$$\hat{H}(\mathbf{k}) \to \hat{H}(\mathbf{k}) + b\, \hat{s}_x \otimes \hat{\sigma}_x \tag{4.67}$$

to the BHZ model. In parallel to changing the parameter u as in equation (4.14), the amplitude b is turned on during the quench as

$$b(t) = b_0 \sin^2(\pi t/\tau). \tag{4.68}$$

In this way the Hamiltonian has the time-reversal symmetry before and after the quench but for $0 < t < \tau$ the symmetry is broken and the band gap remains open. When the quench is done slowly enough compared to the inverse of the minimal band gap during the quench, there are almost no excitations to conduction bands. This can be seen in figure 4.21 (a) where the momentum distribution of excitations

after the $P_0 \to P_1$ quench is shown for various quench times. In the adiabatic limit, the system ends up in the ground state of the final Hamiltonian and thus in the topological phase with $N_{\text{bulk}} = 1$.

Time-reversal properties of the system during the quench can be observed from the graphs of the Wannier centre flow in figure 4.21 (b). At $t/\tau = 0$ and $t/\tau = 1$ the Wannier centre flow has the typical form for the trivial and topological phase, respectively, while at $t/\tau = 0.5$ and $t/\tau = 0.6$ the system does not exhibit the time-reversal symmetry as can be seen by the absence of double degeneracy at $k_y = 0$.

After the quench, the electric field is turned on. At long times, the spin Hall response oscillates around a constant value with the frequency equal to the band gap of the final Hamiltonian, as shown in figure 4.21 (c). For a quench slower than the inverse of the minimal band gap during the quench, the system exhibits ground-state spin Hall response. It also coincides with the spin Hall response of the system after an infinitely slow symmetry preserving quench. For faster quenches, there are excitations present even in the symmetry breaking case (see figure 4.21 (a)) so the growth of oscillations and the deviation of the time-averaged value from the ground-state value can be observed. However, compared to the case of symmetry preserving quench, the oscillations are less prominent because of the smaller number of excitations.

4.3 Conclusions

This chapter was dedicated to the critical behaviour of translation-invariant topological insulators in the ground state and in the non-equilibrium state produced by a quench across a topological phase transition. Two two-dimensional models belonging to two different symmetry classes were studied; a Chern insulator represented by the QWZ model and a topological insulator with time-reversal symmetry, represented by the BHZ model. Their topological phase is characterized by distinct topological invariants and they exhibit different phenomena in a topological phase; a Chern insulator exhibits the quantum Hall effect while a time-reversal symmetric topological insulator exhibits the spin Hall effect.

The models are band insulators, with the energy dispersion forming a Dirac cone near a topological phase transition. At the quantum critical point, the energy gap closes, which results in the divergence of the relaxation time. The power by which it diverges was found to be $z\nu = 1$, where z and ν are the critical exponents. The divergence of the relaxation time is also accompanied by the divergence of the correlation length. The latter was extracted from the width of the curvature function, which exhibits a peak of Lorentzian form near a critical point. The QWZ model was found to have the correlation length critical exponent $\nu = 1$ and the BHZ model $\nu = 1$ if the spin projection is conserved otherwise $\nu = 1/2$. The models therefore belong to different universality classes, which is reflected in different scaling of excitations and transport coefficients after the quench.

Dynamical critical properties are probed by driving a system across a topological phase transition. Due to the closing of the energy gap, the system evolves non-adiabatically, which produces excitations. The dynamics of the system is for slow quenches captured by the Landau-Zener model, which provides an exact result for the momentum distribution of excitations. The total density of excitations follows the Kibble-Zurek scaling of point defects. The Kibble-Zurek scaling is also observed

in the length scale, which is present in the system after the quench. For a Chern insulator it is extracted from the post-quench Berry curvature, which is deformed from its ground state value for momenta close to the energy gap closing. Following the evolution of the Berry curvature and the correlation length during the quench shows a freeze-out regime and two adiabatic regimes. In the freeze-out regime, the correlation length, lagging behind the ground state one, grows linearly with time and oscillates about a constant value after the exit from the freeze-out zone. Such dynamical behaviour goes beyond the adiabatic-impulse approximation.

The (spin) Hall response to a weak electric field was analysed with the time-dependent perturbation theory and expressed as an integral over the Brillouin zone of the (spin) Berry curvature weighted by the band occupancy. Therefore, transport properties after slow quenches can universally be expected to be close to those of the ground state of the final Hamiltonian as the quench is adiabatic for all states except for those in a small region in the momentum space. The deviation of the (spin) Hall conductivity from the ground-state one is proportional to the number of excitations and therefore inherits the Kibble-Zurek scaling with quench time.

While the transport properties of the two systems after the quench behave in a similar way, their topological properties vary vastly. The topological invariant of Chern insulators, the Chern number, is conserved under unitary time evolution. This is reflected in the deformation of the post-quench Berry curvature from the one corresponding to the instantaneous ground state and the emergence of the Kibble-Zurek length scale. On the other hand, the classification of time-reversal symmetric topological insulators with the $\mathbb{Z}_2$ invariant breaks down after the quench. This is because unitary time-evolution in general destroys time-reversal symmetry of the system. This also prevents the calculation of the typical length scale from the curvature function, as its integral, the topological invariant, is not well defined. It would be interesting to find another way of calculating of the typical length scale, which would evade this problem.

For time-reversal symmetric topological insulators one can adiabatically connect different topological phases by introducing an additional symmetry breaking potential that keeps the band gap open at the critical point. After a slow enough quench, the system arrives in the ground state of the final Hamiltonian, which has a different topological phase as the initial one. In case of Chern insulators such an adiabatic connection is not possible since the topology does not rely on any symmetry. The adiabatic connection (and associated possibility of changing Chern number adiabatically) is however possible by enlarging the system to more bands, as only the total Chern number is conserved. One can couple a 'target' Chern insulator (e.g., described by QWZ model) to its conjugate time-reversal partner spin-down subsystem and create a system described by the BHZ model with $c = 0$. The full system has a Chern number $C_\uparrow + C_\downarrow$ which is maintained by the evolution of the system, but because $\mathbb{Z}_2$ invariant $C_\uparrow - C_\downarrow$ can be modified, the subsystems can attain any desired Chern number adiabatically. Such a protocol was implemented in reference [135].

Chapter 5

Quenches in systems with edges

An important aspect of topological insulators is the edge physics: a system in a topological phase hosts in-gap conducting states that are localized at the edges. They allow for dissipation-less transport and are robust against disorder. This explains the exact quantization of the Hall conductance. The existence of the edge states is connected to the non-trivial topological invariant of the bulk via a concept called the bulk-boundary correspondence.

As is known from studies of quenches in translation-invariant systems, topological invariants do not follow the change of the Hamiltonian during the quench [53]. In Chern insulators the Chern number is conserved [50, 54, 56] while for time-reversal symmetric topological insulators [56] and chains with chiral symmetry [57, 58] the classification with a topological invariant breaks down after a quench. This poses a question, what happens to the bulk-boundary correspondence after the quench? In other words, does the presence of the edge states follow the behaviour of the topological invariant? This question was already considered in studies of sudden quenches [52, 54, 144], which showed that after a sudden quench from a topological to a trivial regime, edge currents relax into the interior of the system. Reference [140] studied slow quenches in Floquet Chern insulators in which Floquet Hamiltonian is approximately given by the Haldane model [8]. The degeneracy point of the in-gap states moves in momentum space during the quench, which results in a perfect population of selected in-gap states after the quench. As a consequence of this anomalous in-gap excitation production, the excitations in the system do not follow the Kibble-Zurek scaling. Deviations from the Kibble-Zurek scaling due to edge states were also observed in the one-dimensional Creutz ladder [136, 166].

This chapter, closely following our published work [119], presents our results [119] on slow quenches in a two-dimensional Chern insulator with edges, represented by the QWZ model in a ribbon geometry. The system has the inversion symmetry, which is absent in the Haldane model and has profound consequences on the evolution of the in-gap states. After a quench to the topological regime, the in-gap states appear and are occupied. The number of generated excitations decreases as the quench becomes slow. The number of the excitations in the in-gap states scales with the quench time τ as $\tau^{-1/2}$ whereas the number of excitations in the bulk states scales as τ^{-1}. The scaling of the in-gap and the bulk excitations is well described by the Kibble-Zurek mechanism. These results differ from the ones in reference [140] because in the case of the QWZ model the degeneracy point is pinned to an inversion symmetric momentum due to the inversion symmetry. Calculations of the

Hall conductance are presented and they are shown to approach the ground-state value of the final Hamiltonian. The deviation of the post-quench Hall conductance from the quantized value arises both due to bulk and in-gap excitations. Both bulk and in-gap contributions scale as τ^{-1}, which in turn is the same as also for the "bulk-only" Chern insulator with periodic boundary conditions in both directions.

5.1 The Qi-Wu-Zhang model on a ribbon geometry

In order to study edge physics of Chern insulators we investigate the QWZ model on the ribbon geometry. Periodic boundary conditions are imposed along y-direction and open boundary conditions along x-direction, as presented in figure 5.1. Due to

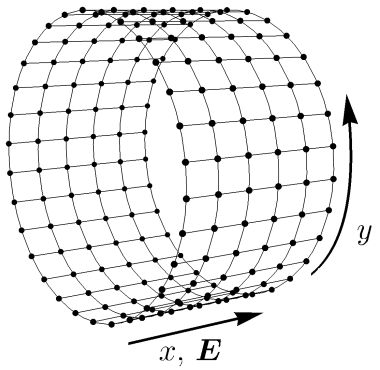

Figure 5.1: Ribbon geometry with periodic and open boundary conditions along y- and x-directions, respectively. Homogeneous electric field $\boldsymbol{E}$ is applied in x-direction to probe the Hall conductance.

the translation invariance in y-direction it is convenient to use the basis $|k_y\rangle \otimes |x\rangle$, where $k_y \in [-\pi, \pi)$ is a Bloch wave vector and $x \in \{1, \ldots, N_x\}$ is a lattice site in x-direction. In this basis the QWZ Hamiltonian is block-diagonal, $\hat{H} = \sum_{k_y} |k_y\rangle\langle k_y| \otimes \hat{H}(k_y)$ with

$$\begin{aligned}\hat{H}(k_y) = &\sum_{x=1}^{N_x-1} |x+1\rangle\langle x| \otimes \frac{\hat{\sigma}_z + i\hat{\sigma}_x}{2} + \text{h.c.} + \\ &\sum_{x=1}^{N_x} |x\rangle\langle x| \otimes \left((\cos k_y + u)\,\hat{\sigma}_z + \sin k_y \hat{\sigma}_y\right).\end{aligned} \tag{5.1}$$

The momentum-space Hamiltonian $\hat{H}(k_y)$ is of dimension $2N_x \times 2N_x$. It posses an inversion symmetry (4.3) and particle-hole (4.4) symmetry, which are inherited from its translation-invariant analogue presented in chapter 4. On a ribbon geometry, the operation of the inversion symmetry is presented as

$$\hat{H}(k_y) = (\hat{P} \otimes \hat{\sigma}_z)^\dagger \hat{H}(-k_y) \hat{P} \otimes \hat{\sigma}_z, \tag{5.2}$$

and for the particle-hole symmetry as

$$\hat{H}(k_y) = -(\hat{P} \otimes \hat{\sigma}_x)^\dagger \hat{H}(k_y) \hat{P} \otimes \hat{\sigma}_x, \tag{5.3}$$

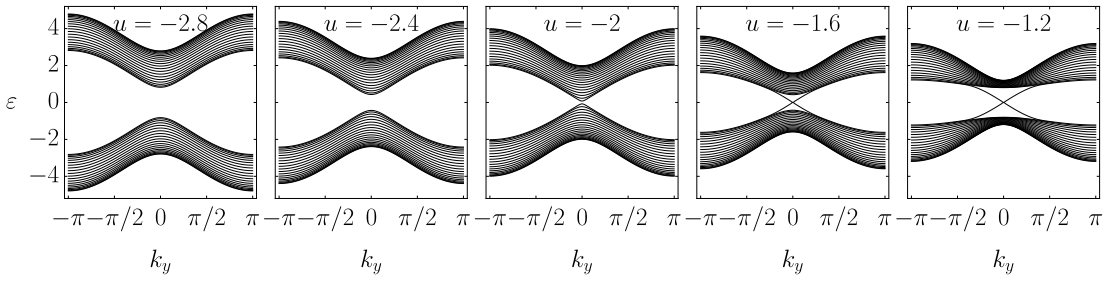

Figure 5.2: Energy dispersion at different values of parameter u.

where

$$\hat{P}|x\rangle = |N_x + 1 - x\rangle. \tag{5.4}$$

The energy dispersion consists of the eigenenergies $E_n(k_y)$ of $\hat{H}(k_y)$ that belong to $2N_x$ subbands. An electron occupying the n-th subband with the eigenenergy $E_n(k_y)$ is described by the wave function $|\Psi_n(k_y)\rangle = |k_y\rangle \otimes |\psi_n(k_y)\rangle$, where $|\psi_n(k_y)\rangle$ is an eigenstate of $\hat{H}(k_y)$. The energy dispersion is shown in figure 5.2. In a topologically non-trivial phase (for $u > -2$) a ribbon hosts chiral in-gap states that are localized at the edges and exhibit an exponentially small gap of the order $e^{-N_x/\xi}$, where ξ is the localization length of the in-gap states. Due to the inversion symmetry of the ribbon Hamiltonian, the avoided crossing is pinned to an inversion-symmetric momentum $k_y = 0$ or $k_y = \pi$. The particle-hole symmetry makes the energy spectrum symmetric and thus pins the crossing to zero energy. The effects of breaking of these symmetries are studied in sections 5.2.4 and 5.2.5. Neglecting the avoided crossing, we assign indices L and R to in-gap subbands with a positive and with a negative slope, respectively, as the former are localized to the left ($x = 1$) edge while the latter are localized to the right ($x = N_x$) edge near $k_y = 0$.

5.2 Non-equilibrium dynamics

We perform quenches by smoothly varying the parameter u as in equation (4.14) for $t \in [0, \tau]$ from deep in the trivial regime at $u_0 = -2.8$ to deep in the topological regime at $u_1 = -1.2$. The system, that was initially in the ground state of $\hat{H}(k_y, t = 0)$ and described by the set of eigenstates $|\psi_n(k_y, t = 0\rangle)$ with $n \leq N_x$, evolves under a time-dependent Hamiltonian $\hat{H}(k_y, t)$ and ends up in the non-equilibrium state described by

$$|\varphi_n(k_y, t)\rangle = \overrightarrow{\mathcal{T}} e^{-i\int_0^t \hat{H}(k_y,t')dt'} |\psi_n(k_y, 0)\rangle. \tag{5.5}$$

Inspecting the time dependence of the energy levels during the quench gives a lot of information about the time evolution of the states. As presented in the following sections, this analysis provides us with a framework for analytic evaluation of the in-gap excitations via the Landau-Zener model.

The topological transition at $u_c = -2$ is characterized by the fact that, in an extended system with periodic boundary conditions in both directions, the valence and the conduction bands form a Dirac cone at $\mathbf{k} = 0$ at that value of u. In the ribbon geometry, the valence and the conduction bands split into a set of subbands. The energy dispersion at the end of the quench is shown in figure 5.3(a) and the

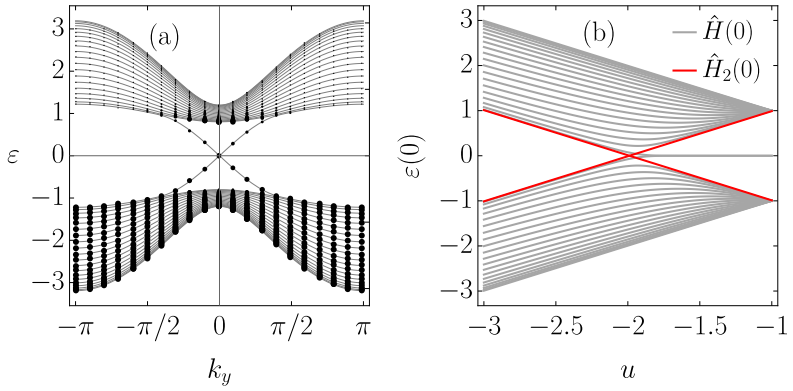

Figure 5.3: a) Occupancy of energy bands of the ribbon of width $N_x = 20$ at $u = -1.2$ after the quench with $\tau = 1$. The surface of a point is proportional to the probability of finding a particle in the corresponding eigenstate. (b) Energy levels of the whole Hamiltonian $\hat{H}(k_y)$ (gray) and of the two-level Hamiltonian $\hat{H}_2(k_y)$ (red) at $k_y = 0$ as a function of u.

time evolution of the eigenenergies at $k_y = 0$ in figure 5.3(b). While the system is in the trivial phase, there are no in-gap states present and all of the states are delocalized throughout the whole sample. Near the critical point at $u_c = -2$ the in-gap bands are formed. As u enters the topological phase, the energy gap between the bulk bands reopens while the dispersion of the in-gap bands appears to be static for k_y close to 0. The (avoided) crossing of the in-gap bands is, due to the inversion symmetry and the particle-hole symmetry, pinned to $k_y = 0$ and $E = 0$, respectively.

5.2.1 Density of excitations

When during a quench the parameter u reaches this critical point, the energy gap both to conduction subbands as well as to excited in-gap states is minimal at $k_y = 0$ and excitations occur predominantly around that point. The final occupancy of energy bands after the quench with $\tau = 1$ is shown in figure 5.3(a). As shown, the in-gap bands emerge and are partially populated. Excitations are also present in conduction and valence subbands representing the bulk of the ribbon and their number is maximal at $k_y = 0$.

We now explore how the number of both kinds of excitations depends on the quench time τ. Let us first define the momentum distributions of bulk and in-gap excitations,

$$\begin{aligned} n^{\mathrm{b}}_{\mathrm{exc}}(k_y) &= \sum_{n=N_x+2}^{2N_x} \sum_{m=1}^{N_x} |\langle \psi_n(k_y) | \varphi_m(k_y) \rangle|^2, \\ n^{\mathrm{g}}_{\mathrm{exc}}(k_y) &= \sum_{n\in\{L,R\}} \sum_{m=1}^{N_x} |\langle \psi_n(k_y) | \varphi_m(k_y) \rangle|^2 \Theta(E_n(k_y)). \end{aligned} \tag{5.6}$$

For bulk excitations the sum over n runs over the conduction subbands while for in-gap excitations it runs over the two in-gap bands for states with positive energy, the latter condition imposed by the Heaviside function Θ.

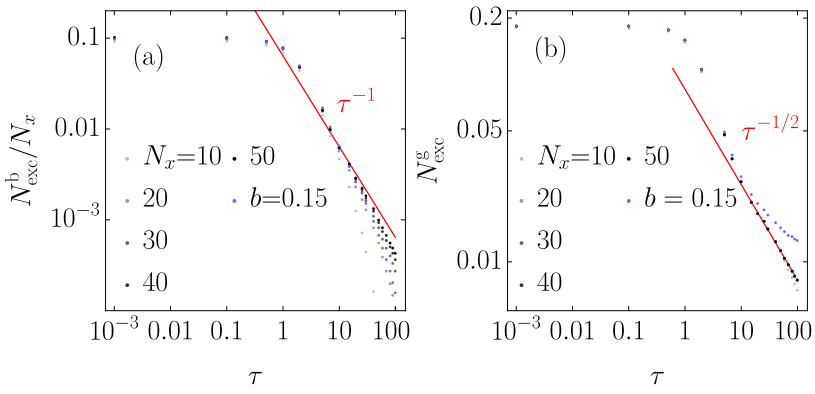

Figure 5.4: Density of excitations (a) in the bulk and (b) in the in-gap states as functions of τ for different ribbon widths, ranging from $N_x = 10$ (light grey) to $N_x = 50$ (black). Red lines denote (a) the exact result for the system with periodic boundary conditions in both directions which scales as τ^{-1} and (b) a fitted $\tau^{-1/2}$ line. Blue dots show results for a Hamiltonian with a broken inversion symmetry of magnitude $b = 0.15$ and $N_x = 20$.

The density of excitations in the bulk $N^{\rm b}_{\rm exc}$ and in the in-gap states $N^{\rm g}_{\rm exc}$ are expressed as

$$N^{\rm b\,(g)}_{\rm exc} = \int_{-\pi}^{\pi} \frac{{\rm d}k_y}{2\pi}\, n^{\rm b\,(g)}_{\rm exc}(k_y). \tag{5.7}$$

Figure 5.4 shows the corresponding quantities as a function of quench time τ. With increasing τ the density of bulk and edge excitations decreases. For a large range of τ from about $\tau \approx 1$ to the upper limit which increases with N_x, the density of in-gap excitation scales as $N^{\rm g}_{\rm exc} \propto \tau^{-1/2}$, while the density of excitations in the bulk scales as $N^{\rm b}_{\rm exc} \propto \tau^{-1}$.

To understand the origin of this difference it is instructive to first consider the momentum distribution of excitations. Results are shown for several τ in figure 5.5 as a function of the scaled momentum $k_y\sqrt{\tau}$, where the left panel displays the distribution of the bulk and the right panel the distribution of the in-gap excitations. One immediately notices a crucial difference. The distribution of the bulk excitations and its dependence on the quench time can be essentially understood by integrating over k_x the standard Landau-Zener result (4.20), valid for a system with periodic boundary conditions in both directions:

$$n^{\rm pbc}_{\rm exc}(k_y) = N_x \sqrt{\frac{|u_1 - u_0|}{8\pi\tau}}\, e^{-2\tau k_y^2/|u_1-u_0|}. \tag{5.8}$$

One can understand the good agreement of this expression with numerical results (see figure 5.5(a)) from the fact that the edges do not matter importantly for the behaviour of the bulk (some corrections become apparent for longer quench times only). The momentum distribution of the in-gap excitations, in contrast, behaves differently. It can be described by a function which has a sharper peak close to $k_y = 0$ and reaches value $1/2$ there. On the other hand, as presented on the plot, still different curves collapse when the momentum is scaled with $\sqrt{\tau}$ (with deviations at long quench times that we discuss later). An analytic expression for the momentum distribution of the in-gap excitations is presented in section 5.2.2.

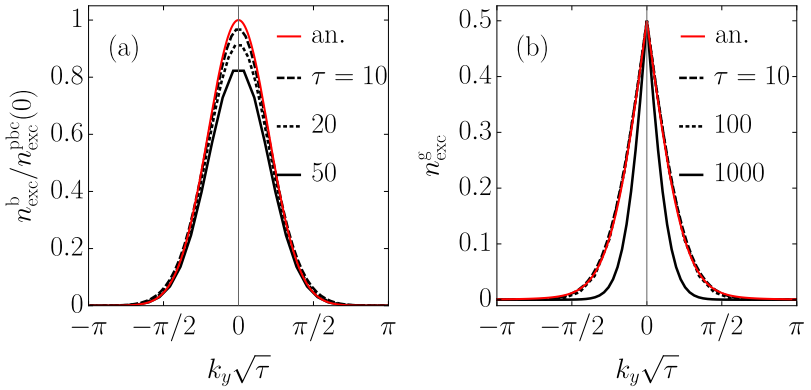

Figure 5.5: (a) Momentum distribution of bulk excitations in a ribbon with $N_x = 70$ after quenches with $\tau = 10$ (dashed), $\tau = 20$ (dotted), and $\tau = 50$ (full). Analytical result of equation (5.8) is shown by the red line. (b) Momentum distribution of in-gap excitations in a ribbon with $N_x = 20$ after quenches with $\tau = 10$ (dashed), $\tau = 100$ (dotted), and $\tau = 1000$ (full). A rescaled ($\tau \to 2.6\tau$) analytical result of equation (5.14) in section 5.2.2 is shown by the red line.

One can exploit the observed scaling of momentum distributions to explain the scaling of the number of excitations. The density of excitations is given by

$$N_{\mathrm{exc}} = \frac{L^D}{(2\pi)^D} \int \mathrm{d}^D\mathbf{k} n_{\mathrm{exc}}(\mathbf{k}) = \int \mathrm{d}^D\mathbf{k} g(k\sqrt{\tau}) \propto \tau^{-D/2}, \tag{5.9}$$

where L^D is the volume of the system and $k = |\mathbf{k}|$. Hence, for in-gap states, $N^{\mathrm{g}}_{\mathrm{exc}} \propto \tau^{-1/2}$. It is important that the integral was done in $D = 1$. If the calculation was repeated for the bulk with periodic boundary conditions it is the $D = 2$ that gives the scaling that holds for the bulk states (whereas for the case of a ribbon, the role of k_x momentum that is not conserved due to the edges is played by the band-index).

As observed in figure 5.4, power-law scalings of the number of excitations are valid only in a certain range of quench times. If a quench is performed too quickly, excitations are created also far away from the $k_y = 0$, where the dynamics cannot be correctly described by the Landau-Zener model. This happens when $\tau \lesssim 1$. If a quench is performed too slowly, the system evolves adiabatically across the critical point. The relevant energy gap here is the level spacing which scales as N_x^{-1} near a critical point. As in the Landau-Zener physics the square of the energy gap determines the boundary between adiabatic and non-adiabatic evolution, the dynamics becomes adiabatic for $\tau \gtrsim N_x^2$. The number of bulk excitations drops exponentially with quench time in this regime. On the other hand, the dynamics of in-gap states is non-adiabatic even for very long quench times, which is due to a fact that the energy gap in the in-gap states is exponentially small. However, as observed in figure 5.5(b), momentum distribution of the in-gap excitations for $\tau = 1000$ does not follow the universal scaling of slower quenches. This is due to the fact that for slower quenches than $\tau \sim N_x^2$, the dynamics becomes non-adiabatic only deep in the topological regime.

5.2.2 Analytical evaluation of the density of in-gap excitations

In this section we derive the momentum distribution of in-gap excitations for quenches with $1 \ll \tau \ll N_x^2$, which is the regime where the power-law scaling of the total density of excitations holds. In this regime, the time-evolution of the system is strongly non-adiabatic at the critical point. On the other hand, quenches are slow enough for the excitations to be formed only close to the $k_y = 0$ point where the Landau-Zener calculation applies.

The derivation is based on a simplistic picture based on the evolution of eigenenergies as displayed in figure 5.3(b). While the system is in the trivial phase, there are no in-gap states present and all of the states are delocalized throughout the whole sample. Near the critical point at $u_c = -2$ the in-gap bands are formed from the lowest conduction state and the highest valence. Energy levels approach $E = 0$ roughly linearly in $u - u_c$ on the non-topological side. As u enters the topological phase, the energy gap between the bulk bands reopens while the dispersion of the in-gap bands appears to be static for k_y close to 0. Figure 5.6 shows the density

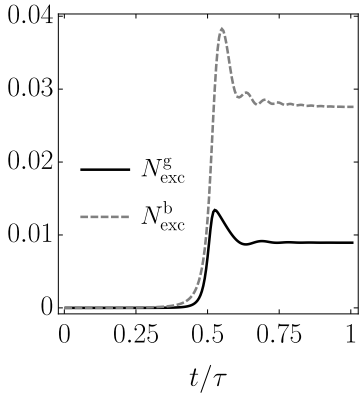

Figure 5.6: Density of excitations in the in-gap states (solid) and in the bulk (dashed) during the quench with $\tau = 80$ and $N_x = 50$.

of in-gap excitations during the quench with $\tau = 80$ and $N_x = 50$. The density of excitations jumps to a non-zero value when the system is near the critical point at $t/\tau = 1/2$. From the critical point on, the density of excitations is approximately constant. In our analytical evaluation we will therefore assume that the density of in-gap excitations does not change from the critical point on and together with the fact that the energy gap between the in-gap states stays closed, we will describe the dynamics of the in-gap states as a half of an effective in-gap two-band Landau-Zener problem.

In order to calculate the density of excitations in the in-gap states, we first express the Hamiltonian $\hat{H}(k_y)$ in the diabatic basis

$$|\psi_{n\sigma}\rangle = \sum_{x=1}^{N_x} \sqrt{\frac{2}{N_x+1}} \sin(k_n x)|x\rangle \otimes |\sigma\rangle, \quad k_n = \frac{\pi n}{N_x+1}, \tag{5.10}$$

where index n runs over $\{1, \ldots, N_x\}$ and $\sigma = \{A, B\}$. $|\psi_{n\sigma}\rangle$ is an eigenstate of the Hamiltonian that does not couple the $|A\rangle$ and $|B\rangle$ orbitals (when $\hat{\sigma}_x$ and $\hat{\sigma}_y$ terms

are put to zero in equation (5.1)) with the eigenenergy

$$E_{n\sigma}(k_y) = \pm(u + \cos k_y + \cos k_n). \tag{5.11}$$

Near the critical point u and therefore eigenenergies of the diabatic states vary linearly in time, which corresponds to the multi-level Landau-Zener model. As this problem is not exactly solvable, we approximate the dynamics of electrons in the in-gap bands with a two-level Hamiltonian

$$\hat{H}_2(k_y) = (u + \cos k_y + \cos k_1)\hat{\sigma}_z + \sin k_y \hat{\sigma}_y, \tag{5.12}$$

which is the projection of the full Hamiltonian (5.1) to the subspace spanned by diabatic states $|\psi_{1A}\rangle$ and $|\psi_{1B}\rangle$. These two states represent the lower conduction and the upper valence band. The energy levels of $\hat{H}_2(k_y)$ as functions of u are shown with red color in figure 5.3. $\hat{H}_2(k_y)$ recreates the exact eigenenergies well up until the critical point. As the excitations are for slow quenches generated only at momenta k_y close to 0 and at times near the critical point, we approximate the Hamiltonian (5.12) up to the first order in t and k_y. The dynamics is dictated by the time-dependent Schrödinger equation,

$$i\frac{\mathrm{d}}{\mathrm{d}t}|\varphi(k_y,t)\rangle = \left[\frac{\alpha}{2}t\hat{\sigma}_z + k_y\hat{\sigma}_y\right]|\varphi(k_y,t)\rangle, \tag{5.13}$$

where $\alpha = (u_1 - u_0)\pi/\tau$. As the number of excitations stays approximately constant from the critical point on, we evaluate the final distribution of the in-gap excitations as the one at the critical point. Using the result for a half Landau-Zener (3.9) the expression for the momentum distribution of excitations is

$$n^{\mathrm{g}}_{\mathrm{exc}}(k_y) = \frac{\pi}{4}e^{-\frac{\pi k_y^2}{2\alpha}}\left|\frac{-1+i}{\Gamma\left(\frac{1}{2}+i\frac{k_y^2}{2\alpha}\right)} + \frac{|k_y|}{\sqrt{\alpha}\Gamma\left(1+i\frac{k_y^2}{2\alpha}\right)}\right|^2. \tag{5.14}$$

This analytical result only roughly describes the number of excitations, its deviations originating from the approximation that the in-gap states evolve as a two-level system. We fitted the function in equation (5.14) to the numerical results and obtained the parameter $\alpha = (u_1 - u_0)\pi/(2.6\tau)$ that fits the actual number of excitations the best. The fitted function is shown in figure 5.5(b) (red curve). As the agreement between the fitted function and the actual momentum distribution of in-gap excitations is perfect for small k_y, we are confident that the analytical result gives the correct scaling of the total number of in-gap excitations with quench time.

5.2.3 Critical properties of the effective in-gap Hamiltonian

The fact that the total density of excitations in the bulk and in the in-gap states scales with τ as a power-law indicates that the physics of the in-gap states may be captured by the Kibble-Zurek mechanism. In fact, the total density of bulk excitations scales in ribbons of large width N_x as τ^{-1}, which matches the Kibble-Zurek predictions for a bulk-only system (see section 4.1.5). In order to test this relation for the in-gap states, one has to calculate the critical exponents of the in-gap states. As shown in section 5.2.2, the low-energy dynamics of the in-gap states

may be effectively described as an independent one-dimensional system with the Hamiltonian $\hat{H}_2(k_y)$:

$$\hat{H}_2(k_y) = \mathbf{d}(k_y) \cdot \hat{\boldsymbol{\sigma}}, \quad \mathbf{d}(k_y) = (0, \sin k_y, u - u_c + \cos k_y - 1), \tag{5.15}$$

where $u_c = -1 - \cos \frac{\pi}{N_x+1}$. The Hamiltonian possesses the chiral symmetry

$$\hat{\sigma}_x \hat{H}_2(k_y) \hat{\sigma}_x = -\hat{H}_2(k_y), \tag{5.16}$$

which entails the system with the topological invariant w, in literature called *the winding number*:

$$w = \int_{-\pi}^{\pi} \mathrm{d}k_y \, F(k_y, u), \tag{5.17}$$

where $F(k_y, u)$ is *the Berry connection* [154, 167]

$$F(k_y, u) = \frac{1}{2\pi} \left(\frac{\mathbf{d}(k_y)}{|\mathbf{d}(k_y)|} \times \partial_{k_y} \frac{\mathbf{d}(k_y)}{|\mathbf{d}(k_y)|} \right)_x. \tag{5.18}$$

The topological phase is controlled by the control parameter u. The energy levels as a function of u are shown in figure 5.3(b).

We extract the critical exponent $z\nu$ from the characteristic time scale, which is the inverse of the band gap. The spectrum near the gap closing on the trivial side is of the form

$$E_{c,v}(k_y) = \pm\sqrt{(u - u_c)^2 + k_y^2}. \tag{5.19}$$

The gap vanishes as $|u - u_c|^{z\nu} = |u - u_c|$, yielding the critical exponent $z\nu = 1$.

The length scale is then extracted from the scaling of the Berry connection, which is close to the critical point of Lorentzian form

$$F(k_y, u) = -\frac{u - u_c}{(u - u_c)^2 + k_y^2}, \tag{5.20}$$

and the correlation length can be extracted from the width of the peak

$$\xi(u) = |u - u_c|^{-1}, \tag{5.21}$$

yielding the critical exponent $\nu = 1$.

Taking into account the one-dimensional nature of in-gap states and the obtained critical exponents, the scaling of in-gap excitations $\tau^{-1/2}$ as found using the Landau-Zener approach is reproduced.

5.2.4 Breaking of the inversion symmetry

As shown in section 5.1 the QWZ model in the ribbon geometry possesses the inversion symmetry which pins the in-gap subbands crossing to $k_y = 0$ during quenches. If the inversion symmetry is broken, as is, e.g., the case in the Haldane model studied in reference [140], the k_y-point where the crossing occurs may move during the quench. After the quench, this results in a perfect population of the excited in-gap states in the interval of k_y-s swept over by the crossing. As discussed in reference [140], the reason behind this behaviour is that, at each of these momenta, an

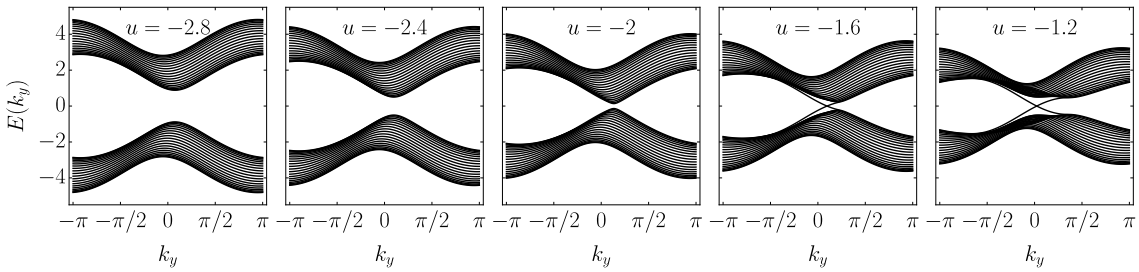

Figure 5.7: Energy dispersion of the QWZ model with inversion symmetry breaking term of magnitude $b = 1$ for different values of u that range across a critical point at $u = -2$. Ribbon width is $N_x = 20$.

electron performs a complete Landau-Zener tunneling process with a unit transition probability due to an exponentially small Landau-Zener gap.

To break the inversion symmetry in the QWZ model, we add a perturbing term to the Hamiltonian

$$\hat{H}(k_y) \to \hat{H}(k_y) + \sum_{x=1}^{N_x-1} |x+1\rangle\langle x| \otimes b\frac{-i\hat{\sigma}_x - \hat{\sigma}_y}{4} + \text{h.c.} \tag{5.22}$$

The energy dispersion is for large inversion symmetry breaking $b = 1$ shown in figure 5.7. As the parameter u enters the topological regime at $u_c = -2$, the in-gap subbands exhibit the crossing at a k_y of the order of b. As the quench progresses, the crossing shifts towards $k_y = 0$. Therefore, the in-gap excitations are generated in an interval of k_y of width of the order of b. On the other hand, if the inversion symmetry is not broken, in-gap excitations are generated in an interval of k_y of width of the order of $\tau^{-1/2}$. For slow quenches, $\tau \gg b^{-2}$, the density of in-gap excitations thus saturates while in the opposite limit, $\tau \ll b^{-2}$, the effect of the inversion symmetry breaking on the scaling of the in-gap excitations on τ can be neglected. This can be seen in figure 5.6(b) where blue dots show the scaling of the density of in-gap excitations with quench time for $b = 0.15$. In contrast, the scaling of the bulk excitations, shown in figure 5.6(a), is not affected by the inversion-symmetry breaking.

The mechanism described above leads to asymmetrically populated in-gap bands after a quench with $b \neq 0$. This results in a finite current in y-direction already in the absence of electric field. This is not observed in the presence of the inversion symmetry as there a quench by itself cannot lead to a finite current as excitations are produced symmetrically in in-gap bands, $n_L(k_y) = n_R(-k_y)$, which, taking into account the fact that the corresponding dispersion curves have opposite slopes, leads to a perfect cancellation of current. As shown in a later discussion in section 5.3.6 in figure 5.10(b), turning on the electric field in x-direction induces an additional Hall current, which, is not significantly affected by the inversion-symmetry breaking.

We note that not every perturbation breaking the inversion symmetry leads to a violation of the Kibble-Zurek scaling. A perturbation may break the symmetry of the energy spectrum and shift the in-gap crossing to $k_y \neq 0$, however as long as the in-gap crossing is pinned to a certain k_y throughout the quench, the Kibble-Zurek scaling holds. The inversion symmetry assures Kibble-Zurek scaling but is not necessarily needed.

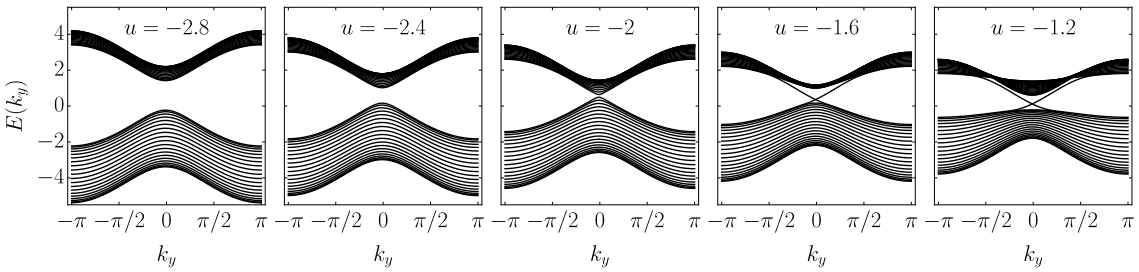

Figure 5.8: Energy dispersion of the QWZ model with particle-hole symmetry breaking term of magnitude $b = 0.3$ for different values of u that range across a critical point at $u = -2$. Ribbon width is $N_x = 20$.

5.2.5 Breaking of the particle-hole symmetry

The QWZ ribbon possesses the particle-hole symmetry due to which the in-gap bands crossing is pinned to zero energy. Here we break this symmetry by adding a symmetry-breaking term to the Hamiltonian

$$\hat{H}(k_y) \to \hat{H}(k_y) + \sum_{x=1}^{N_x-1} |x+1\rangle\langle x| \otimes b\hat{1} + \text{h.c.} \tag{5.23}$$

The energy dispersion is for $b = 0.3$ shown in figure 5.8. During the quench, the in-gap crossing moves along the $k_y = 0$ line (due to the inversion symmetry), starting at $E \propto b$ at $u = -2$ and moving towards zero energy at $u = -1$. We performed quenches for several values of b up to $b = 0.3$. Breaking the particle-hole symmetry in this way did not affect the scaling of the number of excitations, neither the scaling of deviations of the Hall conductance. The Kibble-Zurek scaling still holds because the momentum distribution of excitations is not affected and still behaves as $n_{\text{exc}}(\mathbf{k}) = g(k\sqrt{\tau})$. This can be seen by considering the in-gap two-level Landau-Zener problem (see equation (5.12)) with additional term which shifts the in-gap crossing from zero energy: the minimal energy gap during the quench remains proportional to $|k_y|$ and the velocity α with which the two energy bands approach is unchanged.

5.3 The Hall conductance

5.3.1 Evaluation of Hall conductance

We evaluate the Hall conductance G_{yx} by calculating the current in y-direction,

$$\hat{J}_y = \frac{1}{N_y} \sum_{k_y} |k_y\rangle\langle k_y| \otimes e\partial_{k_y}\hat{H}(k_y), \tag{5.24}$$

as a response to turning on a homogeneous electric field in x-direction adiabatically as $E_x(t) = E_0[1 - \exp(-t/\tau_E)]$. In presence of the electric field, the ribbon Hamiltonian $\hat{H}(k_y)$ thus acquires an additional term

$$\hat{V}(t) = -eE_x(t)\left(\hat{x} - \frac{N_x+1}{2}\right), \tag{5.25}$$

with $\hat{x} = \sum_{x=1}^{N_x} x|x\rangle\langle x|$ being the position operator. The Hall conductance is then calculated as

$$G_{yx} = J_y/U, \quad U = E_0(\langle\psi_R(0)|\hat{x}|\psi_R(0)\rangle - \langle\psi_L(0)|\hat{x}|\psi_L(0)\rangle), \tag{5.26}$$

where U is the voltage between the edges of the ribbon and J_y the expectation value of the current.

In order to investigate the distribution of the current across a ribbon we calculate the current flowing through a particular site [54] at position $\mathbf{r} = (x, y)$,

$$\hat{\boldsymbol{j}}(\mathbf{r}) = e\sum_{\mathbf{r}'} -\frac{i}{2}\boldsymbol{\delta}_{\mathbf{r}'\mathbf{r}}\left(|\mathbf{r}'\rangle\langle\mathbf{r}| \otimes \hat{t}_{\mathbf{r}'\mathbf{r}} - \text{h.c.}\right), \tag{5.27}$$

where $\boldsymbol{\delta}_{\mathbf{r}'\mathbf{r}}$ is the vector pointing from site $\mathbf{r}$ to site $\mathbf{r}'$ and $\hat{t}_{\mathbf{r}'\mathbf{r}}$ is the corresponding hopping operator of the model (6.1) that in non-zero only between nearest neighbour sites, $\hat{t}_{x,x+1} = (\hat{\sigma}_z + i\hat{\sigma}_x)/2$ and $\hat{t}_{y,y+1} = (\hat{\sigma}_z + i\hat{\sigma}_y)/2$.

5.3.2 Ground state response to electric field

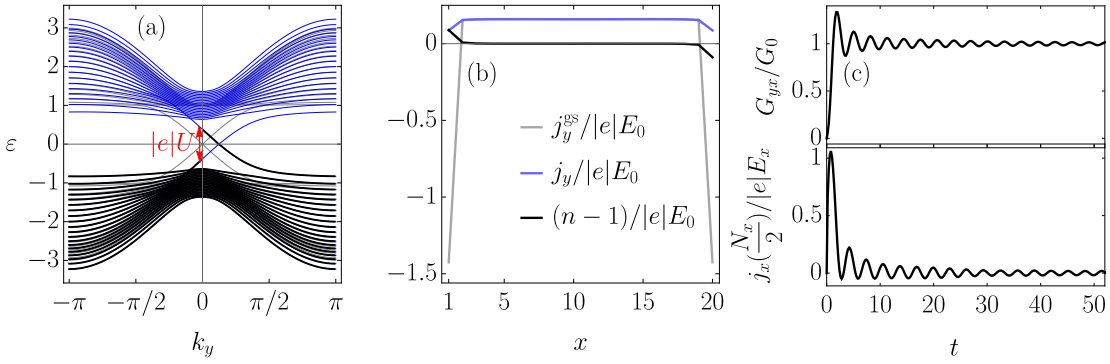

Figure 5.9: a) Energy spectrum in the topologically non-trivial phase in absence (gray) and in presence of the electric field (blue and black). Black lines denote the occupied states of the system that adiabatically evolved due to insertion of the electric potential from the ground state without the electric potential. b) Current densities j_y^{gs} in the ground state of the system with a static electric field (gray) and j_y in the state which adiabatically evolved from the ground state of the system without the electric field at $t \gg \tau_E$ (blue). The deviation of the particle density $n-1$ is also shown (black). c) Conductance G_{yx} and the current density in x-direction in the middle of the ribbon $j_x(N_x/2)$ as a response to the adiabatically inserted electric potential. The system size is $N_x = 20$, $N_y = 201$, $u = -1$ and the electric field $E_0 = 0.04$, $\tau_E = 5$.

In the ground state in absence of the electric field the current density $\langle\hat{\boldsymbol{j}}(\mathbf{r})\rangle = (j_x(\mathbf{r}), j_y(\mathbf{r}))$ is zero throughout the system and the particle density

$$n(\mathbf{r}) = \sum_{k_y}\sum_{n=1}^{N_x} |\langle\mathbf{r}|\Psi_n(k_y)\rangle|^2 \tag{5.28}$$

is equal to 1 on every site. As the electric field is turned on adiabatically in the topologically non-trivial phase, the current and the particle densities develop profiles

shown in figure 5.9(b). The current starts flowing in y-direction mostly through the bulk, while the density deviates from 1 at the edges: on the $x = 1$ edge where the electric potential is higher the particle density is increased while on the opposite edge where the electric potential is lower the particle density is lowered. Note that these profiles are invariant of the electric field strength E_0 as long as it can be treated as an adiabatic perturbation. Also, the current density in the bulk is constant and invariant of N_x.

The time-dependence of the Hall conductance is shown in figure 5.9(c). The conductance rises steeply and then oscillates around a quantized value of 1 in units of $G_0 = e^2/h$ with the frequency corresponding to the bulk energy gap. The amplitude of the oscillations diminishes with time and it also becomes smaller if the electric field is turned on more adiabatically (i.e., with a longer τ_E). In contrast to the Hall conductance, the current density j_x oscillates around zero except for small times $t \lesssim \tau_E$ where it is positive. This corresponds to the current flowing from $x = 1$ to $x = N_x$ until the final inhomogeneous particle density profile is established.

For completeness let us also consider the case when the electric field is adiabatically turned on in the topologically trivial phase. The particle density and the current density j_x behave as in the topologically non-trivial phase discussed above. The current density j_y is non-vanishing, however the time average of the total current J_y, proportional to the Hall conductance, is exactly zero.

The quantization of the Hall conductance can be explained by comparing the adiabatically evolved system to: (1) the system in the ground state in presence of the electric field; (2) the system in the ground state without electric field.

5.3.3 Comparison to the ground state with electric field

In presence of the electric field, the energy bands are deformed as shown in figure 5.9(a) (blue and black lines). According to the first order perturbation theory, the eigenenergy of an eigenstate $|\Psi_n(k_y)\rangle$ changes due to the perturbing potential $\hat{V}$,

$$\begin{aligned} \delta E_n(k_y) = \langle \Psi_n(k_y)|\hat{V}|\Psi_n(k_y)\rangle = \\ -eE_x\langle \psi_n(k_y)|\hat{x} - \tfrac{N_x+1}{2}|\psi_n(k_y)\rangle. \end{aligned} \tag{5.29}$$

As the in-gap states near $k_y = 0$ are localized at opposite edges, their eigenenergies change significantly. The change of the energy dispersion results in a shift of the degeneracy point of the in-gap states from $k_y = 0$ to $k_y = k_0 > 0$.

In the ground state of the system with static electric field the total current is zero. This can be explicitly seen by summing all the contributions to the current carried by the occupied eigenstates, where the contribution of an eigenstate $|\Psi_n(k_y)\rangle$ is equal to [154]

$$\langle \Psi_n(k_y)|\hat{J}_y|\Psi_n(k_y)\rangle = \frac{e}{N_y}\partial_{k_y}E_n(k_y). \tag{5.30}$$

The calculated current density $j_y^{\mathrm{gs}}(\mathbf{r})$ is shown in figure 5.9(b) (gray). As the current density in the bulk is constant, the edge current flows in the opposite direction so it completely cancels out the bulk contributions to the net current.

The quantization of the Hall conductance can be explained by comparing the occupations of the energy bands in the adiabatically-evolved system with those in the system in the ground state with static electric field. As the electric field is turned

on, the electrons adiabatically follow the bands which get deformed. This results in the final occupancy, shown in figure 5.9(a) (black lines), which is different from that in the ground state of the Hamiltonian with electric field. The difference lies only in the in-gap bands: band L is occupied up until $E_L(0) = -eE_x\langle\psi_L(0)|\hat{x}-\frac{N_x+1}{2}|\psi_L(0)\rangle$, while band R is occupied up until $E_R(0) = -eE_x\langle\psi_R(0)|\hat{x}-\frac{N_x+1}{2}|\psi_R(0)\rangle$. The same occupancy would be observed in a quantum wire contacted to two electron reservoirs, one having the chemical potential at $-eU/2$ and the other at $eU/2$ with $U = E_x(\langle\psi_R(0)|\hat{x}|\psi_R(0)\rangle - \langle\psi_L(0)|\hat{x}|\psi_L(0)\rangle)$. As the total current in the ground state is zero, only the difference in occupations with respect to those in the ground state contributes to the current,

$$\delta J_y = \frac{e}{2\pi}\left(\int_{E_R(0)}^{E_R(k_0)} \mathrm{d}E_R - \int_{E_L(0)}^{E_L(k_0)} \mathrm{d}E_L\right) = G_0 U. \tag{5.31}$$

U is equal to the voltage between ribbon edges measured by attaching voltage probes as the chemical potential at $x = 1$ edge is equal to $E_L(0)$ while the chemical potential at the $x = N_x$ edge is equal to $E_R(0)$. Therefore, the Hall conductance is quantized in units of G_0.

5.3.4 Comparison to the ground state without electric field

The quantization of the Hall conductance in a system with adiabatically inserted electric field can be also explained by comparing it to the system in the ground state without electric field. As the electrons in the adiabatically evolved system are occupying eigenstates with perturbed eigenenergies, the additional current due to the electric field carried by an electron in an eigenstate $|\Psi_n(k_y)\rangle$ is according to equations (5.29) and (5.30) equal to $\frac{e^2E_x}{N_y}\Omega_n(k_y)$, where we denoted

$$\Omega_n(k_y) = -\partial_{k_y}\langle\psi_n(k_y)|\hat{x}|\psi_n(k_y)\rangle. \tag{5.32}$$

As the total current in the ground state is zero, only this contribution needs to be taken into account, resulting in

$$\begin{aligned}\delta J_y &= \frac{e^2E_x}{2\pi}\sum_{n=1}^{2N_x}\int_{-\pi}^{\pi}\mathrm{d}k_y f(E_n(k_y))\Omega_n(k_y) = \\ &G_0E_x\Big(-\langle\psi_L(k_y)|\hat{x}|\psi_L(k_y)\rangle\Big|_{-\pi}^{0} - \langle\psi_R(k_y)|\hat{x}|\psi_R(k_y)\rangle\Big|_{0}^{\pi}\Big) = G_0U,\end{aligned} \tag{5.33}$$

where $f(E)$ is the Fermi distribution.

5.3.5 $\Omega_m(k_y)$ in systems with periodic boundary conditions in both directions

For a system with periodic boundary conditions in both directions the quantity $\Omega_m(k_y)$ corresponds to the Berry curvature. This can be shown by treating such a system as quasi-one-dimensional and assigning a band index α together with a momentum k_x to each subband m, $|\psi_m(k_y)\rangle \to |\psi_{\alpha k_x}(k_y)\rangle = |k_x\rangle \otimes |\psi_\alpha(\mathbf{k})\rangle$. With the orthogonality of states $|k_x\rangle$ taken into account, equation (5.32) reads

$$\Omega_{\alpha k_x}(k_y) = -2\mathrm{Re}\sum_{\beta\neq\alpha}\langle\partial_{k_y}\psi_{\alpha k_x}(k_y)|\psi_{\beta k_x}(k_y)\rangle\langle\psi_{\beta k_x}(k_y)|\hat{x}|\psi_{\alpha k_x}(k_y)\rangle. \tag{5.34}$$

While the position operator $\hat{x}$ is ill defined within periodic boundary conditions, its off-diagonal elements over the Hamiltonian eigenstates are well defined.[168] Using $\langle\psi_{\beta k_x}(k_y)|\hat{x}|\psi_{\alpha k_x}(k_y)\rangle = \langle\psi_\beta(\mathbf{k})|i\partial_{k_x}|\psi_\alpha(\mathbf{k})\rangle$ for $\beta \neq \alpha$[169] leads to

$$\Omega_\alpha(\mathbf{k}) = 2\mathrm{Im}\sum_\beta \langle\partial_{k_y}\psi_\alpha(\mathbf{k})|\psi_\beta(\mathbf{k})\rangle\langle\psi_\beta(\mathbf{k})|\partial_{k_x}\psi_\alpha(\mathbf{k})\rangle. \tag{5.35}$$

We were allowed to add the $\beta = \alpha$ term to the sum as it is real. By using the completeness relation $\sum_\beta |\psi_\beta(\mathbf{k})\rangle\langle\psi_\beta(\mathbf{k})| = 1$ we obtain the well known equation for the Berry curvature $\Omega_\alpha(\mathbf{k}) = 2\,\mathrm{Im}\langle\partial_{k_y}\psi_\alpha(\mathbf{k})|\partial_{k_x}\psi_\alpha(\mathbf{k})\rangle$.

5.3.6 Non-equilibrium Hall conductance

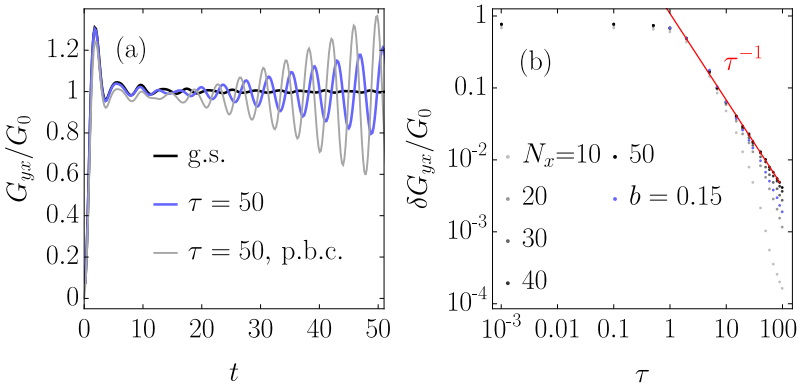

Figure 5.10: a) Hall conductance of the ground state of the final Hamiltonian (black) and after a quench with $\tau = 50$ (blue), and Hall conductivity after a quench with $\tau = 50$ in a system with periodic boundary conditions in both spatial directions (gray), for $N_x = 20$, $E_0 = 0.001$ and $\tau_E = 5$. (b) Deviations from the ground state Hall conductance as a function of τ for different ribbon widths, ranging from $N_x = 10$ (light gray) to $N_x = 50$ (black). The red line is a fitted τ^{-1} scaling. Blue dots show results for a Hamiltonian with a broken inversion symmetry of magnitude $b = 0.15$ and $N_x = 20$.

The Hall conductance is calculated after the quench by time-evolving the post-quench states with time-dependent Hamiltonian with electric field. In figure 5.10(a) we show the Hall conductances of two states of a ribbon, namely of its ground state at $u = u_1$ and of the state created by a slow quench, together with the Hall conductivity of a system with periodic boundary conditions in both directions, again after a slow quench (see section 4.1.9). In all of the cases the response first experiences a transient behaviour and then oscillates around a non-zero value $\bar{G}_{yx}$, with the frequency corresponding to the band gap of the final Hamiltonian. Deviations of $\bar{G}_{yx}$ of a quenched ribbon from its quantized ground state value $G_0 = e^2/h$, $\delta G_{yx} = |\bar{G}_{yx} - G_0|$, are presented in figure 5.10(b). For quenches faster than $\tau \approx 1$ the average Hall conductance almost vanishes. For slower quenches the average Hall conductance increases towards the quantized value. In wide ribbons, the deviations diminish as τ^{-1}, as in systems with periodic boundary conditions in both directions.

One might expect the excitations in the in-gap states to dominate the deviations and hence anticipate a scaling with their number that goes as $\tau^{-1/2}$, instead. In

order to understand the observed behaviour, we evaluated the Hall conductance using the time-dependent perturbation theory. The derivation is equivalent to the one presented in section 4.1.10, only the perturbing time-dependent potential has to be changed to $\hat{V}$ in equation (5.25). One obtains the following result for the time-averaged Hall current at large times:

$$\bar{J}_y = G_0 E_0 \sum_{n=1}^{2N_x} \int \mathrm{d}k_y \, n_n(k_y) \Omega_n(k_y). \tag{5.36}$$

The Hall conductance is expressed as an integral of the quantity $\Omega_n(k_y)$, shown in figure 5.11, weighted by the occupation $n_n(k_y)$ of the eigenstate $|\psi_n(k_y)\rangle$ of the final Hamiltonian. This result comes from the fact that the current is given by the change of the dispersion due to the electric potential $-eE_x\hat{x}$, which leads to terms of the form $\partial_{k_y}\langle\hat{x}\rangle$. For a system with periodic boundary conditions in both directions, the quantity $\Omega_n(k_y)$ corresponds to the Berry curvature (see section 5.3.5). If the system is in the ground state, $n_n(k_y)$ is equal to the Fermi distribution $f(E_n(k_y))$ and the conductance is quantized as shown in equation (5.33) in section 5.3.4. The deviation of the post-quench Hall conductance from the ground state one can thus be attributed to excitations

$$\begin{aligned} \delta G_{yx} &\propto \sum_{n=1}^{2N_x} \int \mathrm{d}k_y \, \delta n_n(k_y) \Omega_n(k_y), \\ \delta n_n(k_y) &= n_n(k_y) - f(E_n(k_y)). \end{aligned} \tag{5.37}$$

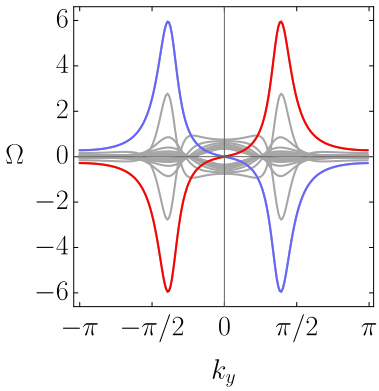

Figure 5.11: $\Omega_L(k_y)$ (blue) and $\Omega_R(k_y)$ (red) for a ribbon with $N_x = 10$ at $u = -1.2$. $\Omega_m(k_y)$ for bulk subbands are plotted in gray color.

Let us first analyse the in-gap contributions to δG_{yx}. $\Omega_m(k_y)$ at $u = -1.2$ are shown in figure 5.11. Deep in the topological phase, i.e. for small $|u+1|$, $\Omega_m(k_y)$ for in-gap bands is linear in k_y in the vicinity of $k_y = 0$ where the excitations are produced:

$$\Omega_{L,R}(k_y) = \pm 2(u+1)k_y, \quad |u+1| \ll 1, \, |k_y| \ll 1. \tag{5.38}$$

As

$$\delta n_{L,R}(k_y) = \pm n^{\mathrm{g}}_{\mathrm{exc}}(k_y)\mathrm{sgn}(k_y), \tag{5.39}$$

the in-gap contribution to δG_{yx} is proportional to

$$\delta G_{yx} \propto \int \mathrm{d}k_y \, n^{\mathrm{g}}_{\mathrm{exc}}(k_y)|k_y| = \int \mathrm{d}k_y \, g(k_y\sqrt{\tau})|k_y| \propto \tau^{-1}. \tag{5.40}$$

This is the same scaling as for the 'bulk-only' system with periodic boundary conditions in both directions. As the current is easily measured, this provides a good strategy for measuring the Kibble-Zurek scaling in experiment.

On the other hand, $\Omega_n(k_y)$ for bulk subbands take a finite value at $k_y = 0$. After slow quenches, subbands near the bottom of the conduction band and those near the top of the valence band carry most of the bulk excitations. Therefore we can, to a good approximation, evaluate δG_{yx} by replacing $\Omega_n(k_y)$ for conduction and valence subbands in equation (5.36) with values at $k_y = 0$ for the lowest conduction and the highest valence subband, respectively. As these two values differ only in sign, this approximation leads to a deviation of the post-quench time-averaged Hall conductance from the ground state value which scales as the number of bulk excitations, i.e. as τ^{-1}, as is also the case in a system with periodic boundary conditions in both directions.

5.4 Conclusions

This chapter was dedicated to Chern insulators in the ribbon geometry. In systems with edges, in-gap edge states emerge in the topological phase. The in-gap states are localized at the edges and allow for dissipationless transport. By introducing a weak time-dependent electric field in the direction from one edge to another edge, we showed that electrical current is induced along the ribbon that accounts for exact quantization of the Hall conductance. The number of edge states is in the ground state related to the topological invariant via the bulk-boundary correspondence. As is known from studies of the non-equilibrium bulk properties, the Chern number is conserved under unitary time-evolution, even if the quench is done across a topological phase transition. By performing quenches in a system in ribbon geometry, we investigated what happens to edge related quantities.

After a slow quench from the trivial to the topological regime the excitations are generated both in the bulk bands as well as in the in-gap states. The density of excitations in the bulk drops with quench time τ as τ^{-1} while the density of in-gap excitations, provided the ribbon possesses the inversion symmetry, drops as $\tau^{-1/2}$. While the former result is well known from the studies of bulk systems, we explained the latter by taking into account that the in-gap bands, once they form upon entering the topological regime, are stationary. This allowed us to approximately map the quench dynamics related to the in-gap bands to a half of the two-level Landau-Zener problem. Taking additionally into account the one-dimensional nature of the in-gap states we derived the $\tau^{-1/2}$ scaling. The effective two-level one-dimensional Hamiltonian of the in-gap states has the chiral symmetry, which entails the effective in-gap system with a topological phase, characterized by the winding number. The topological phase transition coincides with the one for the Chern insulator. We calculated the critical exponents of the topological transition of the in-gap states and showed that the scaling of in-gap excitations follows the Kibble-Zurek prediction. Finally, we characterized the quenched state by calculating the Hall conductance.

We found that its deviations from the quantized value characteristic of the post-quench Hamiltonian drop as τ^{-1}, which was also found in systems with periodic boundary conditions.

The studied QWZ model has the particle-hole symmetry and the inversion symmetry. Breaking the particle-hole symmetry does not significantly affect the post-quench properties of the system. On the other hand, breaking the inversion symmetry may cause the avoided crossing of the in-gap states to travel through the Brillouin zone during the quench. This causes a perfect population of one in-gap band in a range of momenta through which the avoided crossing travelled. Such a quench thus breaks the Kibble-Zurek scaling of the in-gap excitations and produces a finite current in the system even in the absence of electric field. As the in-gap band is localized on one edge, the current will flow only along the corresponding edge. With such a protocol it is thus possible to control the edge currents flowing at the boundaries of the sample.

Chapter 6

Quenches in weakly disordered systems

The motivation to study non-equilibrium dynamics in weakly disordered topological insulators stems from the finding that non-equilibrium dynamics in momentum space of translation invariant insulators follows the Kibble-Zurek scaling. The number of excitations after the quench was shown to follow the Kibble-Zurek scaling [56, 58, 63, 64, 119] and the dynamical evolution of the correlation length is well captured by the adiabatic-impulse approximation [153]. The Kibble-Zurek mechanism is usually associated with phase transitions with spontaneous symmetry breaking and degeneracy of the ground state. Non-adiabatic evolution produces in such systems regions corresponding to different choices of the ground state. At meeting points of these regions topological defects can be formed. The Kibble-Zurek mechanism connects the size of the regions with the quench time and equilibrium critical exponents. These defects are shown in the local order parameter in real space and have been extensively measured in experiments and shown to follow the Kibble-Zurek scaling. As we observed the emergence of the Kibble-Zurek length scale in momentum space, this poses a question whether it is possible to observe real space structures in analogy to phase transitions with spontaneous symmetry breaking.

This analogy is however not expected on the first sight as topological insulators have no spontaneously broken symmetries, lack degeneracy of the ground state and have no local order parameter. Recently, however, the local Chern marker (LCM) [79] was introduced as a local indicator of the topological phase in Chern insulators. Caio et al. showed that in clean systems with edges the LCM exhibits a length scale that grows as $|u - u_c|^{-\nu}$ close to a topological phase transitions [80].

In this chapter we address the critical behaviour of Chern insulators that emerges in real space. In order to reveal real space structures, we calculate the LCM in the presence of weak disorder, which breaks the translational symmetry. The disorder leads to the appearance of inhomogeneities in the LCM. We show that in the ground state their size grows as $|u - u_c|^{-1}$ as the topological transition is approached. Then we study a quench where we drive the system across a critical point in a finite time τ. After the quench, we find inhomogeneities the size of which scales as $\tau^{1/2}$, as predicted by the Kibble-Zurek mechanism. Evaluating the LCM during the quench shows that the growth of inhomogeneities during the quench exhibits the freeze-out behaviour, which establishes an almost full analogy to the dynamical critical behaviour of systems with a spontaneously broken symmetry. The text closely

follows our published work [153].

6.1 Disordered Qi-Wu-Zhang model

We study the QWZ model on a periodic geometry with a weak disorder. The Hamiltonian in the real-space basis is

$$\begin{aligned}\hat{H} =& \sum_{\mathbf{r}} |x,y\rangle\langle x,y| \otimes [u+\delta u(\mathbf{r})]\hat{\sigma}_z + \\ &+ \sum_{\mathbf{r}} \left(|x+1,y\rangle\langle x,y| \otimes \tfrac{\hat{\sigma}_z + i\hat{\sigma}_x}{2} + |x,y+1\rangle\langle x,y| \otimes \tfrac{\hat{\sigma}_z+i\hat{\sigma}_y}{2} + \text{h.c.} \right),\end{aligned} \tag{6.1}$$

where $\mathbf{r} = (x, y)$ are the Bravais lattice vectors of a square lattice, measured in units of the lattice constant. The system size is $N \times N$ unit cells, each of which hosts two orbitals $|\mathbf{r}, \sigma\rangle$, $\sigma \in \{A, B\}$ that are located at the same site. The Hamiltonian is therefore of dimension $2N^2 \times 2N^2$ and we denote eigenstates by $|\Psi_n\rangle$ with corresponding eigenenergies E_n. The disorder is present in the staggered orbital binding energies $u + \delta u(\mathbf{r})$, where $\delta u(\mathbf{r})$ are uncorrelated and uniformly distributed on the interval $[-\delta u_0, \delta u_0]$. Such a disorder preserves the particle-hole symmetry (4.4). The energy gap closes near the critical point of the clean system.

The effects of strong disorder on topological phases are rich with interesting phenomena, for example in a chiral-symmetric chain a topological phase is present despite completely localized states and the disorder induces a transition to a trivial phase across a critical point that is characterized with delocalization of zero energy states [170]. In HgTe/CdTe quantum wells strong disorder was shown to destroy the topological phase. However, it also causes an emergence of a novel Anderson topological phase, which is present at a Fermi energy which is for a clean system inside the conduction band and does not have an inverted energy gap [171]. In three-dimensional time-reversal symmetric topological insulators strong disorder induces a phase transition to a metal [172, 173]. In the QWZ model disorder extends the topological phase inside the region of parameter u, which is trivial in the clean limit [174]. This is also reflected in the profile of the LCM, as discussed in section 6.2.5. However, this thesis deals with effects of weak disorder, which is introduced in order to break translation invariance and thus enables formation of real space structures. For disorder amplitude $\delta u_0 = 0.05$ we found that the critical point u_c shifts for less than 10^{-4}. This result was obtained by finding the eigenenergies for different values of u at a fixed δu_0 and determining u_c as the one where the energy gap closes.

6.1.1 Localization properties of the system

One-band two-dimensional systems are Anderson localized for any magnitude of disorder only in the thermodynamic limit. We work with finite-sized systems and as we want to probe the critical properties of a Chern insulator and not of Anderson localized states, we can choose a sufficiently weak disorder such that the Anderson localization length scale is larger than the system and the critical scale of topological phase transition. A quantity which signals localization is the inverse participation

ratio (IPR) of the energy eigenstates $|\Psi_n\rangle$ [175],

$$P_n = \left(\sum_{\mathbf{r}} |\langle \mathbf{r}|\Psi_n\rangle|^4 \right)^{-1} . \tag{6.2}$$

IPR is the highest for a plane wave, its value scaling as $P_n \propto N^D$, where N is the

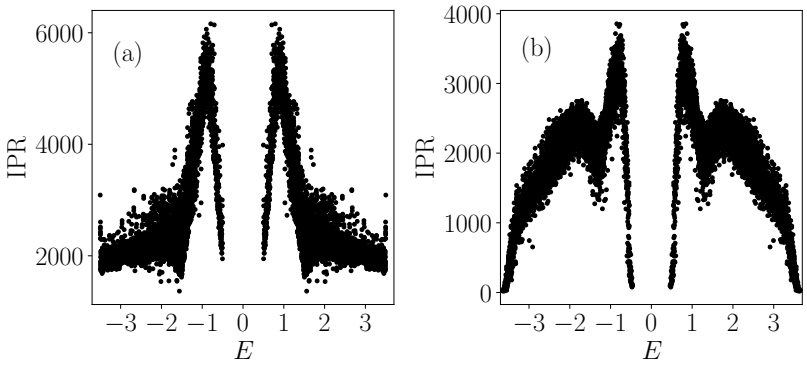

Figure 6.1: Inverse participation ratio of the energy eigenstates of a system of $N = 70$ size at $u = -1.5$ and disorder magnitude (a) $\delta u_0 = 0.05$ and (b) $\delta u_0 = 0.5$.

linear dimension of a D-dimensional system. The IPR is small for localized states, $P = 1$ for a state localized on one site. In figure 6.1 we show the IPR of the QWZ model with disorder strength $\delta u_0 = 0.05, 0.5$ and of the linear size $N = 70$. All of the states are extended in the case of disorder we use in our simulations $\delta u_0 = 0.05$, while we can see localization of the states at the edges of the band at $\delta u_0 = 0.5$.

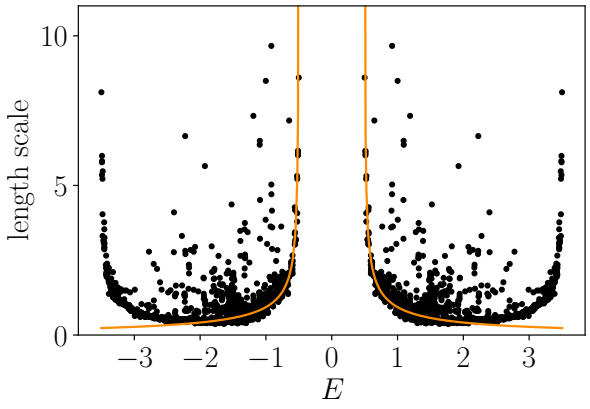

Figure 6.2: Typical length scale of the energy eigenstates at $u = -1.5$, $\delta u_0 = 0.05$ and system size $N = 40$ (black dots) and a Bloch wave estimate (orange) for the low energy eigenstates.

Figure 6.2 shows the typical length scale of the energy eigenstates. The typical length scale was determined as r at which the autocorrelation function of the real space probability distribution of an eigenstate fell to 0.5 (see section 6.2.3). The typical length case can be well approximated up to a constant factor as the wave length

of the Bloch wave $\lambda_n = 2\pi/k$, where $k = |\mathbf{k}|$ is the magnitude of momentum that is given by the dispersion relation for a clean system $|\mathbf{k}| = \sqrt{(E^2 - (u+2)^2)/(-1-u)}$. Figure 6.2 shows the agreement of the typical length with the Bloch wave estimate for energies near the bottom of the conduction band.

6.2 Local Chern marker

6.2.1 Calculation of the local Chern marker

The LCM $c(\mathbf{r})$, the real-space analogue of the Berry curvature, derives from the calculation of the Chern number of disordered systems, proposed in references [79, 176],

$$C = \lim_{N\to\infty} \frac{1}{N^2} \sum_{\mathbf{r}} c(\mathbf{r}), \tag{6.3}$$

$$c(\mathbf{r}) = 2\pi i \sum_{\sigma} \langle \mathbf{r}, \sigma | \hat{P}[-i[\hat{x}, \hat{P}], -i[\hat{y}, \hat{P}]] | \mathbf{r}, \sigma \rangle. \tag{6.4}$$

Here $\hat{x}$ and $\hat{y}$ are the position operators, acting on position basis as $\hat{x}|\mathbf{r}, \sigma\rangle = x|\mathbf{r}, \sigma\rangle$, and $\hat{P} = \sum_{n\in v} |\Psi_n\rangle\langle\Psi_n|$ is the projector onto the subspace spanned by eigenstates $|\Psi_n\rangle$ of the valence band. For a system with periodic boundary conditions, the commutator with $\hat{x}$ can be calculated as

$$-i[\hat{x}_i, \hat{P}] = \sum_{m=-N/2}^{N/2} c_m e^{-im\triangle \hat{x}_i} \hat{P} e^{im\triangle \hat{x}_i}, \tag{6.5}$$

where $\triangle = 2\pi/N$ and c_m are the finite difference coefficients chosen such that $x - \sum_{m=-N/2}^{N/2} c_m e^{im\triangle x} = O(\triangle^N)$. In clean systems in the thermodynamic limit the LCM is uniform and equals the Chern number [79]. References [177, 178] connect the LCM to physical observables, namely to the Hall conductivity in inhomogeneous systems.

6.2.2 Critical behaviour of the local Chern marker

Critical behaviour of the LCM was first exposed in reference [80], which studied the Haldane model on a clean system with open boundary conditions. There, it was shown that in finite systems the LCM deviates from the quantized value close to the critical point. By assuming that this finite-size effect becomes relevant when the correlation length is of order of system size L, it was shown and numerically confirmed that the LCM scales as

$$c \sim f(\xi/L) = f((u-u_c)^{-\nu}/L) = \tilde{f}((u-u_c)L^{1/\nu}), \tag{6.6}$$

where $\nu = 1$ is the correlation length critical exponent.

In our work [153] we show that the critical scaling of the length scale is also observed in the real space profile of the LCM when translational invariance is broken. The real-space profiles of the LCM are shown in figure 6.3(a) for several values of u, ranging from deep in the trivial phase, across the critical point to deep in the topological phase. The profiles are inhomogeneous and feature regions where the

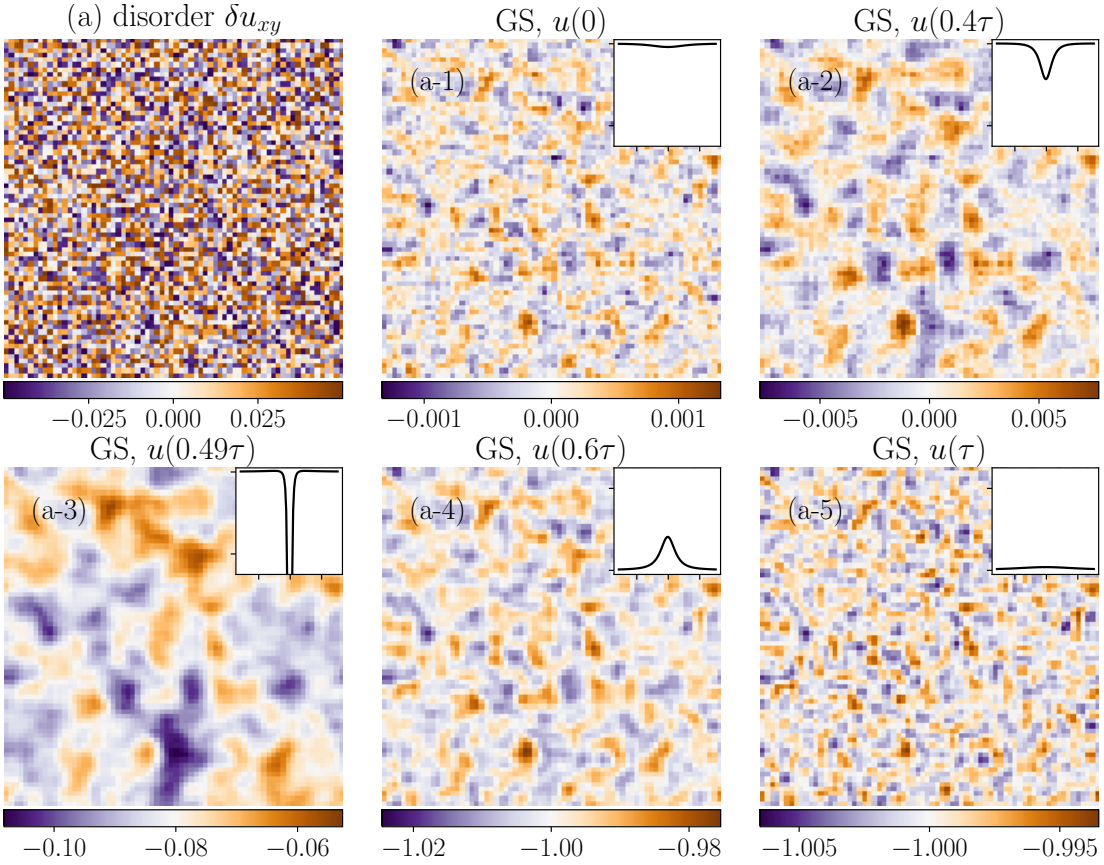

Figure 6.3: (a) Disorder realization and the LCM in the ground state of the Hamiltonian ranging from trivial to topological phase: at (1) $u = -2.5$, (2) $u = -2.15$, (3) $u = -2$, (4) $u = -1.85$, and (5) -1.5. The system size is $N = 70$ and the disorder amplitude is $\delta u_0 = 0.05$. The insets show the Berry curvature of corresponding states of a clean system along the $k_x = 0$ line from $k_y = -\frac{\pi}{4}$ to $k_y = \frac{\pi}{4}$. The range of the vertical axis is from zero to 0.005π in panels (a-4) and (a-5), and from -0.005π to zero in other panels.

LCM deviates above (brown) and below (blue) the clean system value. Figure 6.4 shows that while the amplitude of those deviations is proportional to δu_0, their size does not depend on the disorder strength, when the disorder is weak. The basic point is that, as the critical point is approached, the size of those regions grows. In the topological phase the deviations of the LCM from its clean system value are dominated by a contribution proportional to disorder. In figure 6.3(a-4) and figure 6.3(a-5), the disorder contribution is filtered out. This behaviour is commented in section 6.2.4 and the unfiltered LCM profiles are shown.

We measure the typical size of inhomogeneities ξ by finding the distance where the disorder-averaged autocovariance function of a real-space profile of the LCM drops below zero (see section 6.2.3). Figure 6.5 shows that ξ exhibits a power-law scaling as u approaches the critical point. Increasing the system size, the estimate of the scaling exponent approaches one. This is in agreement with the correlation length of a clean system evaluated from the divergence of the Berry curvature, presented in Section 4.1.3. Analogous results are obtained by measuring the radius of the peak in the LCM profile around a single impurity (see following section 6.2.4).

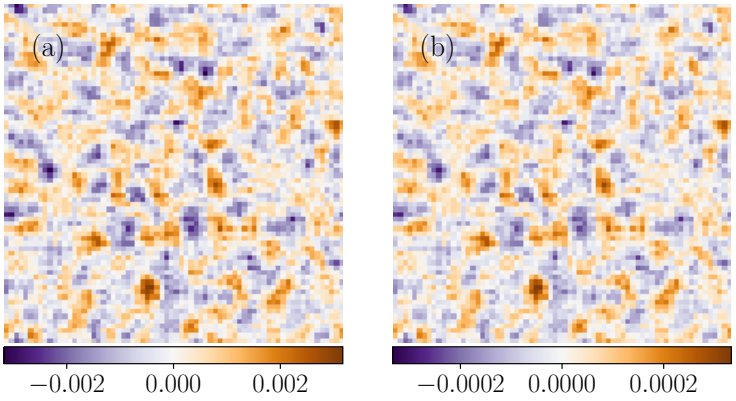

Figure 6.4: Ground-state LCM profiles at $u = -2.3$ with (a) $\delta u_0 = 0.05$ and (b) $\delta u_0 = 0.005$. $N = 70$.

All this confirms that, in the presence of disorder, the criticality of the correlation length in Chern insulators is observable in real space via the LCM.

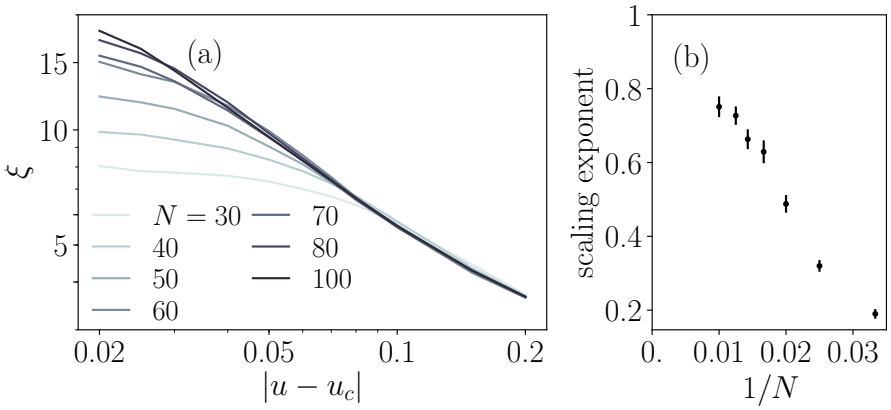

Figure 6.5: (a) ξ in the ground states of the trivial phase, plotted for different N in the log-log scale as a function of $|u - u_c|$. Average is performed over 100 disorder realizations with $\delta u_0 = 0.05$. (b) The scaling exponent, estimated by fitting a power-law to the ξ vs. $|u - u_c|$ data for individual disorder realizations in the interval $0.02 \leq |u - u_c| \leq 0.1$. The means are plotted as a function of $1/N$ and the error bars are standard errors obtained by bootstrap resampling.

6.2.3 Estimation of the size of inhomogeneities

We estimate the size of the inhomogeneities in a real-space profile $A(\mathbf{r})$ from its position autocovariance function

$$R_{AA}(r) = \frac{\sum_{|\mathbf{r}|=r} \sum_{\mathbf{r}'} A(\mathbf{r}')A(\mathbf{r}+\mathbf{r}')}{\sum_{|\mathbf{r}|=r} \sum_{\mathbf{r}'} A(\mathbf{r}')^2}. \tag{6.7}$$

We identify the typical length scale ξ in the LCM as the distance at which the autocovariance function crosses zero, $R_{cc}(\xi) = 0$. The autocovariance functions of

the LCM profiles shown in figure 6.4 are plotted in figure 6.6 as a function of $r|u-u_0|$. Note that rescaling the distance with the inverse of the correlation length collapses the points where autocovariance function crosses zero to the same point.

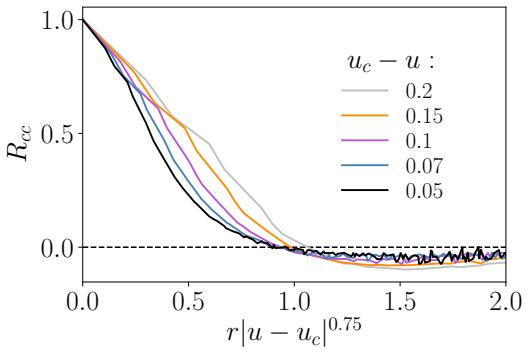

Figure 6.6: Autocovariance functions of the LCM profiles for a system of size $N = 100$ with the disorder amplitude $\delta u_0 = 0.05$ at different values of u.

6.2.4 Local Chern marker around a single impurity

The critical scaling of the LCM in real space is also observed in a simple single-impurity model. The impurity is centred at $\mathbf{r} = 0$ and is of weak strength δu. Here, we explicitly study deviations $\delta c_1(\mathbf{r})$ of the LCM from its clean system value. Figures 6.7(a) and 6.8(a) show typical $\delta c_1(\mathbf{r})$ profiles in the trivial and in the topological phases, respectively. In figures 6.7(b) and 6.8(b), $\delta c_1(\mathbf{r})$ are plotted along the $y = 0$ line for several values of u in the trivial and in the topological phases, respectively. The position is rescaled as $x|u-u_c|^{0.8}$, showing that the radius ξ of the region around the impurity where the LCM deviates below (for $\delta u > 0$) the clean system value scales as a power law. The estimate of the scaling exponent on the trivial side approaches one as the system size is increased, see figure 6.7(c). Note, however, that ξ is not the only scale in present in $\delta c_1(\mathbf{r})$: it has also an internal structure.

A notable feature is that the behaviour of $\delta c_1(\mathbf{r})$ on the topological and on the trivial side are quite different. On the topological side, $|\delta c_1(\mathbf{r})|$ is maximal at the position of the impurity. There it takes a value that is at least five times larger than the value on neighbouring sites, whereas on the trivial side it has a minimum at the position of the impurity and takes a maximum on the neighbouring sites. This distinction has important consequences for the behaviour of the LCM in a disordered system. Namely, for a weak disorder one can write

$$\delta c(\mathbf{r}) \sim \int \mathrm{d}\mathbf{r}' \delta c_1(\mathbf{r} - \mathbf{r}') \delta u(\mathbf{r}'), \tag{6.8}$$

where $\delta c(\mathbf{r})$ is the deviation of the LCM in the disordered system from the clean system value and $\delta u(\mathbf{r})$ the distribution of the disorder. $\delta c_1(\mathbf{r})$ thus plays the role of the integration kernel through which the disorder is averaged. Now, on the topological side, because the largest contribution to $\delta c_1(\mathbf{r})$ is local, one can expect that the $\delta c(\mathbf{r})$ is dominated by a contribution directly proportional to disorder. This is indeed what one observes in figure 6.9.

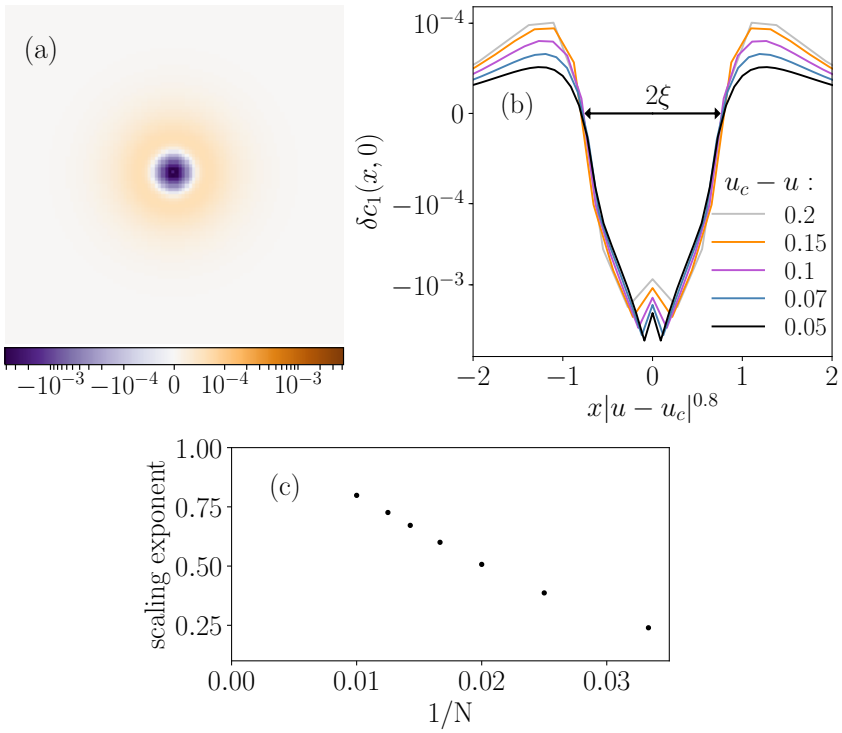

Figure 6.7: (a) $\delta c_1(\mathbf{r})$ around an impurity with strength $\delta u = 0.1$ at $\mathbf{r} = 0$. $N = 100$ and $u = -2.07$. (b) $\delta c_1(\mathbf{r})$ around the same impurity plotted along the $y = 0$ line as a function of $x|u - u_c|^{0.8}$ for various u in the trivial phase. $N = 100$. In both (a) and (b), linear scale is used for $|\delta c_1(\mathbf{r})| < 10^{-4}$ and log scale elsewhere. (c) The scaling exponent, estimated by fitting a power-law to the ξ vs. $|u - u_c|$ data in the interval $0.02 \leq |u - u_c| \leq 0.1$ and plotted as a function of $1/N$.

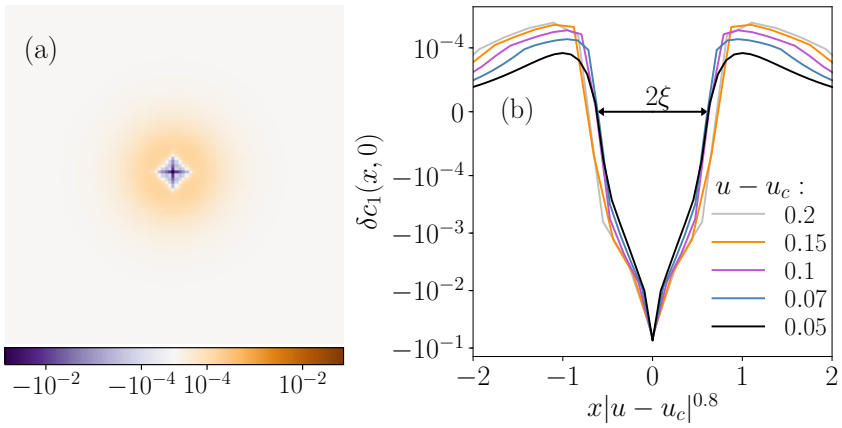

Figure 6.8: (a) $\delta c_1(\mathbf{r})$ around an impurity with strength $\delta u = 0.1$ at $\mathbf{r} = 0$. $N = 100$ and $u = -1.93$. (b) $\delta c_1(\mathbf{r})$ around the same impurity plotted as a function of $x|u - u_c|^{0.8}$ along the $y = 0$ line for various u in the topological phase. $N = 100$. In both (a) and (b), linear scale is used for $|\delta c_1(\mathbf{r})| < 10^{-4}$ and log scale elsewhere.

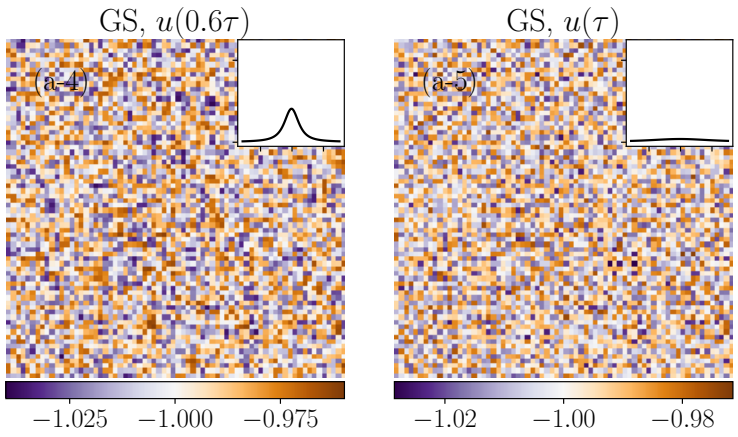

Figure 6.9: Unfiltered LCM profiles corresponding to Figs. 1(a-4) at $u = -1.85$ and 1(a-5) at $u = -1.5$ of figure 6.3.

6.2.5 Local Chern marker in systems with strong disorder

As already mentioned in section 6.1, strong disorder modifies the phase diagram. This is also reflected in the profile of the LCM. The LCM of the ground states for different values of disorder strength δu_0 and values of u ranging across a clean system critical point $u_c = -2$ is shown in figure 6.10. The topological phase is characterized by the presence of disorder in the LCM and by the mean value of the LCM being equal to -1. The topological phase is still present at disorder strength $\delta u_0 = 2$, while it is absent at $\delta u_0 = 5$. The value of the critical point u_c becomes smaller than -2. This is also signalled in the growth of inhomogeneities on increasing the disorder strength δu_0 at a fixed u (see the first column of figure 6.10, $u = -2.5$). These results are consistent with the results from reference [174], where the authors studied the BHZ model with disorder on onsite-energies.

6.3 Non-equilibrium dynamics

Quenches are performed in systems initially in the ground state, i.e., with the valence band filled and the conduction band empty, starting in the trivial regime at $u_0 = -2.5$, smoothly varying the parameter u with time as in equation (4.14), and ending up at $t = \tau$ in the topological regime at $u_1 = -1.5$. Because disorder breaks the translation symmetry, the band description in momentum space is lost and the dynamics cannot be modelled by a 2×2 Hamiltonian which reduces for slow quenches to the Landau-Zener model as in section 4.1.4. Each initially occupied state $|\Psi_n\rangle$ evolves under a $2N^2 \times 2N^2$ Hamiltonian as

$$|\Phi_n(t)\rangle = \overrightarrow{\mathcal{T}} e^{-i\int_0^t \hat{H}(t')dt'} |\Psi_n\rangle. \tag{6.9}$$

The projector onto the valence band, used for the calculation of the LCM, is then replaced by the projector onto the occupied subspace

$$\hat{P}(t) = \sum_{n\in v} |\Phi_n(t)\rangle\langle\Phi_n(t)|. \tag{6.10}$$

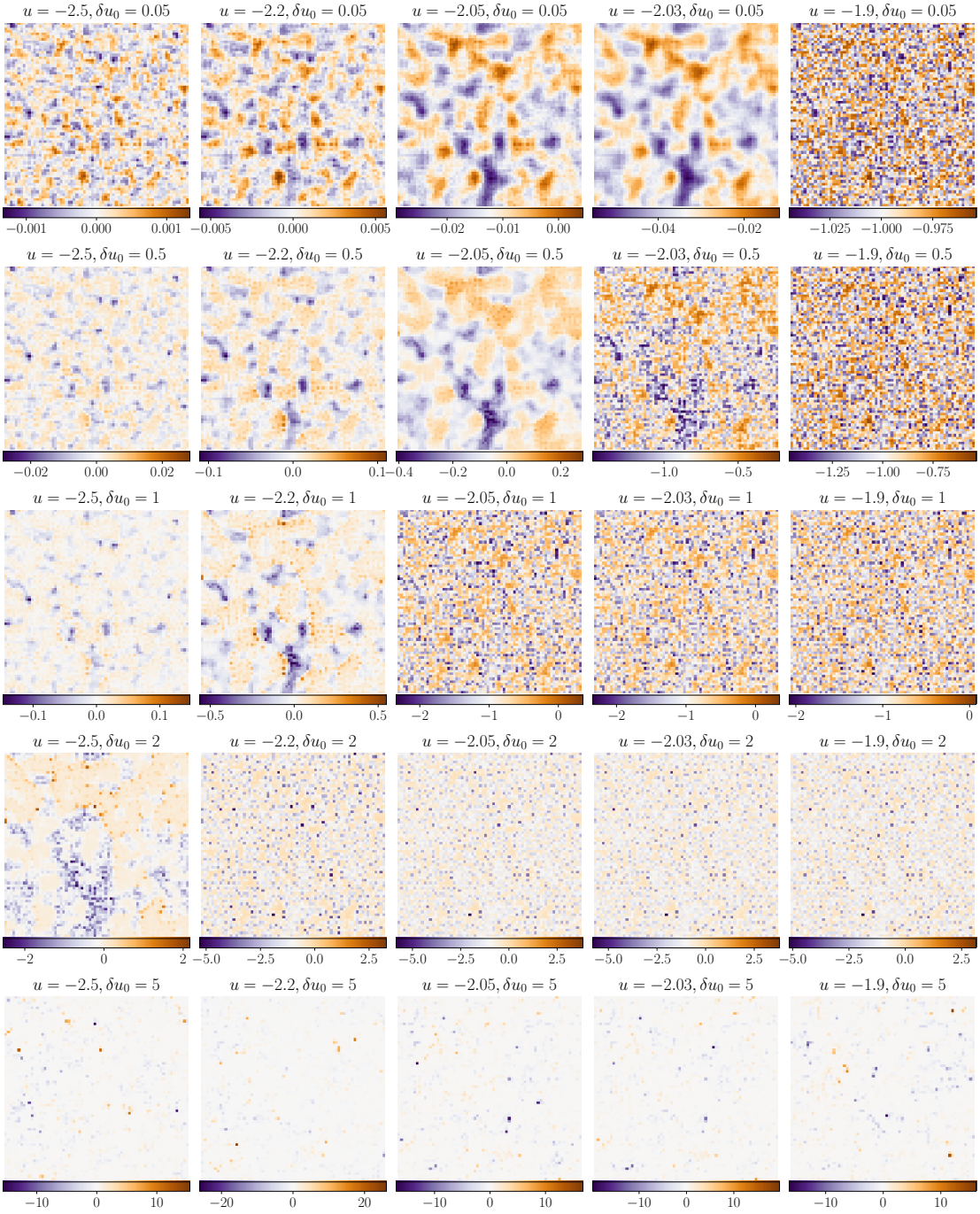

Figure 6.10: LCM in the ground states corresponding to values of u ranging across $u_c = -2$ at different disorder strengths δu_0. System size is $N = 70$ and disorder realization is the same as in figure 6.3.

Because the disorder is weak, these eigenstates maintain a definite value of the momentum magnitude $k = |\mathbf{k}|$ up to a good approximation. The post-quench probability of an excitation in an energy eigenstate is therefore given by the Landau-Zener formula

$$n_{\mathrm{exc}}(k) = e^{-2k^2\tau/|u_1-u_0|}, \tag{6.11}$$

where k can be calculated from the eigenenergy by using the dispersion relation for a clean system. Excitation density as a function of $k\sqrt{\tau}$ is shown in figure 6.11 for one disorder realization for multiple quench times and exhibits the scaling with τ derived from clean systems.

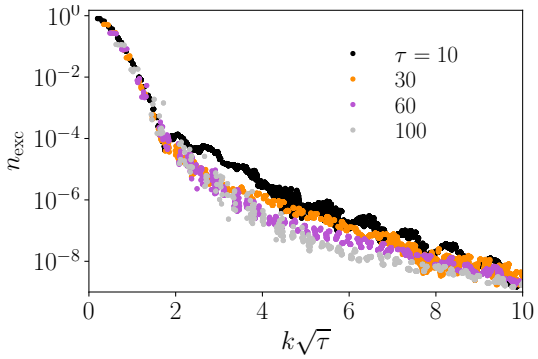

Figure 6.11: Number of excitations as a function of momentum magnitude k for several quenches with different quench times. The momentum is rescaled by $\sqrt{\tau}$, which collapses the curves on a universal curve for small momenta. System size is $N = 60$ and disorder amplitude $\delta u_0 = 0.05$.

6.3.1 Non-equilibrium local Chern marker

The Kibble-Zurek length scale observed in a clean system 4.1.6 manifests itself in a disordered system as the size of inhomogeneities in the post-quench LCM profile. The evolution of the LCM profile during the quench with $\tau = 20$ is shown in figure 6.12(a). Due to the conservation of the Chern number (see section 4.1.7), the average value of the LCM is zero throughout the quench. Let us now focus on deviations from this value. Prior to entering the freeze-out zone (figures 6.12(a-1) and (a-2)), the system evolves adiabatically and the LCM profiles match the ground-state ones, shown in figures 6.3(a-1) and (a-2). The growth of ξ in the freeze-out zone, although present (figures 6.12(a-2),(a-3) and (a-4)), lags behind that in instantaneous ground states. After the exit from the freeze-out zone (figures 6.12(a-4) and (a-5)), the profiles do not significantly change anymore. The amplitude of the deviations of the LCM, however, grows strongly throughout the quench. In figure 6.12(b) ξ during quenches with different τ and in the corresponding ground states are shown with coloured and black dots, respectively. They are seen to follow the behaviour of the correlation length extracted from the Berry curvature (coloured and black lines).

The post-quench inhomogeneities are larger for quenches performed more slowly as shown in figure 6.13. Their size exhibits a power-law scaling with quench time as shown in figure 6.14(a). The scaling exponent (figure 6.14(b)) lies somewhere

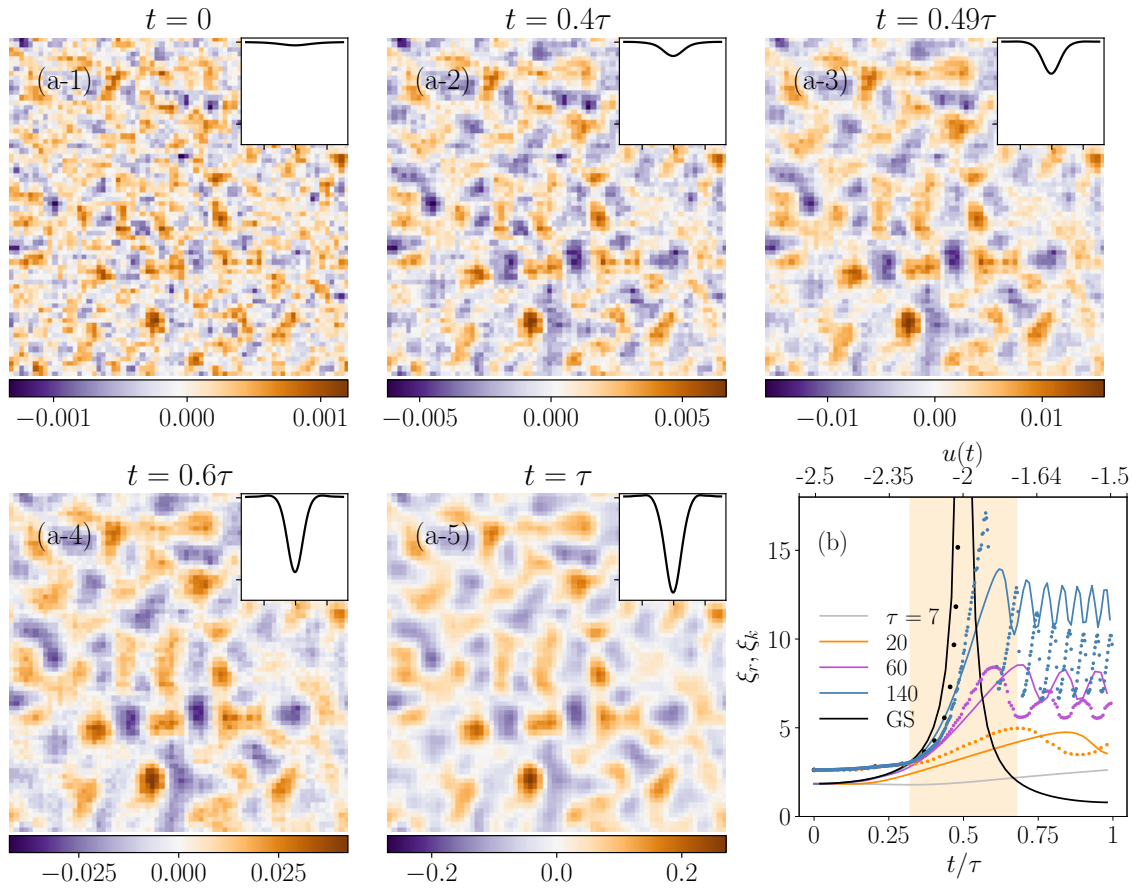

Figure 6.12: (a) LCM in a system during the $\tau = 20$ quench (1) at the initial time, (2) at the entry to the freeze-out, (3) at the critical point, (4) at the exit from the freeze-out, and (5) at the end of the quench. The system size is $N = 70$ and the disorder amplitude is $\delta u_0 = 0.05$. The insets show the Berry curvature of corresponding states of a clean system along the $k_x = 0$ line from $k_y = -\frac{\pi}{4}$ to $k_y = \frac{\pi}{4}$. The range of the vertical axis is from zero to 0.005π in panels (a-4) and (a-5), and from -0.005π to zero in other panels. (b) Full lines show ξ extracted from the Berry curvature during quenches with various τ (coloured) and of instantaneous ground states (black). Coloured and black dots show ξ of the LCM during quenches and in instantaneous ground states ($N = 100$), respectively. The shaded region is the freeze-out zone for the $\tau = 20$ quench.

between 0.4 and 0.5 for the largest system considered here, depending on the chosen fitting range. In the absence of disorder much larger systems can be considered and the scaling exponent obtained from the ξ, extracted from the Berry curvature, (orange dots) is close to 1/2 (0.497 for $N = 6400$). ξ in figure 6.14 saturates at a certain τ. This is a finite-size effect, it happens when the correlation length at the freeze-out time is larger than the system size. The value of τ where this happens increases with the system size N.

The scaling of ξ can be explained by the Landau-Zener dynamics, taking additionally into account the effect of disorder on eigenstates of the post-quench Hamiltonian. Because the disorder is weak, the probability for an excitation is given by the Landau-Zener formula, which provides a rough estimate for the highest mo-

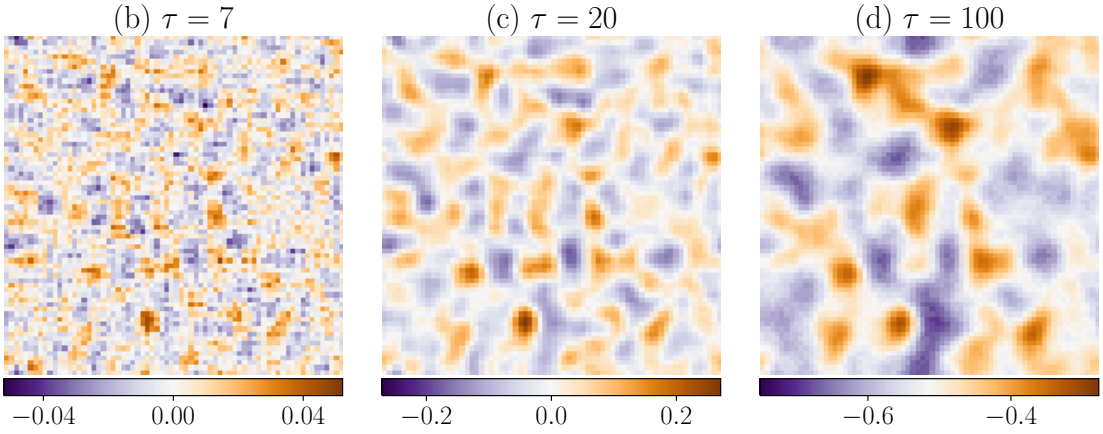

Figure 6.13: LCM after quenches with (a) $\tau = 7$, (b) $\tau = 20$ and (c) $\tau = 100$. The disorder realization is the same as in figure 6.3, $\delta u_0 = 0.05$ and $N = 70$.

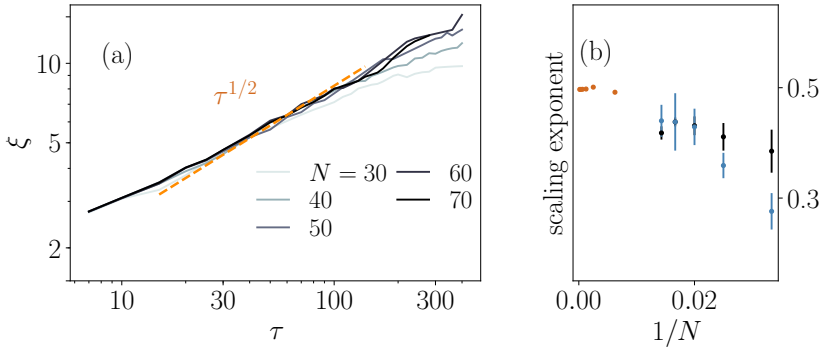

Figure 6.14: (a) Time-averaged ξ after the end of a quench of the LCM as a function of τ for different N, plotted in the log-log scale. Average is performed over 20 disorder realizations with $\delta u_0 = 0.05$. The orange dashed line represents the $\tau^{1/2}$ scaling. (b) The corresponding scaling exponents, estimated as in figure 6.5 using the ξ vs. τ data in intervals $15 \leq \tau \leq 140$ (black) and $30 \leq \tau \leq 300$ (blue). Orange dots are exponents extracted from the ξ vs. τ data after the end of a quench in the clean system, where ξ is calculated from the Berry curvature.

mentum where excitations are present, $k_{\max} = (\frac{|u_1 - u_0|}{2\tau})^{1/2}$. In the presence of weak disorder, the eigenstates preserve the length scale $\frac{2\pi}{|\mathbf{k}|}$, as shown in figure 6.2. The post-quench projector to the occupied subspace $\hat{P}(\tau)$ is expected to contain within itself the finest of those length scales present, $\frac{2\pi}{k_{\max}} \propto \tau^{1/2}$. $\hat{P}(\tau)$ is an ingredient of for LCM, which consequently after quench exhibit the $\tau^{1/2}$ scaling of ξ.

6.3.2 Real-space distribution of excitations

Here we define the real space distribution of excitations to the conduction band. We follow the derivation of the local Chern marker from the reference [79]. Let us first consider a clean system. Let $|\Psi_\alpha(\mathbf{k}, t)\rangle = |\mathbf{k}\rangle \otimes |\psi_\alpha(\mathbf{k}, t)\rangle$ be the instantaneous eigenstates, i.e., the eigenstates of the Hamiltonian $\hat{H}(t)$, and $|\Phi_\alpha(\mathbf{k}, t)\rangle = |\mathbf{k}\rangle \otimes |\varphi_\alpha(\mathbf{k}, t)\rangle$ the states obtained by time-evolving the pre-quench eigenstates $|\Psi_\alpha(\mathbf{k}, 0)\rangle$

to time t. Here $|\mathbf{k}\rangle = \frac{1}{N^2}\sum_{\mathbf{r}} e^{i\mathbf{k}\cdot\mathbf{r}}|\mathbf{r}\rangle$ and $\alpha = v$ and $\alpha = c$ denote the valence and the conduction bands, respectively. The total number of excitations is

$$\begin{aligned} N_{\mathrm{exc}}(t) &= \sum_{\mathbf{k}} |\langle \Psi_c(\mathbf{k},t)|\Phi_v(\mathbf{k},t)\rangle|^2 = \\ &= \sum_{\mathbf{k},\mathbf{k}'} \langle \Psi_c(\mathbf{k},t)|\Phi_v(\mathbf{k}',t)\rangle\langle \Phi_v(\mathbf{k}',t)|\Psi_c(\mathbf{k},t)\rangle, \end{aligned} \tag{6.12}$$

where the second line owes to the orthogonality of the plane waves. Recognizing $\hat{P}(t) = \sum_{\mathbf{k}} |\Phi_v(\mathbf{k},t)\rangle\langle\Phi_v(\mathbf{k},t)|$ as the projector onto the occupied subspace and $\hat{P}_{\mathrm{c}}(t) = \sum_{\mathbf{k}} |\Psi_c(\mathbf{k},t)\rangle\langle\Psi_c(\mathbf{k},t)|$ as the projector onto the instantaneous conduction band, equation (6.12) may be written as a trace over the whole Hilbert space:

$$N_{\mathrm{exc}}(t) = \mathrm{Tr}\{\hat{P}(t)\hat{P}_{\mathrm{c}}(t)\}. \tag{6.13}$$

When calculating the trace in the real-space basis, $N_{\mathrm{exc}}(t) = \sum_{\mathbf{r},\sigma}\langle \mathbf{r},\sigma|\hat{P}(t)\hat{P}_{\mathrm{c}}(t)|\mathbf{r},\sigma\rangle$, one may define the real-space distribution of excitations as

$$n_{\mathrm{exc}}(\mathbf{r},t) = \sum_{\sigma}\langle \mathbf{r},\sigma|\hat{P}(t)\hat{P}_{\mathrm{c}}(t)|\mathbf{r},\sigma\rangle. \tag{6.14}$$

This expression can also be evaluated in a disordered system using equation (6.10) for projector onto the occupied subspace and

$$P_{\mathrm{c}}(t) = \sum_{n\in c} |\Psi_n(t)\rangle\langle\Psi_n(t)| \tag{6.15}$$

for the projector onto the instantaneous conduction band, spanned by eigenstates $|\Psi_n(t)\rangle$.

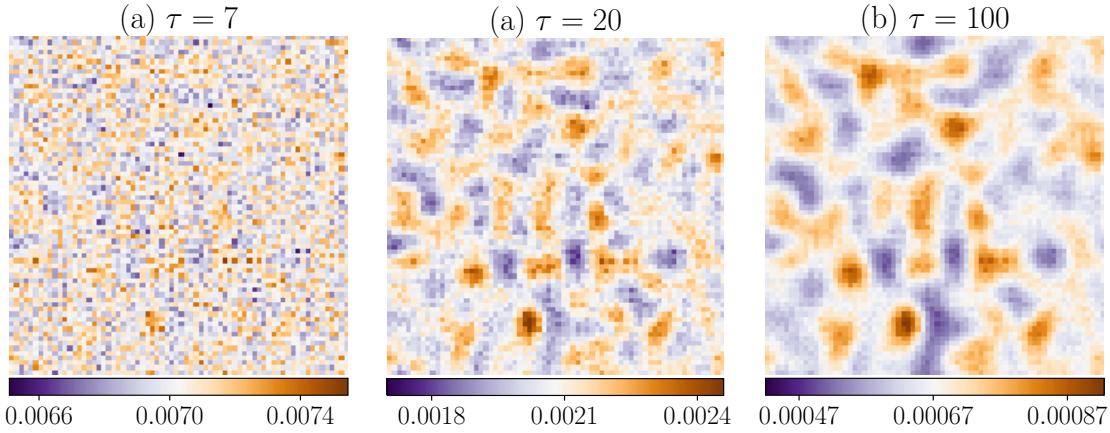

Figure 6.15: Spatial distribution of excitations after quenches with (a) $\tau = 7$, (b) $\tau = 20$ and (c) $\tau = 100$. The disorder realization is the same as in figure 6.3, $\delta u_0 = 0.05$ and $N = 70$.

Interestingly, the real space profile of excitations also exhibits the inhomogeneities that are present in the LCM. In figure 6.15 some post-quench profiles of excitations are shown. Comparing them to the post-quench profiles of LCM one notices that while the average value and the amplitude of deviations from it are different, the

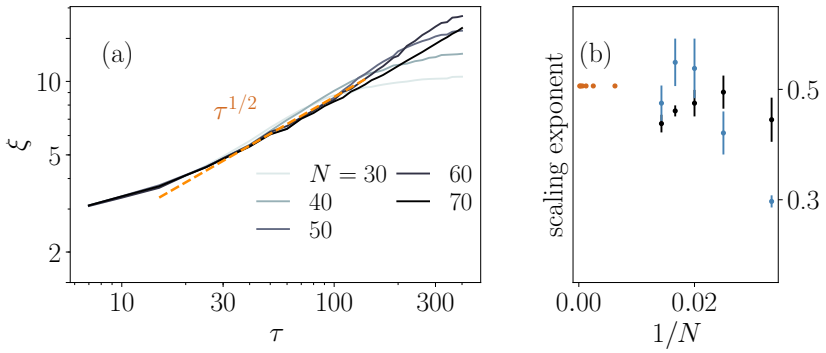

Figure 6.16: (a) Time-averaged ξ after the end of a quench of the real-space density of excitations as a function of τ for different N, plotted in the log-log scale. Average is performed over 20 disorder realizations with $\delta u_0 = 0.05$. The orange dashed line represents the 1/2 scaling. (b) The corresponding scaling exponents, as in figure 6.5 using the ξ vs. τ data in intervals $15 \leq \tau \leq 140$ (black) and $30 \leq \tau \leq 300$ (blue). Orange dots are exponents extracted from the $n_{\text{exc}}^{-1/2}$ vs. τ data after the end of a quench in the clean system.

structure appears visually the same. The average value is very well reproduced by the result for clean systems (4.20) given by the Landau-Zener formula. The fluctuations from the average value are way smaller than in the LCM. The analysis of the size of inhomogeneities is shown in figure 6.16. The size of the inhomogeneities scales as a power-law with τ, with the power close to 1/2 as predicted by the Kibble-Zurek mechanism.

The emergence of the length scale in the real space profile of excitations cannot be explained by the Kibble-Zurek mechanism or freeze-out regime as for example the case of LCM is. Unlike in LCM, there are no excitations in the ground state near the critical point, therefore the profile cannot be associated to the one in the ground state at the freeze-out time. However, it can be explained with the same argument as for LCM, which states that the projector $\hat{P}(\tau)$ contains within itself the smallest length scale of the highest occupied state (see section 6.3.1).

6.3.3 Real-space distribution of the orbital polarization

Orbital polarization is a quantity already measured in experiments of the QWZ model after the quench [134]. It is defined as the difference between the occupation of the orbital A and the occupation of the orbital B:

$$p(\mathbf{r}, t) = \sum_{n \in v} |\langle \mathbf{r}, A | \Phi_n(t) \rangle|^2 - |\langle \mathbf{r}, B | \Phi_n(t) \rangle|^2 = \sum_{\sigma} \langle \mathbf{r}, \sigma | \hat{P}(t) \hat{\sigma}_z | \mathbf{r}, \sigma \rangle. \tag{6.16}$$

While the orbital polarization does not exhibit any critical length scale in the ground state, the Kibble-Zurek length scale emerges after the quench. Some post-quench profiles of the deviation of the orbital polarization from the ground state one are shown in figure 6.17. The profiles are highly correlated to the profiles of the excitations and the LCM corresponding to the same disorder realization and quench time. As in the case of excitations, the fluctuations of polarization from the average one are small compared to the ones observed in LCM. As shown in figure 6.18, the

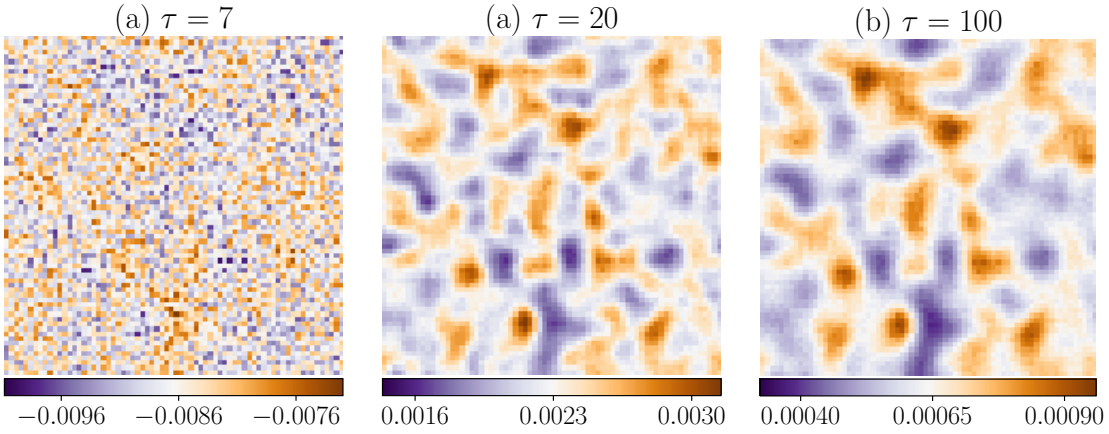

Figure 6.17: Deviation of the post-quench orbital polarization from the ground-state one for quenches with (a) $\tau = 7$, (b) $\tau = 20$ and (c) $\tau = 100$. The disorder realization is the same as in figure 6.3, $\delta u_0 = 0.05$ and $N = 70$.

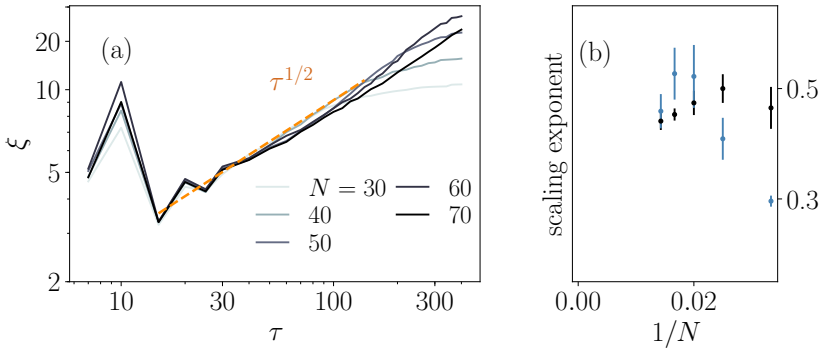

Figure 6.18: (a) Time-averaged ξ after the end of a quench of the orbital polarization as a function of τ for different N, plotted in the log-log scale. Average is performed over 20 disorder realizations with $\delta u_0 = 0.05$. The orange dashed line represents the 1/2 scaling. (b) The corresponding scaling exponents, as in figure 6.5 using the ξ vs. τ data in intervals $15 \leq \tau \leq 140$ (black) and $30 \leq \tau \leq 300$ (blue).

size of inhomogeneities scales as a power law with quench time τ with the power exponent close to the Kibble-Zurek predictions.

6.3.4 Quench between topologically non-trivial phases

Quenches across a phase transition between two non-trivial phases lead to the same behaviour both in clean systems as well as in weakly disordered systems. We investigated a quench starting at $u_0 = -0.5$ and ending at $u_1 = 0.5$. The critical point at $u_c = 0$ separates the phases with $C = -1$ $(-2 < u < 0)$ and $C = 1$ $(0 < u < 2)$. The energy dispersion forms two Dirac cones at $u_c = 0$, centred at $\mathbf{k}_c = (0, \pi)$ and $\mathbf{k}_c = (\pi, 0)$. The presence of two Dirac points does not modify the critical behaviour and the results are thus equivalent to the ones discussed in the main text. The Berry curvature develops peaks about momenta where the energy gap closes. Its value along $k_x = 0$, rescaled with $\tau^{1/2}$, is shown in figure 6.19(a). At the end of the

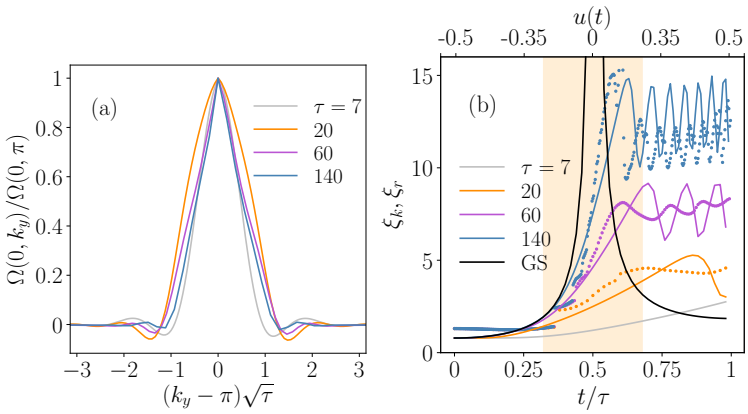

Figure 6.19: (a) Berry curvature along the $k_x = 0$ line at the end of a quench for various τ, plotted as a function of scaled momentum $(k_y - \pi)\sqrt{\tau}$. (b) Full lines show ξ extracted from the Berry curvature during quenches with various τ (coloured) of instantaneous ground states (black). Coloured dots show ξ of the LCM of a disordered system with $\delta u_0 = 0.05$ during quenches ($N = 70$). The shaded region is the freeze-out zone for the $\tau = 20$ quench.

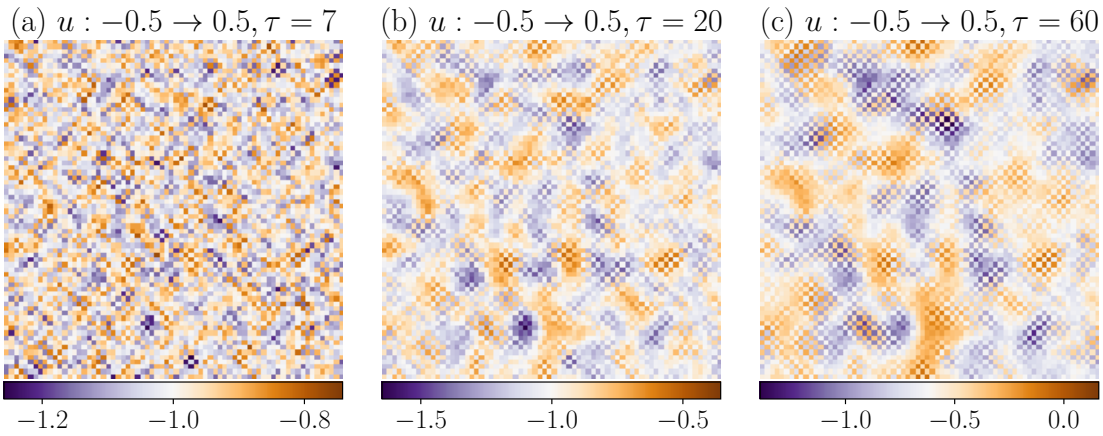

Figure 6.20: Post-quench LCM profiles for quenches starting at $u_0 = -0.5$ and ending at $u_1 = 0.5$ with (a) $\tau = 7$, (b) $\tau = 20$ and (c) $\tau = 60$. The disorder realization is shown in figure 6.3(a), $N = 70$ and $\delta u_0 = 0.05$.

quench, the width of the peak scales as $\tau^{-1/2}$ and thus $\xi \propto \tau^{1/2}$. The time evolution of ξ, extracted from the Berry curvature as well as from the size of inhomogeneities in disordered systems, during the quench is the same as in the case of transitions from trivial to topological phase. These results are presented in figure 6.19(b).

Figure 6.20 shows the LCM profiles after quenches for various quench times. The LCM exhibits inhomogeneities, which become larger for longer quenches. They are modulated by a checkerboard pattern, the emergence of which can be connected to the presence of two Dirac points at $\mathbf{k} = (0, \pi)$ and $\mathbf{k} = (\pi, 0)$ which introduces the corresponding modulation wavevector in the results for weakly disordered system where the translational symmetry is slightly broken.

6.4 Conclusions

In this chapter the equilibrium and the dynamical critical properties in a Chern insulator were investigated in real space. In order to reveal the critical properties in real space, a weak disorder was introduced that broke the translation invariance. The disorder was kept weak such that the Anderson localization length was larger than the system size. Such a weak disorder does not change the topological phase diagram and the energy eigenstates maintain a definite momentum, which is assigned to them through the energy dispersion of a clean system.

The critical length scale, observed in the Berry curvature, arises in a real space structure of the LCM. This novel result was unexpected since topological insulators lack a Landau order parameter. The LCM is the real space analogue of the Berry curvature and physically it is connected to the Hall conductivity in inhomogeneous systems. Near a critical point, its profile is inhomogeneous, consisting of regions where it deviates above and below the average value that is equal to the Chern number. The size of these regions grows on approaching the critical point, diverging by the power that grows towards 1 as the system size is increased. This matches the predictions from momentum space. The same results were obtained for a simpler model with disorder on a single impurity.

After a quench the LCM exhibits inhomogeneities of a length scale that depends on the quench time as $\tau^{1/2}$, matching the predictions of the Kibble-Zurek mechanism and the result obtained from momentum space calculations of the non-equilibrium Berry curvature. We followed the growth of the inhomogeneities during the quench and demonstrated that the Kibble-Zurek freeze-out mechanism applies. Through the lens of the LCM the critical behaviour of weakly disordered Chern insulators is analogous to the one found in systems with spontaneously broken symmetries. The important difference is that the amplitude of the inhomogeneities vanishes with the vanishing disorder strength. The Kibble-Zurek length scale arises also in the real space profiles of the excitations of the orbital polarization. At the end of the quench, their profiles are highly correlated to the profile of LCM. Contrary to the LCM, these two quantities do not exhibit a critical length scale in the ground state, therefore the Kibble-Zurek freeze-out scheme does not apply to them.

The Kibble-Zurek scaling with τ can be experimentally tested by looking at the orbital polarization. Measurements of the polarization of the QWZ model, realized in an ultracold ^{87}Rb atom gas, were performed experimentally by Sun et al. in reference [134]. After a quantum quench, the dipole trap and the lasers of the 2D lattice are switched off and the atoms are let free to expand in a Stern-Gerlach gradient magnetic field, which separated the spin-up and spin-down states. The time-of-flight image resolves the polarization and momentum distribution of the atom gas. An original space distribution of polarization could be obtained by a Fourier transform of the time-of-flight image.

Alternatively, the Kibble-Zurek length scale could be measured in the real space profile of the charge density. While in the QWZ model this quantity is equal to 1 after a quench on every site due to the particle-hole symmetry, breaking the symmetry is expected to result in inhomogeneous profiles of the charge density with the Kibble-Zurek length scale arising after the quench. A prominent example of such a system is the Haldane model.

Chapter 7

Conclusions

The thesis discussed the non-equilibrium properties of topological insulators that were driven in time across a topological phase transition. We investigated two different translation invariant topological systems, a two-dimensional Chern insulator, represented by the Qi-Wu-Zhang (QWZ) model, and a two-dimensional time-reversal symmetric topological insulator, represented by the Bernevig-Hughes-Zhang (BHZ) model. Another line of investigation considered the validity of the bulk-boundary correspondence out of equilibrium by studying systems in ribbon geometry. Lastly, we studied weakly disordered Chern insulators, where a weak disorder was used to reveal the dynamical critical properties in real space. The motivation for this stems from phase transitions with spontaneous symmetry breaking, where after a quench topological defects may arise in the profile of the local order parameter.

We find that the (spin) Hall conductivity approaches the ground-state one after a slow quench while the topological invariant does not follow the change it experiences in the ground state. In particular, the unitary time evolution conserves the Chern number and breaks the time-reversal symmetry and consequently the $\mathbb{Z}_2$ invariant is not well defined. Similarly, the bulk-boundary correspondence is broken since after a quench of a Chern insulator from a trivial to a topological regime, the in-gap edge states appear and are populated with electrons, opposing the unchanged Chern number. These results show that some of the main ground-state characteristics of topological insulators break down. We also characterized the deviations of the transport coefficients from the final ground-state ones and showed that they are proportional to the density of excitations. Those scale as a power-law function of the quench time and match the predictions of the Kibble-Zurek mechanism.

The critical point between two different topological phases is characterized by the energy gap closing and thus by the divergence of the typical time scale, which exhibits a universal power-law behaviour with an exponent equal to $z\nu = 1$ for the considered models. The vicinity of the critical point is also accompanied by a power-law divergence of the correlation length. The divergence of the length scale can be observed from the curvature function, which on approaching the critical point reveals a diverging critical length scale. The QWZ model was found to have $\nu = 1$ and the BHZ model $\nu = 1$, if the spin projection is conserved, and $\nu = 1/2$ otherwise. For such critical exponents the Kibble-Zurek scaling of zero-dimensional defects matches the observed scaling of the density of excitations. The Kibble-Zurek mechanism connects the defect density with the non-equilibrium length scale that appears in a system. By following the time evolution of the Berry curvature

we showed that in Chern insulators the correlation length fits the freeze-out behaviour: at the beginning of the quench the correlation length follows the ground state one, while upon entering the freeze-out regime it starts to deviate from it. On the exit from the freeze-out regime it oscillates about a constant value that follows the Kibble-Zurek predictions.

The study of a Chern insulator in ribbon geometry showed that the density of bulk excitations scales as τ^{-1} and of excitations in the in-gap states as $\tau^{-1/2}$. Different exponents are a consequence of different dimensionality of the systems, the bulk being two-dimensional and the in-gap states one-dimensional, and are consistent with the Kibble-Zurek predictions. We also examined the Hall conductance by inducing an electric potential between the ribbon edges. Interestingly, similarly to the bulk-only systems, the deviation of the post-quench Hall conductance from the ground state one follows the scaling of the bulk excitations. The studied QWZ model possesses the inversion symmetry, which pins the in-gap band crossing to an inversion symmetric momentum. By breaking the inversion symmetry, we demonstrated that the in-gap band crossing can travel during the quench through a range of momenta, which results in a perfect population of the corresponding in-gap states. This breaks the Kibble-Zurek scaling of the in-gap states and allows for selective population of the in-gap bands, which may produce electrical current along a single edge even in the absence of an electric field.

Provided that a weak disorder is introduced to break the translational symmetry, the quench induced correlation length emerges in the real space distributions of the local Chern marker, the excitations and the orbital polarization. The local Chern marker profiles reveal regions with size that grows as the critical point is approached. The associated length scale can be evaluated also during the quench and grows consistently with the correlation length extracted from the time-evolved Berry curvature. The critical behaviour of topological insulators is thus analogous to the one found in systems with spontaneously broken symmetries.

The results of the thesis set basis for further theoretical as well as experimental research. The studied models have both been realized in experiments, the QWZ model in ultracold atoms [19, 21] and the BHZ model in semiconductor heterostructure quantum wells [11]. The Hall conductance of systems in ribbon geometry is a measurable quantity. Given that the deviation of the post-quench Hall conductance from the ground-state one in Chern ribbons is proportional to the density of excitations of the bulk-only systems, the Kibble-Zurek scaling of the density of excitations could be verified in experiment by measuring the Hall conductance. The Kibble-Zurek scaling of the post-quench length scale could be measured from the size of inhomogeneities that arise in the local Chern marker [80] or in more directly measurable quantities, such as the post-quench orbital polarization [134] and, in the case of broken particle-hole symmetry as for example in the Haldane model [20], the charge density. From the theoretical aspect, it would be interesting to investigate how interacting topological systems behave during quenches. Especially of interest would be to explore the interplay between spontaneous symmetry breaking and topological phases [179, 180] in the light of Kibble-Zurek mechanism and relate them to results obtained for the non-interacting system in this thesis. It would also be interesting to find a way to extract the non-equilibrium length scale in topological insulators with time-reversal symmetry and chiral symmetric topological chains. The classification of the topological phase in these systems breaks down after a quench and with it

the basis for the calculation of the associated length scale from the corresponding curvature function.

Bibliography

[1] S. D. Sarma, M. Freedman and C. Nayak, *Majorana zero modes and topological quantum computation*, npj Quantum Information **1**, 15001 (2015).

[2] A. R. Mellnik, J. S. Lee, A. Richardella, J. L. Grab, P. J. Mintun, M. H. Fischer, A. Vaezi, A. Manchon, E.-A. Kim, N. Samarth and D. C. Ralph, *Spin-transfer torque generated by a topological insulator*, Nature **511**, 449 (2014).

[3] Y. Fan, P. Upadhyaya, X. Kou, M. Lang, S. Takei, Z. Wang, J. Tang, L. He, L.-T. Chang, M. Montazeri, G. Yu, W. Jiang, T. Nie, R. N. Schwartz, Y. Tserkovnyak and K. L. Wang, *Magnetization switching through giant spin–orbit torque in a magnetically doped topological insulator heterostructure*, Nature Materials **13**, 699 (2014).

[4] N. Xu, Y. Xu and J. Zhu, *Topological insulators for thermoelectrics*, npj Quantum Materials **2**, 51 (2017).

[5] G. Gupta, M. B. A. Jalil and G. Liang, *Evaluation of mobility in thin Bi_2Se_3 topological insulator for prospects of Local electrical interconnects*, Scientific Reports **4**, 6838 (2014).

[6] W. Tian, W. Yu, J. Shi and Y. Wang, *The property, preparation and application of topological insulators: A review*, Materials **10**, 814 (2017).

[7] K. v. Klitzing, G. Dorda and M. Pepper, *New method for high-accuracy determination of the fine-structure constant based on quantized Hall resistance*, Phys. Rev. Lett. **45**, 494 (1980).

[8] F. D. M. Haldane, *Model for a quantum Hall effect without Landau levels: Condensed-matter realization of the 'parity anomaly'*, Phys. Rev. Lett. **61**, 2015 (1988).

[9] C. L. Kane and E. J. Mele, *Quantum spin Hall effect in graphene*, Phys. Rev. Lett. **95**, 226801 (2005).

[10] C. L. Kane and E. J. Mele, *Z_2 topological order and the quantum spin Hall effect*, Phys. Rev. Lett. **95**, 146802 (2005).

[11] B. A. Bernevig, T. L. Hughes and S.-C. Zhang, *Quantum spin Hall effect and topological phase transition in HgTe quantum wells*, Science **314**, 1757 (2006).

[12] M. König, S. Wiedmann, C. Brüne, A. Roth, H. Buhmann, L. W. Molenkamp, X.-L. Qi and S.-C. Zhang, *Quantum spin Hall insulator state in HgTe quantum wells*, Science **318**, 766 (2007).

[13] L. Fu and C. L. Kane, *Topological insulators with inversion symmetry*, Phys. Rev. B **76**, 045302 (2007).

[14] A. P. Schnyder, S. Ryu, A. Furusaki and A. W. W. Ludwig, *Classification of topological insulators and superconductors in three spatial dimensions*, Phys. Rev. B **78**, 195125 (2008).

[15] A. Kitaev, *Periodic table for topological insulators and superconductors*, AIP Conference Proceedings **1134**, 22 (2009).

[16] X.-L. Qi, T. L. Hughes, S. Raghu and S.-C. Zhang, *Time-reversal-invariant topological superconductors and superfluids in two and three dimensions*, Phys. Rev. Lett. **102**, 187001 (2009).

[17] I. Knez, R.-R. Du and G. Sullivan, *Evidence for helical edge modes in inverted InAs/GaSb quantum wells*, Phys. Rev. Lett. **107**, 136603 (2011).

[18] M. Aidelsburger, M. Atala, M. Lohse, J. T. Barreiro, B. Paredes and I. Bloch, *Realization of the Hofstadter Hamiltonian with ultracold atoms in optical lattices*, Phys. Rev. Lett. **111**, 185301 (2013).

[19] X.-J. Liu, K. T. Law and T. K. Ng, *Realization of 2D spin-orbit interaction and exotic topological orders in cold atoms*, Phys. Rev. Lett. **112**, 086401 (2014).

[20] G. Jotzu, M. Messer, R. Desbuquois, M. Lebrat, T. Uehlinger, D. Greif and T. Esslinger, *Experimental realization of the topological Haldane model with ultracold fermions*, Nature **515**, 237 (2014).

[21] Z. Wu, L. Zhang, W. Sun, X.-T. Xu, B.-Z. Wang, S.-C. Ji, Y. Deng, S. Chen, X.-J. Liu and J.-W. Pan, *Realization of two-dimensional spin-orbit coupling for Bose-Einstein condensates*, Science **354**, 83 (2016).

[22] J. Balakrishnan, G. K. W. Koon, A. Avsar, Y. Ho, J. H. Lee, M. Jaiswal, S.-J. Baeck, J.-H. Ahn, A. Ferreira, M. A. Cazalilla, A. H. C. Neto and B. Özyilmaz, *Giant spin Hall effect in graphene grown by chemical vapour deposition*, Nature Communications **5**, 4748 (2014).

[23] F. Reis, G. Li, L. Dudy, M. Bauernfeind, S. Glass, W. Hanke, R. Thomale, J. Schäfer and R. Claessen, *Bismuthene on a SiC substrate: A candidate for a high-temperature quantum spin Hall material*, Science **357**, 287 (2017).

[24] C. K. Safeer, J. Ingla-Aynés, F. Herling, J. H. Garcia, M. Vila, N. Ontoso, M. R. Calvo, S. Roche, L. E. Hueso and F. Casanova, *Room-temperature spin Hall effect in graphene/MoS_2 van der Waals heterostructures*, Nano Letters **19**, 1074 (2019).

[25] Z. Tajkov, D. Visontai, L. Oroszlány and J. Koltai, *Uniaxial strain induced topological phase transition in bismuth–tellurohalide–graphene heterostructures*, Nanoscale **11**, 12704 (2019).

[26] A. A. Taskin and Y. Ando, *Quantum oscillations in a topological insulator $Bi_{1-x}Sb_x$*, Phys. Rev. B **80**, 085303 (2009).

[27] Y. Xia, D. Qian, D. Hsieh, L. Wray, A. Pal, H. Lin, A. Bansil, D. Grauer, Y. S. Hor, R. J. Cava and M. Z. Hasan, *Observation of a large-gap topological-insulator class with a single Dirac cone on the surface*, Nature Physics **5**, 398 (2009).

[28] D. Hsieh, Y. Xia, D. Qian, L. Wray, F. Meier, J. H. Dil, J. Osterwalder, L. Patthey, A. V. Fedorov, H. Lin, A. Bansil, D. Grauer, Y. S. Hor, R. J. Cava and M. Z. Hasan, *Observation of time-reversal-protected single-Dirac-cone topological-insulator states in Bi_2Te_3 and Sb_2Te_3*, Phys. Rev. Lett. **103**, 146401 (2009).

[29] Y. L. Chen, J. G. Analytis, J.-H. Chu, Z. K. Liu, S.-K. Mo, X. L. Qi, H. J. Zhang, D. H. Lu, X. Dai, Z. Fang, S. C. Zhang, I. R. Fisher, Z. Hussain and Z.-X. Shen, *Experimental realization of a three-dimensional topological insulator, Bi_2Te_3*, Science **325**, 178 (2009).

[30] Y. Jiang, Y. Wang, M. Chen, Z. Li, C. Song, K. He, L. Wang, X. Chen, X. Ma and Q.-K. Xue, *Landau quantization and the thickness limit of topological insulator thin films of Sb_2Te_3*, Phys. Rev. Lett. **108**, 016401 (2012).

[31] A. B. Khanikaev, S. H. Mousavi, W.-K. Tse, M. Kargarian, A. H. MacDonald and G. Shvets, *Photonic topological insulators*, Nature Materials **12**, 233 (2012).

[32] B. Yan and C. Felser, *Topological materials: Weyl semimetals*, Annual Review of Condensed Matter Physics **8**, 337 (2017).

[33] A. Ghatak and T. Das, *New topological invariants in non-Hermitian systems*, Journal of Physics: Condensed Matter **31**, 263001 (2019).

[34] A. Lau and C. Ortix, *Novel topological insulators from crystalline symmetries*, The European Physical Journal Special Topics **227**, 1309 (2018).

[35] M. Z. Hasan and C. L. Kane, *Colloquium: Topological insulators*, Rev. Mod. Phys. **82**, 3045 (2010).

[36] X.-L. Qi and S.-C. Zhang, *Topological insulators and superconductors*, Rev. Mod. Phys. **83**, 1057 (2011).

[37] L. D. Landau, *On the theory of phase transitions*, Zh. Eksp. Teor. Fiz. **7**, 19 (1937).

[38] X.-G. Wen, *Colloquium: Zoo of quantum-topological phases of matter*, Rev. Mod. Phys. **89**, 041004 (2017).

[39] R. B. Laughlin, *Anomalous quantum Hall effect: An incompressible quantum fluid with fractionally charged excitations*, Phys. Rev. Lett. **50**, 1395 (1983).

[40] L. Savary and L. Balents, *Quantum spin liquids: a review*, Reports on Progress in Physics **80**, 016502 (2016).

[41] J. C. Budich, B. Trauzettel and G. Sangiovanni, *Fluctuation-driven topological Hund insulators*, Phys. Rev. B **87**, 235104 (2013).

[42] A. Amaricci, J. C. Budich, M. Capone, B. Trauzettel and G. Sangiovanni, *First-Order Character and Observable Signatures of Topological Quantum Phase Transitions*, Phys. Rev. Lett. **114**, 185701 (2015).

[43] S. Barbarino, G. Sangiovanni and J. C. Budich, *First-order topological quantum phase transition in a strongly correlated ladder*, Phys. Rev. B **99**, 075158 (2019).

[44] S. Raghu, X.-L. Qi, C. Honerkamp and S.-C. Zhang, *Topological Mott Insulators*, Phys. Rev. Lett. **100**, 156401 (2008).

[45] D. Pesin and L. Balents, *Mott physics and band topology in materials with strong spin–orbit interaction*, Nature Physics **6**, 376 (2010).

[46] G. Li, W. Hanke, G. Sangiovanni and B. Trauzettel, *Interacting weak topological insulators and their transition to Dirac semimetal phases*, Phys. Rev. B **92**, 235149 (2015).

[47] A. Amaricci, J. C. Budich, M. Capone, B. Trauzettel and G. Sangiovanni, *Strong correlation effects on topological quantum phase transitions in three dimensions*, Phys. Rev. B **93**, 235112 (2016).

[48] A. P. Schnyder, S. Ryu, A. Furusaki and A. W. W. Ludwig, *Classification of topological insulators and superconductors*, AIP Conference Proceedings **1134**, 10 (2009).

[49] S. Ryu, A. P. Schnyder, A. Furusaki and A. W. W. Ludwig, *Topological insulators and superconductors: tenfold way and dimensional hierarchy*, New Journal of Physics **12**, 065010 (2010).

[50] L. D'Alessio and M. Rigol, *Dynamical preparation of Floquet Chern insulators*, Nature Communications **6**, 8336 (2015).

[51] H. Dehghani, T. Oka and A. Mitra, *Out-of-equilibrium electrons and the Hall conductance of a Floquet topological insulator*, Phys. Rev. B **91**, 155422 (2015).

[52] H. Dehghani and A. Mitra, *Occupation probabilities and current densities of bulk and edge states of a Floquet topological insulator*, Phys. Rev. B **93**, 205437 (2016).

[53] M. McGinley and N. R. Cooper, *Classification of topological insulators and superconductors out of equilibrium*, Phys. Rev. B **99**, 075148 (2019).

[54] M. D. Caio, N. R. Cooper and M. J. Bhaseen, *Quantum quenches in Chern insulators*, Phys. Rev. Lett. **115**, 236403 (2015).

[55] M. S. Foster, M. Dzero, V. Gurarie and E. A. Yuzbashyan, *Quantum quench in a $p + ip$ superfluid: Winding numbers and topological states far from equilibrium*, Phys. Rev. B **88**, 104511 (2013).

[56] L. Ulčakar, J. Mravlje, A. Ramšak and T. Rejec, *Slow quenches in two-dimensional time-reversal symmetric $\mathbb{Z}_2$ topological insulators*, Phys. Rev. B **97**, 195127 (2018).

[57] M. McGinley and N. R. Cooper, *Topology of one-dimensional quantum systems out of equilibrium*, Phys. Rev. Lett. **121**, 090401 (2018).

[58] S. P. Marinček, J. Mravlje and T. Rejec, *Slow quenches in the band insulator described by the Su–Schrieffer–Heeger model*, physica status solidi (b) , 1900425 (2019).

[59] A. J. Heeger, S. Kivelson, J. R. Schrieffer and W. P. Su, *Solitons in conducting polymers*, Rev. Mod. Phys. **60**, 781 (1988).

[60] M. D. Caio, N. R. Cooper and M. J. Bhaseen, *Hall response and edge current dynamics in Chern insulators out of equilibrium*, Phys. Rev. B **94**, 155104 (2016).

[61] F. N. Ünal, E. J. Mueller and M. O. Oktel, *Nonequilibrium fractional Hall response after a topological quench*, Phys. Rev. A **94**, 053604 (2016).

[62] Y. Hu, P. Zoller and J. C. Budich, *Dynamical buildup of a quantized Hall response from nontopological states*, Phys. Rev. Lett. **117**, 126803 (2016).

[63] B. Damski, *The simplest quantum model supporting the Kibble-Zurek mechanism of topological defect production: Landau-Zener transitions from a new perspective*, Phys. Rev. Lett. **95**, 035701 (2005).

[64] A. Dutta, R. R. P. Singh and U. Divakaran, *Quenching through Dirac and semi-Dirac points in optical lattices: Kibble-Zurek scaling for anisotropic quantum critical systems*, EPL (Europhysics Letters) **89**, 67001 (2010).

[65] T. W. B. Kibble, *Topology of cosmic domains and strings*, Journal of Physics A: Mathematical and General **9**, 1387 (1976).

[66] W. H. Zurek, *Cosmological experiments in superfluid helium?*, Nature **317**, 505 (1985).

[67] W. H. Zurek, U. Dorner and P. Zoller, *Dynamics of a quantum phase transition*, Phys. Rev. Lett. **95**, 105701 (2005).

[68] A. Polkovnikov, *Universal adiabatic dynamics in the vicinity of a quantum critical point*, Phys. Rev. B **72**, 161201 (2005).

[69] R. Monaco, J. Mygind and R. J. Rivers, *Zurek-Kibble domain structures: The dynamics of spontaneous vortex formation in annular Josephson tunnel junctions*, Phys. Rev. Lett. **89**, 080603 (2002).

[70] R. Monaco, J. Mygind, M. Aaroe, R. J. Rivers and V. P. Koshelets, *Zurek-Kibble mechanism for the spontaneous vortex formation in Nb-Al/Al_{ox}/Nb Josephson tunnel junctions: New theory and experiment*, Phys. Rev. Lett. **96**, 180604 (2006).

[71] S. C. Chae, N. Lee, Y. Horibe, M. Tanimura, S. Mori, B. Gao, S. Carr and S.-W. Cheong, *Direct observation of the proliferation of ferroelectric loop domains and vortex-antivortex pairs*, Phys. Rev. Lett. **108**, 167603 (2012).

[72] S. M. Griffin, M. Lilienblum, K. T. Delaney, Y. Kumagai, M. Fiebig and N. A. Spaldin, *Scaling behavior and beyond equilibrium in the hexagonal manganites*, Phys. Rev. X **2**, 041022 (2012).

[73] Q. N. Meier, M. Lilienblum, S. M. Griffin, K. Conder, E. Pomjakushina, Z. Yan, E. Bourret, D. Meier, F. Lichtenberg, E. K. H. Salje, N. A. Spaldin, M. Fiebig and A. Cano, *Global formation of topological defects in the multiferroic hexagonal manganites*, Phys. Rev. X **7**, 041014 (2017).

[74] S. Ulm, J. Roßnagel, G. Jacob, C. Degünther, S. T. Dawkins, U. G. Poschinger, R. Nigmatullin, A. Retzker, M. B. Plenio, F. Schmidt-Kaler and K. Singer, *Observation of the Kibble–Zurek scaling law for defect formation in ion crystals*, Nature Communications **4**, 2290 (2013).

[75] K. Pyka, J. Keller, H. L. Partner, R. Nigmatullin, T. Burgermeister, D. M. Meier, K. Kuhlmann, A. Retzker, M. B. Plenio, W. H. Zurek, A. del Campo and T. E. Mehlstäubler, *Topological defect formation and spontaneous symmetry breaking in ion Coulomb crystals*, Nature Communications **4**, 2291 (2013).

[76] G. Lamporesi, S. Donadello, S. Serafini, F. Dalfovo and G. Ferrari, *Spontaneous creation of Kibble–Zurek solitons in a Bose–Einstein condensate*, Nature Physics **9**, 656 (2013).

[77] A. Keesling, A. Omran, H. Levine, H. Bernien, H. Pichler, S. Choi, R. Samajdar, S. Schwartz, P. Silvi, S. Sachdev, P. Zoller, M. Endres, M. Greiner, V. Vuletić and M. D. Lukin, *Quantum Kibble–Zurek mechanism and critical dynamics on a programmable Rydberg simulator*, Nature **568**, 207 (2019).

[78] W. Chen, *Scaling theory of topological phase transitions*, Journal of Physics: Condensed Matter **28**, 055601 (2016).

[79] R. Bianco and R. Resta, *Mapping topological order in coordinate space*, Phys. Rev. B **84**, 241106 (2011).

[80] M. D. Caio, G. Möller, N. R. Cooper and M. J. Bhaseen, *Topological marker currents in Chern insulators*, Nature Physics **15**, 257 (2019).

[81] D. J. Thouless, M. Kohmoto, M. P. Nightingale and M. den Nijs, *Quantized Hall conductance in a two-dimensional periodic potential*, Phys. Rev. Lett. **49**, 405 (1982).

[82] M. Nakahara, *Geometry, topology and physics, second edition (Graduate student series in physics)* (CRC Press, 2003).

[83] B. I. Halperin, *Quantized Hall conductance, current-carrying edge states, and the existence of extended states in a two-dimensional disordered potential*, Phys. Rev. B **25**, 2185 (1982).

[84] R. Jackiw and C. Rebbi, *Solitons with fermion number 1/2*, Phys. Rev. D **13**, 3398 (1976).

[85] P. W. Anderson, *Absence of diffusion in certain random lattices*, Phys. Rev. **109**, 1492 (1958).

[86] A. Altland and M. R. Zirnbauer, *Nonstandard symmetry classes in mesoscopic normal-superconducting hybrid structures*, Phys. Rev. B **55**, 1142 (1997).

[87] A. K. Geim and I. V. Grigorieva, *Van der Waals heterostructures*, Nature **499**, 419 (2013).

[88] Y. Ando, *Topological insulator materials*, Journal of the Physical Society of Japan **82**, 102001 (2013).

[89] Y. Tokura, K. Yasuda and A. Tsukazaki, *Magnetic topological insulators*, Nature Reviews Physics **1**, 126 (2019).

[90] R. Yu, W. Zhang, H.-J. Zhang, S.-C. Zhang, X. Dai and Z. Fang, *Quantized anomalous Hall effect in magnetic topological insulators*, Science **329**, 61 (2010).

[91] J. Ge, Y. Liu, J. Li, H. Li, T. Luo, Y. Wu, Y. Xu and J. Wang, *High-Chern-number and high-temperature quantum Hall effect without Landau levels*, National Science Review **7**, 1280–1287 (2020).

[92] M. Atala, M. Aidelsburger, J. T. Barreiro, D. Abanin, T. Kitagawa, E. Demler and I. Bloch, *Direct measurement of the Zak phase in topological Bloch bands*, Nature Physics **9**, 795 (2013).

[93] E. J. Meier, F. A. An and B. Gadway, *Observation of the topological soliton state in the Su–Schrieffer–Heeger model*, Nature Communications **7**, 13986 (2016).

[94] C. Liu, T. L. Hughes, X.-L. Qi, K. Wang and S.-C. Zhang, *Quantum spin Hall effect in inverted type-II semiconductors*, Phys. Rev. Lett. **100**, 236601 (2008).

[95] I. Žutić, A. Matos-Abiague, B. Scharf, H. Dery and K. Belashchenko, *Proximitized materials*, Materials Today **22**, 85 (2019).

[96] S. Murakami, *Quantum spin Hall effect and enhanced magnetic response by spin-orbit coupling*, Phys. Rev. Lett. **97**, 236805 (2006).

[97] Z. Liu, C.-X. Liu, Y.-S. Wu, W.-H. Duan, F. Liu and J. Wu, *Stable montrivial Z_2 topology in ultrathin Bi (111) films: A first-principles study*, Phys. Rev. Lett. **107**, 136805 (2011).

[98] M. Wada, S. Murakami, F. Freimuth and G. Bihlmayer, *Localized edge states in two-dimensional topological insulators: Ultrathin Bi films*, Phys. Rev. B **83**, 121310 (2011).

[99] M. Aidelsburger, *Artificial gauge fields and topology with ultracold atoms in optical lattices*, Journal of Physics B: Atomic, Molecular and Optical Physics **51**, 193001 (2018).

[100] P. G. Harper, *Single band motion of conduction electrons in a uniform magnetic field*, Proc. Phys. Soc., Section A **68**, 874 (1955).

[101] D. R. Hofstadter, *Energy levels and wave functions of Bloch electrons in rational and irrational magnetic fields*, Phys. Rev. B **14**, 2239 (1976).

[102] X.-L. Qi, Y.-S. Wu and S.-C. Zhang, *Topological quantization of the spin Hall effect in two-dimensional paramagnetic semiconductors*, Phys. Rev. B **74**, 085308 (2006).

[103] V. S. Letokhov, M. A. Ol'shanii and Y. B. Ovchinnikov, *Laser cooling of atoms: a review*, Quantum and Semiclassical Optics: Journal of the European Optical Society Part B **7**, 5 (1995).

[104] W. Ketterle and N. V. Druten, *Evaporative cooling of trapped atoms* (Elsevier, 1996) pp. 181–236.

[105] I. Bloch, *Ultracold quantum gases in optical lattices*, Nature Physics **1**, 23 (2005).

[106] A. Eckardt, *Colloquium: Atomic quantum gases in periodically driven optical lattices*, Reviews of Modern Physics **89**, 011004 (2017).

[107] H. M. Price and N. R. Cooper, *Mapping the Berry curvature from semiclassical dynamics in optical lattices*, Phys. Rev. A **85**, 033620 (2012).

[108] J. Dziarmaga, *Dynamics of a quantum phase transition and relaxation to a steady state*, Advances in Physics **59**, 1063 (2010).

[109] M. Greiner, O. Mandel, T. W. Hänsch and I. Bloch, *Collapse and revival of the matter wave field of a Bose–Einstein condensate*, Nature **419**, 51 (2002).

[110] T. Kinoshita, *Observation of a one-dimensional Tonks-Girardeau gas*, Science **305**, 1125 (2004).

[111] T. Kinoshita, T. Wenger and D. S. Weiss, *A quantum Newton's cradle*, Nature **440**, 900 (2006).

[112] B. Paredes, A. Widera, V. Murg, O. Mandel, S. Fölling, I. Cirac, G. V. Shlyapnikov, T. W. Hänsch and I. Bloch, *Tonks–Girardeau gas of ultracold atoms in an optical lattice*, Nature **429**, 277 (2004).

[113] S. Trotzky, P. Cheinet, S. Folling, M. Feld, U. Schnorrberger, A. M. Rey, A. Polkovnikov, E. A. Demler, M. D. Lukin and I. Bloch, *Time-resolved observation and control of superexchange interactions with ultracold atoms in optical lattices*, Science **319**, 295 (2008).

[114] A. Friedenauer, H. Schmitz, J. T. Glueckert, D. Porras and T. Schaetz, *Simulating a quantum magnet with trapped ions*, Nature Physics **4**, 757 (2008).

[115] K. Henderson, C. Ryu, C. MacCormick and M. G. Boshier, *Experimental demonstration of painting arbitrary and dynamic potentials for Bose–Einstein condensates*, New Journal of Physics **11**, 043030 (2009).

[116] E. Farhi, J. Goldstone, S. Gutmann, J. Lapan, A. Lundgren and D. Preda, *A quantum adiabatic evolution algorithm applied to random instances of an NP-complete problem*, Science **292**, 472 (2001).

[117] R. Schützhold and G. Schaller, *Adiabatic quantum algorithms as quantum phase transitions: First versus second order*, Phys. Rev. A **74**, 060304 (2006).

[118] J. Dziarmaga, *Dynamics of a Quantum Phase Transition: Exact Solution of the Quantum Ising Model*, Phys. Rev. Lett. **95**, 245701 (2005).

[119] L. Ulčakar, J. Mravlje and T. Rejec, *Slow quenches in Chern insulator ribbons*, Phys. Rev. B **100**, 125110 (2019).

[120] B. Damski and W. H. Zurek, *Adiabatic-impulse approximation for avoided level crossings: From phase-transition dynamics to Landau-Zener evolutions and back again*, Phys. Rev. A **73**, 063405 (2006).

[121] A. del Campo and W. H. Zurek, *Universality of phase transition dynamics: Topological defects from symmetry breaking*, International Journal of Modern Physics A **29**, 1430018 (2014).

[122] W. Chen, M. Sigrist and A. P. Schnyder, *Scaling theory of $\mathbb{Z}_2$ topological invariants*, Journal of Physics: Condensed Matter **28**, 365501 (2016).

[123] W. Chen, M. Legner, A. Rüegg and M. Sigrist, *Correlation length, universality classes, and scaling laws associated with topological phase transitions*, Phys. Rev. B **95**, 075116 (2017).

[124] W. Chen and A. P. Schnyder, *Universality classes of topological phase transitions with higher-order band crossing*, New Journal of Physics **21**, 073003 (2019).

[125] L. Landau, *Zur Theorie der Energieübertragung. II*, Physikalische Zeitschrift der Sowjetunion **2**, 46 (1932).

[126] C. Zener, *Non-adiabatic crossing of energy levels*, Proceedings of the Royal Society of London A: Mathematical, Physical and Engineering Sciences **137**, 696 (1932).

[127] E. Majorana, *Atomi orientati in campo magnetico variabile*, Il Nuovo Cimento **9**, 43 (1932).

[128] E. Stückelberg, *Theorie der unelastischen Stösse zwischen Atomen*, Helvetica Physica Acta **5**, 369 (1932).

[129] E. T. Whittaker and G. N. Watson, *A course of modern analysis* (Cambridge University Press, 1996).

[130] N. V. Vitanov and B. M. Garraway, *Landau-Zener model: Effects of finite coupling duration*, Phys. Rev. A **53**, 4288 (1996).

[131] N. V. Vitanov, *Transition times in the Landau-Zener model*, Phys. Rev. A **59**, 988 (1999).

[132] C. N. Weiler, T. W. Neely, D. R. Scherer, A. S. Bradley, M. J. Davis and B. P. Anderson, *Spontaneous vortices in the formation of Bose–Einstein condensates*, Nature **455**, 948 (2008).

[133] W. H. Zurek, *Causality in condensates: gray solitons as relics of BEC formation*, Phys. Rev. Lett. **102**, 105702 (2009).

[134] W. Sun, C.-R. Yi, B.-Z. Wang, W.-W. Zhang, B. C. Sanders, X.-T. Xu, Z.-Y. Wang, J. Schmiedmayer, Y. Deng, X.-J. Liu, S. Chen and J.-W. Pan, *Uncover topology by quantum quench dynamics*, Phys. Rev. Lett. **121**, 250403 (2018).

[135] S. Barbarino, J. Yu, P. Zoller and J. C. Budich, *Preparing Atomic Topological Quantum Matter by Adiabatic Nonunitary Dynamics*, Phys. Rev. Lett. **124**, 010401 (2020).

[136] A. Bermudez, L. Amico and M. A. Martin-Delgado, *Dynamical delocalization of Majorana edge states by sweeping across a quantum critical point*, New Journal of Physics **12**, 055014 (2010).

[137] W. DeGottardi, D. Sen and S. Vishveshwara, *Topological phases, Majorana modes and quench dynamics in a spin ladder system*, New Journal of Physics **13**, 065028 (2011).

[138] P. D. Sacramento, *Fate of Majorana fermions and Chern numbers after a quantum quench*, Phys. Rev. E **90**, 032138 (2014).

[139] M. S. Foster, V. Gurarie, M. Dzero and E. A. Yuzbashyan, *Quench-induced Floquet topological p-wave superfluids*, Phys. Rev. Lett. **113**, 076403 (2014).

[140] L. Privitera and G. E. Santoro, *Quantum annealing and nonequilibrium dynamics of Floquet Chern insulators*, Phys. Rev. B **93**, 241406 (2016).

[141] J. H. Wilson, J. C. W. Song and G. Refael, *Remnant geometric Hall response in a quantum quench*, Phys. Rev. Lett. **117**, 235302 (2016).

[142] P. Wang, M. Schmitt and S. Kehrein, *Universal nonanalytic behavior of the Hall conductance in a Chern insulator at the topologically driven nonequilibrium phase transition*, Phys. Rev. B **93**, 085134 (2016).

[143] P. Wang and S. Kehrein, *Phase transitions in the diagonal ensemble of two-band Chern insulators*, New Journal of Physics **18**, 053003 (2016).

[144] U. Bhattacharya, J. Hutchinson and A. Dutta, *Quenching in Chern insulators with satellite Dirac points: The fate of edge states*, Phys. Rev. B **95**, 144304 (2017).

[145] M. Schüler and P. Werner, *Tracing the nonequilibrium topological state of Chern insulators*, Phys. Rev. B **96**, 155122 (2017).

[146] H. Miyake, G. A. Siviloglou, C. J. Kennedy, W. C. Burton and W. Ketterle, *Realizing the Harper Hamiltonian with Laser-Assisted Tunneling in Optical Lattices*, Phys. Rev. Lett. **111**, 185302 (2013).

[147] G. Jotzu, M. Messer, R. Desbuquois, M. Lebrat, T. Uehlinger, D. Greif and T. Esslinger, *Experimental realization of the topological Haldane model with ultracold fermions*, Nature **515**, 237 (2014).

[148] M. Aidelsburger, M. Lohse, C. Schweizer, M. Atala, J. Barreiro, S. Nascimbéne, N. Cooper, I. Bloch and N. Goldman, *Measuring the Chern number of Hofstadter bands with ultracold bosonic atoms*, Nature Physics **11**, 162 (2015).

[149] N. Fläschner, B. S. Rem, M. Tarnowski, D. Vogel, D.-S. Lühmann, K. Sengstock and C. Weitenberg, *Experimental reconstruction of the Berry curvature in a Floquet Bloch band*, Science **352**, 1091 (2016).

[150] D. G. Rothe, R. W. Reinthaler, C.-X. Liu, L. W. Molenkamp, S.-C. Zhang and E. M. Hankiewicz, *Fingerprint of different spin–orbit terms for spin transport in HgTe quantum wells*, New Journal of Physics **12**, 065012 (2010).

[151] D. Xiao, W. Zhu, Y. Ran, N. Nagaosa and S. Okamoto, *Interface engineering of quantum Hall effects in digital transition metal oxide heterostructures*, Nature Communications **2**, 596 (2011).

[152] J. Wang, B. Lian and S.-C. Zhang, *Electrically tunable magnetism in magnetic topological insulators*, Phys. Rev. Lett. **115**, 036805 (2015).

[153] L. Ulčakar, J. Mravlje and T. Rejec, *Kibble-Zurek Behavior in Disordered Chern Insulators*, Phys. Rev. Lett. **125**, 216601 (2020).

[154] J. K. Asbóth, L. Oroszlány and A. Pályi, *A short course on topological insulators* (Springer, 2016).

[155] C. Gorini, R. Raimondi and P. Schwab, *Onsager relations in a two-dimensional electron gas with spin-orbit coupling*, Phys. Rev. Lett. **109**, 246604 (2012).

[156] M. Rigol, V. Dunjko and M. Olshanii, *Thermalization and its mechanism for generic isolated quantum systems*, Nature **452**, 854 (2008).

[157] L. Vidmar and M. Rigol, *Generalized Gibbs ensemble in integrable lattice models*, Journal of Statistical Mechanics: Theory and Experiment **2016**, 064007 (2016).

[158] R. Yu, X. L. Qi, A. Bernevig, Z. Fang and X. Dai, *Equivalent expression of $\mathbb{Z}_2$ topological invariant for band insulators using the non-Abelian Berry connection*, Phys. Rev. B **84**, 075119 (2011).

[159] J. Shi, P. Zhang, D. Xiao and Q. Niu, *Proper definition of spin current in spin-orbit coupled systems*, Phys. Rev. Lett. **96**, 076604 (2006).

[160] M.-F. Yang and M.-C. Chang, *Středa-like formula in the spin Hall effect*, Phys. Rev. B **73**, 073304 (2006).

[161] F. Matusalem, M. Marques, L. K. Teles, L. Matthes, J. Furthmüller and F. Bechstedt, *Quantization of spin Hall conductivity in two-dimensional topological insulators versus symmetry and spin-orbit interaction*, Phys. Rev. B **100**, 245430 (2019).

[162] D. Monaco and L. Ulčakar, *Spin Hall conductivity in insulators with nonconserved spin*, Phys. Rev. B **102**, 125138 (2020).

[163] E. I. Rashba, *Spin currents in thermodynamic equilibrium: The challenge of discerning transport currents*, Phys. Rev. B **68**, 241315 (2003).

[164] Y. Yao and Z. Fang, *Sign changes of intrinsic spin Hall effect in semiconductors and simple metals: First-principles calculations*, Phys. Rev. Lett. **95**, 156601 (2005).

[165] A. Alexandradinata, X. Dai and B. A. Bernevig, *Wilson-loop characterization of inversion-symmetric topological insulators*, Phys. Rev. B **89**, 155114 (2014).

[166] A. Bermudez, D. Patanè, L. Amico and M. A. Martin-Delgado, *Topology-induced anomalous defect production by crossing a quantum critical point*, Phys. Rev. Lett. **102**, 135702 (2009).

[167] J. Zak, *Berry's phase for energy bands in solids*, Phys. Rev. Lett. **62**, 2747 (1989).

[168] R. Resta, *Quantum-mechanical position operator in extended systems*, Phys. Rev. Lett. **80**, 1800 (1998).

[169] S. Baroni, S. de Gironcoli, A. Dal Corso and P. Giannozzi, *Phonons and related crystal properties from density-functional perturbation theory*, Rev. Mod. Phys. **73**, 515 (2001).

[170] I. Mondragon-Shem, T. L. Hughes, J. Song and E. Prodan, *Topological criticality in the chiral-symmetric AIII class at strong disorder*, Phys. Rev. Lett. **113**, 046802 (2014).

[171] J. Li, R.-L. Chu, J. K. Jain and S.-Q. Shen, *Topological Anderson insulator*, Phys. Rev. Lett. **102**, 136806 (2009).

[172] K. Kobayashi, T. Ohtsuki and K.-I. Imura, *Disordered Weak and Strong Topological Insulators*, Phys. Rev. Lett. **110**, 236803 (2013).

[173] K. Kobayashi, T. Ohtsuki, K.-I. Imura and I. F. Herbut, *Density of states scaling at the semimetal to metal transition in three dimensional topological insulators*, Phys. Rev. Lett. **112**, 016402 (2014).

[174] A. Yamakage, K. Nomura, K.-I. Imura and Y. Kuramoto, *Disorder-induced multiple transition involving Z2 topological insulator*, Journal of the Physical Society of Japan **80**, 053703 (2011).

[175] B. Kramer and A. MacKinnon, *Localization: theory and experiment*, Reports on Progress in Physics **56**, 1469 (1993).

[176] E. Prodan, T. L. Hughes and B. A. Bernevig, *Entanglement spectrum of a disordered topological Chern insulator*, Phys. Rev. Lett. **105**, 115501 (2010).

[177] R. Bianco and R. Resta, *Orbital magnetization as a local property*, Phys. Rev. Lett. **110**, 087202 (2013).

[178] A. Marrazzo and R. Resta, *Locality of the anomalous Hall conductivity*, Phys. Rev. B **95**, 121114 (2017).

[179] S. Rachel, *Interacting topological insulators: a review*, Reports on Progress in Physics **81**, 116501 (2018).

[180] S. Julià-Farré, M. Müller, M. Lewenstein and A. Dauphin, *Interaction-induced polarons and topological defects in a topological Mott insulator* (2020), arXiv:2006.04671 [cond-mat.quant-gas] .

Razširjeni povzetek v slovenskem jeziku

Topološki izolatorji so pasovni izolatorji, na robovih katerih se pojavijo robna stanja, ki so zaščitena pred disipacijo in imajo energijo znotraj energijske reže. Obstoj robnih stanj je povezan z netrivialno topologijo sistema. Ta izhaja iz geometričnih lastnosti pasovne strukture in prepozna se jo kot globalno 'obliko', ki je invariantna na adiabatske transformacije elektronske strukture, ki ne zaprejo energijske reže in ne podrejo simetrij sistema, kot so simetrija na obrat časa, kiralna simetrija in simetrija delec-luknja. Robna stanja se pojavijo na robovih sistema zaradi spremembe topološke lastnosti ob prehodu iz topološko netrivialne notranjosti materiala v trivialno zunanjost. Omenjene eksotične lastnosti, ki obljubljajo možno uporabo v nanoelektroniki, spintroniki in kvantnem računalništvu [1, 2, 3, 4, 5, 6], so v zadnjem desetletju spodbudile mnogo teoretičnih in eksperimentalnih raziskav. Področje se je začelo leta 1980 z odkritjem kvantnega Hallovega efekta, ki se pojavi v dvodimenzionalnem elektronskem plinu ob prisotnosti močega magnetnega polja [7]. Leta 1988 je Haldane [8] pokazal, da se kvantni Hallov efekt lahko pojavi tudi v sistemih v odsotnosti magnetnega polja. Pravi zagon je dobilo področje šele leta 2005, ko sta Kane in Mele [9, 10] predvidela novo fazo snovi – topološki izolator s simetrijo na obrat časa – v kateri se lahko pojavi spinski Hallov efekt. Eksperimentalno so slednjo topološko fazo potrdili leta 2007 v polprevodniških kvantnih jamah [11, 12, 17]. Tesno so sledile napovedi tridimenzionalnega topološkega izolatorja [13], na površini katerega se pojavijo površinska stanja, in topoloških superprevodnikov [14, 15, 16]. Od teh so veliko pozornosti prejeli enodimenzionalni sistemi, ki na robovih gostijo Majorana fermione z energijo nič. Topološki izolatorji so bili sintetizirani in eksperimentalno potrjeni še v fizikalnih materialih [26, 27, 28, 29, 30], v laboratorijih s hladnimi atomi [18, 19, 20, 21] in v polprevodniških heterostrukturah [22, 23, 24, 25].

Topološki izolatorji [35, 36] so zanimivi tudi iz teoretičnega vidika, saj padejo izven dosega Landauove teorije faznih prehodov [37]. Po Landauovi teoriji pride ob faznem prehodu v urejeno fazo do spontanega zloma simetrije. Ob tem dobi lokalni ureditveni parameter neničelno vrednost, ki se spremeni ob simetrijski operaciji in je zaradi tega ničelna v neurejeni visokosimetrijski fazi. V kvantnih sistemih je s tem tesno povezana degeneracija osnovnega stanja. Topološki izolatorji ne spadajo v okvir te teorije, saj se ob faznem prehodu ne zgodi spontani zlom simetrije, nimajo degeneracije osnovnega stanja in lokalnega parametra ureditve. Njihove faze opiše celoštevilska topološka invarianta, ki ni odvisna od mikroskopskih lokalnih lastnosti sistema. Njena vrednost opisuje globalne lastnosti sistema, kot je recimo prisotnost kvantnega (spinkega) Hallovega pojava in robnih stanj. Za translacijsko invariantne sisteme se jo lahko izrazi z integralom funkcije ukrivljenosti, ki je geometrijska lastnost pasovne strukture. Dejstvo, da je topološka invarianta integral nakazuje, da

gre za globalno lastnost sistema. Tip topološke faze zavisi od simetrijskega razreda in od dimenzionalnosti izolatorja [14, 15, 48, 49]. Simetrijski razred določa prisotnost oziroma odsotnost simetrije na obrat časa, simetrije delec-luknja in kiralne simetrije, ter vrednost $\hat{\mathcal{P}}^2 = \pm 1$, kjer je $\hat{\mathcal{P}}$ operator pripadajoče simetrije. Topološka invarianta je lahko tipa $\mathbb{Z}$ (vsa cela števila), $\mathbb{Z}_2$ (vrednost 0 ali 1) ali 0 (sistem je za vse vrednosti parametrov trivialen). Dva sistema sva v isti topološki fazi tedaj, ko imata isto topološko invarianto in ko se ju da pretvoriti enega v drugega z adiabatsko transformacijo. Trivialni izolator je sistem, ki ima topološko invarianto enako 0 in je topološko ekvivalenten atomski limiti. Za tak sistem obstaja set eksponentno lokaliziranih Wannierjevih stanj, ki upoštevajo vse simetrije sistema, in v limiti, ko gre razdalja med atomi proti neskončnosti, postanejo Wannierjeva stanja enaka lokaliziranim atomskim orbitalam.

Na stiku dveh izolatorjev z različnima topološkima fazama se pojavijo robna stanja, ki so topološko zaščitena pred disipacijo. V primeru dvodimenzionalnih izolatorjev robna stanja potujejo vzdolž enodimenzionalnih robov. Korespondenca notranjost-rob poveže število robnih stanj s spremembo topološke invariante ob prehodu čez rob. Ta teorem nakazuje, da dokler je notranjost materiala čista, tako da je topološka faza nezmotena, so robna stanja zaščitena pred disipacijo zaradi nereda, prisotnega na robu. Posledično je v sistemih s kvantnim Hallovim pojavom Hallova prevodnost točno kvantizirana. Stanja so kiralna, saj elektroni potujejo po robu le v eni smeri. Drugačne lastnosti nastopijo v dvodimenzionalnih izolatorjih s simetrijo na obrat časa, v katerih se lahko zgodi spinski Hallov pojav. Tam zaradi simetrije na obrat časa vsa lastna stanja Hamiltonke nastopijo v dvakrat degeneriranih Kramerjevih parih. Vsako robno stanje ima partnerja, ki potuje po istem robu v nasprotno smer. En par robnih stanj je topološko zaščiten pred neredom, ki ne krši simetrije na obrat časa. Stanja so helična, saj je projekcija spina povezana s smerjo propagacije elektronov vzdolž roba.

Modeli topoloških izolatorjev

Chernov izolator

Chernovi izolatorji so dvodimenzionalni sistemi, v katerih je prisoten kvantni Hallov pojav, njihovo topološko fazo pa opisuje Chernovo število C, ki je tipa $\mathbb{Z}$. Znana primera sta Haldanov model [8] in Qi-Wu-Zhangov (QWZ) model [102], ki ga obravnavamo v tem delu. Opisuje neinteragirajoče elektrone na kvadratni kristalni mreži, kjer ima vsak atom dve orbitali $|A\rangle$ in $|B\rangle$ z vezavnima energijama $\pm u$. Hamiltonka translacijsko invariantnega QWZ modela je bločno diagonalna v Blochovi bazi $\hat{H} = \sum_{\mathbf{k}} |\mathbf{k}\rangle\langle\mathbf{k}| \otimes \hat{H}(\mathbf{k})$ in Blochova Hamiltonka sledeča

$$\hat{H}(\mathbf{k}) = \mathbf{d}(\mathbf{k}) \cdot \hat{\boldsymbol{\sigma}}, \quad \mathbf{d}(\mathbf{k}) = (\sin k_x, \sin k_y, u + \cos k_x + \cos k_y). \tag{7.1}$$

Pasovna struktura sestoji iz dveh energijskih pasov $E_{c,v}(\mathbf{k}) = \pm|\mathbf{d}(\mathbf{k})|$ in iz pripadajočih lastnih stanj $|\psi_{c,v}(\mathbf{k})\rangle$. Geometrijske lastnosti pasovne strukture določa Berryjeva ukrivljenost, ki je za valenčni pas definirana kot

$$\Omega(\mathbf{k}) = i\partial_{k_x}\langle\psi_v(\mathbf{k})|\partial_{k_y}|\psi_v(\mathbf{k})\rangle - i\partial_{k_y}\langle\psi_v(\mathbf{k})|\partial_{k_x}|\psi_v(\mathbf{k})\rangle. \tag{7.2}$$

Fizikalni pomen Berryjeve ukrivljenosti je sledeč: če elektron v lastnem stanju adiabatsko transformiramo tako, da njegov moment $\mathbf{k}$ potuje po ciklični poti, bo elektron

pridobil Berryjevo geometrijsko fazo, ki je do 2π enaka integralu Berryjeve ukrivljenosti po momentih, ki jih zaobjema prepotovana pot. Topološka invarianta je Chernovo število, ki je enako integralu Berryjeve ukrivljenosti po celi Brillouinovi coni,

$$C = -\frac{1}{2\pi}\int \mathrm{d}\mathbf{k}\,\Omega(\mathbf{k}). \tag{7.3}$$

V QWZ modelu je njegova vrednost določena s parametrom u, $C = \mathrm{sgn(u)}$ če $|u| < 2$, sicer 0. Ob prisotnosti majhnega električnega polja v recimo smeri y se zaradi netrivialne topologije pojavi kvantiziran električni tok v smeri x, ki je sorazmeren Chernovem številu, $J_x = \sigma_{xy}E_y$ in $\sigma_{xy} = Ce^2/h$.

Chernovo število se spremeni ob prehodu čez kritično točko, v QWZ modelu so to $u_c = -2, 0$ in 2. V kritični točki se energijska reža zapre pri momentu $\mathbf{k}_c$ in energijski pasovi tvorijo Diracov stožec z disperzijo $\pm\hbar v_F q$, kjer je v_F Fermijeva hitrost in $q = |\mathbf{k} - \mathbf{k}_c|$. Gre torej za fazni prehod drugega reda, katerega zaznamuje divergenca časovne skale τ_r s potenco $z\nu$ in dolžinske skale (ali korelacijske dolžine) ξ s potenco ν, kjer sta z in ν kritična eksponenta. Časovno skalo se lahko izračuna kot inverz energijske reže in za QWZ model dobimo $\tau_r(u) = 2|u-u_c|^{-1}$, torej $z\nu = 1$. Dolžinsko skalo ocenimo iz kritičnega obnašanja Berryjeve ukrivljenosti [78, 122, 123, 124]. V veliki večini sistemov s simetrijo inverzije je funkcija ukrivljenosti blizu kritične točke opisana z Lorentzovo funkcijo. Ob približevanju kritični točki se funkcija ukrivljenosti oža in raste v višino. Ob prehodu čez kritično točko, v kateri divergira, se ji obrne predznak, kar posledično povzroči skok topološke invariante. Dolžinsko skalo se izračuna kot inverz širine funkcije ukrivljenosti. V primeru QWZ modela je dolžinska skala v bližini kritične točke $u_c = -2$ oblike $\xi(u) \propto |u - u_c|^{-1}$, torej je $\nu = 1$.

Topološki izolator s simetrijo na obrat časa

V doktorskem delu obravnavamo Bernevig-Hughes-Zhangov (BHZ) model, ki opisuje prvi eksperimentalno portjeni topološki izolator s simetrijo na obrat časa [12]. Model sestoji iz dveh sklopljenih časovno simetričnih kopij QWZ modela z različnima spinoma. Blochova Hamiltonka je sledeča,

$$\begin{aligned}\hat{H}(\mathbf{k}) = \hat{s}_0 \otimes [(u + \cos k_x + \cos k_y)\hat{\sigma}_z + \sin k_y \hat{\sigma}_y] \\ + \hat{s}_z \otimes \sin k_x \hat{\sigma}_x + c\,\hat{s}_x \otimes \hat{\sigma}_y,\end{aligned} \tag{7.4}$$

kjer Paulijevi operatorji $\hat{s}_i$ delujejo na spinsko prostostno stopnjo. $c \in \mathbb{R}$ je velikost sklopitve spinskih sektorjev in ko je enaka 0, je projekcija spina s_z ohranjena količina. Pasovna struktura vsebuje štiri energijske pasove $E_n(\mathbf{k})$ in pripadajoča lastna stanja $|\psi_n(\mathbf{k})\rangle$. V osnovnem stanju so vsa lastna stanja z negativno energijo ($n = 1, 2$) zasedena. Energijska reža se za $c \ll 1$ zapre na krožnici z radijem c okrog momenta $\mathbf{k}_c$, kjer se energijska reža zapre pri $c = 0$. V radialni smeri iz krožnice je disperzija linearna.

Hamiltonka ima simetrijo na obrat časa, ki jo predstavlja antiunitarni operator $\hat{\mathcal{T}} = i\hat{s}_y K$, kjer je K operator kompleksne konjugacije. Spekter energij je posledično simetričen okrog točk $\mathbf{k}_{\mathrm{TRIM}}$, ki so invariantne na obrat časa (center in robovi Brillouinove cone). Zaradi lastnosti $\hat{\mathcal{T}}^2 = -1$ vsa lastna stanja nastopajo v Kramerjevih parih, kar pomeni, da za vsako lastno stanje $|\psi_n(\mathbf{k})\rangle$ z energijo $E_n(\mathbf{k})$ obstaja stanje

$\hat{\mathcal{T}}|\psi_n(\mathbf{k})\rangle$ z enako energijo. V točkah $\mathbf{k}_{\mathrm{TRIM}}$ so tako stanja vsaj dvakrat degenerirana. Zaradi prisotnosti simetrije na obrat časa je Chernovo število in s tem Hallova prevodnost vedno enako nič. Netrivialno topološko fazo določa $\mathbb{Z}_2$ invarianta, ki zavzame vrednost 1 v topološki fazi in 0 v trivialni fazi. V topološki fazi je na robu sistema prisoten topološko zaščiten Kramerjev par robnih stanj in v sistemu se pojavi spinski Hallov efekt. Ob prisotnosti električnega polja začne v pravokotni smeri teči spinski tok in v primeru ohranjene s_z komponente spina je sorazmernostna konstanta $\sigma_{xy}^{\mathrm{spin}}$, spinska Hallova prevodnost, kvantizirana v enotah $e/2\pi$.

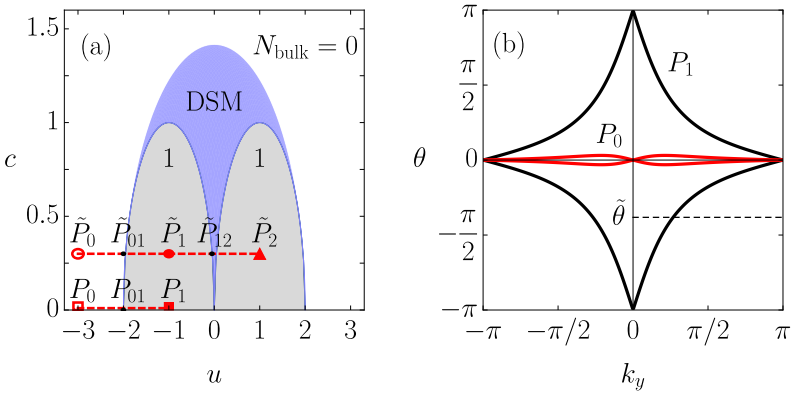

Slika 7.1: (a) Fazni diagram BHZ modela v prostoru parametrov $P = (u, c)$. Siva barva označuje topološka območja z $N_{\mathrm{bulk}} = 1$, bela barva trivialna z $N_{\mathrm{bulk}} = 0$ in modra barva območje, v katerem je energijska reža zaprta. Točke $P_0 = (-3, 0)$, $\tilde{P}_0 = (-3, 0.3)$, $P_1 = (-1, 0)$, $\tilde{P}_1 = (-1, 0.3)$ in $\tilde{P}_2 = (1, 0.3)$ označujejo začetne in končne vrednosti parametrov, med katerimi je sistem preklopljen v času vzdolž rdečih črtkanih črt. (b) Wannierjev tok osnovnega stanja v trivialni (rdeča) in topološki fazi (črna). Število presečišč poljubno izbrane $\tilde{\theta}$ s $\theta(k_y)$ podaja $\mathbb{Z}_2$ invarianto.

Za izračun $\mathbb{Z}_2$ invariante N_{bulk} obstaja mnogo ekvivalentnih definicij, med drugim jo je možno podobno kot Chernovo število izraziti kot integral funkcije ukrivljenosti. V sistemih z ohranjeno s_z komponento spina velja enostavna zveza s Chernovimi števili spinskih sektorjev: $N_{\mathrm{bulk}} = (C_\uparrow - C_\downarrow)/2 \bmod 2$. V naših izračunih smo uporabili naslednjo definicijo [158]:

$$N_n(\tilde{\theta}) = \text{število rešitev } k_y \in (0, \pi) \text{ za } \theta_n(k_y) = \tilde{\theta}, \tag{7.5}$$

$$N_{\mathrm{bulk}} = \left(\sum_{n=1}^{N_F} N_n(\tilde{\theta}) \right) \bmod 2. \tag{7.6}$$

Wannierjev tok $\theta_n(k_y)$ je enak n-ti lastni vrednosti Wilsonove zanke $W(k_y)$, ki je večorbitalna posplošitev Berryjeve faze,

$$W(k_y) = M^{(12)} M^{(23)} \dots M^{(N-1,N)} M^{(N,1)}, \tag{7.7}$$

$$M_{nm}^{(kl)} = \langle \psi_n(k\delta_k - \pi, k_y) | \psi_m(l\delta_k - \pi, k_y) \rangle. \tag{7.8}$$

Tu je $\delta_k = 2\pi/N$ diskretizacijski korak v momentnem prostoru sistema z $N \times N$ osnovnimi celicami in N_F je število zasedenih energijskih pasov. $\mathbb{Z}_2$ invarianta je dobro definirana le v sistemu, ki ima Wannierjeve tokove simetrične in dvakrat

degenerirane pri $k_y = 0, \pi$, kar je posledica simetrije na obrat časa. Fazni diagram BHZ modela je prikazan na sliki 7.1(a). Metoda odčitavanja N_{bulk} je naslikana na sliki 7.1(b), ki prikazuje primer Wannierjevih tokov v trivialni (rdeča) in v topološki fazi (črna).

Izračuna kritičnih eksponentov smo se lotili podobno kot za QWZ model. Relaksacijski čas divergira v kritični točki s potenco $z\nu = 1$, medtem ko korelacijska dolžina divergira s potenco $\nu = 1$, če je $c = 0$, sicer pa $\nu = 1/2$.

Neravnovesna dinamika

Medtem ko je fizika osnovnega stanja topoloških izolatorjev že dobro znana, je področje neravnovesne dinamike manj raziskano. Fundamentalno vprašanje je, kako se ti sistemi odzovejo na časovno odvisno spreminjanje parametrov. Poleg teoretičnega vidika je časovno odvisni odziv topoloških izolatorjev pomemben za uporabne namene, saj nekatere eksperimentalne realizacije topoloških izolatorjev v laboratorijih s hladnimi atomi zahtevajo časovno odvisno poganjanje sistema. Pomembni primer so Floquetovi izolatorji [50, 51, 52], katerih topološko fazo inducira periodično poganjanje sistema. Doktorsko delo je posvečeno drugi veji raziskav in sicer dinamičnim kritičnim lastnostim topoloških sistemov. Te lastnosti so razkrite z izvajanjem časovno odvisnih preklopov čez topološki fazni prehod. Med preklopom se parametri sistema spremenijo tako, da sta začetni in končni Hamiltonki v različnih topoloških fazah. Ponavadi se preklop (angleško 'quench') razume kot nenadno spremembo parametrov Hamiltonke. V tem delu raziskujemo počasne preklope, kjer se parameter $u(t)$ QWZ (7.1) in BHZ Hamiltonke (7.4) spremeni zvezno v času τ kot

$$u(t) = u_0 + (u_1 - u_0) \sin^2 \left(\frac{\pi}{2} \frac{t}{\tau} \right). \tag{7.9}$$

Ker različne topološke faze ločuje zaprtje energijske reže, se po preklopu sistem vedno znajde v neravnovesnem stanju ne glede na to, kako počasi je bil preklop izveden. V primeru dvonivojskih sistemov je dinamika sistema opisana z Landau-Zenerjevim modelom, ki podaja točno rešitev za valovno funkcijo po preklopu. S pomočjo Landau-Zenerjevega modela smo pojasnili neravnovesne lastnosti kot na primer gostoto vzbuditev in transportne koeficiente. S primerjavo rezultatov z napovedmi Kibble-Zurekovega mehanizma [65, 66, 67] pokažemo, da se neravnovesno dinamiko lahko razloži v okviru Kibble-Zurekovega mehanizma. Ta opiše dinamiko s poenostavljeno shemo imenovano adiabatski-impulzni približek, ki razdeli časovni razvoj na tri režime: (1) adiabatski, ko je sistem še daleč od kritične točke in je relaksacijski čas majhen; (2) zamrznjen režim, ki se nahaja v okolici kritične točke in je sistem zaradi divergence relaksacijskega časa efektivno zamrznjen; (3) adiabatski režim, ko je sistem že daleč od kritične točke in je relaksacijski čas zopet majhen. V sistemih z degeneracijo osnovnega stanja in spontanim zlomom simetrije pride v zamrznjenem režimu do območij z različno izbiro osnovnega stanja. Velikost teh območij je enaka korelacijski dolžini ob času zamrznitve

$$\xi(-t_F) \sim \tau^{\nu/(1+z\nu)}, \tag{7.10}$$

kjer se čas zamrznitve oceni kot čas, ob katerem je relaksacijski čas enak času do kritične točke. Na stičišču območij se lahko pojavijo topološki defekti, gostota katerih

je podana z

$$n \sim \xi(-t_F)^{d-D} \sim \tau^{-(D-d)\nu/(1+z\nu)}, \tag{7.11}$$

kjer D označuje dimenzijo sistema, d pa dimenzijo defekta.

Raziskave smo izvedli za translacijsko invariantne sisteme, sisteme z robom in sisteme s šibkim neredom.

Translacijsko invariantni sistemi

V delu smo obravnavali neravnovesno dinamiko QWZ modela in BHZ modela, ki pripadata različnima simetrijskima razredoma in sta tako opisana z različno topološko invarianto. Raziskali smo njune topološke in transportne lastnosti ter gostoto vzbuditev po preklopu in s tem nakazali, katere lastnosti se podobno obnašajo in katere močno zavisijo od simetrijskega razreda.

Topološka invarianta

Topološka invarianta neravnovesnega stanja močno zavisi od simetrijskega razreda. Chernovo število se ohranja za vsak časovni razvoj [50, 54, 56]. To se odseva v Berryjevi ukrivljenosti, ki po preklopu odstopa od oblike za končno osnovno stanje za momente v okolici zaprtja energijske reže. Obdrži približno obliko, ki jo je imelo osnovno stanje ob vhodu v zamrznjen režim pred prehodom čez kritično točko. V nasprotju s tem $\mathbb{Z}_2$ invarianta ni več dobro definirana po preklopu, saj časovni razvoj podre simetrijo na obrat časa. Slika 7.2(a) prikazuje Wannierjeve tokove sistemov z različno konstanto c po preklopu iz trivialne v topološko fazo. Odsotnost simetrije na obrat časa se očitno vidi iz Wannierevih tokov sistemov s $c = 0.3$ in $c = 0.6$, ki niso degenerirani pri $k_y = 0$ in zato je izračun $\mathbb{Z}_2$ invariante nemogoč.

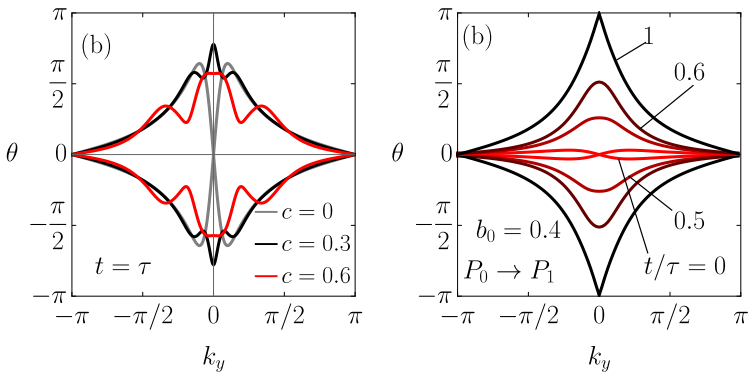

Slika 7.2: Preklop trajajoč $\tau = 15$ z začetkom pri $u_0 = -3$ in koncem pri $u_1 = -1$. (a) Wannierjevi tokovi po koncu preklopa v sistemih s $c = 0$ (siva), $c = 0.3$ (črna) in $c = 0.6$ (rdeča). (b) Wannierjev tokovi sistema s $c = 0$ in z zlomom simetrije na obrat časa velikosti $b_0 = 0.4$, prikazani med preklopom ob $t/\tau = 0$ (rdeča), $t/\tau = 0.5$ (temno rdeča), $t/\tau = 0.6$ (temnejša rdeča), in po preklopu ob $t/\tau = 1$ (črna).

Ker klasifikacija z $\mathbb{Z}_2$ invarianto zavisi od prisotnosti simetrije na obrat časa, obstajajo zvezne transformacije, ki zlomijo simetrijo med preklopom in tako adiabatsko povežejo različne topološke faze. To smo pokazali z uvedbo potenciala $b_0 \sin^2(\pi t/\tau)\, \hat{s}_x \otimes \hat{\sigma}_x$ v BHZ Hamiltonko, ki odpre energijsko režo ob prehodu čez kritično točko. Po dovolj počasnem preklopu se sistem znajde v osnovnem stanju

končne Hamiltonke s spremenjeno $\mathbb{Z}_2$ invarianto. Časovni razvoj Wannierjevih stanj je prikazan na sliki 7.2(b) in njihova končna oblika pripada topološko netrivialni fazi. Z uporabo tega mehanizma bi se lahko spremenilo Chernovo število $C_\uparrow = 0$ tarčnega sistema, ki se ga sklopi z dodatnim sistemom s Chernovim številom $C_\downarrow = 0$ tako, da tvorita BHZ model. Po zgoraj opisanem adiabatskem prehodu se sistema razklopi tako, da ima tarčni sistem $C_\uparrow = -1$, dodatni sistem pa $C_\downarrow = 1$.

Gostota vzbuditev

Zaradi zaprtja energijske reže se med preklopom pojavijo vzbuditve v prevodni pas. QWZ model je dvopasovni in za počasne preklope njegovo dinamiko opisuje Landau-Zenerjev model. BHZ model sestoji iz štirih energijskih pasov, vendar ker se med preklopom energijska reža zapre le med dvema pasovoma, se njuno efektivno dinamiko prav tako da prevesti na Landau-Zenerjev model. Model podaja točno rešitev za neadiabatski prehod, z uporabo katere smo izrazili porazdelitev vzbuditev v momentnem prostoru

$$n_{\mathrm{exc}}(\mathbf{k}) = e^{-(q-c)^2 2\tau/|u_0-u_1|}, \tag{7.12}$$

kjer je $q = |\mathbf{k} - \mathbf{k}_c|$. V primeru QWZ modela velja gornja enačba pri $c = 0$, saj tedaj BHZ model razpade na dve neodvisni kopiji QWZ modela. V primeru BHZ modela s $c = 0$ je potrebno izraz (7.12) podvojiti. Število vzbuditev ima največjo vrednost 1 pri momentih, kjer se je energijska reža zaprla. Celotna gostota vzbuditev je podana z naslednjima izrazoma

$$\begin{aligned} N_{\mathrm{exc}} &= \frac{|u_1 - u_0|}{4\pi\tau}, \quad c = 0, \\ N_{\mathrm{exc}} &= c\sqrt{\frac{|u_1 - u_0|}{8\pi\tau}}, \quad 0 < c \ll 1, \end{aligned} \tag{7.13}$$

kjer je vrednost za QWZ model enaka polovični vrednosti za $c = 0$. Zanimivo pri tem rezultatu je, da potenca, s katero gostota vzbuditev skalira s τ zavisi od prisotnoti sklopitve c. Gostota vzbuditev v obeh primerih sledi Kibble-Zurekovem skaliranju nič dimenzionalnih defektov in tako vidimo, da se različno skaliranje s τ pojavi, ker prisotnost sklopitve c vpliva na kritične eksponente in tako na univerzalnostni razred, kateremu pripada model.

Korelacijska dolžina

Kibble-Zurekovo skaliranje smo opazili tudi v dolžinski skali, ki je prisotna v sistemu po preklopu. V primeru Chernovega izolatorja smo jo razbrali iz širine Berryjeve ukrivljenosti, ki je deformirana glede na Berryjevo ukrivljenost osnovnega stanja, kakor je prikazano na sliki 7.3(a). Na sliki različne krivulje pripadajo sistemom po preklopih z različnim τ. Grafi so reskalirani s $\sqrt{\tau}$ vzdolž k_y in se prilegajo univerzalni krivulji. To nakazuje, da končna vrednost dolžinske skale skalira kot $\sqrt{\tau}$, kar je v skladu z napovedmi Kibble-Zurekovega mehanizma. Slika 7.3(b) prikazuje korelacijsko dolžino med preklopi z različnim τ. Vidimo, da dinamika kot po napovedih Kibble-Zurekovega mehanizma razpade na dva adiabatska in en zamrznjen režim. V prvem adiabatskem režimu se neravnovesna korelacijska dolžina sklada z dolžino osnovnega stanja (črna), nakar ji neha slediti v zamrznjenem območju (oranžno senčenje za $\tau = 20$), v katerem raste za vse τ z enako konstantno hitrostjo. Ob izhodu iz zamrznjenega območja niha okrog konstantne vrednosti.

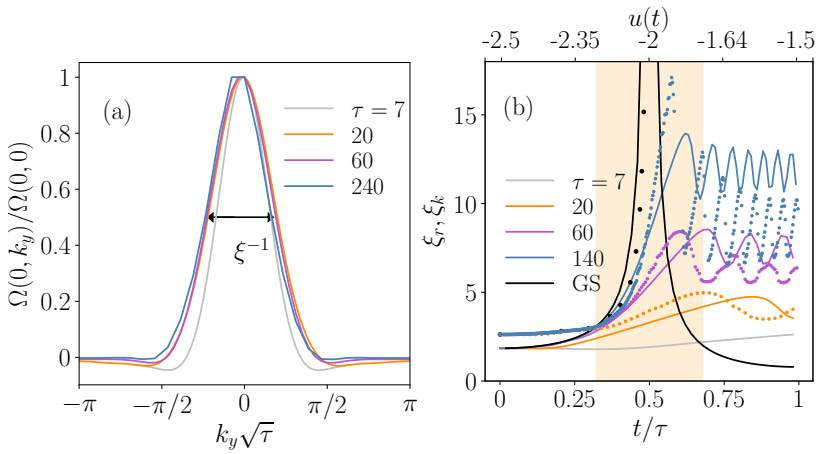

Slika 7.3: (a) Berryjeva ukrivljenost vzdolž $k_x = 0$ na koncu preklopov z različnimi τ, prikazana kot funkcija $k_y\sqrt{\tau}$. (b) Polne barvne črte prikazujejo ξ, razbrano iz Berryjeve ukrivljenosti, med preklopi z različnimi τ, črna črta pa pripada trenutnemu osnovnemu stanju. Točke prikazujejo velikostno skalo, ki je razbrana iz lokalnega Chernovega markerja. Oranžno območje označuje zamrznjen režim za preklop s $\tau = 20$.

Dolžinske skale v sistemih s simetrijo na obrat časa nismo bili zmožni razbrati iz funkcije ukrivljenosti, saj je njen integral – $\mathbb{Z}_2$ invarianta – nedefinirana po koncu preklopa. Zanimivo bi bilo poiskati način izračuna velikostne skale, ki ne zavisi od topološke invariante, in preveriti, če tudi v sistemih s simetrijo na obrat časa časovni razvoj dolžinske skale ustreza napovedim Kibble-Zurekovega mehanizma.

(Spinka) Hallova prevodnost

Ogledali smo si še, kaj se po preklopu zgodi s (spinsko) Hallovo prevodnostjo, ki je v osnovnem stanju določena z vrednostjo topološke invariante. (Spinski) Hallov tok smo po preklopu inducirali z vklopom šibkega časovno odvisnega homogenega vektorskega potenciala $A_x(t)$, ki povzroči električni tok, $E_x(t) = -\int A_x(t)\mathrm{d}t$. Električni tok v začetnem prehodnem režimu skokovito naraste in nato za dolge čase oscilira okrog povprečne vrednosti. Povprečna vrednost je blizu vrednosti v osnovnem stanju končne Hamiltonke in ker topološka invarianta ne sledi spremembi Hamiltonke, je korespondenca med topološko invarianto in (spinsko) Hallovo prevodnostjo izven ravnovesja podrta. Odziv sistema smo obravnavali v okviru časovno odvisne perturbacijske teorije in izrazili časovno povprečje (spinske) Hallove prevodnosti kot integral (spinske) Berryjeve ukrivljenosti in zasedenosti nivojev $n_n(\mathbf{k})$,

$$\bar{\sigma}_{yx}^{(\mathrm{spin})} = \frac{e^2}{(2\pi)^2} \sum_{n=1}^{2N_F} \int \mathrm{d}\mathbf{k}\, n_n(\mathbf{k}) \Omega_n^{(\mathrm{spin})}(\mathbf{k}). \tag{7.14}$$

Vsota gre po vseh energijskih pasovih. Od tod se vidi, da je (spinska) Hallova prevodnost po počasnih preklopih blizu vrednosti v osnovnem stanju končne Hamiltonke, saj je preklop adiabatski za vsa stanja razen za tista, katerih momenti se nahajajo v bližini zaprtja energijske reže. V limiti počasnih preklopov je odstopanje (spinske) Hallove prevodnosti od vrednosti končnega osnovnega stanja sorazmerno gostoti vzbuditev in tako od nje podeduje Kibble-Zurekovo skaliranje s časom preklopa.

Chernov izolator z robovi

Robna stanja so ključni pojav topoloških izolatorjev in v našem delu smo raziskali, kaj se zgodi z zasedenostjo stanj in s transportom po preklopu iz trivialne v topološko fazo. V ta namen smo obravnavali Chernov izolator v obliki traku, ki je končne širine N_x in ohranja periodične robne pogoje vzdolž osi y. Pasovna struktura razpade na $2N_x$ energijskih pasov z disperzijo po k_y. V topološki fazi sta prisotna dva energijska pasova, ki segata v energijsko režo, v kateri imata linearno disperzijo po k_y in pripadajoča lastna stanja so lokalizirana na robovih sistema. QWZ model ima simetrijo inverzije ter simetrijo delec-luknja in v delu smo obravnavali efekte zloma teh dveh simetrij na neravnovesno stanje po preklopu.

Gostota vzbuditev

Med preklopom čez kritično točko pri $u_c = -2$ se prevodni in valenčni energijski pasovi najbolj približajo točno v kritični točki pri $k_y = 0$. Po prehodu se razmaknejo pasovi, ki ustrezajo notranjosti sistema, pasova robnih stanj pa ostaneta staknjena pri k_y (z eksponentno majhno energijsko režo). Vzbuditve se ustvarijo tako v robnih stanjih kot v stanjih, ki ustrezajo notranjosti sistema. Celotna gostota vzbuditev pada s časom preklopa τ kot τ^{-1} za stanja notranjosti, kar je pričakovan rezultat iz obravnave translacijsko invariantnih sistemov. Porazdelitev vzbuditev notranjosti po $k_y\sqrt{\tau}$ je prikazana za različne τ na sliki 7.4(a) in se dobro ujema z analitično napovedjo (rdeča) za $1 < \tau \ll N_x^2$. Analitično napoved podaja kar rezultat za translacijsko invariantne sisteme (7.12), pointegriran po k_x. Pri počasnejših preklopih odstopa od napovedi, ker postane časovni razvoj adiabatski zaradi diskretizacije nivojev v x smeri. Gostota vzbuditev v robnih stanjih pada kot

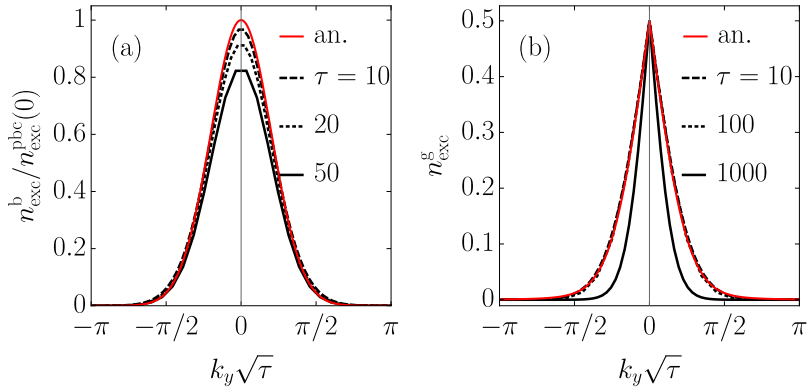

Slika 7.4: (a) Porazdelitev vzbuditev notranjosti v momentnem prostoru traku $N_x = 70$ po preklopih s $\tau = 10$ (črtkano), $\tau = 20$ (pike) in $\tau = 50$ (polne črte). Analitični izraz je prikazan z rdečo črto. (b) Porazdelitev vzbuditev v momentnem prostoru traku širine $N_x = 20$ po preklopih s $\tau = 10$ (črtkano), $\tau = 100$ (pike) in $\tau = 1000$ (polne črte). Rdeča barva prikazuje analitični rezultat.

$\tau^{-1/2}$, kar sledi iz enodimenzionalne narave robnih stanj in dejstva, da momentna porazdelitev skalira kot funkcija $k_y\sqrt{\tau}$,

$$N_{\mathrm{exc}} = \frac{L^D}{(2\pi)^D}\int \mathrm{d}^D\mathbf{k} n_{\mathrm{exc}}(\mathbf{k}) = \int \mathrm{d}^D\mathbf{k} g(k\sqrt{\tau}) \propto \tau^{-D/2}. \tag{7.15}$$

Skaliranje momentne porazdelitve vzbuditev na robu je prikazano na sliki 7.4(b). Skaliranje se podre za $\tau \gg N_x^2$, saj tedaj postane preklop neadiabatski šele daleč stran od kritične točke. Skaliranje smo izpeljali tudi analitično preko obravnave efektivne dvonivojske Hamiltonke robnih stanj, ki ustreza Landau-Zenerjevem modelu. Verjetnost za neadiabatski prehod smo izvrednotili v kritični točki, saj so energijski nivoji robnih stanj od tam dalje približno statični. Preko obravnave efektivne dvonivojske Hamiltonke robnih stanj smo izpeljali kritična eksponenta $\nu = 1$ in $z = 1$ ter s tem pokazali, da skaliranje gostote robnih vzbuditev s τ sledi napovedim Kibble-Zurekovega mehanizma za enodimenzionalne sisteme. S tem je kršena korespondenca notranjost-rob, saj so robna stanja skoraj popolnoma zasedena po počasnih preklopih, medtem ko se Chernovo število ne spremeni in ustreza trivialni fazi.

Skaliranje gostote vbuditev v robnih stanjih s τ je pogojeno s prisotnostjo simetrije inverzije. Ta poskrbi, da je med preklopom stičišče robnih energijskih pasov pritrjeno v $k_y = 0$ ali $k_y = \pi$. V kolikor je simetrija inverzije podrta, lahko med preklopom stičišče robnih energijskih pasov potuje po k_y. Prepotovano območje je velikosti b, kjer je b amplituda perturbacije, ki zlomi simetrijo inverzije. Elektroni znotraj prepotovanega območja se z verjetnostjo 1 vzbudijo v prevodni pas in tako se skaliranje s τ podre za $\tau \gg b^{-2}$. Simetrija delec-luknja pritrdi stičišče robnih energijskih pasov na $E = 0$. Podrtje te simetrije lahko povzroči, da stičišče potuje med preklopom po energijah znotraj energijske reže. Ta pojav ne vpliva na skaliranje vzbuditev v sistemu.

Hallova prevodnost

Šibki električni linearni potencial v smeri x inducira Hallov tok J_y vzdolž traku v smeri y. Električno polje velikosti E_0 smo vključili adiabatsko in obravnavali Hallov tok v linearnem približku ter izpeljali izraz

$$\bar{J}_y = G_0 E_0 \sum_{n=1}^{2N_x} \int \mathrm{d}k_y \, n_n(k_y) \Omega_n(k_y), \tag{7.16}$$

$$\Omega_n(k_y) = -\partial_{k_y} \langle \psi_n(k_y) | \hat{x} | \psi_n(k_y) \rangle. \tag{7.17}$$

Izraz za $\Omega_n(k_y)$ se za sisteme s periodičnimi robnimi pogoji prevede na Berryjevo ukrivljenost. $n_n(k_y)$ je zasedenost n-tega lastnega stanja pri k_y. Hallova prevodnost G_{yx} je definirana kot

$$G_{yx} = J_y/U, \quad U = E_0(\langle \psi_R(0) | \hat{x} | \psi_R(0) \rangle - \langle \psi_L(0) | \hat{x} | \psi_L(0) \rangle), \tag{7.18}$$

kjer je $|\psi_{R(L)}(0)\rangle$ lastno stanje pri $k_y = 0$, lokalizirano na desnem (levem) robu. U predstavlja napetost med robovoma traku. Za sistem v osnovnem stanju je $n_n(k_y)$ enak Fermi-Diracovi porazdelitvi in v tem primeru je Hallova prevodnost kvantizirana v enotah G_0. Za stanje po preklopu je $n_n(k_y)$ opisana s porazdelitvijo vzbuditev s slike 7.4. Ker se po počasnih preklopih vzbuditve pojavijo le na majhnem območju k_y blizu zaprtja energijske reže, je po preklopu Hallova prevodnost blizu kvantizirani vrednosti končnega osnovnega stanja. Deviacije od le-te padajo kot τ^{-1}, torej enako kot v sistemih s periodičnimi robnimi pogoji. Preko merjenja električnega toku v traku bi lahko torej merili skaliranje Kibble-Zurek, ki velja za neskončne translacijsko invariantne sisteme.

Preklop v sistemih z zlomljeno simetrijo inverzije ne vpliva na skaliranje Hallove prevodnosti. Ker se po preklopu ustvarijo vzbuditve z verjetnostjo 1 na le enem robnem pasu, bo v sistemu že v odsotnosti električnega polja prisoten neničelni električni tok, ki bo tekel le po enem robu sistema.

Chernov izolator s šibkim neredom

Kritično obnašanje osnovnega stanja in dinamiko po preklopu Chernovega izolatorja smo opazovali še v realnem prostoru. V ta namen smo v QWZ model vpeljali majhen nered v parameter u, ki je zlomil translacijsko simetrijo in tako razkril kritične lastnosti v realnem prostoru. Motivacija za to izhaja iz dejstva, da topološke izolatorje dobro opiše Kibble-Zurekov mehanizem, ki v sistemih s spontanim zlomom simetrije napove tvorbo topoloških defektov in domen. Kot analog lokalnega ureditvenega parametra smo opazovali lokalni Chernov marker [79, 176],

$$c(\mathbf{r}) = 2\pi i \sum_{\sigma} \langle \mathbf{r}, \sigma | \hat{P}[-i[\hat{x}, \hat{P}], -i[\hat{y}, \hat{P}]] | \mathbf{r}, \sigma \rangle, \tag{7.19}$$

integral katerega da Chernovo število in tako služi kot prostorski analog Berryjeve ukrivljenosti. V zgornji enačbi $\hat{P}$ označuje projektor na zasedena stanja, $\hat{x}$ in $\hat{y}$ pa operatorja pozicije.

Osnovno stanje

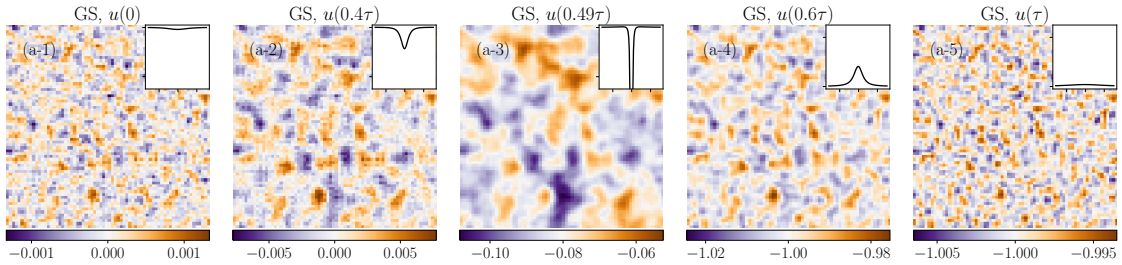

Slika 7.5: Lokalni Chernov marker osnovnega stanja Hamiltonk, ki segajo iz trivialne v topološko fazo pri (1) $u = -2.5$, (2) $u = -2.15$, (3) $u = -2$, (4) $u = -1.85$ in (5) -1.5. Velikost sistema je $N = 70$ in amplituda nereda $\delta u_0 = 0.05$. Vstavljene slike prikazujejo Berryjevo ukrivljenost čistega sistema pri pripadaojčih vrednostih u, vzdolž linije $k_x = 0$ od $k_y = -\frac{\pi}{4}$ do $k_y = \frac{\pi}{4}$. Vertikalna os gre od nič do 0.005π v panelih (a-4) ain (a-5), in od -0.005π do nič v ostalih.

V referenci [80] so pokazali, da v čistih sistemih z robom lokalni Chernov marker odraža dolžinsko skalo, ki blizu topološkega faznega prehoda skalira kot dolžinska skala, izračunana iz Berryjeve ukrivljenosti. V našem delu smo pokazali, da se kritična dolžinska skala pojavi v realnem profilu lokalnega Chernovega markerja in sicer kot velikost območij, v katerih lokalni Chernov marker odstopa nad (oranžna) oziroma pod (modra) povprečno vrednostjo, ki je enaka Chernovem številu. Slika 7.5 prikazuje profile za različne vrednosti u, ki segajo čez topološki fazni prehod pri $u_c = -2$. Kakor je razvidno s slike, nehomogenosti v profilu rastejo ob približevanju kritične točke. Rastejo kot potenčna funkcija $|u - u_c|$ s potenco, ki v limiti

neskončno velikega sistema narašča proti 1 in se tako ujema z napovedmi iz Berryjeve ukrivljenosti.

Stanje po preklopu

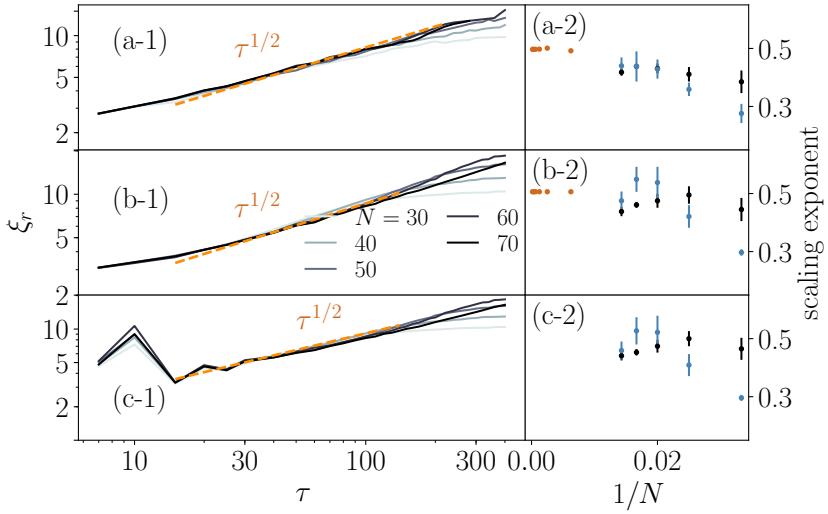

Slika 7.6: (1) Polne črte prikazujejo velikost nehomogenosti ξ na koncu preklopa, izpovprečeno po 20 realizacij nereda velikosti $\delta u_0 = 0.05$, za (a) lokalni Chernov marker, (b) porazdelitev vzbuditev v realnem prostoru in (c) orbitalno polarizacijo kot funkcijo τ za sisteme različnih velikosti N. Rezultati so predstavljeni na log-log skali. Oranžne črtkane črte prikazujejo najbolje prilagajočo funkcijo $\tau^{1/2}$. (2) Skalirna potenca za neurejene (črna) in čiste (oranžna) sisteme, ocenjena iz podatkov ξ od τ na intervalu $15 \leq \tau \leq 140$. Za neurejene sisteme je ocenjena še na območju $30 \leq \tau \leq 300$ (modra).

Po preklopu profil lokalnega Chernovega markerja vsebuje nehomogenosti, velikost katerih skalira kot potenčna funkcija τ z eksponentom, ki je blizu 1/2, torej sledi napovedi Kibble-Zurekovega mehanizma in rezultatu iz Berryjeve ukrivljenosti. Rezultati so prikazani na sliki 7.6(a). Na sliki 7.3(b) je s pikami prikazan časovni razvoj velikosti nehomogenosti lokalnega Chernovega markerja med preklopom. Velikost nehomogenosti sledi obnašanju velikostne skale izvrednotene iz Berryjeve ukrivljenosti in tako Kibble-Zurekovem opisu dinamike z adiabatskim-impulznim približkom.

Nehomogenosti s podobnim skaliranjem se pojavijo še v porazdelitvi vzbuditev v realnem prostoru in v orbitalni polarizaciji, ki je definirana kot $\langle \mathbf{r}, \sigma | \hat{P}(t) \hat{\sigma}_z | \mathbf{r}, \sigma \rangle$. Profili teh dveh količin so visoko korelirani s profilom lokalnega Chernovega markerja in prav tako skalirajo kot potenčna funkcija τ z eksponentom blizu 1/2 (sliki 7.6(b) in 7.6(c)). Orbitalna polarizacije je bila že merjena v eksperimentu, ki je realiziral QWZ Hamiltonko v laboratoriju s hladnimi ^{87}Rb atomi [134]. Poleg te možne meritve bi lahko opazovali nehomogenosti v gostoti naboja, ki se pojavijo v sistemih s kršeno simetrijo delec-luknja, kakor je recimo Haldanov model.

List of publications

1. Lara Ulčakar, Jernej Mravlje, Tomaž Rejec, *Kibble-Zurek behavior in disordered Chern Insulators*, accepted to Phys. Rev. Lett. **00**, 00 (2020).

2. Domenico Monaco, Lara Ulčakar, *Spin Hall conductivity in insulators with non-conserved spin*, Phys. Rev. B **102**, 125138 (2020), `https://doi.org/10.1103/PhysRevB.102.125138`.

3. Brecht Donvil, Lara Ulčakar, Tomaž Rejec, Anton Ramšak, *Thermal effects on a nonadiabatic spin-flip protocol of spin-orbit qubits*, Phys. Rev. B **101**, 205427 (2020), `https://journals.aps.org/prb/abstract/10.1103/PhysRevB.101.205427`.

4. Lara Ulčakar, Jernej Mravlje, Tomaž Rejec, *Slow quenches in Chern insulator ribbons*, Phys. Rev. B **100**, 125110 (2019), `https://doi.org/10.1103/PhysRevB.100.125110`.

5. Lara Ulčakar, Tomaž Rejec, Jure Kokalj, Sara Sangtarash, Hatef Sadeghi, Anton Ramšak, John H. Jefferson, Colin J. Lambert, *On the resilience of magic number theory for conductance ratios of aromatic molecules*, Scientific Reports **9**, 3478 (2019), `https://www.nature.com/articles/s41598-019-39937-1`.

6. Lara Ulčakar, Jernej Mravlje, Anton Ramšak, Tomaž Rejec, *Slow quenches in two-dimensional time-reversal symmetric Z2 topological insulators*, Phys. Rev. B **97**, 195127 (2018), `https://doi.org/10.1103/PhysRevB.97.195127`.

7. Anton Ramšak, Tilen Čadež, Ambrož Kregar, Lara Ulčakar, *Exact spin-orbit qubit manipulation*, Eur. Phys. J. Special Topics **227**, 353–363 (2018), `https://link.springer.com/article/10.1140/epjst/e2018-00094-2`.

8. Lara Ulčakar, Anton Ramšak, *Effects of noise on fidelity in spin-orbit qubit transformations*, Int. J. Mod. Phys. B **32**, 1840028 (2018), `https://www.worldscientific.com/doi/abs/10.1142/S0217979218400283`.

9. Lara Ulčakar, Anton Ramšak, *Exact analysis of gate noise effects on non-adiabatic transformations of spin-orbit qubits*, New J. Phys. **19**, 093015 (2017), `https://iopscience.iop.org/article/10.1088/1367-2630/aa7faf`.

10. Lara Ulčakar, Tomaž Rejec, Anton Ramšak, *Linear conductances of gated graphene structures with selected connectivity*, Acta chimica slovenica **63**, no. 3 (2016), `https://journals.matheo.si/index.php/ACSi/article/view/2560`.